Universidade do Minho
I3Bs - Instituto de Investigação em Biomateriais,
Biodegradáveis e Biomiméticos

Helena Rocha Moreira

Novel platforms for vascularization in skin wound healing

Novel platforms for vascularization in skin wound healing

Helena Rocha Moreira

UMinho | 2022

dezembro de 2022

Universidade do Minho

I3Bs - Instituto de Investigação em Biomateriais, Biodegradáveis e Biomiméticos

Helena Rocha Moreira

Novel platforms for vascularization in skin wound healing

Tese de Doutoramento em Engenharia de Tecidos, Medicina Regenerativa e Células Estaminais

Trabalho efetuado sob a orientação

Doutora Alexandra Margarida Pinto Marques

Professor Doutor Rui Luís Gonçalves dos Reis

dezembro de 2022

ACKNOWLEDGMENTS

First, I would like to acknowledge my supervisors, Doctor Alexandra P. Marques and Professor Rui L. Reis. Their guidance deeply marked the construction of my scientific identity and shaped my attitude and stance towards science. Words cannot express my gratitude to Doctor Alexandra P. Marques for her invaluable patience, dedication, support, and knowledge. Her hard work, and scientifically rigorous skills always left me astonished. Thank you, Xana! To Professor Rui L. Reis for the opportunity to develop my PhD in the institute of excellence giving me a rare chance to pursue a science path in I3Bs. Either through the attribution of a scholarship or by providing me with all the brilliant insights.

During this PhD I was lucky enough to visit, work and learn from Professor Fergal O'Brien and his team members. Thank you for the sharing with me valuable knowledge and for the encouragement to pursue the scientific path.

I am also thankful to my mentors in the lab: Lucília, Mariana and Rogério. You have always provided me with assistance, guidance, and ideas whenever I needed. To all my co-authors for the help in the development of the different works in research areas that I was less familiar. I would also to acknowledge the *Fundo Social Europeu através do Programa Operacional do Capital Humano* under the scope of the PD/169/2013, for giving me the financial support to develop this thesis (NORTE-08- 5369-FSE-000037).

Daniel, Manuela, Sara, Andreia e Raquel, a big thank you, for all the moments we have spent together and for making hard work days into better days. Thank you for your friendship in the past years. I am sure that we will have many more adventures to come. Daniel, a big thank you is not even enough.

To my parents and to my brother. Thank you so much for your love, for believing in me unconditionally, for all the support in every step I make, for encouraging me in pursuing my dreams. For always encouraging me and for giving me all the opportunities. For your wise advices and patience. I could have not done this without you. You are my model and my inspiration. I would never be able to thank you enough.

To David, who has been by my side in this rollercoaster journey. Thank you for your care, patience, support, help, technical advice. Most importantly, thank you for your love.

STATEMENT OF INTEGRITY

I hereby declare having conducted this academic work with integrity. I confirm that I have not used plagiarism or any form of undue use of information or falsification of results along the process leading to its elaboration.

I further declare that I have fully acknowledged the Code of Ethical Conduct of the University of Minho.

ABSTRACT

In cutaneous wounds, neovascularization is critical for tissue repair, influencing the healing cascade from the early onset to the remodeling phase. When vascularization is affected by alterations in angiogenic signaling, the healing process is impaired and the quality of the neotissue formed is affected. Several strategies have been explored to promote neovascularization in cutaneous wounds; however, their clinical translation is still to be achieved. Therefore, this thesis aimed to explore innovative strategies to promote *in vitro* vascularization of tissue engineered (TE) constructs for wound healing. To this end, we took advantage of gellan gum-based spongy-like hydrogels to explore i) the modulation of a fibroblast-driven angiogenic microenvironment fostering endothelial cell (ECs) potential, and ii) the ability of the stromal vascular fraction (SVF) from adipose tissue to generate a self-regulatory angiogenic microenvironment in the absence of extrinsic growth factors.

To minimize batch-to-batch variability associated to the processing of dried polymeric networks/spongy-like hydrogels, we designed two freezing devices and mapped the effect of the thermal parameters on the properties of the obtained structures. We were then able to fabricate highly reproducible materials with fine-tuned microarchitecture according to our specific needs. A bilayered structure was used as a template to explore the distinct functions of the dermal fibroblast's subpopulations, providing evidence that pre-selection of papillary and reticular fibroblasts is relevant for promoting the *in vitro* prevascularization of skin TE constructs. We further explored the delivery of genes-encoding angiogenic factors to fibroblasts, generating a microenvironment prone to vascularization while the spongy-like hydrogel offered structural support for new matrix deposition. Finally, we exploited specific integrins found in ECs present in SVF by designing integrin-specific spongy-like hydrogels to retain those cells, to ultimately triggering vasculogenesis. This *in vitro* vasculogenesis platform benefited neovascularization upon implantation by fostering inosculation with the host vasculature, but negatively impacted the healing of cutaneous wounds.

Overall, the works herein reported provide valuable contributions in the field of vascularization of TE constructs, proposing complementary and alternative approaches to the use of ECs, taking a step towards the development of better therapies for cutaneous wounds.

Keywords: cutaneous wounds, endothelial cells, fibroblasts, spongy-like hydrogels, stromal vascular fraction, vascularization.

RESUMO

Em feridas cutâneas, a neovascularização é crítica para a reparação do tecido, influenciando a cicatrização do início à fase de remodelação. Quando a vascularização é afetada por alterações na sinalização angiogénica, o processo de cicatrização é prejudicado, afetando a qualidade do neotecido formado. Várias estratégias têm sido exploradas para promover a neovascularização em feridas cutâneas; no entanto, vários fatores dificultam a sua translação para a clínica. Esta tese, teve como objetivo explorar estratégias inovadoras de vascularização *in vitro* de estruturas de engenharia de tecidos (ET) para cicatrização de feridas. Para tal, tirámos partido dos hidrogéis esponjosos à base de goma gelana para explorar i) a modulação do microambiente angiogénico mediado por fibroblastos para promover o potencial das células endoteliais (CEs), e ii) a capacidade da fração vascular estromal (FVE) do tecido adiposo em gerar um microambiente autorregulador angiogénico sem fatores de crescimento extrínsecos.

Para minimizar a variabilidade associada ao processo de preparação de redes poliméricas secas/hidrogéis esponjosos, desenvolvemos dois dispositivos de congelamento e mapeamos o efeito dos parâmetros térmicos nas propriedades das estruturas obtidas. Isto permitiu fabricar materiais com características altamente reprodutíveis com microarquitetura ajustada de acordo com nossas necessidades específicas. Uma estrutura baseada em bicamada foi utilizada como modelo para explorar as funções típicas de cada subpopulação de fibroblastos da derme, demonstrando que a pré-seleção dos fibroblastos papilares e reticules promove a pré-vascularização *in vitro* de estruturas de ET de pele. Explorámos ainda a entrega de genes codificadores de fatores de crescimento angiogénicos aos fibroblastos para gerar um microambiente propenso à vascularização, enquanto o hidrogel esponjoso ofereceu suporte estrutural para a deposição de nova matriz. Finalmente, explorámos integrinas específicas encontradas nas CEs presentes na FVE e desenhámos hidrogéis esponjosos integrina-específicos capazes de reter essas células e desencadear a vasculogénese *in vitro*. Esta plataforma de vasculogénese *in vitro* beneficiou a neovascularização *in vivo* após a implantação, promovendo a inosculação com a vasculatura hospedeira, mas teve um impacto negativo na cicatrização de feridas cutâneas.

Em suma, os trabalhos relatados fornecem contribuições valiosas no campo da vascularização de estruturas de ET, propondo abordagens complementares e alternativas ao uso de CEs e contribuindo para o desenvolvimento de terapias para feridas cutâneas.

Palavras-chave: células endoteliais, feridas cutâneas, fibroblastos, fração vascular do estroma, hidrogéis esponjosos, vascularização.

TABLE OF CONTENTS

LIST OF ABBREVIATIONS

A
Abs – Absorbance
Al – Aluminum
Ang – Angiopoietin
Angio-1 – Angiopoietin-1
ANOVA – Analysis of variance
ASCs – Adipose-derived stem cells
atm – atmosphere

B
bFGF – basic Fibroblast growth factor
bp – base pair
BSA – Bovine serum albumin

C
Ca-AM – Calcein-Acetoxymethyl
cDNA – complementary DNA
Ch – Chitosan
ChS – Chondroitin sulfate
cm – centimeter
CO_2 – Carbon dioxide
COL – Collagen
CTR(L) – control
Cu – Copper

D
°C – Degree celsius
°C min^{-1} – Degree celsius *per* minute
2D – 2-Dimensional
3D – 3-Dimensional
d – Days
Da – Dalton
DAPI – 4',6-diamidino-2-phenylindole
DD – Degree of deacetylation
DGAV – *Direcção Geral de Alimentação e Veterinária*
DHT – Dehydrothermally
DI – Deionized water
Dk – donkey
DM – Degree of modification
DMEM – Dulbecco's modified Eagle's medium
DNA - Deoxyribonucleic acid
DVS – Divinyl sulfone

E
EC – Endothelial cells
ECM – Extracellular matrix
EDC – N-(3-Dimethylaminopropyl)-N'-ethylcarbodiimide hydrochloride
EGF – Epidermal growth factor

ELISA – Enzyme-linked immunosorbent assay
EPC – Endothelial progenitor cells
EPS – Expanded polystyrene
et al. – "and others", from latin *et alii*
EtOH – ethanol
Ex/Em – Excitation/Emission

F
FACS – Fluorescence-activated cell sorting
FBS – Fetal bovine serum
FGF-2 – basic Fibroblast growth factor

G
g – grams
g L^{-1} – grams *per* liter
GAG – Glycosaminoglycan
GAM – Gene-activated matrices
GFs – Growth factors
GG – Gellan gum
GGDVS – Divinyl sulfone-modified gellan gum
Gly – Glycine

H
h – Hours
H&E – Hematoxylin–eosin
hDFbs – Human dermal fibroblasts
hDMECs – Human dermal microvascular endothelial cells
HGF/SF – Hepatocyte growth factor/scatter factor
HOAc – Glacial acetic acid
HUVECs – Human umbilical vein endothelial cells
HyA – Hyaluronic acid

I
i.e. – "In other words", from latin *id est*
IFD – Insulated freezing device
IGF-1 – Insulin growth factor 1
IL-6 – Interleukin-6
i.p – Intraperitoneal

K
kDa – kilodalton
keV – kiloelectron-volt
KGF – Keratinocyte growth factor
kPa – kilopascal

M
α-MEM – Minimum Essential Medium

μA – microampere
μ-BCA – Micro-bicinchoninic acid
μ-CT – Micro-computed tomography
μg mL^{-1} – microgram *per* milliliter
μg μL^{-1} – microgram *per* microliter
μL – microliter
μm – micrometer
μM – micromolar
M – Molar
MDa – Megadalton
mg – milligram
mg kg^{-1} – milligram *per* kilo
mg mL^{-1} – milligram *per* milliliter
MHz – Megahertz
min – minute
mL – Milliliter
mm – Millimeter
mM – Millimolar
mm min^{-1} – millimeter *per* minute
Mol – Mole
Ms – mouse
MT – Masson's Trichrome
MTS – 3-(4,5-dimethylthiazol-2-yl)-5-(3-carboxymethoxyphenyl)-2-(4-sulfophenyl)-2H-tetrazolium
MW– Molecular weight

N
N - Newton
n – Number of samples
N/P – nitrogen:phosphate ratio
NFD – Non-insulated freezing device
NHS – N-Hydroxysuccinimide
nm – Nanometer

P
(v/v) – Percentage of volume/volume
(w/v) – Percentage of weight/volume
% – Percentage
p – Statistical level of significance
PBS – Phosphate buffer saline
PDGF – Platelet-derived growth factor
pDNA – plasmid DNA
PECAM1 – Platelet and endothelial cell adhesion molecule 1
PEI – Polyethyleneimine
PenStrep – Penicillin-Streptomycin
pFGF2 – plasmid encoding basic fibroblast growth factor gene
PGF – Placental growth factor
pGFP – pDNA enconding Green Fluorescent Protein
pGLuc – pDNA encoding Gaussia Luciferase

Phalloidin – Phalloidin–Tetramethylrhodamine B isothiocyanate
PI – Propidium iodide
PR – Picrosirius red
Pro – Proline
PRP – Platelet-rich plasma
pVEGF – plasmid encoding vascular endothelial growth factor gene

Q
qPCR – quantitative real-time Polymerase Chain Reaction

R
Rb – rabbit
RFU – Relative fluorescence unit
RGD – Cyclo(-RGDfC)
RNA – Ribonucleic acid
Rpm – Rotations *per* minute
RT – Room temperature

S
s – second
SD – Standard deviation
SDF-1 – Stromal-derived factor 1
SEM – Scanning electron microscopy
SVF – Stromal vascular fraction

T
T1 - CTTSWSQCSKS
TCPS – Tissue culture polystyrene
TE – Tissue engineering
TERM – Tissue Engineering and Regenerative Medicine
TGF – Transforming growth factor
TRITC - Tetramethylrhodamine B isothiocyanate

U
U – Units
U mL^{-1} – Units *per* milliliter

V
V – Volume
VEGF – Vascular endothelial growth factor
VEGFR-2/KDR – Vascular endothelial growth factor receptor-2
vWF – von Willebrand factor

W
λ – Wavelength
WB – Western blot
W$_d$ – Dry weight
W$_w$ – Wet weight

LIST OF EQUATIONS

LIST OF FIGURES

LIST OF SUPPLEMENTARY FIGURES

LIST OF TABLES

LIST OF SUPPLEMENTARY TABLES

SHORT *CURRICULUM VITAE*

Helena Rocha Moreira was born on the 7th of August 1990, in Vila Nova de Gaia, Portugal. In 2013, Helena graduated in Bioengineering with a major in Biomedical Engineering (MSc) with a final graduation mark of 15 over 20 at the Faculty of Engineering of the University of Porto. During this period, she developed her ERASMUS project in Biomaterials, under the supervision of Professor Paola Petrini and Doctor Fabiola Munarin in the "Politecnico di Milano" (Milan, Italy), and her MSc dissertation under the scope of pectin hydrogels for skin regeneration, under the supervision of Professor Pedro Granja, from the Institute of Biomedical Engineering from the University of Porto.

Helena joined the 3B's Research Group at the University of Minho in 2014. After doing research under the scope of hydrogels from skin regeneration, she proceeded her academic career to a more applied field, applying tissue engineering for skin vascularization. In 2016, Helena was awarded with a PhD grant from Horizonte Norte2020 and started the PhD in Tissue Engineering, Regenerative Medicine and Stem Cells (TERM&SC) in the University of Minho, being the main focus of her research the development of strategies to target vascularization. In 2017, she had the opportunity to travel to the Royal College of Surgeons in Ireland (RCSI, Dublin, Ireland) and work at the TERG group from Professor Fergal O'Brien, advancing on gene-actived matrices for the formation of capillary-like structures in 3D microenvironments.

As a PhD student in the 3B's Research Group, Helena was also actively involved in other projects and supported the instruction and advice of several students and colleagues. As detailed in this thesis, as a result of her research work during the PhD, Helena developed her skills on materials, cellular and molecular biology. Her work was presented in important international meetings in the field of her research and resulted in 1 patent, 6 peer-reviewed papers (5 as first author), 2 first-author oral presentations in international conferences, and several poster presentations (2 indexed).

LIST OF PUBLICATIONS

The work performed during the PhD period resulted in the publications listed below:

PAPERS IN INTERNATIONAL SCIENTIFIC JOURNALS WITH PEER-REVIEW (as first-author)

Moreira HR, da Silva LP, Reis RL, Marques AP. (2020) Tailoring spongy-like hydrogels' microstructure by controlling freezing parameters. Polymers 12 (2): 329. DOI: 10.3390/polym12020329.

Moreira HR, Raftery RM, da Silva LP, Cerqueira MT, Reis RL, Marques AP, O'Brien FJ. (2021) *In vitro* vascularization of tissue engineered constructs by non-viral delivery of pro-angiogenic genes. Biomaterials Science 9 (6): 2067-2081. DOI: 10.1039/d0bm01560a.

Moreira HR, Marques AP. (2022) Vascularization in skin wound healing: where do we stand and where do we go? Current Opinion in Biotechnology 73: 253-262. DOI: 10.1016/j.copbio.2021.08.019.

Moreira HR, Rodrigues DB, Freitas-Ribeiro S, da Silva LP, Morais AS, Jarnalo M, Horta R, Reis RL, Pirraco RP, Marques AP. (2022) Integrin-specific hydrogels for growth factor-free vasculogenesis. npj Regenerative Medicine 7 (57). DOI: 10.1038/s41536-022-00253-4.

Moreira HR, Rodrigues DB, Freitas-Ribeiro S, da Silva LP, Morais AS, Jarnalo M, Horta R, Reis RL, Pirraco RP, Marques AP. (2022) Spongy-like hydrogels prevascularization with the adipose tissue vascular fraction delays cutaneous wound healing by sustaining inflammatory cell influx. Materials Today Bio 17: 100496. DOI: 10.1016/j.mtbio.2022.100496.

Moreira HR, Cerqueira MT, da Silva LP, Pires J, Jarnalo M, Horta R, Reis RL, Marques AP. (2022) Pre-selection of fibroblasts subsets prompt prevascularization of tissue engineered skin analogues. *(submitted)*

PAPERS IN INTERNATIONAL SCIENTIFIC JOURNALS WITH PEER-REVIEW (as co-author)

Rodrigues DB, **Moreira HR**, Cerqueira MT, Marques AP, Castro AG, Reis RL, Pirraco RP. (2022) Highly tailorable gellan gum nanoparticles as a platform for the development of T cell activator systems. Biomaterials Research 26 (48). DOI: 10.1186/s40824-022-00297-z.

Rodrigues DB, **Moreira HR**, Jarnalo M, Horta R, Marques AP, Reis RL, Pirraco RP. (2022) Generation of 3D melanoma models with higher complexity using an assembloid-based approach. Advanced Science. *(under review, major revisions)*

PATENTS

Rodrigues DB, **Moreira HR**, Gasperini L, Cerqueira MT, Marques AP, Pirraco RP, Reis RL. "HYDROGEL-LIKE PARTICLES, METHODS AND USES THEREOF", WO/2021/064678 (PCT/IB2020/059275).

CONFERENCE ORAL PRESENTATIONS

Moreira HR, da Silva LP, Reis RL, Marques AP, Production of a bilayered spongy-like hydrogel as skin templates. Gene2Skin Final Conference, Porto, Portugal, 2018.

Rodrigues DB, **Moreira HR**, Reis RL, Marques AP. Generation of an *in vitro* 3D cell sheet-based model of scar-like tissue. O0913, World Congress of Biomechanics, Dublin, Ireland, 2018.

Moreira HR, Raftery R., Reis RL, Marques AP, O'Brien FJ. Development of skin models with stable capillary-like structures using gene-activated scaffolds. O0881, World Congress of Biomechanics, Dublin, Ireland, 2018.

ABSTRACTS PUBLISHED IN INDEXED JOURNALS

Rodrigues DB, **Moreira HR**, Reis RL, Marques AP. (2017) *In vitro* 3D cell sheet-based model for unraveling scar pathophysiology. P-09-02-48, Toxicology Letters 280S: S269. http://dx.doi.org/10.1016/j.toxlet.2017.07.952.

Moreira HR, Rodrigues DB, Reis RL, Marques AP. (2017) Unravelling the path to create a cell sheet-based model of skin scar-like tissue. 0236, European Cells and Materials 33 (2). ISSN 1473-2262.

CONFERENCE POSTERS

Moreira HR, Rodrigues DB, Pires RA, Reis RL, Marques AP (2016) Cell sheet-based model for understanding scarring pathophysiology. The Gene2Skin Conference.

Abreu CM, Lago MEL, Silva LP, **Moreira HR**, Cerqueira MT, Reis RL, and Marques AP (2016) Gellan gum-based hydrogels for the recreation of hair follicle microenvironments. The Gene2skin conference.

Abreu CM, Lago MEL, Silva LP, **Moreira HR**, Cerqueira MT, Reis RL, and Marques AP (2016) Gellan gum-based hydrogels as a suitable platform to recreate the hair follicle 3D compartments. Chem2Nature Conference.

Moreira HR, Raftery R, Reis RL, Marques AP, O'Brien FJ (2017) Development of a gene-activated scaffold for long-term stability of capillary-like structures in a skin model. Gene2Skin Winter School.

Rodrigues DB, **Moreira HR**, Gasperini L, Cerqueira MT, Silva LP, Marques AP, Santos TC, Reis RL (2017) Gellan gum-based antigen presenting cells for immunomodulation through T-cell priming. TERM STEM/Forecast, Porto, Portugal.

Moreira HR, Rodrigues DB, Pires RA, Reis RL, Marques AP (2018) Creating a 3D *in vitro* scar-like tissue model based on cell sheet technology. Gene2Skin Summer School, G2S06, Porto, Portugal.

Rodrigues DB, **Moreira HR**, Gasperini L, Cerqueira MT, Marques AP, Santos TC, Reis RL (2018) Tailoring of an artificial antigen presenting cell system for immunotherapy. Chem2Nature, P79, Porto, Portugal.

Moreira HR, Cerqueira MT, Silva LP, Reis RL, Marques AP (2019) Bi-layered gellan gum spongy-like hydrogels for skin tissue engineering. TERMSTEM

Moreira HR, Cerqueira MT, Silva LP, Reis RL, Marques AP (2019) Development of a stratified bi-layered skin equivalent. TERMSTEM

Rodrigues DB, **Moreira HR**, Gasperini L, Cerqueira MT, Marques AP, Pirraco RP, Reis RL (2019) Gellan gum as a platform for the development of T-cell activator systems. Advanced Cell Therapies and Tissue Engineering, P60/90, Milan, Italy.

AWARDS

Awarded with a 4-year Horizonte Norte2020 PhD scholarship (NORTE-08-5369-FSE-000037).

Awarded the "Best Short Oral Presentation" prize, Gene2Skin Final Conference, Porto, Portugal, 2018.

PEER REVIEWING

Peer Review of Journal of the Mechanical Behavior of Biomedical Materials (Publons-indexed).

Peer Review of Journal of Tissue Engineering and Regenerative Medicine (Publons-indexed).

Peer Review of Applied Biomaterials & Functional Materials.

INTRODUCTION TO THE STRUCTURE OF THE THESIS

This thesis comprises distinct strategies that were explored for the *in vitro* vascularization of tissue engineered (TE) constructs aimed for skin wound healing.

A fundamental literature overview of the recent strategies of vascularization in skin wound healing is provided in **Chapter I**. This section describes the main concepts associated with vascularization, namely vasculogenesis and angiogenesis, as well as the processes that occur during wound healing. Moreover, it provides an updated state-of-the-art summary of the strategies that have been explored to promote vascularization considering two perspectives: biomaterial- and cell-based approaches.

In **Chapter II**, the materials and methodologies used throughout the experimental work are thoroughly described. The main goal of this chapter is to provide a solid description of the materials and methods used, and the rationale behind them. Although the subsequent chapters also include a materials and methods section, the methodological description present in this section is more detailed, better ensuring the reproduction of the methodologies used and/or developed.

The chapters that follow represent the main body of the thesis and are based on the manuscripts that are accepted or submitted for publication in different peer-reviewed journals. For each of these chapters, an introduction with the motivation for the work and hypothesis are presented, followed by the materials and methods used, the description of the results, and an integrated discussion of the results obtained in relation to the bibliography, together with the concluding remarks.

Gellan gum (GG) spongy-like hydrogel-based approaches have proven to positively impact cutaneous wound healing depending on their intrinsic polymeric composition and cellular components. However, due to variations that occur during the freezing step of the well-defined process of preparation of these materials, they are also prone to batch-to-batch discrepancies. Therefore, to minimize this variability, in **Chapter III** we designed two freezing devices and tested their effect over the properties of GG spongy-like hydrogels. We confirmed that batch-to-batch variations were mostly due to the freezing step and that the tested devices allow fine-tuning the microarchitecture of the GG spongy-like hydrogels.

Prevascularization of TE constructs is still one of the most successful approaches in fostering vascularization. As such, we explored two major strategies to promote the prevascularization of GG spongy-like hydrogels. The first one was based on the known communication between fibroblasts and endothelial cells (EC), and intended to explore the modulation of a fibroblast-driven angiogenic microenvironment to foster ECs potential. In the second approach, we took advantage of the ability of the

stromal vascular fraction (SVF) from adipose tissue to generate a self-regulatory angiogenic microenvironment in the absence of extrinsic growth factors.

The dermis comprises two distinct layers – the papillary and reticular dermis – with different functions such as the maintenance of skin's microvasculature, which is highly linked to the respective fibroblast's subpopulations. Thus, in **Chapter IV**, we hypothesized that pre-selection of the subpopulations of fibroblasts would benefit the generation of skin TE constructs, promoting its prevascularization *in vitro*. We developed a bilayered structure comprising papillary-like and reticular-like dermal layers for housing the respective dermal fibroblast's subsets as a template for the generation of an *in vitro* vascularized skin construct. The communication between fibroblasts and endothelial cells greatly relies on the angiogenic factors secreted by the former. Therefore, in **Chapter V**, we hypothesized that delivering genes-encoding angiogenic growth factors to fibroblasts, then cultured in spongy-like hydrogels, would generate a microenvironment prone to vascularization while simultaneously offering structural support for new matrix deposition.

While the source of ECs for the prevascularization of TE constructs remains to be standardized, SVF comprising several cell types including fibroblasts, pericytes, ECs and hematopoietic cells, might be a valuable alternative. Knowing that endothelial progenitor cells and ECs present in SVF express specific integrins, in **Chapter VI** we hypothesized that integrin-specific spongy-like hydrogels would be able to retain those cells triggering vasculogenesis *in vitro*. Moreover, in **Chapter VII** we investigated whether those prevascularized constructs accelerated the cutaneous wound healing cascade by fostering early vascularization *vis-à-vis* SVF use immediately prior to implantation.

In **Chapter VIII** the concluding remarks are presented, highlighting the main accomplishments and significance to the field.

Chapter IV
Pre-selection of fibroblasts subsets prompt prevascularization of tissue engineered skin analogues

pFbs

rFbs

papillary-like layer

reticular-like layer

Chapter V
In vitro vascularization of tissue engineered constructs by non-viral delivery of pro-angiogenic genes

Fbs

gene delivery

Chapter III
Tailoring gellan gum spongy-like hydrogels' microstructure by controlling freezing parameters

Temperature (°C)

Time (min)

Chapter VI
Integrin-specific hydrogels for growth factor-free vasculogenesis

SVF

Chapter VII
Spongy-like hydrogels prevascularization with the adipose tissue vascular fraction delays cutaneous wound healing by sustaining inflammatory cell influx

Wound
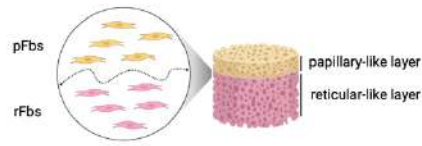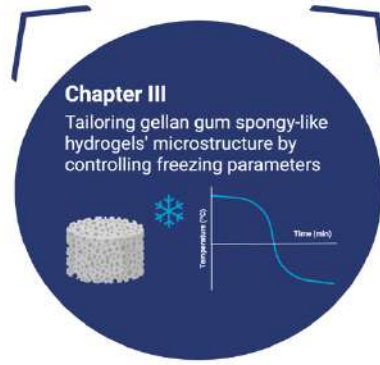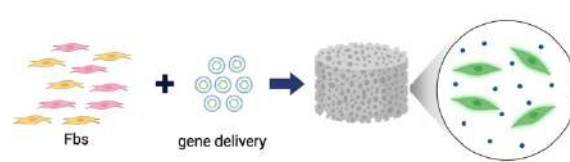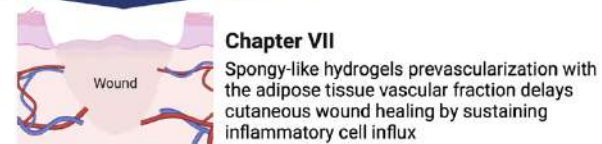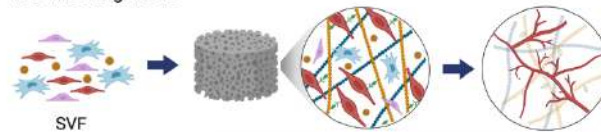
GG   GGDVS-RGD   Vasculogenic cells   Adipose-derived stem cells   Haematopoietic cells   Pericytes   integrins   angiogenic growth factors

Scheme illustrating the different approaches used in this thesis towards vascularization of tissue engineering constructs for skin wound healing. Fbs – Fibroblasts; pFbs – papillary fibroblasts; rFbs – reticular fibroblasts; SVF – stromal vascular fraction.

"When you aim for perfection, you discover it's a moving target."

Geoffrey Fisher

CHAPTER I

GENERAL INTRODUCTION

CHAPTER I

GENERAL INTRODUCTION *

I-1.   CONTEXTUALIZATION

Wound healing is a complex and highly regulated process, commonly organized in phases that include (i) hemostasis, (ii) inflammation, (iii) proliferation, and (iv) remodeling [1]. Upon injury, intravascular platelets are activated and secrete a series of growth factors that act as chemoattractants to neutrophils and monocytes [2]. The latter differentiate into macrophages in the inflammatory phase [3] releasing cytokines (vascular endothelial growth factor (VEGF)-A, fibroblast growth factors (FGFs) and angiopoietin 1 (Ang1)) that stimulates fibroblasts migration and activates microvascular endothelial cells (ECs) [4]. Within a few days, angiogenic capillary sprouts invade the fibrin/fibronectin-rich wound clot and organize into a microvascular network due to the dynamic interaction that occurs among ECs, angiogenic cytokines and the extracellular matrix (ECM) environment produced by fibroblasts (**Box I-1, Figure I-1**) [5]. However, when the wound healing cascade is affected, for instance due to delayed vascularization, dysfunctional healing occurs, hence impacting the quality of the neotissue formed. Moreover, in chronic wounds, the angiogenic process is impaired which, associated to a persistent inflammatory state, hinders healing progression. These wounds are associated to other co-morbidities such as diabetes and arterial and venous insufficiencies [6], being therefore the most challenging. For example, lower limb amputation due to diabetic foot ulcers occurs in 14 % to 24 % of diabetes patients. Moreover, while approximately 77 % of those ulcers heal within 1 year, roughly 40 % of the patients have a recurrence within 1 year after healing, almost 60 % within 3 years, and 65 % within 5 years [7,8]. It is then clear that chronic wounds have a growing prevalence worldwide being a major health problem with important social and economic implications with an urge need for improved therapeutic approaches.

As neovascularization of cutaneous wounds can occur through vasculogenesis and angiogenesis, in order to understand these concepts, a full comprehension of the process of vascularization from early embryonic development throughout the adult phase is required. The knowledge attained while comprehending key mechanisms of both processes has led to significant progress in promoting neotissue vascularization during tissue repair/regeneration [9]. Whether these have considered the needs of each cutaneous wound where a local and temporal effect must be attained to promote not only wound closure - open skin wounds might be life-threatening - but also improve the neotissue quality - directly associated to tissue functionality also critical for keeping body homeostasis – should be analyzed. We dissected the strategies that have been explored and how each one of them contributes to regulate vascularization in the context of cutaneous wound healing from two different perspectives - biomaterial- and a cell-based approaches. We discuss the efforts that have been made to optimize biomaterials/scaffolds to have spatial, temporal or spatio-temporal control of angiogenesis/vascularization at wound site (**Figure I-2**) [10,11]. Spatial regulation can be mostly associated to the target of local cells by presenting specific peptides at the biomaterials surface that then drive integrin-mediated angiogenesis. On the other hand, regulation of angiogenesis along time is intrinsically linked to angiogenic byproducts or to the controlled release/delivery of angiogenic growth factors (GFs) or respective encoding genetic material. Regarding cell-based approaches, prevascularization of cellular tissue engineered constructs using both mature [12] and progenitor [13,14] ECs is one of the most successful approaches in fostering vascularization at wound site. However, the clinical use those cells is highly hampered by an insufficient number required for therapy due to senescence and impaired capacities for vascular repair associated to their expansion *in vitro* [15]. Knowing that ECs wound surroundings are key to the process of new vessels formation [16] we discuss how the angiogenic signals secreted by other skin cells, represent an opportunity to define new strategies capable of directing wound healing angiogenesis (**Figure I-3**). Moreover, we discuss how adipose tissue has been contributing to promote the neovascularization of wounds focusing on the angiogenic secretome of ASCs and on the cellular complexity of adipose tissue stromal vascular fraction (SVF) highlighting its potential as an alternative to promote constructs prevascularization.

I-2.   SKIN VASCULOGENESIS AND ANGIOGENESIS

I-2.1.   Vasculogenesis *versus* angiogenesis

Neovascularization occurs through blood vessel formation *via* vasculogenesis or angiogenesis. Vasculogenesis concerns the generation of primitive vascular networks in the absence of preexisting blood vessels while angiogenesis refers to the growth of new blood vessels from a pre-existing vasculature [17]. The formation of new blood vessels occurs through both vasculogenesis and angiogenesis during embryonic development, while in the adult phase is achieved mainly *via* angiogenesis, including in response to injury such as in the case of cutaneous wound healing.

At the early stage of embryonic development (third week after fertilization) gastrulation leads to the formation of the three primary embryonic germ layers: (1) ectoderm, (2) mesoderm, and (3) endoderm. Shortly after, ectoderm subdivides into neuroectoderm and presumptive epidermis, a basal layer of cells that gives rise to all the cells of the epidermis after experiencing stratification and further differentiation (after 8 weeks of gestational age), and ultimately keratinization which begins at 15 weeks.

In turn, the embryonic tissue that forms the dermis depends on the specific body site; from the neural crest ectoderm if dermal mesenchyme of the face and anterior scalp, from the lateral plate mesoderm if limb and ventral body wall mesenchyme, or from the dermomyotomes of the embryonic somite in the case of the dorsal body wall mesenchyme. At 6 weeks the cellular and amorphous embryonic dermis – constituted by a variety of pluripotent stem cells in a rich hyaluronic acid gel - also starts to develop [18]. The reticular and the papillary dermis start to change in appearance at 12-15 weeks becoming successively thicker and well organized.

EC-forming tube-like structures have been described in the human embryonic dermis as early as 6 weeks [19,20]. Vasculogenesis begins approximately at the 17th gestational day with the formation of blood islets – mesodermal cell aggregates - in the wall of the yolk sac [21]. The cells in those aggregates are hemangioblasts – expressing the VEGF receptor-2 (VEGFR2), Ang-1 receptor Tie-2, stem cell antigen-1 (Sca-1) and CD34 - the common precursors of both endothelial and hematopoietic cells [22]. Within the blood islands, the internal cells become hematopoietic percussors that will give rise to blood cells. In turn, due to the secretion of factors from the FGF family by the mesoderm, the cells in the periphery differentiate into angioblasts [23,24]. These cells then organize as cords that fuse together forming a tubular structure, the dorsal aorta around the 18th gestational day [25]. Moreover, angioblasts from the

blood islets proliferate in response to VEGF that is produced by the endoderm forming a primitive vascular plexus throughout the extraembryonic tissue on about gestational day 23 [26]. The expansion of this primitive network occurs with the differentiation of the angioblasts and into ECs that lead the subsequent increasing complexity by intussusceptive and sprouting angiogenesis [27].

At weeks 6-7, despite no distinction between papillary and reticular dermis being yet observed in the embryonic dermis, capillaries form one single lane parallel – horizontal plexus – within the subpapillary and one in the deep reticular dermis, which are interconnected by groups of vertical vessels [18]. These vessels continue to divide and become more heterogeneous, such that by week 10, the vasculature in the dermis consists of two well-defined and interconnected plexuses located parallel to the future epidermis [18]. The interconnected plexus gives origin to the dermis vascular system which consists of a superficial vascular plexus just beneath the epidermal surface, and a deep vascular plexus situated above the boundary between the reticular dermis and the adipose tissue [28]. At this point, the plexus is stabilized with the recruitment of pericytes that promotes the establishment of a mature circulatory network through platelet-derived growth factor-B (PDGF-B) signaling [29].

Although the vasculature on the dermis only fully matures after birth, its complexity increases during the third trimester of gestation with the formation of capillary loops that arise from the superficial vascular plexus at sites between epidermal rete ridges [19].

I-2.2. Vascularization in wound healing

Effective wound healing requires vascularization of the newly tissue formed. Notwithstanding, during wound healing, only sprouting angiogenesis occurs [30]. Upon an injury, in the hemostasis phase of wound healing vasoconstriction in observed due to vascular damage [30,31]. Despite damaged, these vessels at the wound site are still essential to deliver intravascular platelets that rapidly form a fibrin clot and secrete a series of growth factors, such as epidermal growth factor (EGF), insulin-like growth factor 1 (IGF-1), PDGF, TGFs, that act as chemoattracts of neutrophils and monocytes to the wound [2]. Moreover, among the recruited inflammatory cells, the monocytes-derived macrophages [3] produce high levels of proangiogenic factors, such as VEGF-A, FGFs and Ang1, that activates host microvascular ECs [4,32]. Macrophages also secrete FGF-2 that stimulates ECs to release plasminogen activator and procollagenase. As plasminogen activator converts plasminogen into plasmin and procollagenase into active collagenase, these two proteases digest the vessels basement membrane constituents. This digestion allows EC migration and proliferation and consequently formation of capillary sprouts into the

injured site [33] (See Box I-1 for details on angiogenesis mechanisms). Although angiogenesis is the main process of neovascularization in wound healing, vasculogenesis can also occur in adult tissues, especially in response to ischemia [34,35]. In postnatal vasculogenesis, bone marrow-derived EPCs are recruited to the injury site, proliferate and differentiate resulting in the formation of functional blood vessels [36]. Notwithstanding, the potential role of vasculogenesis process in this cutaneous healing process is controversial and not yet clear [37].
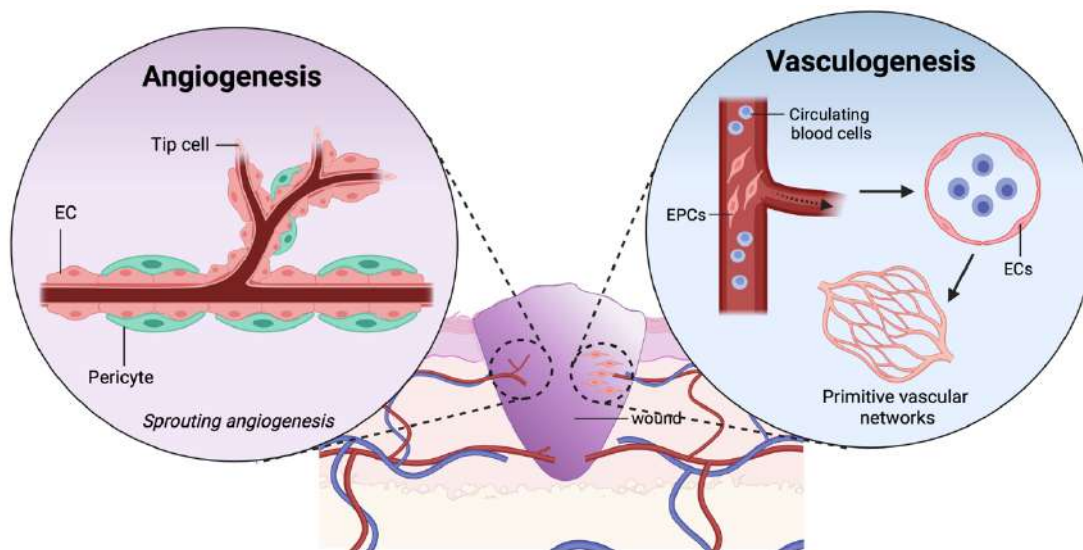
Figure I-1 Angiogenesis and vasculogenesis in wound healing.

Sprouting angiogenesis occurs when an existing vessel starts by branching off one or more of its ECs by degrading the original basement membrane with a highly controlled proteolysis that occurs at the surface of the EC. Since this proteolytic activity also cleaves many proteins in the basement membrane and interstitium, additional angiogenic growth factors are liberated. As a result, the EC projects extrusions through the gap in the basement membrane into the interstitium, which, on guidance of angiogenic factors activate the cell to acquire new properties, namely that of the so-called tip cell [39]. This tip cell is the prime invading cell of an angiogenic sprout and is characterized by multiple filopodia, which harbor many VEGFR-2 molecules that responds to the stimulated VEGF-A [40]. In response to these, the tip cell starts invading the surrounding matrix while maintaining contact with its neighboring ECs. The tip of the sprout induces another vessel also to sprout, after which both sprouts anastomose to allow establishment of perfusion [41,42]. Vasculogenis occurs takes place when progenitor endothelial cells (EPCs) home to the damaged site and differentiate into ECs to form primitive vascular networks. EC – endothelial cell; EPCs – endothelial progenitor cells.

In the proliferative phase, from day 3 to 5 after injury, the capillary sprouts invade the fibrin clot and the ECs deposit a provisional matrix containing fibronectin and proteoglycans from the periphery of the clot to the center of the wound [33]. Afterwards, in response to cytokines produced by macrophages, fibroblasts invade the fibrin clot and start to synthesize a fibronectin and hyaluronan-rich clot that gives origin to the granulation tissue [38]. As the restoration of the blood vessels in the metabolically active wound bed is essential to provide nutrients and oxygen along with the removal of debris, the number of

blood vessels in the granulation tissue increases at a ferocious rate [37]. This increase is correlated with the hypoxic environment of the wound, which leads to the expression of hypoxia-inducible factor-1α (HIF-1α) by macrophages and triggers VEGF and nitric oxide production by ECs resulting in a continuous capillary network expansion.

Box I-1 – Types of angiogenesis

The angiogenic process occurs by intussusceptive angiogenesis, sprouting angiogenesis and pruning [27]. The intussusceptive angiogenesis is a process of splitting pre-existing vessels along its length axis. It starts with proliferation of the ECs inside a vessel, leading to the formation of the intussusceptive pillar, a structure that starts as protrusive extensions of the endothelium that bridge both inner sides of the vessel lumen. This bridge expands and divide the luminal compartment along the vessel length, which results in two parallel vessels [45]. Sprouting angiogenesis starts with an EC — tip cell — in an existing vessel that degrades the original basement membrane with a highly controlled proteolytic activity cleaving basement membrane and interstitial proteins. As a result, EC projects protrusions through the gap in the basement membrane into the interstitium leading a string of ECs that are able to proliferate and create a branch, increasing in complexity with the growth of the vascular network [17]. Angiogenesis is a process that demands high metabolic activity as it requires high delivery of oxygen and nutrients. Once these angiogenic mechanisms cease, the metabolic demand decreases resulting in an excess of vessel formation which is not necessary for normal tissue functioning [46,47]. Hence, to limit the number of vascular branches, an additional type of adaptation intrinsic to angiogenesis - vascular pruning - is required. This process is regulated by vessel contraction and/or closure of vessel branches, which is followed by disintegration of the EC contacts and apoptosis. However, the processes that drives vascular pruning are still poorly understood. So far it is known that the withdrawal of factors such as the VEGF due to hyperoxia [48,49], and the secretion of pruning inducing factors, such as Ang2 or delta-like 4 (DLL4) [50] are involved in this process.

In the remodeling phase, as the provisional matrix clears and is replaced by collagen-rich tissue produced by fibroblasts, some capillary sprouts branch and join to form capillary networks through which blood flows begin while the non-perfused suffers vascular pruning (**Box I-1**) [43]. The perfused blood vessels will then return to a quiescent state with the phalanx cell – quiescent ECs that line the inner

surface of vessels - phenotype restored, the formation of a new basement membrane composed of collagen type IV and laminin, and the recruitment of pericytes and smooth muscle cells through PDGF signaling [44].

I-3. BIOMATERIAL-CONTROLLED VASCULARIZATION IN SKIN WOUND HEALING

I-3.1. Spatial regulation

Due to the recognition of biological cues by cell integrins, peptide-functionalized materials have been explored to promote adhesion of angiogenic cells, such as ECs and EPCs, fostering angiogenesis locally at the wound site. These cells recognize the underlying matrix through different sets of integrins, which are known to be involved in triggering signaling pathways related to migration, proliferation and organization in vascular networks [9,51]. Early studies showed that materials functionalized with the A13 and C16 sequence from laminin [52] and the RGD and the heparin-binding domain of fibrin (Fg β15–66(2)) [53] promoted higher EC migration and improved neovessel formation in full-thickness wounds. However, most of these peptides have no selectivity for angiogenic cells and therefore can mediate adhesion of other cells resulting in a competitive environment that can be detrimental for local angiogenesis. This was in fact demonstrated with alginate hydrogels functionalized with peptides specific for α4β1 integrin. Materials with the REDV sequence showed superior capability to promote selective adhesion and proliferation of ECs *in vitro* and higher density of newly formed vessels after subcutaneous implantation in rats, than the ones with the RGD or the YIGSR peptides [54]. The importance of this specificity was recently reinforced with hyaluronic acid hydrogels functionalized with the fibronectin fragment (Fn9-10) that was designed to be specific for α3/α5β1- or αvβ3-integrin [55]. Matrices with the α3/α5β1 led to the formation of non-leaky blood vessels in opposition those with specificity for αvβ3 integrin, which was attributed to the higher expression of VE-cadherin at cell-cell junctions. Interestingly, RGD and αvβ3-ligand functionalized matrices led to similar ECs sprouting and formation of disorganized structures however, this was observed only for a much higher concentration of RGD peptide (>500 μM) than fibronectin fragments used (2 μM).

While these approaches highlight the possibility of spatially control vascularization, whether they are effective in cutaneous wound healing is still to be demonstrated. Moreover, the fundamental understanding of integrin-mediated responses to peptide-functionalized biomaterials, including

concentration, and other neighboring ligands, and their engagement as angiogenic/vasculogenic initiators requires further investigation.

I-3.2. Temporal regulation

In processes like angiogenesis and vascularization, temporal ECM remodeling is crucial for vascular cell migration and cell-cell organization [9]. Therefore, biomaterials - ECM mimickers - that are susceptible to hydrolytic or enzymatic degradation are intrinsically potential regulators of temporal tissue response. It is long known that biomaterial degradation byproducts, such as those of fibrin [56,57] or hyaluronic acid [58], modulate the proliferation and migration of angiogenic cells. However, the temporal control of angiogenesis using these materials is limited by their degradation rates [59,60], being therefore mostly suited for addressing angiogenesis at early wound healing stages. The combination of these materials with others that are not degraded enzymatically has allowed to tackle this limitation. This is the case of hyaluronic acid and gellan gum structures that promoted the neovascularization of ischemic mice hind limb in a material-dependent manner, consistent with the *in vitro* degradation profile (up to 28 days) [58]. These materials were also able to support significantly higher vessel density in diabetic mice full-thickness wounds along the whole healing timeframe [61].

While biomaterial degradation byproducts are a valid option, temporal regulation of angiogenesis during wound healing has been mostly associated to the biomaterial-mediated delivery/release of biomolecules. These approaches take advantage of the kinetics of diffusion controlled through materials' bulk properties (polymer concentration, crosslinking degree, wettability), or the degradation rate of the matrices to which biomolecules are coupled to. Early studies showed that VEGF [62], basic FGF (bFGF) [63] and stromal-derived factor 1 (SDF-1) [64] delivered using fibrin matrices, gelatin sheets and decellularized dermis, respectively, enhanced the vascularization of full-thickness mice wounds. Despite this, co-delivery of two GFs, being VEGF the prime angiogenic factor, seems to be more effective than their individual administration. Moreover, the use of angiogenic factors that are known to have specific roles at different times of the angiogenic process was considered. This was shown with a bioengineered mussel adhesive protein-based gel entrapping VEGF and platelet derived growth factor (PDGF)-containing microparticles in a full-thickness rat wound. While 40 % of VEGF was release during one day, PDGF was release slowly over 4 days resulting in significantly higher capillary density and overall improved neotissue quality [65]. However, the link between the role of each one of those factors and the observed response was not made.

41

An extension of the delivery window was also considered *via* covalent immobilization, yet this has not been necessarily linked to a higher control of the delivery/release. Chitosan scaffolds functionalized with VEGF and bFGF *via* PEG, shown to be sensitive to the action of lysozyme releasing *in vitro* up to 70% of the coupled GFs, led to enhanced vascularization of full-thickness rat wounds at early time-points but details on the temporal effect of the GFs were not provided [66]. Similarly, collagen functionalized with bFGF and keratinocyte growth factor (KGF) *via* EDC/NHS supported increased blood flow in a full-thickness rat wound between days 7 and 14 [67]. Interestingly, at day 14 this is significantly different from groups with single GFs which demonstrates an enhanced effect of the dual system. However, the blood flow profile along the time was similar in all conditions which might correlate with the sustained release profile observed *in vitro*, similar for both GFs. In other approach, collagen scaffolds to which VEGF and SDF-1α were coupled *via* a collagen binding domain also led to the formation of a higher number of vessels in full-thickness wounds in diabetic rats. Interestingly, the mount of ECs recruited to the site of injury by scaffolds loaded with up to 20 μg of VEGF was almost null while a dose-dependent response was observed for SDF-1α-containing scaffolds. Thus, this work seems to show that SDF-1α is responsible for ECs recruitment that are then led by VEGF to organize and form the vessels [68]. Also, fibrin hydrogels containing VEGF-165 and PDGF-BB coupled *via* a high GFs affinity peptide (LAMA33043-3067), led to a significantly increased frequency of proliferative cells in full-thickness wounds in type-2 diabetic mice compared to other treatment groups at day 5. This is consistent with an early effect of the co-delivery of those GFs that results in an accelerated healing [69]. In this case, neovascularization might also have been potentiated by the synergistic effect of the fibrin byproducts although authors do not take this into consideration.

Despite what was achieved with the delivery of GFs, limitations that includes bolus release of proteins, short half-life due to lack of protection from proteolytic degradation, and the requirement of high doses to achieve a therapeutic effect [70], which in the case of angiogenic factors can be linked to tumor development [71] are still a reality. Biomaterials delivering genetic material encoding for specific angiogenic proteins have been shown to foster the sustained production of GFs by host cells. Gene-activated matrices (GAMs) or scaffolds rely on combining non-viral vector therapeutic genes within 3D structures that offer structural support and a matrix for new tissue deposition [72]. Up to now, collagen/chitosan scaffolds loaded with lipofectamine 2000/pVEGF transplanted into full-thickness wounds in rats lead to an upregulation of VEGF secretion that resulted in an increased number of newly-formed vessels 9 days post-implantation than the structures with non-complexed pVEGF or with lipofectamine/pGFP [73]. Similarly, hyaluronic acid/dextran hydrogels containing polyethyleneimine

(PEI)/pVEGF promoted microvessels formation in full-thickness rat burns, in a higher extent than the hydrogel alone due to the effective secretion of VEGF from the *in situ* transfected cells over 7 days [74].

Overall, regardless of the strategy the challenge to control vascularization in cutaneous wound, healing still relies on matching the exact temporal profile of delivery that responds to its evolution.
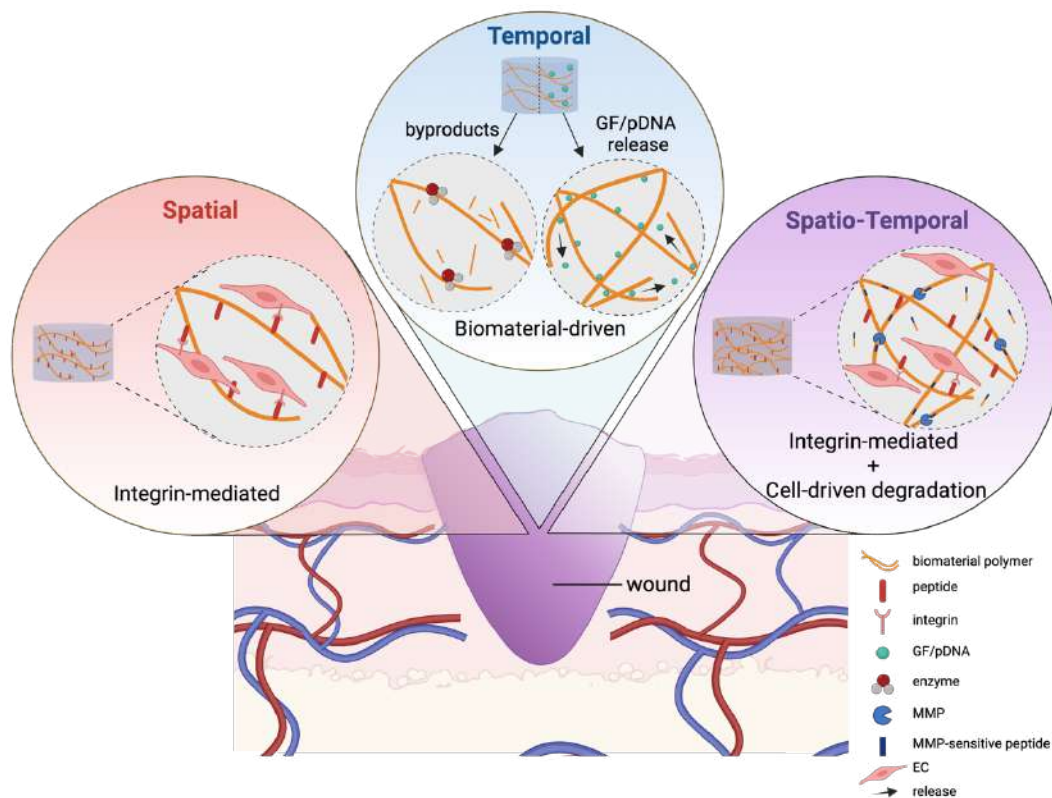
Figure I-2 Biomaterial-based strategies to promote vascularization in wound healing.
EC – endothelial cell, GF – growth factor, MMP – metalloproteinase, pDNA – plasmid encoding DNA.

I-3.3.   Spatio-temporal regulation

As discussed, biomaterial-based approaches are capable of individually impacting neovascularization both at spatial and temporal level. One might question if spatio-temporal strategies synergize towards this, being more successful in accelerating vascularization in wound healing. Biomaterials have been functionalized with peptides that are recognized by angiogenic cells promoting adhesion and act as sensitive biodegradation sites supporting, along time and depending on the degradative milieu, cell migration, proliferation and organization. In hyaluronic acid-modified hydrogels, EC migration throughout the matrices was enabled through the MMP-sensitive crosslinker (GCRDGPQG↓IWGQDRCG), and vacuole and lumen formation were RGD dose-dependent [75]. This organization was observed within 3-6 hours, while the cell migration was assumed to lead the creation of "vascular guidance tunnels" that supported

branching and sprouting after 2-3 days. In another approach, T1 (GQKCIVQTTSWSQCSKS) or C16 (CGGKAFDITYVRLKF) peptides linked to gellan gum were shown to determine EC adhesion in a concentration dependent manner, while the MMP-1 cleavable peptide (CRDGPQGIWGQDRC) allowed opening space in the polymeric network of the hydrogel for subsequent cell spreading [76]. Despite the modest results, it might be argued that the *in vitro* concentration of MMP-1 and the time of culture were not sufficient to further degrade the matrix allowing ECs organization.

Overall, as precise spatial and temporal regulation of angiogenesis is necessary for enhanced wound healing and formation of neotissue with a quality closer to the native one, the combinatorial approach may be the best approach to mimic regulation of angiogenesis using biomaterials properties.

I-4. CELL-CONTROLLED VASCULARIZATION IN SKIN WOUND HEALING

I-4.1. Relevant cell sources for neovascularization

Injection of single ECs suspensions has been shown to promote neovascularization in full-thickness mice wounds [77,78]. Nonetheless, prevascularization approaches using both mature and progenitor ECs within 3D matrices remain one of the most successful approaches in fostering wound vascularization. A comparative study involving human dermal microvascular ECs (hDMECs) organized into capillary-like structures or randomly dispersed in a fibrin hydrogel confirmed a higher degree of neovascularization with human capillaries stabilized by host mural cells in full-thickness athymic rat wounds for the prevascularized construct [79]. Besides microvascular ECs, mature macrovascular ECs, such as human umbilical cord vein ECs (HUVECs) have also been used to prevascularize tissue engineered constructs. Similarly to hDMECs, constructs prevascularized with HUVECs promoted neovascularization in full-thickness rodent wounds [80,81]. However, in contrast to hDMECs, it was not demonstrated whether the vessel-like structures formed *in vitro* remained functional after implantation [80]. Moreover, the use of macrovascular cells such as HUVECs remains questionable due to functional differences. The barrier formed by HUVECs was shown to be significantly more permeable than that formed by hDMECs, owing to significant differences in the amounts and types of adhesion and tight junctions [82]. Indeed, the skin vasculature is only composed of microvascular ECs, which form a high-resistance endothelium with a restrictive barrier [83]. Thus, additional studies are necessary to clarify whether these differences compromise pre-formed structures and the overall functionality of the neovasculature after anastomosis leading to vessel regression.

Independently of the nature, the major limitations of using mature ECs are associated with insufficient numbers after isolation and low-replication rates during cultivation, culminating in loss of phenotype and highly hampered functionality upon transplantation [15,84]. EPCs isolated from blood, including a rare subset - the endothelial colony-forming cells (ECFCs) - mostly found in the umbilical cord blood [85], have been explored as an alternative due to high *in vitro* replication rate [86,87]. Moreover, constructs prevascularized with EPCs have confirmed a positive effect over the neovascularization of full-thickness mice wounds [14,88,89]. Interestingly, a direct comparison of EPCs and hDMECs showed that these integrate in a lower extent in the neovasculature of the wound granulation tissue [90]. Despite this, comparative studies with prevascularized constructs are not available and consequential understanding of EPCs role in wound healing, and in particular in its neovascularization, is still not well understood [91].

Induced pluripotent stem cells (iPSC) can be differentiated into ECs (iPSC-EC) being then an option to prompt wound neovascularization [92]. Indeed, iPSC-EC-treated wounds showed increased blood perfusion and vessel density when compared to non-treated wounds [93,94]. Interestingly, iPSC-EC seem to have a greater effect than HUVECs over the arteriole density in full-thickness mice wounds, which also showed accelerated healing [94]. Importantly, while robust protocols exist to differentiate iPSCs in ECs [95], no data is yet available on whether these cells recapitulate the functional and transcriptional profile of "true" ECs and whether the "EC" phenotype is stable.

I-4.2. Dermal and epidermal cells signaling

While poorly representing the complexity of native tissue, skin substitutes are in general effective in promoting wound healing. Dermal and dermal-epidermal products composed respectively by fibroblasts, and fibroblasts and keratinocytes can, however, be associated to delayed engraftment mostly due to deficient neovascularization. It is also known that both keratinocytes and fibroblasts impact ECs, which seems to reveal that the potential of those cells as part of dermal-epidermal skin substitutes is not maximized. During the proliferation and remodeling phases of the wound healing, fibroblasts secretion of keratinocyte GF-1 (KGF-1), KGF-2 and interleukin-6 (IL-6) have a profound effect on migration, proliferation, and differentiation of keratinocytes [96,97]. In response to these factors, keratinocytes are also prompt to secret VEGF, which guides angiogenesis in the wound tissue through the upregulation of nitric oxide (NO) in ECs [98]. This is in line with the enhanced wound vascularization observed after transplantation of skin substitutes containing keratinocytes genetically modified to overexpress VEGF [99,100]. Moreover, keratinocyte-to-EC crosstalk is known to be involved in wound angiogenesis. Impaired

EC migration and angiogenesis was observed in epidermis-specific α3-integrin-knockout mice due to the reduced expression of the pro-angiogenic factor MRP3 by keratinocytes [101]. Therefore, novel signaling mechanisms may prospectively be targeted in keratinocytes to promote angiogenesis during wound-healing, particularly at the re-epithelialization stage.
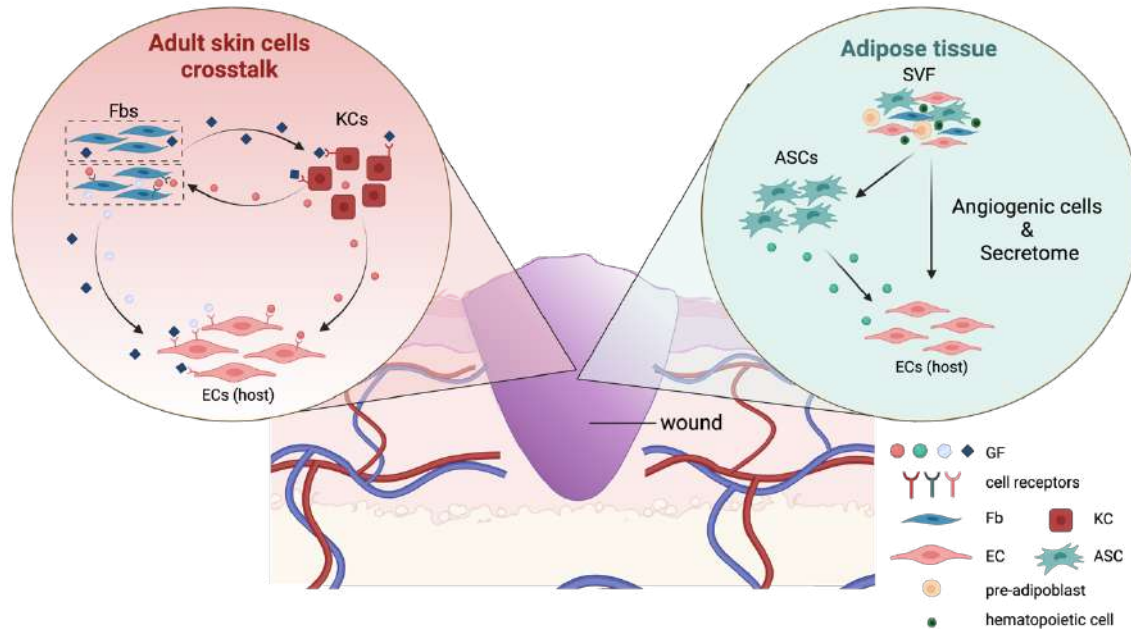
Figure I-3 Cell-based strategies in skin wound healing vascularization.
ASC- adipose-derived stem cell, EC – endothelial cell, Fbs – fibroblasts, GF – growth factors, KCs - keratinocytes, SVF – stromal vascular fraction.

The crosstalk between keratinocytes-fibroblasts-ECs is thought to be responsible for regulating microvascular density within the papillary and reticular dermis [102], being therefore also an axis of interest to target during wound healing. Keratinocytes secretome was shown to trigger the secretion of factors such as VEGF-A, FGFs, Ang-1 and hepatocyte growth factor/scatter factor (HGF/SF) by fibroblasts [103–105], known to induce EC migration, tubule formation and stabilization [106,107]. Additionally, a stiffer microenvironment formed by ECM proteins deposited by fibroblasts correlates with enhanced EC vessel sprouting with lumen formation [108]. It is also known that the capacity ECM has to retain specific molecules is also determinant for this fibroblasts-ECs crosstalk [109]. This is the case of the ECM produced by the papillary fibroblasts that supports the formation of a robust array of highly branched tube-like structures due to the capacity to link HGF/SF, known to be critical for EC differentiation [110]. While this differentiated capacity of fibroblasts to support ECs could be explored for cutaneous wound healing, the use of pure papillary and reticular fibroblasts is still dependent on the identification of specific surface for their isolation [111]. There are also other fibroblasts subpopulations that could be of interest

to explore in this context [111], therefore, the subsequent elucidation of the role of each fibroblast subpopulation in angiogenesis is pivotal for their use as alternative to target vascularization.

I-4.3.   Adipose tissue as a cell source

The adipose tissue constitutes a relevant source of cells for tissue repair and regeneration due to a wide range of features [112]. The adipose-derived stem cell (ASCs), in particular, are known to secrete various growth factors, including VEGF-A, FGFs, transforming growth factor-β (TGF-β), placental growth factor (PGF), and anti-apoptotic factors [113–115], which has led to their exploitation as key pro-angiogenic mediators. Increased neovascularization due to the paracrine interaction of the ASCs with host resident cells was in fact confirmed in full-thickness excisional mice wounds [116]. Increased blood flow in a third degree burn in sheep was also attributed to the VEGF secreted by the transplanted ASCs [117]. Similarly, the secretion of HSF by ASCs was also correlated with a significantly higher number of ECs in full-thickness mice ulcers [118]. This effect can be however dependent on the time of residence of the transplanted cells as shown by the secreted VEGF, Ang-1 and bFGF dose-dependent number of vessels formed at early time-points in a deep partial thickness burn in pigs [119]. This angiogenic effect of the ASCs was further shown to synergize with platelet-rich plasma (PRP) as revealed by the higher EPCs recruitment and enhanced neovascularization attained in full-thickness wounds in diabetic rats. This was due to an upregulation of VEGF and SDF-1 when compared to only ASCs and only PRP groups [120]. Interestingly, this did not seem to happen with hyaluronic acid byproducts, at least from 2 weeks after transplantation onward at which the condition only with gellan gum/hyaluronic acid showed higher vessel density than when it was combined with ASCs [61]. This is potentially due to a residence time for the transplanted ASCs lower than 2 weeks.

Adipose tissue stromal vascular fraction (SVF) comprises, in addition to ASCs, several other cell types including fibroblasts, pre-adipocytes, ECs and hematopoietic cells [121,122]. This cell complexity present in SVF allows generating a dynamic and self-regulating angiogenic microenvironment capable of promoting the neovascularization of ischemic tissues [115]. A comparative study involving ASCs and SVF injected in full-thickness wound in diabetic mice, showed that the number of EC at the wound site was superior in the SVF group [123]. Interestingly, the angiogenic environment supported by SVF cells also permits to attain complex and interconnected capillary-like networks in the absence of extrinsic growth factors *in vitro* [124]. This allowed the use of SVF cells to generate prevascularized dermo-epidermal constructs that inosculated with the host tissue after implantation in a full-thickness rat model, forming

abundant perfused human/rat chimeric vessels [125]. Authors underline that SVF cell composition, specially the transplanted ECs/EPCs (CD31+ cells) and the ASCs (CD90+ cells) are responsible for the generation of mature and stable capillaries [125]. Another study showed that the level of maturation of the prevascular network formed from SVF cells also influences the vascularization of full-thickness rat wounds [126]. Faster inosculation and superior survival of transplanted cells is linked to pericytes, whose number was significantly higher in the more mature constructs [126]. A full-scale randomized clinical trial for the treatment of chronic wounds showed that prevascularized dermal-epidermal skin constructs using the SVF-derived endothelial cell population promote vascular network regeneration. The preliminary results published so far showed that the vascular beds of the hypodermis were denser in the prevascularized group, which also depicted faster wound closure [127]. These results positively support the use of SVF to enhance the vascularization of cutaneous wounds, and additional knowledge regarding the involved mechanisms of action will certainly allow to take a greater number of approaches in the clinical setting.

I-5.   CONCLUSION AND FUTURE PERSPECTIVES

There is a pressing need to improve vascularization in skin wound healing, as it is a crucial step to promote better healing and improve neotissue quality. However, it is also clear that strategies capable of triggering-controlled vascularization by vasculogenesis or angiogenesis are still a challenge. Biomaterial- and cell-based approaches open up the possibility of engineering constructs that allow the regulation of angiogenesis/vasculogenesis at different levels. Biomaterial-based strategies were proven capable of regulating localized vascularization during healing through integrin-mediated responses to peptide-functionalized biomaterials. However, its effectiveness in cutaneous wounds is still to be demonstrated and the fundamental understanding of those responses and the engagement of those peptides as angiogenic/vasculogenic initiators requires further investigation. Concomitantly, the use of angiogenic biomaterials or the release/delivery of angiogenic biomolecules or respective encoding genetic material in the wound allow to achieve a temporal effect on vascularization. While this is critical, those approaches have shown limited control due to the low dependence of the release/delivery profiles on the wound environment, and in particular on wound features such as pH and temperature. Therefore, the use of materials that respond to those *stimuli* releasing a certain biomolecule, for example, would allow responding to the specific needs of each stage of wound healing or different type of wounds. Additionally, given the temporal complexity of the wound healing process, the combination of those features with the

spatial cell response mediated by integrins is likely to be relevant not only in successfully accelerating angiogenesis, critical to foster wound closure, but also to mediate the transition from the inflammatory to the proliferative phase of the healing, supporting the formation of neotissue with a quality closer to the native one. Nonetheless, new knowledge about the spatial and temporal regulation of angiogenesis during the healing of different types of wounds will also pave the way to further advance biomaterials' properties to improve effectiveness.

Prevascularized cellular approaches are highly effective in fostering inosculation with host tissue and consequently enhancing neovascularization. However, the availability of the ECs in clinically relevant numbers for constructs prevascularization has been challenging to attain. On the other side, current skin substitutes are in general effective in promoting wound healing but can be associated to delayed neovascularization. Knowing that the crosstalk between the epidermal cells, dermal fibroblasts, and ECs, favors angiogenesis-associated responses from ECs, skin substitutes might be further advanced by taking advantage of this knowledge. Advances in genetic engineering might be critical to explore those interactions by modifying fibroblasts and/or keratinocytes to respond, as part of skin substitutes, to a specific signaling or to secrete a molecule that directly interacts with host ECs. Moreover, this vision in combination with what was discussed from the biomaterial-based perspective, can also foster the development of improved GAMs.

From the perspective of having cellular approaches with low to none cell manipulation, adipose tissue must be considered a highly relevant source of cells. It is well demonstrated that the ASCs angiogenic secretome positively impacts the vascularization of cutaneous wounds. What is still to be better understood is how this potential can be maximized in different wounds. One might speculate that strategies that enhance ASCs residence time and support this angiogenic phenotype such as for example the use of integrin-specific biomaterials could be considered. On the other hand, due to their composition, SVF has allowed the development of prevascularized constructs which generate a self-regulatory angiogenic environment being therefore an extremely powerful alternative for promoting vascularization in cutaneous wounds. Notwithstanding, the associated mechanisms of action should be further investigated, to unravel their true role fostering the translation of these approaches to the clinical setting.

Overall, there are a wide range of approaches that can contribute in different ways to tackle cutaneous wound healing vascularization. Yet, their clinical relevance will be determined from the generated outputs and how deeply they respond to the ultimate need that is to promote the formation of good quality neotissue. From the vascularization point of view, that goes beyond the current analysis of

the number of vessel and relies on the maturity of the generated vasculature and more importantly on the extent of blood flow provided to the neotissue to guarantee long term functionality of the skin. Moreover, with the advance of the knowledge and tools that were discussed above, it is critical that strategies are thought having in consideration the type of wound and, consequently, its microenvironment. Taking into play what is known about the healing progression, those might also require connection not only to different wounds but also to the stage of healing.

I-6. REFERENCES

1   Chouhan D, Dey N, Bhardwaj N, Mandal BB. Emerging and innovative approaches for wound healing and skin regeneration: Current status and advances. Biomaterials 216, 119267 (2019).

2   Kiritsy CP, Lynch SE. Role of growth factors in cutaneous wound healing: A review. Crit. Rev. Oral Biol. Med. 4(5), 729–760 (1994).

3   Diegelmann RF, Cohen IK, Kaplan AM. The role of macrophages in wound repair: A review. Plast. Reconstr. Surg. 68(1), 107–113 (1981).

4   Barrientos S, Stojadinovic O, Golinko MS, Brem H, Tomic-Canic M. Growth factors and cytokines in wound healing. Wound Repair Regen. 16(5) (2008).

5   Rouwkema J, Rivron NC, van Blitterswijk CA. Vascularization in tissue engineering. Trends Biotechnol. 26(8), 434–441 (2008).

6   Sen CK. Human Wound and Its Burden: Updated 2020 Compendium of Estimates. Adv. Wound Care 10(5), 281–292 (2021).

7   Tresierra-Ayala MÁ, García Rojas A. Association between peripheral arterial disease and diabetic foot ulcers in patients with diabetes mellitus type 2. Med. Univ. 19(76), 123–126 (2017).

8   Armstrong DG, Boulton AJM, Bus SA. Diabetic Foot Ulcers and Their Recurrence. N. Engl. J. Med. 376(24), 2367–2375 (2017).

9   Lee JH, Parthiban P, Jin GZ, Knowles JC, Kim HW. Materials roles for promoting angiogenesis in tissue regeneration. Prog. Mater. Sci. 117, 100732 (2020).

10   Novosel EC, Kleinhans C, Kluger PJ. Vascularization is the key challenge in tissue engineering. Adv. Drug Deliv. Rev. 63(4–5), 300–311 (2011).

11   Sharma D, Ross D, Wang G, Jia W, Kirkpatrick SJ, Zhao F. Upgrading prevascularization in tissue engineering: A review of strategies for promoting highly organized microvascular network formation. Acta Biomater. 95, 112–130 (2019).

12   da Silva LP, Cerqueira MT, Sousa R a., Reis RL, Correlo VM, Marques AP. Engineering cell-adhesive gellan gum spongy-like hydrogels for regenerative medicine purposes. Acta Biomater. 10, 4787–4797 (2014).

13   Sasagawa T, Shimizu T, Yamato M, Okano T. Endothelial colony-forming cells for preparing prevascular three-dimensional cell-dense tissues using cell-sheet engineering. J. Tissue Eng. Regen. Med. 10(9), 739–47 (2016).

14   Baltazar T, Merola J, Catarino C *et al*. Three Dimensional Bioprinting of a Vascularized and Perfusable Skin Graft Using Human Keratinocytes, Fibroblasts, Pericytes, and Endothelial Cells. Tissue Eng. - Part A 26(5–6), 227–238 (2020).

15   Medina RJ, O'Neill CL, O'Doherty TM *et al. Ex vivo* Expansion of Human outgrowth Endothelial Cells Leads to IL-8-Mediated Replicative Senescence and Impaired Vasoreparative Function. Stem Cells 31(8), 1657–1668 (2013).

16   Muñoz-Chápuli R, Quesada AR, Medina MÁ. Angiogenesis and signal transduction in endothelial cells. Cell. Mol. Life Sci. 61(17), 2224–2243 (2004).

17   Kolte D, McClung JA, Aronow WS. Vasculogenesis and Angiogenesis. Transl. Res. Coron. Artery Dis. Pathophysiol. to Treat. 49–65 (2016).

18   Chu DH. Development and structure of skin. In: Fitzpatrick's Dermatology in General Medicine (Chap. 7, Seventh Edition). Wolff K, Goldsmith LA, Katz SI, Gilchrest BA, Paller AS, Leffell DJ (Ed.), Mc Graw Hill - Medical, 57–73.

19   Loomis CA, Koss T. Embryology. In: Dermatology, volume one (Chap. 1.3, 1st Edition). Bolognia JL, Jorizzo JL, Rapini RP (Ed.), Mosby, 39–48 (2003).

20   Johnson CL, Holbrook KA. Development of Human Embryonic and Fetal Dermal Vasculature. J. Invest. Dermatol. 93(s2), 10S-17S (1989).

21   Risau W, Flamme I. Vasculogenesis. Annu. Rev. Cell Dev. Biol. 11, 73–91 (1995).

22   Choi K, Kennedy M, Kazarov A, Papadimitriou JC, Keller G. A common precursor for hematopoietic and endothelial cells. Development 125, 725–732 (1998).

23   Krah K, Mironov V, Risau W, Flamme I. Induction of vasculogenesis in quail blastodisc-derived embryoid bodies. Dev. Biol. 164(1), 123–32 (1994).

24   Cox CM, Poole TJ. Angioblast differentiation is influenced by the local environment: FGF-2 induces angioblasts and patterns vessel formation in the quail embryo. Dev. Dyn. 218(2), 371–82 (2000).

25   Cleaver O, Krieg PA. VEGF mediates angioblast migration during development of the dorsal aorta in Xenopus. Development 125(19), 3905–14 (1998).

26   Schmidt A, Brixius K, Bloch W. Endothelial precursor cell migration during vasculogenesis. Circ. Res. 101(2), 125–136 (2007).

27   Risau W. Mechanisms of angiogenesis. Nature 386(6626), 671–674 (1997).

28   Petzelbauer P, Loewe R, Pober JS. Cutaneous Vasculature. In: Fitzpatrick's Dermatology. Ninth Edition. McGraw Hill, (2019).

29   Hellström M, Gerhardt H, Kalén M et al. Lack of pericytes leads to endothelial hyperplasia and abnormal vascular morphogenesis. J. Cell Biol. 153(3), 543–53 (2001).

30   Bodnar RJ. Chemokine Regulation of Angiogenesis During Wound Healing. Adv. Wound Care 4(11), 641–650 (2015).

31   Bodnar RJ, Yates CC, Wells A. IP-10 blocks vascular endothelial growth factor-induced endothelial cell motility and tube formation via inhibition of calpain. Circ. Res. 98(5), 617–25 (2006).

32   Laschke MW, Menger MD. Vascularization in tissue engineering: Angiogenesis versus inosculation. Eur. Surg. Res. 48(2), 85–92 (2012).

33   Tonnesen MG, Feng X, Clark RAF. Angiogenesis in wound healing. J. Investig. Dermatology Symp. Proc. 5(1), 40–46 (2000).

34   Takahashi T, Kalka C, Masuda H et al. Ischemia- and cytokine-induced mobilization of bone marrow-derived endothelial progenitor cells for neovascularization. Nat. Med. 5(4), 434–8 (1999).

35   Tepper OM, Capla JM, Galiano RD et al. Adult vasculogenesis occurs through in situ recruitment, proliferation, and tubulization of circulating bone marrow-derived cells. Blood 105(3), 1068–77 (2005).

36   Asahara T, Masuda H, Takahashi T et al. Bone marrow origin of endothelial progenitor cells responsible for postnatal vasculogenesis in physiological and pathological neovascularization.

Circ. Res. 85(3), 221–8 (1999).

37   Johnson KE, Wilgus TA. Vascular Endothelial Growth Factor and Angiogenesis in the Regulation of Cutaneous Wound Repair. Adv. Wound Care 3(10), 647–661 (2014).

38   Li J, Zhang YP, Kirsner RS. Angiogenesis in wound repair: Angiogenic growth factors and the extracellular matrix. Microsc. Res. Tech. 60(1), 107–114 (2003).

39   Gerhardt H, Golding M, Fruttiger M *et al.* VEGF guides angiogenic sprouting utilizing endothelial tip cell filopodia. J. Cell Biol. 161(6), 1163–77 (2003).

40   Sawamiphak S, Seidel S, Essmann CL *et al.* Ephrin-B2 regulates VEGFR2 function in developmental and tumour angiogenesis. Nature 465(7297), 487–91 (2010).

41   Isogai S, Lawson ND, Torrealday S, Horiguchi M, Weinstein BM. Angiogenic network formation in the developing vertebrate trunk. Development 130(21), 5281–90 (2003).

42   Lenard A, Ellertsdottir E, Herwig L *et al. In vivo* analysis reveals a highly stereotypic morphogenetic pathway of vascular anastomosis. Dev. Cell 25(5), 492–506 (2013).

43   Carmeliet P. Angiogenesis in health and disease. Nat. Med. 9(6), 653–60 (2003).

44   Carmeliet P, Jain RK. Molecular mechanisms and clinical applications of angiogenesis. Nature 473(7347), 298–307 (2011).

45   van Hinsbergh VWM. Angiogenesis: Basics of Vascular Biology. In: Vascularization for Tissue Engineering and Regenerative Medicine. Springer International Publishing, 1–29 (2016).

46   Demidova-Rice TN, Durham JT, Herman IM. Wound Healing Angiogenesis: Innovations and Challenges in Acute and Chronic Wound Healing. Adv. Wound Care 1(1), 17 (2012).

47   Dulmovits BM, Herman IM. Microvascular remodeling and wound healing: A role for pericytes. Int. J. Biochem. Cell Biol. 44(11), 1800–1812 (2012).

48   Benjamin LE, Golijanin D, Itin A, Pode D, Keshet E. Selective ablation of immature blood vessels in established human tumors follows vascular endothelial growth factor withdrawal. J. Clin. Invest. 103(2), 159–165 (1999).

49   Mourad JJ, des Guetz G, Debbabi H, Levy BI. Blood pressure rise following angiogenesis inhibition by bevacizumab. A crucial role for microcirculation. Ann. Oncol. 19(5), 927–934 (2008).

50   Korn C, Augustin HG. Mechanisms of Vessel Pruning and Regression. Dev. Cell 34(1), 5–17

(2015).

51   Zeng Y, Zhu L, Han Q *et al*. Preformed gelatin microcryogels as injectable cell carriers for enhanced skin wound healing. Acta Biomater. 25, 291–303 (2015).

52   Malinda KM, Wysocki AB, Koblinski JE, Kleinman HK, Ponce ML. Angiogenic Laminin-Derived Peptides Stimulate Wound Healing. Int. J. Biochem. Cell Biol. 40(12), 2771–2780 (2008).

53   Martino MM, Briquez PS, Ranga A, Lutolf MP, Hubbell JA. Heparin-binding domain of fibrin(ogen) binds growth factors and promotes tissue repair when incorporated within a synthetic matrix. Proc. Natl. Acad. Sci. U. S. A. 110(12), 4563–4568 (2013).

54   Wang W, Guo L, Yu Y, Chen Z, Zhou R, Yuan Z. Peptide REDV-modified polysaccharide hydrogel with endothelial cell selectivity for the promotion of angiogenesis. J. Biomed. Mater. Res. - Part A 103(5), 1703–12 (2015).

55   Li S, Nih LR, Bachman H *et al*. Hydrogels with precisely controlled integrin activation dictate vascular patterning and permeability. Nat. Mater. 16(9), 953–961 (2017).

56   Rowland FN, Donovan MJ, Picciano PT, Wilner GD, Kreutzer DL. Fibrin-mediated vascular injury: Identification of fibrin peptides that mediate endothelial cell retraction. Am. J. Pathol. 117(3), 418–28 (1984).

57   Ge M, Ryan TJ, Lum H, Malik AB. Fibrinogen degradation product fragment D increases endothelial monolayer permeability. Am. J. Physiol. - Lung Cell. Mol. Physiol. 261(4 5–2), L283-9 (1991).

58   da Silva LP, Pirraco RP, Santos TC *et al*. Neovascularization Induced by the Hyaluronic Acid-Based Spongy-Like Hydrogels Degradation Products. ACS Appl. Mater. Interfaces 8(49), 33464–33474 (2016).

59   Jarrell DK, Vanderslice EJ, Lennon ML, Lyons AC, VeDepo MC, Jacot JG. Increasing salinity of fibrinogen solvent generates stable fibrin hydrogels for cell delivery or tissue engineering. PLoS One 16(5), e0239242 (2021).

60   Segura T, Anderson BC, Chung PH, Webber RE, Shull KR, Shea LD. Crosslinked hyaluronic acid hydrogels: a strategy to functionalize and pattern. Biomaterials 26(4), 359–371 (2005).

61   da Silva LP, Santos TC, Rodrigues DB *et al*. Stem Cell-Containing Hyaluronic Acid-Based Spongy Hydrogels for Integrated Diabetic Wound Healing. J. Invest. Dermatol. 137(7), 1541–1551

(2017).

62   Traub S, Morgner J, Martino M *et al*. The promotion of endothelial cell attachment and spreading using FNIII10 fused to VEGF-A165. Biomaterials 34(24), 5958–5968 (2013).

63   Matsumoto S, Tanaka R, Okada K *et al*. The effect of control-released basic fibroblast growth factor in wound healing: Histological analyses and clinical application. Plast. Reconstr. Surg. 1(6), e44 (2013).

64   Olekson MAP, Faulknor R, Bandekar A, Sempkowski M, Hsia HC, Berthiaume F. SDF-1 liposomes promote sustained cell proliferation in mouse diabetic wounds. Wound Repair Regen. 23(5), 711–723 (2015).

65   Park TY, Maeng SW, Jeon EY, Joo K II, Cha HJ. Adhesive protein-based angiogenesis-mimicking spatiotemporal sequential release of angiogenic factors for functional regenerative medicine. Biomaterials 272, 120774 (2021).

66   Vijayan A, A. S, Kumar GSV. PEG grafted chitosan scaffold for dual growth factor delivery for enhanced wound healing. Sci. Rep. 9, 19165 (2019).

67   Qu Y, Cao C, Wu Q *et al*. The dual delivery of KGF and bFGF by collagen membrane to promote skin wound healing. J. Tissue Eng. Regen. Med. 12(6), 1508–1518 (2018).

68   Long G, Liu D, He X *et al*. A dual functional collagen scaffold coordinates angiogenesis and inflammation for diabetic wound healing. Biomater. Sci. 8(22), 6337–6349 (2020).

69   Ishihara J, Ishihara A, Fukunaga K *et al*. Laminin heparin-binding peptides bind to several growth factors and enhance diabetic wound healing. Nat. Commun. 9, 2163 (2018).

70   Raftery RM, Tierney EG, Curtin CM, Cryan S-AA, O'Brien FJ. Development of a gene-activated scaffold platform for tissue engineering applications using chitosan-pDNA nanoparticles on collagen-based scaffolds. J. Control. Release 210, 84–94 (2015).

71   Lugano R, Ramachandran M, Dimberg A. Tumor angiogenesis: causes, consequences, challenges and opportunities. Cell. Mol. Life Sci. 77(9), 1745–1770 (2019).

72   Curtin CM, Tierney EG, Mcsorley K, Cryan SA, Duffy GP, O'Brien FJ. Combinatorial gene therapy accelerates bone regeneration: Non-viral dual delivery of VEGF and BMP2 in a collagen-nanohydroxyapatite scaffold. Adv. Healthc. Mater. 4(2), 223–7 (2015).

73   Lou D, Luo Y, Pang Q, Tan WQ, Ma L. Gene-activated dermal equivalents to accelerate healing of

diabetic chronic wounds by regulating inflammation and promoting angiogenesis. Bioact. Mater. 5(3), 667–679 (2020).

74   Wang P, Huang S, Hu Z *et al.* In situ formed anti-inflammatory hydrogel loading plasmid DNA encoding VEGF for burn wound healing. Acta Biomater. 100, 191–201 (2019).

75   Hanjaya-Putra D, Bose V, Shen YI *et al.* Controlled activation of morphogenesis to generate a functional human microvasculature in a synthetic matrix. Blood 118(3), 804–815 (2011).

76   da Silva LP, Jha AK, Correlo VM, Marques AP, Reis RL, Healy KE. Gellan Gum Hydrogels with Enzyme-Sensitive Biodegradation and Endothelial Cell Biorecognition Sites. Adv. Healthc. Mater. 7(5), 1700686 (2018).

77   Cerqueira MT, Da Silva LP, Santos TC *et al.* Human skin cell fractions fail to self-organize within a gellan gum/hyaluronic acid matrix but positively influence early wound healing. Tissue Eng. - Part A 20(9–10), 1369–78 (2014).

78   Cerqueira MT, Pirraco RP, Martins AR, Santos TC, Reis RL, Marques AP. Cell sheet technology-driven re-epithelialization and neovascularization of skin wounds. Acta Biomater 10(7), 3145–3155 (2014).

79   Montaño I, Schiestl C, Schneider J *et al.* Formation of human capillaries *in vitro*: The engineering of prevascularized matrices. Tissue Eng. - Part A 16(1), 269–82 (2010).

80   Chen L, Xing Q, Zhai Q *et al.* Pre-vascularization enhances therapeutic effects of human mesenchymal stem cell sheets in full thickness skin wound repair. Theranostics 7(1), 117–131 (2017).

81   Du P, Suhaeri M, Ha SS, Oh SJ, Kim SH, Park K. Human lung fibroblast-derived matrix facilitates vascular morphogenesis in 3D environment and enhances skin wound healing. Acta Biomater. 54, 333–344 (2017).

82   Kluger MS, Clark PR, Tellides G, Gerke V, Pober JS. Claudin-5 controls intercellular barriers of human dermal microvascular but not human umbilical vein endothelial cells. Arterioscler. Thromb. Vasc. Biol. 33(3), 489–500 (2013).

83   Ono S, Egawa G, Kabashima K. Regulation of blood vascular permeability in the skin. Inflamm. Regen. 37, 11 (2017).

84   Ye L, Poh K-K. Enhancing endothelial progenitor cell for clinical use. World J. Stem Cells 7(6),

894–8 (2015).

85   Zhang H, Tao Y, Ren S *et al*. Isolation and characterization of human umbilical cord-derived endothelial colony-forming cells. Exp. Ther. Med. 14(5), 4160–4166 (2017).

86   Chong MSK, Ng WK, Chan JKY. Concise Review: Endothelial Progenitor Cells in Regenerative Medicine: Applications and Challenges. Stem Cells Transl. Med. 5(4), 530–538 (2016).

87   Shepherd BR, Enis DR, Wang F *et al*. Vascularization and engraftment of a human skin substitute using circulating progenitor cell-derived endothelial cells. FASEB J. 20(10), 1739–1741 (2006).

88   Dai NT, Huang WS, Chang FW *et al*. Development of a Novel Pre-Vascularized Three-Dimensional Skin Substitute Using Blood Plasma Gel. Cell Transplant. 27(10), 1535–1547 (2018).

89   Hendrickx B, Verdonck K, Van Den Berge S *et al*. Integration of blood outgrowth endothelial cells in dermal fibroblast sheets promotes full thickness wound healing. Stem Cells 28(7), 1165–77 (2010).

90   Suh W, Kim KL, Kim J-M *et al*. Transplantation of Endothelial Progenitor Cells Accelerates Dermal Wound Healing with Increased Recruitment of Monocytes/Macrophages and Neovascularization. Stem Cells 23(10), 1571–1578 (2005).

91   Richardson MR, Yoder MC. Endothelial progenitor cells: Quo Vadis? J. Mol. Cell. Cardiol. 50(2), 266–72 (2011).

92   Jang S, Collin de l'Hortet A, Soto-Gutierrez A. Induced Pluripotent Stem Cell–Derived Endothelial Cells: Overview, Current Advances, Applications, and Future Directions. Am. J. Pathol. 189(3), 502–512 (2019).

93   Clayton ZE, Tan RP, Miravet MM *et al*. Induced pluripotent stem cell-derived endothelial cells promote angiogenesis and accelerate wound closure in a murine excisional wound healing model. Biosci. Rep. 38(4), BSR20180563 (2018).

94   Kim KL, Song SH, Choi KS, Suh W. Cooperation of endothelial and smooth muscle cells derived from human induced pluripotent stem cells enhances neovascularization in dermal wounds. Tissue Eng. - Part A 19(21–22), 2478–85 (2013).

95   Klein D. iPSCs-based generation of vascular cells: reprogramming approaches and applications. Cell. Mol. Life Sci. 75(8), 1411–1433 (2018).

96   Smola H, Thiekotter G, Fusenig NE. Mutual induction of growth factor gene expression by

epidermal-dermal cell interaction. J. Cell Biol. 122(2), 417–29 (1993).

97   Xia YP, Zhao Y, Marcus J *et al*. Effects of keratinocyte growth factor-2 (KGF-2) on wound healing in an ischaemia-impaired rabbit ear model and on scar formation. J. Pathol. 188(4), 431–8 (1999).

98   Ziche M, Morbidelli L, Choudhuri R *et al*. Nitric oxide synthase lies downstream from vascular endothelial growth factor-induced but not basic fibroblast growth factor-induced angiogenesis. J. Clin. Invest. 99(11), 2625 (1997).

99   Supp DM, Supp AP, Bell SM, Boyce ST. Enhanced vascularization of cultured skin substitutes genetically modified to overexpress vascular endothelial growth factor. J. Invest. Dermatol. 114(1), 5–13 (2000).

100   Supp DM, Boyce ST. Overexpression of vascular endothelial growth factor accelerates early vascularization and improves healing of genetically modified cultured skin substitutes. J. Burn Care Rehabil. 23(1), 10–20 (2002).

101   Mitchell K, Szekeres C, Milano V *et al*. Alpha3beta1 integrin in epidermis promotes wound angiogenesis and keratinocyte-to-endothelial-cell crosstalk through the induction of MRP3. J. Cell Sci. 122(Pt 11), 1778–87 (2009).

102   Detmar M. The role of VEGF and thrombospondins in skin angiogenesis. J Dermatol Sci 24(Suppl 1), S78-84 (2000).

103   Varkey M, Ding J, Tredget E. Fibrotic remodeling of tissue-engineered skin with deep dermal fibroblasts is reduced by keratinocytes. Tissue Eng. Part A 20(3–4), 716–727 (2014).

104   Grøn B, Stoltze K, Andersson A, Dabelsteen E. Oral fibroblasts produce more HGF and KGF than skin fibroblasts in response to co-culture with keratinocytes. APMIS 110(12), 892–898 (2002).

105   Ayata RE, Chabaud S, Auger M, Pouliot R. Behaviour of endothelial cells in a tridimensional *in vitro* environment. Biomed Res. Int. 2015, 630461 (2015).

106   Caneparo C, Baratange C, Chabaud S, Bolduc S. Conditioned medium produced by fibroblasts cultured in low oxygen pressure allows the formation of highly structured capillary-like networks in fibrin gels. Sci. Rep. 10, 9291 (2020).

107   Stunova A, Vistejnova L. Dermal fibroblasts—A heterogeneous population with regulatory function in wound healing. Cytokine Growth Factor Rev. 39, 137–150 (2018).

108 Newman AC, Nakatsu MN, Chou W, Gershon PD, Hughes CCWW. The requirement for fibroblasts in angiogenesis: Fibroblast-derived matrix proteins are essential for endothelial cell lumen formation. Mol. Biol. Cell 22(20), 3791–800 (2011).

109 Berthod F, Germain L, Tremblay N, Auger FA. Extracellular matrix deposition by fibroblasts is necessary to promote capillary-like tube formation *in vitro*. J. Cell. Physiol. 207(2), 491–498 (2006).

110 Sorrell JM, Baber MA, Caplan AI. Human dermal fibroblast subpopulations; differential interactions with vascular endothelial cells in coculture: Nonsoluble factors in the extracellular matrix influence interactions. Wound Repair Regen. 16(2), 300–309 (2008).

111 Philippeos C, Telerman SB, Oulès B *et al*. Spatial and Single-Cell Transcriptional Profiling Identifies Functionally Distinct Human Dermal Fibroblast Subpopulations. J. Invest. Dermatol. 138(4), 811–825 (2018).

112 Ong WK, Chakraborty S, Sugii S. Adipose Tissue: Understanding the Heterogeneity of Stem Cells for Regenerative Medicine. Biomolecules 11(7), 918 (2021).

113 Melchiorri AJ, Nguyen BNB, Fisher JP. Mesenchymal stem cells: Roles and relationships in vascularization. Tissue Eng. - Part B Rev. 20(3), 218–228 (2014).

114 Laschke MW, Kleer S, Scheuer C *et al*. Vascularisation of porous scaffolds is improved by incorporation of adipose tissue-derived microvascular fragments. Eur. Cells Mater. 24, 266–77 (2012).

115 Rehman J, Traktuev D, Li J *et al*. Secretion of Angiogenic and Antiapoptotic Factors by Human Adipose Stromal Cells. Circulation 109(10), 1292–1298 (2004).

116 Cerqueira MT, Pirraco RP, Santos TC *et al*. Human adipose stem cells cell sheet constructs impact epidermal morphogenesis in full-thickness excisional wounds. Biomacromolecules 14(11), 3997–4008 (2013).

117 Fujiwara O, Prasai A, Perez-Bello D *et al*. Adipose-derived stem cells improve grafted burn wound healing by promoting wound bed blood flow. Burn. trauma 8, tkaa009 (2020).

118 Nagano H, Suematsu Y, Takuma M *et al*. Enhanced cellular engraftment of adipose-derived mesenchymal stem cell spheroids by using nanosheets as scaffolds. Sci. Rep. 11, 14500 (2021).

119 Burmeister DM, Stone R, II *et al*. Delivery of Allogeneic Adipose Stem Cells in Polyethylene Glycol-

Fibrin Hydrogels as an Adjunct to Meshed Autografts After Sharp Debridement of Deep Partial Thickness Burns. Stem Cells Transl. Med. 7(4), 360 (2018).

120   Ebrahim N, Dessouky AA, Mostafa O *et al*. Adipose mesenchymal stem cells combined with platelet-rich plasma accelerate diabetic wound healing by modulating the Notch pathway. Stem Cell Res. Ther. 12(1), 392 (2021).

121   Planat-Benard V, Silvestre J-S, Cousin B *et al*. Plasticity of Human Adipose Lineage Cells Toward Endothelial Cells. Circulation 109(5), 656–663 (2004).

122   Yoshimura K, Shigeura T, Matsumoto D *et al*. Characterization of freshly isolated and cultured cells derived from the fatty and fluid portions of liposuction aspirates. J. Cell. Physiol. 208(1), 64–76 (2006).

123   Bi H, Li H, Zhang C *et al*. Stromal vascular fraction promotes migration of fibroblasts and angiogenesis through regulation of extracellular matrix in the skin wound healing process. Stem Cell Res. Ther. 10(1), 302 (2019).

124   Costa M, Cerqueira MT, Santos TC *et al*. Cell sheet engineering using the stromal vascular fraction of adipose tissue as a vascularization strategy. Acta Biomater. 55, 131–143 (2017).

125   Klar AS, Güven S, Zimoch J *et al*. Characterization of vasculogenic potential of human adipose-derived endothelial cells in a three-dimensional vascularized skin substitute. Pediatr. Surg. Int. 32(1), 17–27 (2016).

126   Cerino G, Gaudiello E, Muraro MG *et al*. Engineering of an angiogenic niche by perfusion culture of adipose-derived stromal vascular fraction cells. Sci. Rep. 7, 14252 (2017).

127   Nilforoushzadeh MA, Sisakht MM, Amirkhani MA *et al*. Engineered skin graft with stromal vascular fraction cells encapsulated in fibrin–collagen hydrogel: A clinical study for diabetic wound healing. J. Tissue Eng. Regen. Med. 14(3), 424–440 (2020).

CHAPTER II

MATERIALS AND METHODS

CHAPTER II

MATERIALS AND METHODS

II-1.   MATERIALS

II-1.1.   Gellan gum-based scaffolds

II-1.1.1.   Gellan gum

Gellan gum (GG) is an exocellular polysaccharide produced by the aerobic submerged fermentation of *Sphingomonas elodea*. GG is a linear anionic polymer composed of repeating units of a tetrasaccharide (1,3-β-D-glucose, 1,4-β-D-glucuronic acid, 1,4-β-D-glucose, 1,4-β-L-rhamnose). At high temperatures, GG has a coil form, which changes to a double helix upon temperature decrease. Hydrogels are formed when anti-parallel double helices self-assemble forming oriented bundles called junction zones that link the untwined regions of extended helical chains. Crosslinking of the hydrogels is further promoted by the presence of ions, specifically monovalent or divalent cations - ionotropic gelation [1] -, which promote physical bonding between the carboxylate groups of the glucuronic acid molecules. In recent years, the potential of GG has been assessed for a range of tissue engineering and regenerative medicine applications [2–11]. In the particular case of skin related purposes, GG-based materials have proven to be beneficial for wound healing [7–11].

The GG used in the following studies was purchased with the designation of Gelzan™ CM, from Sigma-Aldrich (USA).

II-1.1.2.   Chemical modification of gellan gum

Despite the interesting properties of GG-based materials for wound healing, the adhesion of different cell types and the respective associated responses cannot be controlled or understood. Owing to the recognition of biological cues by cell integrins, we then peptide-functionalized GG after chemically modifying with vinyl sulfone moieties (DVS), which facilitates the attachment of adhesive peptides through thiol groups. Since we wanted to promote the adhesion of vasculogenic cells, such as endothelial

progenitor and endothelial cells, which highly express α6β1 integrin and αvβ3 integrin [12,13], peptide sequences important for vascularization derived from the ECM components fibronectin and cysteine-rich angiogenic inducer 61 (CYR61, CCN1) were used. Therefore, cyclic RGD (RGD, cyclo-RGDfC) derived from the fibronectin-III domain with high binding affinity for αvβ3 integrin [14], and T1 (GQKCIVQTTSWSQCSKS) present in the CYR61 III domain that binds to α6β1 integrin [15], were conjugated to GGDVS.

Michael type addition has enabled the functionalization of gellan gum with divinyl sulfone (DVS) in a single step under mild conditions [16]. Gelzan powder (0.25 % (w/v)) was dissolved in deionized (DI) water under stirring at 90 °C. After dissolution, the temperature was lowered to room temperature (RT) and the pH was adjusted to 12. DVS (SIGMA, Portugal) was added in excess (molar ratio of 30:1) to the GG solution and allowed to react for 1 hour (h) under stirring. Divinyl sulfone-modified gellan gum (Figure II-1) was purified by dialysis against DI water at 37 °C for 3 days and precipitated into cold diethyl ether (1:5). The purified GGDVS was filtered with a 0.22 μm filter, freeze-dried and stored at -20 °C until use.

The peptides were chemically bound to the functionalized GGDVS polymer through cysteine residues, forming a thiol-ether linkage. A solution of 0.25 or 0.5 % (w/v) GGDVS was reacted with thiol-cyclo-RGD (800 μM, Cyclo(-RGDfC) 95 %, GeneCust Europe), thiol-T1 (800 μM, CTTSWSQCSKS, GeneCust Europe) or both peptides in a 1:1 ratio for 1 h at RT.
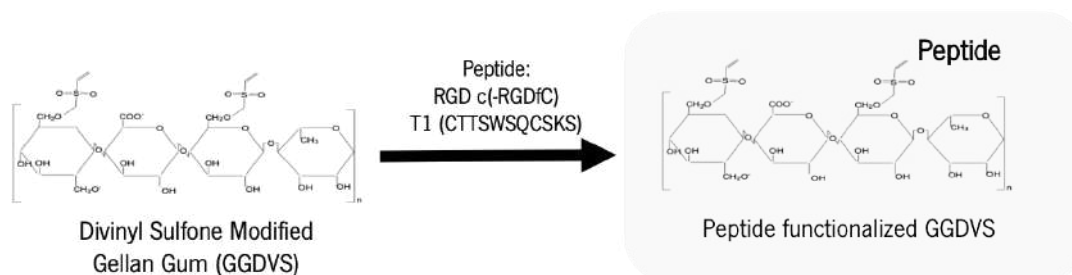
Figure II-1 Schematic representation of GGDVS bond to peptides.

II-1.1.3. Hyaluronic acid

Hyaluronic acid (HyA) is a linear anionic polymer composed of disaccharide units (1,4-β-D-glucuronic acid, 1,3-β-D-*N*-acetyl-glucosamine) [17]. HyA exists in the extracellular matrix (ECM) of human and animal tissues, including in the skin, having different roles in physio- and pathological processes depending on its molecular weight and consequently on its interaction with different cell receptors [18,19]. However, when considering the use of HyA hydrogels in wound healing, they are limited by their

fast degradation rates [20]. Therefore, the combination of HyA with GG tackles this limitation, while providing a higher mimicry of the ECM. Moreover, we have previously optimized the concentration of HyA to be used with GG, confirming an enhanced angiogenic effect [9] and a role in promoting the neovascularization of excisional skin wounds [10,11]. Therefore, in this thesis, we aimed to take advantage of these features using GG-HyA-based materials.

Pharmaceutical grade sodium hyaluronate (1.5 MDa), produced by microbial fermentation, was purchased from Lifecore Biomedical (USA) or Sigma Aldrich (Ireland).

II-1.1.4.   Fabrication of GG-based spongy-like hydrogels

II-1.1.4.1   *GG spongy-like hydrogels*

GG spongy-like hydrogels were obtained through an integrated processing methodology comprising the formation of a precursor hydrogel, its freezing, freeze-drying, and rehydration, as previously demonstrated and patented by the group [2,21]. Spongy-like hydrogels preserve some hydrogels' characteristic features, such as high water content, yet exhibit improved properties, including: i) microstructure - higher porosity, pore size and pore wall thickness; and ii) mechanical performance, such as stiffness and flexibility. These materials are particularly relevant in wound healing, as they are easily available as off-the-self dried networks that can be promptly combined with cells or bioactive cues for their use in different strategies. Moreover, as spongy-like hydrogels result from the hydration of the dried networks, when rehydrated with a cell suspension, cells become entrapped, opening the possibility to a low-manipulation ready-to-use application.

To prepare GG spongy-like hydrogels in a more reproducible way, tackling the variations that can occur during the freezing step leading to batch-to-batch discrepancies, a freezing device was developed and used throughout Chapters III, IV, V, VI and VII. The insulated freezing device (IFD) contains a conductive aluminum multiwell plate with a cover and base of a thermo-conductive copper alloy and an insulator. The non-insulated freezing device (NFD) is composed of the same components as the IFD, except for the insulating outer shell. The conductive multiwell plate (aluminum 6082-T6 alloy, Al) radiates the heat within the plate maintaining an even temperature in all wells. Directly under and above the multiwell plate is placed a layer of a C11000 copper alloy (Cu), a thermo-conductive material to allow a faster and more uniform transfer of thermal energy. The outer shell is constructed from expanded

polystyrene (EPS), a thermal insulating material that prevents/reduces vapor formation from the external surface of the device and reduces heat transfer due to the operator's physical contact.

To prepare the GG hydrogels, gelzan powder was first dissolved in DI water under stirring at 90 °C. After dissolution, the solution was cast into molds and rapidly mixed with α-minimum essential medium (α-MEM, Life Technologies, Scotland) without fetal bovine serum (FBS, Gibco) for crosslinking. The hydrogel progressively formed until RT was reached. Afterwards, the hydrogels were incubated in phosphate-buffered saline solution (PBS) for up to 48h to reach the equilibrium swelling state. Molds were then transferred to freezing devices (NFD and IFD) and frozen for 18 h at -20 °C and -80 °C or for 20 min at -210 °C using liquid nitrogen. A tissue culture polystyrene (TCPS) multi-well plate without any other cover was used in the standard method as previously reported by us [2].

Frozen GG-based hydrogels were freeze-dried to completely remove all water. The time of the freeze-drying process was sufficient to sublime all the water and was completed for one cycle at -80 °C, 0 atm, and for 3 days (LyoAlfa 10/15, Telstar, Spain). The GG-based dried polymeric networks were rehydrated at any time with a solution or with/without cells, as described in the following sections.

II-1.1.4.2   *GG/DVS-modified GG-peptide spongy-like hydrogels*

Hydrogels were prepared by mixing 0.25 or 0.5 % (w/v) GGDVS-RGD/T1 (section I-1.1.2) with 0.5 or 1 % (w/v) GG (section I-1.4.1) solutions. The dual peptide hydrogels were prepared by mixing, GGDVS-RGD:GGDVS-T1 solutions (1:1) with the GG solution. After casting into the desired molds, the hydrogel was progressively formed until RT was reached. Afterwards, hydrogels were frozen at -80 °C overnight and then freeze-dried (Telstar, Spain) for 24 h to obtain GG/GGDVS-peptide dried polymeric networks. Spongy-like hydrogels were formed after rehydration of the dried polymeric networks.

II-1.1.4.3   *GG-HyA spongy-like hydrogels*

A solution of 0.88 % (w/v) HyA and 1 % (w/v) GG was prepared at 90 °C for 30 min and then mixed with a 0.5 % (w/v) GGDVS-RGD solution (section I-1.1.2) at a 1:1 ratio. The final solution was cast into the desired molds and processed as described above (section I-1.4.1) to attain the spongy-like hydrogels.

II-1.1.4.4   *Bilayered GG spongy-like hydrogels*

In order to mimic the two layers of the dermis, the reticular and the papillary dermis, GG bilayered spongy-like hydrogels were prepared using different percentages of GG/GGDVS-RGD (Figure II-5). 1.5 % (w/v) GG/GGDVS-RGD spongy-like hydrogels were prepared as described in section II-1.1.4.1 and processed as described above (section I-1.4.1) to obtain the reticular-like layer. After the freeze drying, the second layer was then added by pipetting the 0.75 % (w/v) GG/GGDVS-RGD GG/GGDVS-RGD solution (75% of the volume used for the first layer) on the top of that. After stabilization, constructs were frozen at -80 °C overnight and then freeze-dried (Telstar, Spain) for 24 h to obtain the bilayer structures. Cylindrical scaffold samples of 5 mm diameter were cut using a metal punch for further analysis.

II-1.2.   Collagen-based scaffolds

Integra, composed of bovine tendon collagen (COL) and shark chondroitin sulphate (ChS), has been the gold standard dermal regeneration template in different types of wounds [22–24]. Bovine tendon COL was purchased from Southern Lights Biomaterials (New Zealand) while ChS sodium salt from shark cartilage was purchased from Sigma Aldrich (Ireland).

II-1.2.1.   Fabrication of COL-glycosaminoglycan scaffolds

COL-GAG scaffolds were fabricated using a technique developed by O'Brien et al [25,26]. A 0.94 % COL-GAG (0.44 % GAG/0.5 % COL) formulation was prepared. COL-HyA or COL-ChS scaffolds were prepared by blending 1.8 g of bovine tendon COL in 300 mL of 0.5 M glacial acetic acid (HOAc, Fisher Scientific, Ireland) for 90 min at RT. A total of 0.16 g HyA or ChS was dissolved in 60 mL of 0.5 M HOAc and added to the collagen slurry at a rate of 5 mL/10 min while blending at 15,000 rpm. The slurry was then blended for 60 min at RT. Gas was removed from the slurries using a vacuum pump and cast into the desired molds. Afterwards, slurries were frozen at -10 °C overnight and then freeze-dried (Advantage EL, VisTir Co., Gardiner NY) for 24 h. Afterwards, dried polymeric structures underwent dehydrothermally (DHT) treatment at 105 °C for 24 h at 0.05 bar in a vacuum oven (Vacucell 22; MMM, Germany) to create crosslinks through a condensation reaction which results in amide bonds. Scaffolds were then 5 mm punched, hydrated with PBS and chemical crosslinked using a mixture of 6 mM N-(3-

Dimethylaminopropyl)-N'-ethylcarbodiimide hydrochloride (EDC) and 5.5 mM N-Hydroxysuccinimide (NHS) to improve bulk stiffness.

II-1.3.   Transfection complexes

II-1.3.1.   Chitosan

Chitosan (Ch) is derived from the exoskeletons of many crustaceans, and has been used in the formulation of microparticles and nanoparticles suitable for drug delivery [27–29]. Moreover, it has been optimized as a non-viral vector with high transfection efficiency and uncompromised cell viability [30,31]. The positively charged amine groups on the chitosan chain can bind to negatively charged DNA and condense it into positively charged nanoparticles (**Figure II-2**). Ch with 7.3 kDA and DD >97 % was provided by Novamatrix (FMC Biopolymer, Norway) and used in the following studies.

II-1.3.2.   Polyethyleneimine

Polyethyleneimine (PEI) is a synthetic, water-soluble cationic polymer that can be used in either the linear or branched form. PEI was first described as a gene delivery vehicle in 1995 and has since become the most popular non-viral gene delivery vector due to its high transfection efficiency [32]. It has a wide-ranging buffering capacity, binding pDNA at a wide range of pH levels, while retaining a positive charge to facilitate endocytosis (**Figure II-2**) [33]. This ability enables highly efficient endosomal release by attracting negatively charged ions into the endosome, causing it to rupture and release polyplexes into the cytoplasm. This mechanism is called the "proton sponge effect" [34]. Branched PEI with an average MW 25 kDa was purchased from Sigma Aldrich (Ireland) and used in the following studies.
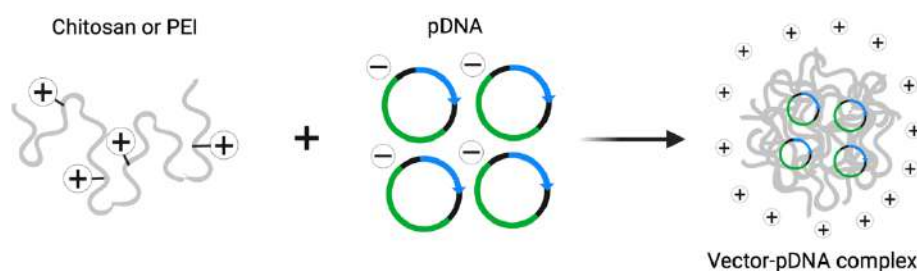
Figure II-2 Gene delivery vector-pDNA complexation.
The high positive charge of Ch and PEI forms strong electrostatic interactions with the pDNA forming stable complexes.

II-1.3.3.   Plasmid propagation & purification

pDNA encoding Gaussia Luciferase (pGLuc; New England Biolabs, USA), Green Fluorescent Protein (pGFP; Amaxa, Lonza, Germany), Vascular Endothelial Growth Factor (pVEGF; Genecopaeia, USA) and basic Fibroblast Growth Factor (pFGF2; kindly provided by Prof. Henning Madry from Saarland University) were propagated *via* the transformation of Subcloning Efficiency™ DH5α™ chemically competent *Escherichia coli* cells (Life Technologies, Ireland). All plasmid DNA was isolated and purified using an Endotoxin-Free Maxi-prep Kit (Qiagen, UK) as *per* the manufacturer's instructions. Bacterial cells were harvested by centrifugation (4500 g, 40 min, 4 °C), resuspended in 10 mL buffer P1 and 10 mL buffer P2 and incubated at RT for 5 min to lyse the cells. Next, 10 mL of chilled buffer P3 was added to the lysate, mixed vigorously, and incubated for 10 min at RT. The lysate was filtered and incubated on ice for 30 min with 2.5 mL buffer ER. Afterwards, the filtered lysate was passed through a resin tip to bind DNA. DNA was washed twice with 30 mL buffer QC and eluted with 15 mL buffer QN. To precipitate DNA, 10.5 mL of isopropanol was added and the solution was centrifuged at 16000 g for 30 min at 4 °C. The supernatant was decanted, DNA was washed with 70 % ethanol, and centrifuged for 10 min at 16000 g. The obtained plasmid was dissolved in Tris-EDTA buffer at a concentration of 0.5 µg/µL and stored at -20 °C until further usage.

II-1.3.4.   Non-viral vector-pDNA polyplex formation

Ch nanoparticles were formulated *via* electrostatic interactions between cationic chitosan and anionic pDNA. The nanoparticles were let to equilibrate for 30 min at room temperature before use. The ratio of chitosan to pDNA (N/P ratio, nitrogen:phosphate ratio) was 10 and the pDNA loading dose was 0.33 µg as optimized previously [30].

Branched PEI was purified by dialysis. PEI was dissolved in deionized water and loaded into Cellu-Sep H1 membranes (25 kDa MWCO). This solution was dialyzed against a 400-fold excess of deionized water four times overnight before the remaining PEI was lyophilized for use. 2 µg of pDNA was added to sterile molecular grade water, followed by dropwise addition of PEI at an N/P ratio of 7 and 30 min equilibration at room temperature [35].

II-2. METHODOLOGY FOR MATERIAL CHARACTERIZATION

II-2.1. Thermal profile analysis

The freezing stage is the most critical step during spongy-like hydrogels formation because it determines ice nucleation and crystal growth, thus influencing their micro-architecture. To understand these freezing parameters and consequentially to be able to tailor dried polymeric network/spongy-like hydrogels properties, the thermal profile along the freezing of the hydrogel was determined. Temperature sensors (Innovative Sensor Technology AG, Ebnat-Kappel, Switzerland) were positioned in the middle part of seven hydrogels randomly distributed throughout the wells. Measurements were recorded every 5 s using a computer program written in Arduino (v1.8.10, Somerville, USA). The cooling rate, nucleation time and temperature, freezing rate, and end freezing time were determined from the thermal profiles.

II-2.2. Micro-bicinchoninic acid protein™ assay

Micro-BCA (μ-BCA) assay was used, according to the manufacturers' instructions (Fisher Scientific, USA), to determine the amount of peptide (RGD, T1) that reacted with GGDVS, that is the modification efficiency. The peptide to be quantified was diluted to different concentrations between 0 and 200 μg/mL to prepare the standards for the calibration curve. Working Reagent was prepared by mixing Micro-BCA reagents MA, MB, and MC at a ratio of 25:24:1. Afterwards, 150 μL of the sample (GGDVS-peptide), control (GGDVS) and standards were mixed with 150 μL of Working Reagent in a multi-well plate and incubated at 37 °C for 2 h. The plate was then cooled to RT and the absorbance was read at 562 nm using a Synergy HT multi-mode microplate reader (Synergy HT, BioTek, USA). The modification efficiency was determined by the ratio of the mass of peptide linked to GGDVS determined by μ-BCA (m $_{peptide\ in\ GGDVS}$) and the mass of peptide that was used for the reaction with GGDVS (m $_{initial\ peptide}$), using **Equation II-1**.

$$Efficiency\ (\%) = \frac{m_{peptide\ in\ GGDVS}}{m_{inicial\ peptide}} \times 100$$

Equation II-1 Modification efficiency.

II-2.3. Micro-computed tomography

Micro-computed tomography (μ-CT) is a non-destructive imaging technique that provides high-resolution 3D images that are the result of the digital projection of 2D trans-axial images of a sample,

based on the attenuation of x-rays passing through the sample being imaged [36]. This technique was used to provide qualitative and quantitative data regarding dried polymeric networks density and microstructure, including porosity, pore size and pore wall thickness.

Dried polymeric networks microarchitecture was analyzed using a high-resolution X-Ray Microtomography System Skyscan 1072 scanner (Skyscan, Kontich, Belgium). Samples were scanned in high-resolution mode using a pixel size of 11.31 μm (magnification of 23.30×) and an integration time of 1.7 s. The X-ray source was set at 35 keV of energy and 215 μA of electric current. Representative datasets of 150 slices were transformed into a binary picture using a dynamic threshold of 45e255 (grey values) to distinguish polymeric material from pore voids. These data were used for morphometric analysis (CT Analyzer v1.5.1.5, Skyscan), which included quantification of the pore wall thickness, structure porosity, and pore size.

II-2.4.   Scanning electron microscopy

Scanning Electron Microscopy (SEM) was used to provide qualitative information regarding samples morphology, including microstructure, porosity, and pore size. A Leica Cambrigde S360 microscope (UK) was used to analyze the microstructure of the dried polymeric networks, after coating with gold (Cressington Sputter Coater), at an accelerating voltage of 15 kV.

II-2.5.   Compression tests

Since the use of different amounts of GG affect the mechanical properties of the GG spongy-like hydrogels, these were analysed under static compression. The compressive modulus was chosen for a relative analysis of different materials as the tensile testing (extensiometry) can only be performed in specific hydrogel geometries, such as strips or rings [39], which does not apply to the produced materials. Before testing, the GG dried polymeric networks were immersed in PBS for 24 h at RT for complete rehydration. The unconfined static compressive mechanical properties of the samples were measured using an INSTRON 5543 (Instron Int. Ltd., USA). Samples (10 x 6 mm) were submitted to a pre-load of 0.1 N before testing and were tested up to 60 % of strain at a loading rate of 2 mm min^{-1}. The compressive modulus of the spongy-like hydrogels was determined from the most linear part of the stress/strain curves using the secant method.

II-2.6.   Water content, water uptake and swelling ratio

The water content of the spongy-like hydrogels, affected by the GG concentration, was determined by measuring the weight of the dried polymeric networks before (W_d) and after (W_w) immersion in PBS or α–MEM solution at 37 °C for 24 h. The water uptake profile and swelling ratio were determined using the same principle; however, the samples were weighed at different time-points over 24 h. The water content, water uptake, and swelling ratio were calculated using **Equations II-2** and **II-3**, respectively.

$$Water\ uptake/content\ (\%) \ = \frac{(W_w - W_d)}{W_d} \times 100$$

Equation II-2 Water uptake/content.

$$Swelling\ ratio\ = \frac{W_w}{W_d}$$

Equation II-3 Swelling ratio.

II-2.7.   SYBR® Safe exclusion assay

A SYBR® Safe (Life Technologies, Ireland) exclusion assay was used to assess how effectively Ch and PEI bound to the pDNA of interest. SYBR® Safe strongly fluoresces upon intercalation between pDNA base pairs. Upon complete and stable binding of Ch or PEI to pDNA, there should be no free pDNA available for intercalation with the probe and the fluorescent signal is quenched [40,41]. Ch-pDNA and PEI-pDNA nanoparticles were prepared as described in Section II.1.4.2 and diluted to 1 mL with molecular grade 20 mM NaCl. 0.5 µL SYBRSafe DNA stain was then added, and the fluorescence signal read (RFU), in triplicate, on a spectrofluorometer (Bio-Tek Synergy HT 188743, Fisher Scientific, Ireland) at an excitation wavelength of 488 nm and an emission wavelength of 522 nm. Binding efficiency was calculated using **Equation II-4**.

$$Binding\ efficiency\ (\%) = 100 - \frac{RFU_{vector-pDNA} \times 100}{RFU_{pDNA}}$$

Equation II-4 Binding efficiency.

II-2.8.   Gel electrophoresis

Gel electrophoresis was used to confirm the complexation efficiency. For this, 5 µL of each non-viral vector-pDNA complex was added to 1 µL of 6x loading dye (ThermoFisher, USA) and run on a 1 % (w/v)

agarose (Lonza, Switzerland) gel for 45 min, along with controls (pDNA alone, non-viral vector alone and a 10000 bp ladder). The gels were viewed in the 600 channel of an Odyssey Fc Imaging System (LI-COR, US) and imaged and quantified using Image Studio Software (LI-COR, US).

II-3. *IN VITRO* METHODOLOGY

II-3.1. Cell sources, isolation and culture

Table II-1 Summary of the cell types used and their tissues of origin

Cell name	Cell type	Tissue source	Abbreviation
Stomal vascular fraction	Primary	Adult adipose tissue	SVF
Keratinocytes	Primary	Adult human skin	hKCs
Dermal fibroblasts	Primary	Adult human skin	hDFbs
Papillary fibroblasts	Primary	Adult human skin	pFbs
Reticular fibroblasts	Primary	Adult human skin	rFbs
Microvascular endothelial cells	Primary	Adult human skin	hDMECs
Umbilical vein endothelial cells	Primary	Neonatal umbilical vein vascular wall	HUVECs

All human biological samples were obtained from Hospital da Prelada (Porto, Portugal) and Hospital São João (Porto, Portugal), with patient's written informed consent and under a protocol with the 3B's Research Group, approved by the ethics committees of all the institutions.

II-3.1.1. Stromal vascular fraction

Adipose tissue was harvested from lipoaspirates or subcutaneous fat tissue from skin specimens of healthy donors undergoing abdominoplasty. Adipose tissue was digested with 0.05 % (w/v) collagenase type II (Sigma, USA) under agitation for 45 min at 37 °C. SVF was obtained by filtration and centrifugation (800 g, 10 min, 4 °C). SVF pellet was re-suspended in red blood cell lysis buffer (155 mM of ammonium chloride, 12 mM of potassium bicarbonate and 0.1 mM of ethylenediaminetetraacetic acid, all from Sigma-Aldrich, Germany) and incubated for 10 min at RT. After centrifugation (300 g, 5 min, RT), the supernatant was discarded and the cell pellet was re-suspended and cultured in α-MEM (Invitrogen, USA) supplemented with 2.2 g L^{-1} sodium bicarbonate (Sigma, USA), 10 % (v/v) fetal bovine serum (FBS, Invitrogen, USA) and 1 % (v/v) antibiotic/antimycotic solution (Invitrogen, USA) and maintained at 37 °C in a humidified incubator with 5 % CO_2 atmosphere.

II-3.1.2.   Human keratinocytes

Skin pieces were cut into small fragments and incubated with 2.4 U mL^{-1} of dispase (BD Biosciences, USA) overnight at 4 °C. The epidermis was peeled off and digested at 37 °C for 8 min using 0.05 % (w/v) trypsin/ethylenediaminetetraacetic acid (EDTA, Invitrogen, UK). Digestion was stopped with FBS and epidermal cells were scraped from the remaining matrix. The cell suspension was filtered through a sterile 100 μm cell strainer, centrifuged (300 g, 5 min), and re-suspended and cultured in Keratinocyte serum free media (Life Technology, Scotland) supplemented with human recombinant Epidermal Growth Factor (5 ng mL^{-1}, Gibco, USA), Bovine Pituitary Extract (50 μg/mL, Gibco, USA), 1 % (v/v) penicillin-streptomycin solution (Lonza, Switzerland) and the ROCK pathway inhibitor Y-27632 (10 μM, STEMCELL Technologies, Canada). Cultures were maintained at 37 °C in a humidified tissue culture incubator with 5 % CO_2 atmosphere. hKCs were routinely passaged with TrypIE™ Express (Life Technologies, UK) and re-suspended at a density of 1×10^5 cells/cm^2.

II-3.1.3.   Human dermal fibroblasts

After incubating the small fragments of skin tissue overnight at 4 °C with 2.4 U mL^{-1} of dispase (BD Biosciences, USA), the dermis (without epidermis) was mechanically dissociated. The dermis was digested for 3 h at 37 °C with collagenase type II (125 U mL^{-1}, Sigma, USA). The resulting cell suspension was filtered through a 70 μm cell strainer, centrifuged at 1500 rpm for 10 min at 4 °C, and placed in culture. hDFbs were cultured in α-MEM, supplemented with 10 % (v/v) FBS and 1 % (v/v) antibiotic/antimycotic at 37 °C in a humidified atmosphere with 5 % CO_2. hDFbs were used at passage 3–4.

II-3.1.3.1   *Human papillary and reticular fibroblasts*

After removal of the epidermis, the dermis was digested using the whole skin dissociation kit (Miltenyi Biotec, USA) as *per* the manufacturer's instructions. Tissue fragments were incubated overnight at 37 °C under agitation (160 rpm) with 435 μL buffer L, 12.5 μL enzyme P, 50 μL enzyme D and 2.5 μL enzyme A. Then, the cell suspension was applied to a 70 μm separation filter placed on a 50 mL falcon. The filter was washed with 4 mL of cold α-MEM, and the cell suspension was centrifuged at 300 g for 10 min at 4 °C. A suspension of freshly isolated human dermal fibroblasts with 7×10^6 cells/mL was incubated with

the surface markers antibodies (**Table II-2**) for 30 min at RT. After washing in PBS, cells were resuspended and then cultured in α-MEM supplemented with 10 % (v/v) FBS and 1 % (v/v) antibiotic/antimycotic. The selection of the CD324·CD45·CD31·CD39·CD26· population corresponding to the papillary subpopulation, and the CD324·CD45·CD31·CD36· population corresponding to the reticular subpopulation, was performed using a FACSAriaIII Cell Sorter and FACSDiva software (BD Biosciences, USA). For cell collection, cell sorter tubes were coated with 100 % (v/v) FBS solution (1 h, RT), to prevent cells from adhering to the tube walls. The subfractions of interest were then recovered in α-MEM supplemented with 10 % (v/v) FBS and 1 % (v/v) antibiotic/antimycotic.

Table II-2 Antibodies used for immunocytochemistry

Antibody	Brand	Ref	Host
CD324 PerCP-Cy5.5	BD Biosciences, USA	563573	Ms
CD45 PE-Cy7	BD Biosciences, USA	557748	Ms
CD31 APC-Cy7	BD Biosciences, USA	563653	Ms
CD90 FITC	eBiosciences, USA	11-0909-42	Dk
CD39 PE	BD Biosciences, USA	555464	Ms
CD26 PE-CF594	BD Biosciences, USA	565158	Ms
CD36 APC	BD Biosciences, USA	550956	Dk

Legend: Dk – Donkey, Ms - Mouse

II-3.1.4.   Human dermal microvascular endothelial cells

After removal of the epidermis and mechanical dissociation of the dermis, the remaining dispase solution containing the endothelial cells was filtered through a sterile 100 μm cell strainer, centrifuged (300 g, 5 min), re-suspended, and cultured on 0.7 % (w/v) gelatin type A (Sigma, USA) coated plates. hDMECs were cultured in EndoGRO MV-VEGF Complete Media Kit (Millipore, USA) or EGM-2 MV Microvascular Endothelial Cell Growth Medium-2 BulletKit (Lonza, USA). hDMECs were routinely trypsinized for 5 min at 37 °C in TrypLE™ Express (Life Technologies, UK), centrifuged (250 g, 5 min) and re-suspended at a cell density of 0.8 - 1 x10^6 cells in T150 cm^2 flasks.

II-3.1.5.   Human umbilical vein endothelia cells

HUVECs were purchased from Lonza (USA) and routinely cultured under the conditions defined by the company over 0.7 % (w/v) gelatin type A coated plates and under EndoGRO-VEGF Complete Media

Kit (Millipore, USA). HUVECs were routinely trypsinized for 5 min at 37 °C in TrypIE™ Express (Life Technologies, UK), centrifuged (220 g, 5 min) and re-suspended at a cell density of 0.8 - 1 x10^6 cells in T150 cm^2 flasks.

II-3.2.   Non-viral transfection

hDFbs were seeded at a density of 2x10^4 cells/well in 24-well adherent plates (Corning, Costar, Ireland). After 24 h, the cells were washed with PBS and incubated with 1 mL OptiMEM (Gibco, Ireland). After 1 h, complexed nanoparticles prepared as in Section II-1.3.4, were added to OptiMEM. After 5 h, the transfection medium was removed, the cells were washed twice in PBS, and the growth medium was replenished.

II-3.3.   Peptide-integrin binding assay

SVF cells were pre-incubated with 100 μg, 200 μg or 600 μg of peptides in serum-free α-MEM for 30 min at 37 °C. Afterwards, cells were centrifuged (300 g, 5 min) prior seeding at a density of 1.5x10^6 cells in a 2D or 3D microenvironments (described in section II-3.4.1).

II-3.4.   Function blocking peptide studies

SVF cells were pre-incubated with i) RGD peptide (100 μg or 200 μg) in suspension in α-MEM without FBS for 30 min at 37 °C, ii) anti-integrin αvβ3 (10 μg mL^{-1}, clone LM609, MAB1976, Millipore, Portugal) in α-MEM without FBS for 1 h at 4 °C or iii) anti-integrin αvβ3 for 1 h at 4 °C plus 7-day period in 37 °C. Afterwards, cells were centrifuged (300 g, 5 min) prior to seeding at a density of 1.5x10^6 cells in a 2D or 3D microenvironments (described in section II-3.4.1).

For the hDMECs (micro ECs) and HUVECs (macro ECs), cells were pre-incubated with the same amounts of RGD peptide in their respective media without growth factors or FBS prior plating on Matrigel. Matrigel assay is described on section II-5.8.

II-3.5. Apoptosis assay

SVF cells were pre-incubated with RGD (100 μg) in suspension or with mitomycin C (100 μg mL^{-1}, Sigma, Portugal) as a positive control of apoptosis, prior to seeding at a density of 1.5x10^6 cells/well in a 6-well plates.

II-3.6. Papillary and reticular fibroblasts labelling

Reticular fibroblasts were labelled with 1 μM Cell Tracker™ Orange CMRA (Invitrogen, Portugal) and papillary fibroblasts with 5 μM Cell Tracker™ Green CMFDA following the manufacturer's instructions. The fibroblast subpopulation suspensions were incubated with the respective probes in serum-free α-MEM for 30 min at 37 °C. Afterwards, cells were centrifuged (300 g, 5 min) to remove the probes and cultured as described in section II-3.5.2.

II-3.7. Co-cultures of fibroblasts subpopulations and hDMECs

Sorted fibroblasts were seeded at sub-confluency (5x10^4 cells/cm^2) and inactivated with mitomycin C (100 μg/mL, Sigma, USA) for 4 h at RT after 3 days of culture. hDMECs were seeded on the top at a density of 2.5x10^4 cells/cm^2 and co-cultures were kept for 7 days in EGM-MV VEGF medium.

II-3.8. Monocultures in GG-based spongy-like hydrogels

hDFbs entrapment within GG spongy-like hydrogels was performed using a cell suspension of 5x10^6 cell/mL in 100 μL of growth medium and then added slowly onto the top of the dried polymeric networks.

For GG/GGDVS-peptide spongy-like hydrogels a cell suspension of 50x10^6 cell/mL SVF cells in 30 μL of growth medium was used. After 30-45 min, fresh media was added up to a total volume of 1 mL and then the constructs were maintained at 37 °C, in a humidified tissue culture incubator with 5 % CO_2 atmosphere.

II-3.9. Co-cultures in GG-based bilayered spongy-like hydrogels

A cell suspension containing 0.5x10^6 reticular fibroblasts was added onto the reticular-like layer of the bilayered GG spongy-like hydrogel. Structures were transferred into polycarbonate transwells with the

reticular part facing down and kept in culture for 7 days in α-MEM, supplemented with 10 % (v/v) FBS and 1 % (v/v) antibiotic/antimycotic. Afterwards, a 2.5 x10^6 cell suspension containing 1:4 papillary fibroblasts:hDMECs was added on the top papillary-like layer. Constructs were cultured for further 7 days in EGM-2 MV-VEGF. hKCs (5x10^5) were then seeded on the surface of the papillary-like layer and cultured for 3 days in KSFM. This medium was then replaced by FAD complete medium (110 mL DMEM (Sigma-Aldrich, USA), 110 mL DMEM:Ham's F12 medium (Sigma-Aldrich, USA) and supplemented with 1.8x10^{-4} M adenine (Sigma-Aldrich, USA), 10 % (v/v) non-inactivated FBS, 0.5 μg μL^{-1} hydrocortisone (Sigma-Aldrich, USA), 5 μg mL^{-1} insulin (Sigma-Aldrich, USA), 10^{-10} M cholera toxin (Sigma-Aldrich, USA), 10 ng mL^{-1} epidermal growth factor (EGF, Peprotech, UK), 1.8 mM calcium chloride (Merck, Germany) and 1 % (v/v) PenStrep, and constructs were cultured for additional 14 days in air-liquid interface.

II-3.10. Co-cultures in GG-HyA and COL-based scaffolds

hDFbs were transfected with PEI-pVEGF N/P 7 (2 μg pDNA), Ch-pFGF2 N/P 10 (0.33 μg pDNA) or the dual combination PEI-pVEGF+Ch-pFGF2 (1 μg pVEGF + 0.165 μg pFGF2; P+C) following section II-3.2. Afterwards, hDFbs were mixed with hDMECs (1:4) and cell entrapment within GG-HyA spongy-like hydrogels and COL-based scaffolds was performed using a cell suspension of 5x10^6 cell/mL in 50 μL of growth medium and then added dropwise onto the top of the scaffolds. After 30-45 min, 1 mL of a mix of DMEM and EndoGRO MV-VEGF (1:1) fresh media was added and then the constructs were maintained at 37 °C, in a humidified tissue culture incubator with 5 % CO_2 atmosphere.

II-4. *IN VIVO* STUDIES

The implantation procedure was approved by the *Direção Geral de Alimentação e Veterinária* (DGAV), the Portuguese National Authority for Animal Health, and all the surgical procedures respected the national regulations and international animal welfare rules, according to the Directive 2010/63/EU. All animals were acclimated for 2 weeks in the bioterium before any experimentation and kept under standard conditions with a 12 h light/dark cycle, and food and water provided *ad libitum* during all the experimental period. During all experiments, animals were checked for pain and discomfort.

II-4.1.   Full thickness wound model

Full-thickness wounds were created in the back of 6 weeks old athymic nude mice NU(NCr)-Foxn1nu (**Figure II-3**). Animals were randomly assigned into 3 groups: A) GG/GGDVS-RGD spongy-like hydrogels – control; B) GG/GGDVS-RGD spongy-like hydrogels with freshly isolated SVF cells – GG/GGDVS-RGD + SVF; C) GG/GGDVS-RGD spongy-like hydrogels cultured for 7 days with SVF cells – GG/GGDVS-RGD + 7dSVF. A total of 36 animals, 6 animals *per* condition and *per* time point (5 and 28 days) were used. Mice were anaesthetized with an i.p injection of a mixture of ketamine (75 mg kg^{-1}, Imalegene, Merial, France) and metedomidine (1 mg kg^{-1}, Domitor, Orion Pharma, Finland). The back of the animals was disinfected with betaisodona prior the creation of a 5 mm Ø skin full-thickness excision, at approximately 0.5 cm caudal to the left scapula (one defect *per* animal in the left side). A donut-shaped 5 mm silicone splint (ATOS Medical, Sweden) was placed around the wound to minimize wound contraction and fixed with glue and four sutures. After transplantation of the constructs, wounds were successively covered with Tegaderm transparent dressing (3M, USA), Omnifix (Hartmann, USA) and Leukoplast (Essity, Spain) to avoid the dislocation and to protect the whole treatment set. After surgery, ANTISEDAN® (Pfizer, Finland) was administered to the animals. The animals were kept separately and received daily analgesia with metamizol (200 µg g^{-1} BW, Nolotil, Lamaçães Farma, Portugal) in drinking water for the first 72 h. At each final time-point the assigned animals were sacrificed by CO$_2$ inhalation and the constructs/tissue were explanted for histological analysis.
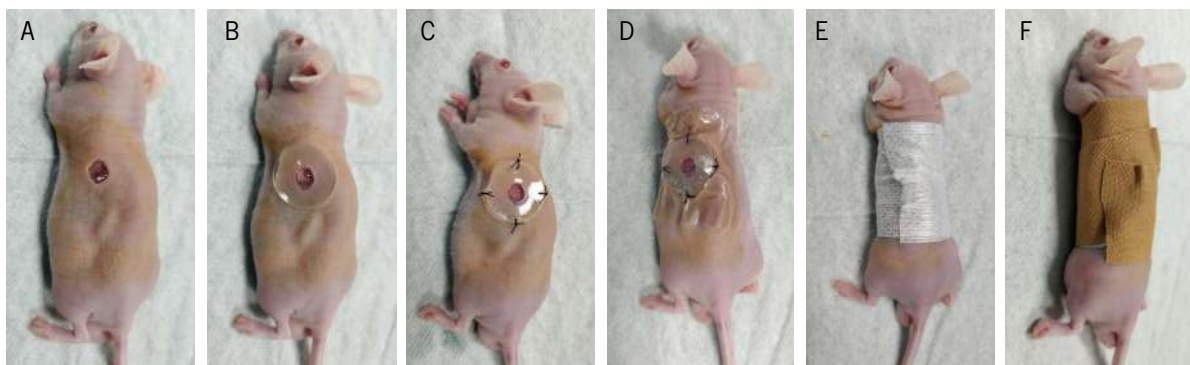
Figure II-3 Full-thickness wound model.
A A biopsy punch was used to make a 5 mm full-thickness wound on the mice upper back and **B** the silicon ring was inserted and **C** sutured on the mice back. **D** The constructs were placed in the punch area and the wound was covered with Tegaderm, **E** followed by Omnifix F and Leukoplast.

II-5.   BIOLOGICAL CHARACTERIZATION

II-5.1.   Gaussia luciferase quantification

Gaussia luciferase measurements were performed using the Pierce™ Gaussia Luciferase Flash Assay Kit (Thermo Scientific, Ireland) to quantify transfection efficiency. For analysis of luciferase production, on days 3, 7 and 14, 1 mL of complete medium was removed from each well and replaced by 1 ml of fresh medium. 20 µL of medium was collected and transferred in triplicate to a black 96-well plate. 50 µL of the working solution was added to each well and luminescence was acquired using a Varioskan Flash multimode plate reader (Fisher Scientific, Ireland).

II-5.2.   3-(4,5-dimethylthiazol-2-yl)-5-(3-carboxymethoxyphenyl)-2-(4-sulfophenyl)-2H-tetrazolium (MTS) assay

To determine the cytotoxicity of non-viral vectors-pDNA polyplexes, metabolic activity was measured at days 0, 3, 7 and 14 post-transfection using the CellTiter 96® AQueous One Solution Cell Proliferation Assay (Promega, USA). At each time-point, after washing with PBS, cells were incubated with 20 µL of MTS solution (4:1 media:MTS) for 3 h at 37 °C in a humidified tissue culture incubator with 5 % CO_2 atmosphere. Then, 100 µL of the supernatant was transferred in triplicate to a 96-well plate and the absorbance of each sample was read at 490 nm in a microplate reader (Synergy HT, Bio-TEK; USA). Results are presented as the % of metabolic activity in relation to the positive control of viability (non-transfected cells).

II-5.3.   Deoxyribonucleic acid quantification

Deoxyribonucleic acid (DNA) was measured using the Quant-iT™ PicoGreen™ Assay Kit (Invitrogen, UK) to determine the entrapment efficiency of cells within spongy-like hydrogels, the proliferation ratio of fibroblast's subpopulations and of the cells transfected with the non-viral vectors-pDNA polyplexes.

Cells were washed twice with PBS and lysed with 0.5 mL of ultra-pure water for 1 h at 37 °C, and then collected and frozen at -80 °C. In the case of the spongy-like hydrogels, samples were incubated at 60 °C for 30 min prior freezing. Before quantification, all samples were thawed at RT. The DNA content was determined by adding, in 96-well white polystyrene plates, 28.7 µL of the sample (experimental, standard or blanks) mixed with 100 µL of 1x Tris-EDTA (10 mM Tris-HCl, 1 mM EDTA, pH 7.5) buffer

and 71.3 µL of 1x Picogreen reagent. After a 10 min incubation at RT, fluorescence was read at 480/520 nm (excitation/emission) using a Varioskan Flash multimode plate reader. The dsDNA quantity was determined by interpolation from a standard curve ranging from 0 to 2 µg/mL, prepared with a DNA stock solution provided with the kit.

The entrapment efficiency (**Equation II-5**) was calculated based on the amount of DNA quantified after 24 h of cell culture (DNA_f) in relation to the correspondent quantity at the time of seeding (DNA_i).

$$Entrapment\ efficiency\ (\%) = \frac{DNA_f}{DNA_i} \times 100$$

Equation II-5 Entrapment efficiency.

II-5.4.   Calcein-AM/Propidium Iodide Staining

Cell viability within spongy-like hydrogels was assessed by staining cells with Calcein-AM (Ca-AM, 1 µg mL^{-1}, Invitrogen, USA) and propidium iodide (PI, 2 µg mL^{-1}, Invitrogen, USA) for 1 h at 37 °C in a humidified tissue culture incubator with 5 % CO_2 atmosphere. The percentage of live/dead cells was assessed with a Leica TCS SP8 confocal microscope (Leica, Germany).

II-5.5.   Phalloidin-TRITC Staining

Phalloidin–tetramethylrhodamine B isothiocyanate (phalloidin-TRITC; Sigma-Aldrich, USA) was employed to visualize the organization of the cell cytoskeleton and analyze cellular morphology, both in 2D culture and in 3D cell-laden scaffolds. Cells were fixed with 10 % (v/v) formalin, followed by incubation with phalloidin-TRITC (0.1 mg mL^{-1}, Sigma, USA) for 1 h at RT. Nuclei were simultaneously counterstained with DAPI (0.02 mg mL^{-1}). Samples were observed using a Leica TCS SP8 confocal microscope (Leica, Germany).

II-5.6.   Flow cytometry

Cells (2.5 x 10^5) were resuspended in medium and centrifuged for 5 min at 300 g. Antigen detection was performed by labelling the cells with fluorescent-labelled antibodies (**Table II-3**) for 20 min at RT. After washing with PBS, cells were centrifuged for 5 min at 400 g, fixed with 1 % (v/v) formalin and analyzed using a fluorescence-activated cell sorting (FACS) Calibur Flow Cytometer (BD Biosciences, USA) using the CELLQuest software V3.3.

Table II-3 Antibodies used for flow cytometry

Cells	Phenotype	Antibody (Brand)	Ref	Host	Amount	Clonality, reactivity
SVF	Mesenchymal	CD105-FITC (Bio-Rad, USA)	MCA1557F	Ms	2 µL	Monoclonal, human
		CD90-PE (BD Biosciences, USA)	559869	Ms	2 µL	Monoclonal, human
		CD73-APC (BD Biosciences, USA)	550257	Ms	2 µL	Monoclonal, human
	Leukocytes	CD45-FITC (BD Biosciences, USA)	555482	Ms	2 µL	Monoclonal, human
	Endothelial	CD34-PE (BD Biosciences, USA)	555822	Ms	2 µL	Monoclonal, human
		CD31-APC (R&D Systems, USA)	FAB3567A	Ms	2 µL	Monoclonal, human
	Pericyte	CD146-PE (BD Biosciences, USA)	561013	Ms	2 µL	Monoclonal, human
hDFbs	Papillary	CD26-PE-CF595 (BD Biosciences, USA)	565158	Ms	2 µL	Monoclonal, human
		CD39-PE (BD Biosciences, USA)	555464	Ms	2 µL	Monoclonal, human
		PDPN-PE			2 µL	Monoclonal, human
	Reticular	CD36-APC (BD Biosciences, USA)	550956	Dk	2 µL	Monoclonal, human
		TGM2-FITC			2 µL	Monoclonal, human

Legend: Dk – Donkey, Ms - Mouse, Rb – Rabbit, PDPN – podoplanin; TGM2 – transglutaminase-2.

The number of GFP+ cells was also analyzed by flow cytometry. The pGFP-transfected hDFbs were analysed in a BD FACSAria III using BD FACSDIVA software (both BD Biosciences, Belgium), where GFP fluorescence was expressed as a percentage of GFP+ cells over the total number of gated cells.

II-5.7. Enzyme-linked immunosorbent assay

Enzyme-linked immunosorbent assay (ELISA) was used to quantify the secretion of growth factors from the fibroblast's subpopulations, the transfected hDFbs, and from the SVF-laden integrin-specific spongy-like hydrogels. After a 24 h starvation period, culture medium was collected, centrifuged (3000 rpm, 10 min), snap frozen (liquid nitrogen), and stored at -80 °C until analysis. ELISA kits were used following the manufacturers' instructions, as summarized in **Table II-4**. High protein-binding 96 well plates (Nunc-Immuno™ MicroWell™; Sigma-Aldrich, USA) were coated with the primary antibody (capture antibody) and incubated overnight. On the following day, the wells were washed and blocked with the kit corresponding washing solution and blocking agent. After another washing step, the samples and

standards were added to the wells and allowed to bind to the capture antibody. The bound antibody was detected by incubation with a biotinylated antibody, followed by the addition of a streptavidin/avidin-HRP conjugate and the addition of the colorimetric substrate. The amount of growth factors present in the samples was determined by interpolation from a standard curve prepared according to each kit's instructions.

Table II-4 ELISA procedure summary

	VEGF	FGF-2	HGF	Angio-1	IGF-1
Brand	R&D Systems, USA		Millipore, USA	Boster Biological Technology, USA	Elabscience, USA
Reference	DY293B	DY233	RAB0212	EK0559	E-EL-H0086
Capture antibody	100 µL, overnight incubation at RT		———	———	———
Block buffer	300 µL of 1 % BSA in PBS, 1 h at RT		———	———	———
Standard/Sample	100 µL, 2 h at RT		100 µL, 2h30 min at RT	100 µL, 1h30 min at 37 ℃	
Detection antibody	100 µL, 2 h at RT		100 µL, 1 h at RT	100 µL, 1 h at 37 ℃	
Streptavidin-HRP	100 µL, 20 min at RT, dark		100 µL, 45 min at RT, dark	100 µL, 30 min at 37 ℃, dark	
Substrate solution	100 µL, 20 min at RT, dark		100 µL, 30 min at RT, dark	90 µL, 20 min at 37 ℃, dark	90 µL, 15 min at 37 ℃, dark
Stop solution	50 µL		50 µL	100 µL	50 µL
Absorbance	OD: 450nm – 540 nm		OD: 450 nm		
Detection range	31-2000 pg/mL	16-1000 pg/mL	2.79-2000 pg/mL	156-10000 pg/mL	156-10000 pg/mL

Legend: Angio1 – Angiopoietin 1, FGF-2 – basic Fibroblast growth factor, HGF – Hepatocyte growth factor, IGF-1 – Insulin-like growth factor 1, VEGF – Vascular endothelial growth factor

II-5.8. Capillary-like structure formation

The *in vitro* formation of capillary-like tubes by endothelial cells was carried out in a Matrigel® assay. Matrigel (Corning, USA) was added to each well of 96 well plates that were then kept in a humidified incubator for 30 min for gelling. hDMECs or HUVECs were then seeded on the top of the formed gel at a density of 1.3×10^4 cells/well and incubated for 24 h in a humidified incubator at 37 ℃ and 5 % of CO_2 in

the presence of the conditioned media filtered with 0.22 μm filters. The conditioned media was obtained from papillary and reticular fibroblasts or from transfected fibroblasts after a starvation period of 24 h in α-MEM without FBS. Controls of the Matrigel assay were prepared with DMEM or α-MEM (negative controls), and with EndoGRO MV-VEGF (positive controls). The organization of cells into capillary-like structures was assessed along 24 h. Micrographs (single time point) or time-lapse imaging (every 30 min over 24 h at 37 °C, 5 % of CO_2) were taken using an Axio Observer inverted Microscope (Zeiss, Germany) with the ZEN Blue 2012 software (Zeiss, Germany).

II-5.9.   Total RNA extraction and cDNA synthesis

At pre-determined time-points, GG/GGDVS-peptide(s) constructs were collected in 400 μL of Tri-reagent (Sigma-Aldrich, USA) and preserved at −80 °C until extraction. For RNA extraction, samples were incubated for 5 min at RT and 80 μL of chloroform (Sigma-Aldrich, USA) was added to the recovered supernatants. Following an incubation period of 15 min at RT, samples were centrifuged at 4 °C for 20 min at 12,000 rpm. After centrifugation, the aqueous phase was collected and 200 μL of isopropanol (VWR, Portugal) were added. Following a 10 min of incubation period at RT, samples were centrifuged at 4 °C for 10 min at 12,000 rpm. The supernatants were discarded, and pellets were washed once with 100 % ethanol and twice with 70 % ethanol, by centrifugation at 4 °C for 5 min at 12,000 rpm. Extracted RNA was kept in 10 μL of RNAse/DNAse free water (Lonza, Belgium).

RNA quantity and purity were assessed using a NanoDrop N-1000 Spectrophotometer (Thermo Fischer Scientific, USA). Samples with a 260/280 nm ratio between 1.6 and 2.2 were used for cDNA synthesis. Synthesis was performed using a QSCript cDNA SuperMix (Quanta Biosciences, USA) and a Reverse Transcription Polymerase Chain Reaction (RT-PCR) Mastercycler (Eppendorf, Germany). An initial amount of 1 μg of RNA in RNAse/DNAse free water was used for a total volume of 20 μL.

II-5.10.   Quantitative real-time polymerase chain reaction

Quantitative polymerase chain reaction (q-PCR) qPCR was used to detect the expression of vasculogenesis-associated genes (**Table II-5**). Primers for the marker candidates and the reference *β-2-microglobulin* (*β2M*) genes were designed using Primer-Blast database (NCBI, USA). qPCR reactions were carried out in a MasterCycler Realplex4 (Eppendorf, Germany) and primer efficient was tested using serial dilutions of cDNA (1, 1:10, 1:100, 1:1000). For qPCR reactions, 1 μL of synthesized cDNA was used in

a 20 μL reaction containing 10 μL of PerfeCTa® SYBR Green FastMix (Quanta Biosciences, USA) and sense and antisense primers at 30 nM. Reaction conditions comprised a 2 min denaturation step at 95 °C, followed by 45 cycles of 95 °C for 10s, a specific annealing temperature, as described in Table II-5, for 30 s and 72 °C for 10 s. Products obtained from real-time PCR were subjected to melting curve analysis to check for the correct amplicon length and the absence of unspecific products. Transcript abundances were normalized to the expression of *β2M*. Samples were run in triplicate in each PCR assay. Normalized expression values were calculated following the mathematical model proposed by Pfaffl using the formula: $2^{\Delta\Delta_{Ct}}$ [42].

Table II-5 Primers sequences

Gene and accession number	Sequence (5'-3')	Annealing temperature (°C)
Human β2M NM_004048.4	TGGAGGCTATCCAGCGTACT	59.5
	CGGATGGATGAAACCCAGACA	
Human VEGFA NM_ 003376.6	GATCCGCAGACGTGTAAATG	59
	CCCTCCCAACTCAAGTCCAC	
Human KDR NM_002253.4	CTAGGTGCCTGTACCAAGCC	59
	GCCCCTTTGGTCTTGTAGGG	
Human FGF2 NM_001361665.2	CACCTATAATTGGTCAAAGTGG	59
	CAGAAATTCAGTAGATGTTTCCC	
Human FGFR1 NM_023110.3	ACCAAACCGTATGCCCGTAG	57.5
	CCCACTGGAAGGGCATTTGA	
Human FGFR2 NM_000141.5	CCTCTCGTTCCCCAAATC	59
	GAGTGGTCCTTGGGTCTT	
Human ANGPT1 NM_001146.5	TGCAGAGAGATGCTCCACAC	56.6
	TCTCAAGTTTTTGCAGCCACT	
Human TEK NM_000459.5	TGCGAGATGGATAGGGCTTG	59.2
	AGGATGGGAAAGGCTGTATCTT	
Human PECAM1 NM_000442.5	GAGGGGCCACATGCATCTAT	59.7
	AGACCTGCTCGGTTCTCTCT	
Human VWF NM_000552.5	CCCTGGGTTACAAGGAAGAAAAT	59
	AGTGTCATGATCTGGCCTCCTCTTAG	

II-5.11. Western blot

For western blot analysis, cell-laden spongy-like hydrogels were collected in loading buffer (3.75 mL 1.975 M Tris pH 8.8, 1.5 g SDS, 12.5 mg Bromophenol blue, 7.5 mL glycerol, 0.3 mL EDTA.NaOH, 13.45 mL DI water) and Dithiothreitol (DTT) (1:100), all from Sigma-Aldrich (USA). Samples were macerated with a tissue grinder (Nippon genetics, Germany), and denatured for 1 h at 65 °C. Before loading, samples were centrifuged for 5 min at 7000 g. For SDS-PAGE, 30 μL equivalents of each sample were loaded in a 8-14 % SDS polyacrylamide gel (Sigma-Aldrich, USA) for electrophoresis, and

subsequently transferred onto a nitrocellulose membrane (GE Healthcare, UK) for staining with a Ponceau solution. For the identification of the proteins, membranes were blocked with 4 % (w/v) bovine serum albumin (BSA) in tris-buffered saline with 0.1 % (v/v) tween 20 (TBST) for 90 min and then incubated at 4 °C overnight with the primary antibodies (**Table II-6**). The bound antibody was detected with an anti-rabbit/mouse IR680/800Cw secondary antibody (Sigma-Aldrich, USA) diluted in TBST at 1:15000 for 1 h. Proteins were visualized in the 700 or 800 channel of an Odyssey Fc Imaging System (LI-COR, US), and quantified using the Image Studio Software (LI-COR, US).

Table II-6 Antibodies used for western blot

Antibody	Brand	Ref	Dilution	Host
FAK	Abcam, UK	ab40794	1:500	Rb
Phospho-FAK	Cell Signaling, USA	1673283S	1:1000	Rb
AKT1	Cell Signaling, USA	9272S	1:1000	Rb
Phospho-AKT	Abcam, UK	ab81283	1:1000	Rb
ERK 1+2	Abcam, UK	ab17942	1:1000	Rb
Phospho-ERK 1+2	Abcam, UK	ab50011	1:1000	Ms
Paxillin	Abcam, UK	ab32084	1:5000	Rb
Talin 1+2	Abcam, UK	ab11188	1:1000	Ms
Vinculin	Sigma, Portugal	V9131	1:200	Ms
KDR	Abcam, UK	ab39256	1:500	Rb
FGFR2	Abcam, UK	ab10648	1:1000	Rb
Caspase 8	Santa Cruz Biotechnology, USA	sc-81656	1:200	Ms
Caspase 3	Abcam, UK	ab32351	1:1000	Rb
GAPDH	Abcam, UK	ab181602	1:10000	Rb

Legend: AKT - Protein kinase B, ERK - Extracellular-signal-regulated kinase, FAK - Focal adhesion kinase, FGFR2 – FGF receptor 2, GAPDH - Glyceraldehyde 3-phosphate dehydrogenase, KDR – VEGF receptor 2, Ms - Mouse, Rb – Rabbit

II-5.12.   Immunostaining

II-5.12.1.   Immunocytochemistry

Cells were fixed with 10 % (v/v) formalin for 24 h at RT, permeabilized with 0.2 % (v/v) Triton X-100 (Sigma, USA) for 45 min and non-specific staining was blocked with 3 % (w/v) BSA (Sigma, USA) for 1 h. Then, samples were incubated with the primary antibodies (**Table II-7**) for 18 h at 4 °C and with the secondary antibodies Alexa Fluor 488 or 594 (Invitrogen, UK) overnight at 4 °C. Between antibodies incubations, cells were washed with PBS. Samples were incubated with DAPI (0.02 mg mL^{-1}) for 1 h for

nuclei counterstaining and were observed with an Olympus Fluoview FV1000 laser confocal (Olympus, Japan) or a Leica TCS SP8 confocal (Leica, Germany) microscope.

Table II-7 Antibodies used for ICC and IHC

Markers group	Antibody	Brand	Ref	Host	Dilution	Clonality, reactivity
ECM proteins	Fibronectin	Abcam, UK	ab2413	Rb	1:100	Polyclonal, mouse/human
	Laminin	Abcam, UK	ab11575	Rb	1:30	Polyclonal, mouse/human
	Collagen type IV	Abcam, UK	ab6586	Rb	1:100	Polyclonal, human
	Collagen type I	Abcam, UK	ab34710	Rb	1:100	Polyclonal, mouse/human
Junction markers	VE-cadherin	Abcam, UK	ab33168	Rb	1 µg/mL	Polyclonal, mouse/human
Epidermal cells	Keratin 5	Covance, USA	PRB-160P	Rb	1:800	Polyclonal, mouse/human
	Keratin 10	Abcam, UK	ab9026	Ms	1:100	Monoclonal, mouse/human
	Involucrin	Abcam, UK	ab68	Ms	1:25	Monoclonal, human
Endothelial cells	CD31	Dako, Denmark	M0823	Ms	1:30	Monoclonal, human
	CD31	Abcam, UK	ab28364	Rb	1:25	Polyclonal, mouse/human
	vWF	Abcam, UK	ab201336	Ms	1 µg/mL	Monoclonal, human
Macrophages polarization	CD86	Cell Signaling, USA	19589S	Rb	1:100	Monoclonal, mouse
	CD163	Abcam, UK	ab182422	Rb	1:500	Monoclonal, mouse/human
Fibroblasts phenotype	Podoplanin	Abcam, UK	ab10288	Ms	1:250	Monoclonal, human
	Transglutaminase-2	Abcam, UK	ab421	Rb	1:75	Polyclonal, human
	FAP	Abcam, UK	ab53066	Rb	1:100	Polyclonal, mouse/human

Legend: FAP – Fibroblast Activation Protein, Ms - Mouse, Rb – Rabbit, vWF – Von Willebrand Factor

II-5.12.2. Immunohistochemistry

Paraffin sections were deparaffinized in xylene, re-hydrated and boiled for 4-5 min in Tris-EDTA (10 mM Tris Base, 1 mM EDTA solution and, 0.05 % (v/v) Tween 20, pH 9), for antigen retrieval. Permeabilization was performed with 0.2 % (v/v) Triton X-100. Non-specific binding was blocked by incubation with a 2.5 % (v/v) Horse serum (Vector Laboratories, UK) for 40 min at RT. Samples were

then incubated with the primary antibody, at a pre-determined concentration, overnight at 4° C (**Table II-7**) and washed in 0.1 % (v/v) PBS-Tween 20, 3 times, 5 min each wash.

For primary antibodies raised in mice, the Vector Mouse on Mouse (M.O.M.) kit (Vector Laboratories, UK) was used. Sections were incubated for 1 h in working solution of M.O.M.™ Mouse Ig Blocking Reagent, followed by PBS rinsing, twice and 2 min each, and then incubated for 5 min in working solution of M.O.M.™ Diluent. Primary antibodies, prepared in the adequate concentration in 1 % (w/v) BSA in PBS (**Table II-7**), were then let to react for 30 min with tissue sections, which were then washed with PBS, twice and 2 min each, and further incubated with working solution of M.O.M. ™ Biotinylated Anti-Mouse IgG Reagent for 10 min.

For fluorescent detection, after reacting with the primary antibody, tissue sections were incubated with fluorescent-tagged secondary antibodies, Alexa Fluor 488 or 594 for 1 h at RT, according to the host of the primary antibody, and then washed with PBS. Nuclei were counterstained with DAPI (0.02 mg mL^{-1}). Samples were mounted with a Fluoromount Aqueous Mounting Medium (Sigma, USA) and analyzed using an AxioImager Z1m fluorescence microscope (Zeiss, Germany). Images acquired with a Zen 2012 software or Microscope Leica DM750 (Germany).

II-5.13. Hematoxylin-eosin, masson's trichrome and picrosirius red stainings

Tissues were fixed in 10 % (v/v) formalin, dehydrated, embedded in paraffin, cut into 4 µm sections and transferred to polylysine-coated slides. Samples were stained with hematoxylin and eosin Y (H&E, Bio-Optica, Italy), with masson's trichrome (MT, Bio-Optica, Italy) or with picrosirius red (PS, Bio-Optica, Italy) following standard protocols. H&E and MT stained samples were analyzed using a Leica Acquire software system (Germany) and with a Microscope Leica DM750, while PR stained ones were analyzed under polarized light in the Axio Observer inverted microscope and ZEN Blue 2012 software.

II-5.14. Wound closure

Wound closure was calculated by analyzing the digital images taken (A) at the time of material implantation and (B) 5, 11 and 28 days post-implantation for five animals *per* condition and time-point, according to **Equation II-6**.

$$Wound\ closure\ (\%) = \frac{A - B}{A} \times 100$$

Equation II-6 Percentage of wound closure.

II-5.15.   Image analysis

II-5.15.1.   Live/dead cell quantification

Five different images of random fields were acquired for each condition and experiment and used to calculate the percentage of live cells. The number of live (Ca-AM$^+$) cells and the total number of cells, sum of live and dead (PI$^+$) cells, were quantified using the Cell Counter plugin of FIJI for ImageJ (version 2.0.0-rc-42). The percentage of live cells was calculated as follows (**Equation II-7**).

$$\%\ Live\ cells\ = \frac{number\ of\ live\ cells}{total\ number\ of\ cells} \times 100$$

Equation II-7 Percentage of live cells.

II-5.15.2.   Analysis of number of PECAM1$^+$ cells

Five different images of random fields were acquired for each condition and experiment and used to count the number of PECAM1$^+$ cells. ImageJ software was used to count the number of PECAM1$^+$ cells, in relation to the total number of cells (DAPI).

II-5.15.3.   Analysis of the capillary-like structures formation

The capillary-like structures formation was evaluated in terms of peak time and retention time. Peak time corresponds to the period required for the maximum tubular-like structure formation while the retention time corresponds to the period between the peak time and the time structures start to regress. Capillary-like structures were screened and an angiogenesis plug-in for ImageJ 1.48 [43] was used to quantitatively analyze their formation and organization.

II-5.15.4.   Immunohistochemistry quantification analysis

Six different images of random fields of four non-consecutive tissue sections *per* time-point and *per* animal were acquired and used to infer about the number of CD163 and CD86 positive cells. The images were automatically quantified with the Cell Profiler software using an algorithm for the identification of nuclei (hematoxylin)-associated DAB staining. Results are presented as positive cells *per* total cell amount. Ratio of the CD163 positive cells *per* CD86 positive cells (CD163$^+$/CD86$^+$) was calculated from the average values of positive cells for each animal.

The same procedure was followed to quantify the number of vessels and respective diameter. Vessels in the implantation site were quantified from the PECAM1 immunostained tissue sections. ImageJ software was used to count the vessels and measure all the vessels diameter for each image. Number of vessels is presented as an average of the counted fields and expressed as number of vessels mm^{-2}. Vessel diameter is presented as an average of all measured vessels *per* condition and expressed in μm.

II-5.15.5.   Epidermal thickness quantification

Six different images of random fields of two non-consecutive tissue sections *per* time-point and *per* animal were acquired after Masson's Trichrome staining. Neoepidermal thickness in the wounded area was measured in the end-point samples. Analysis was carried out considering the basal epidermis layer up to the outermost layer of nucleated cells.

II-5.15.6.   Collagen fibers quantification

Six different images of random fields of two non-consecutive tissue sections *per* time-point and *per* animal were acquired from the Picrosirius Red staining. Green pixels were considered thin, yellow pixels were considered mixed, and red pixels were considered thick fibers [44]. Using a custom-written algorithm, pixels were identified and, by using the same colour segmentation settings for each image, gradients of fiber density were identified. After identifying the green, yellow and red pixels that corresponded to collagen presence, the number of pixels was expressed as percentage of total pixels.

II-6.   STATISTICAL ANALYSIS

GraphPad Prism 8.2.1 software (La Jolla, USA) was used to perform statistical analysis. Data were analyzed by Shapiro–Wilk normality test. A one-way analysis of variance (ANOVA) with a Tukey post-test was used to analyze the results with a normal distribution. Otherwise, data were analyzed with the Kruskal–Wallis test with Dunn's multiple comparison post-test. The significance of data variability was determined with the Brown–Forsythe test. Results are presented as mean ± standard deviation (SD) and as coefficient of variation (reproducibility analysis). Significance was set to 0.05 (95 % of confidence interval). All quantitative data refer to at least 3 independent experiments (n=3) with at least 3 replicates in each condition.

II-7.   REFERENCES

1.   Oliveira, J.T.; Martins, L.; Picciochi, R.; Malafaya, P.B.; Sousa, R.A.; Neves, N.M.; Mano, J.F.; Reis, R.L. Gellan gum: A new biomaterial for cartilage tissue engineering applications. J. Biomed. Mater. Res. Part A 2010, 93A, 852–863.

2.   da Silva, L.P.; Cerqueira, M.T.; Sousa, R. a.; Reis, R.L.; Correlo, V.M.; Marques, A.P. Engineering cell-adhesive gellan gum spongy-like hydrogels for regenerative medicine purposes. Acta Biomater. 2014, 10, 4787–4797.

3.   Cerqueira, M.T.; da Silva, L.P.; Correlo, V.M.; Reis, R.L.; Marques, A.P. Epidermis recreation in spongy-like hydrogels. Mater. Today 2015, 18, 468–9.

4.   Gantar, A.; Da Silva, L.P.; Oliveira, J.M.; Marques, A.P.; Correlo, V.M.; Novak, S.; Reis, R.L. Nanoparticulate bioactive-glass-reinforced gellan-gum hydrogels for bone-tissue engineering. Mater. Sci. Eng. C 2014, 43, 27–36.

5.   Berti, F. V.; Srisuk, P.; Da Silva, L.P.; Marques, A.P.; Reis, R.L.; Correlo, V.M. Synthesis and characterization of electroactive Gellan gum spongy-like hydrogels for skeletal muscle tissue engineering applications. Tissue Eng. - Part A 2017, 23, 968–979.

6.   Srisuk, P.; Berti, F. V.; Da Silva, L.P.; Marques, A.P.; Reis, R.L.; Correlo, V.M. Electroactive Gellan Gum/Polyaniline Spongy-Like Hydrogels. ACS Biomater. Sci. Eng. 2018, 4, 1779–1787.

7.   Cerqueira, M.T.; Da Silva, L.P.; Santos, T.C.; Pirraco, R.P.; Correlo, V.M.; Marques, A.P.; Reis, R.L. Human skin cell fractions fail to self-organize within a gellan gum/hyaluronic acid matrix but

positively influence early wound healing. Tissue Eng. - Part A 2014, 20, 1369–78.

8.   Da Silva, L.P.; Oliveira, S.; Pirraco, R.P.; Santos, T.C.; Reis, R.L.; Marques, A.P.; Correlo, V.M. Eumelanin-releasing spongy-like hydrogels for skin re-epithelialization purposes. Biomed. Mater. 2017, 12, 025010.

9.   da Silva, L.P.; Pirraco, R.P.; Santos, T.C.; Novoa-Carballal, R.; Cerqueira, M.T.; Reis, R.L.; Correlo, V.M.; Marques, A.P. Neovascularization Induced by the Hyaluronic Acid-Based Spongy-Like Hydrogels Degradation Products. ACS Appl. Mater. Interfaces 2016, 8, 33464–33474.

10.   da Silva, L.P.; Santos, T.C.; Rodrigues, D.B.; Pirraco, R.P.; Cerqueira, M.T.; Reis, R.L.; Correlo, V.M.; Marques, A.P. Stem Cell-Containing Hyaluronic Acid-Based Spongy Hydrogels for Integrated Diabetic Wound Healing. J. Invest. Dermatol. 2017, 137, 1541–1551.

11.   Cerqueira, M.T.; Da Silva, L.P.; Santos, T.C.; Pirraco, R.P.; Correlo, V.M.; Reis, R.L.; Marques, A.P. Gellan gum-hyaluronic acid spongy-like hydrogels and cells from adipose tissue synergize promoting neoskin vascularization. ACS Appl. Mater. Interfaces 2014, 6, 19668–79.

12.   Weis, S.M.; Cheresh, D.A. αv Integrins in Angiogenesis and Cancer. Cold Spring Harb Perspect Med 2011, 1, a006478.

13.   Silva, R.; D'Amico, G.; Hodivala-Dilke, K.M.; Reynolds, L.E. Integrins: The keys to unlocking angiogenesis. Arterioscler. Thromb. Vasc. Biol. 2008, 28, 1703–1713.

14.   Kapp, T.G.; Rechenmacher, F.; Neubauer, S.; Maltsev, O. V.; Cavalcanti-Adam, E.A.; Zarka, R.; Reuning, U.; Notni, J.; Wester, H.J.; Mas-Moruno, C.; et al. A comprehensive evaluation of the activity and selectivity profile of ligands for RGD-binding integrins. Sci. Rep. 2017, 7, 39805.

15.   Grote, K.; Salguero, G.; Ballmaier, M.; Dangers, M.; Drexler, H.; Schieffer, B. The angiogenic factor CCN1 promotes adhesion and migration of circulating CD34+ progenitor cells: potential role in angiogenesis and endothelial regeneration. Blood 2007, 110, 877–885.

16.   da Silva, L.P.; Jha, A.K.; Correlo, V.M.; Marques, A.P.; Reis, R.L.; Healy, K.E. Gellan Gum Hydrogels with Enzyme-Sensitive Biodegradation and Endothelial Cell Biorecognition Sites. Adv. Healthc. Mater. 2018, 7, 1700686.

17.   Hargittai, I.; Hargittai, M. Molecular structure of hyaluronan: an introduction. Struct. Chem. 2008, 19, 697–717.

18.   STERN, R.; ASARI, A.; SUGAHARA, K. Hyaluronan fragments: An information-rich system. Eur. J.

Cell Biol. 2006, 85, 699–715.

19.   Vigetti, D.; Karousou, E.; Viola, M.; Deleonibus, S.; De Luca, G.; Passi, A. Hyaluronan: Biosynthesis and signaling. Biochim. Biophys. Acta - Gen. Subj. 2014, 1840, 2452–2459.

20.   Segura, T.; Anderson, B.C.; Chung, P.H.; Webber, R.E.; Shull, K.R.; Shea, L.D. Crosslinked hyaluronic acid hydrogels: a strategy to functionalize and pattern. Biomaterials 2005, 26, 359–371.

21.   da Silva, L.P.; Cerqueira, M.T.; de Sousa, R.P.R.A.; Marques, A.M.P.; da Silva, V.M.C.; dos Reis, R.L.G. Gellan gum spongy-like hydrogels, its preparation and biomedical applications thereof 2014.

22.   Heimbach, D.; Luterman, A.; Burke, J.; Cram, A.; Herndon, D.; Hunt, J.; Jordan, M.; McManus, W.; Solem, L.; Warden, G.; et al. Artificial dermis for major burns. A multi-center randomized clinical trial. Ann. Surg. 1988, 208.

23.   Stiefel, D.; Schiestl, C.; Meuli, M. Integra Artificial Skin® for burn scar revision in adolescents and children. Burns 2010, 36.

24.   Driver, V.R.; Lavery, L.A.; Reyzelman, A.M.; Dutra, T.G.; Dove, C.R.; Kotsis, S. V.; Kim, H.M.; Chung, K.C. A clinical trial of Integra Template for diabetic foot ulcer treatment. Wound Repair Regen. 2015, 23.

25.   O'Brien, F.J.; Harley, B. a.; Yannas, I. V.; Gibson, L. Influence of freezing rate on pore structure in freeze-dried collagen-GAG scaffolds. Biomaterials 2004, 25, 1077–1086.

26.   O'Brien, F.J.; Harley, B.A.; Yannas, I. V.; Gibson, L.J. The effect of pore size on cell adhesion in collagen-GAG scaffolds. Biomaterials 2005, 26, 433–441.

27.   Mao, H.-Q.; Roy, K.; Troung-Le, V.L.; Janes, K.A.; Lin, K.Y.; Wang, Y.; August, J.T.; Leong, K.W. Chitosan-DNA nanoparticles as gene carriers: synthesis, characterization and transfection efficiency. J. Control. Release 2001, 70, 399–421.

28.   Ishii, T.; Okahata, Y.; Sato, T. Mechanism of cell transfection with plasmid/chitosan complexes. Biochim. Biophys. Acta - Biomembr. 2001, 1514, 51–64.

29.   Csaba, N.; Köping-Höggård, M.; Alonso, M.J. Ionically crosslinked chitosan/tripolyphosphate nanoparticles for oligonucleotide and plasmid DNA delivery. Int. J. Pharm. 2009, 382, 205–214.

30.   Raftery, R.M.; Tierney, E.G.; Curtin, C.M.; Cryan, S.-A.A.; O'Brien, F.J. Development of a gene-

activated scaffold platform for tissue engineering applications using chitosan-pDNA nanoparticles on collagen-based scaffolds. J. Control. Release 2015, 210, 84–94.

31.   Raftery, R.M.; Mencía Castaño, I.; Chen, G.; Cavanagh, B.; Quinn, B.; Curtin, C.M.; Cryan, S.A.; O'Brien, F.J. Translating the role of osteogenic-angiogenic coupling in bone formation: Highly efficient chitosan-pDNA activated scaffolds can accelerate bone regeneration in critical-sized bone defects. Biomaterials 2017, 149, 116–127.

32.   Boussif, O.; Lezoualc'h, F.; Zanta, M.A.; Mergny, M.D.; Scherman, D.; Demeneix, B.; Behr, J.P. A versatile vector for gene and oligonucleotide transfer into cells in culture and *in vivo*: polyethylenimine. Proc. Natl. Acad. Sci. 1995, 92, 7297–7301.

33.   Akinc, A.; Thomas, M.; Klibanov, A.M.; Langer, R. Exploring polyethylenimine-mediated DNA transfection and the proton sponge hypothesis. J. Gene Med. 2005, 7, 657–663.

34.   Behr, J.-P.P. The Proton Sponge: a Trick to Enter Cells the Viruses Did Not Exploit. Chimia (Aarau). 1997, 51, 34–36.

35.   Tierney, E.G.; Duffy, G.P.; Hibbitts, A.J.; Cryan, S.A.; O'Brien, F.J. The development of non-viral gene-activated matrices for bone regeneration using polyethyleneimine (PEI) and collagen-based scaffolds. J. Control. Release 2012, 158, 304–311.

36.   Boerckel, J.D.; Mason, D.E.; McDermott, A.M.; Alsberg, E. Microcomputed tomography: approaches and applications in bioengineering. Stem Cell Res. Ther. 2014, 5, 144.

37.   McMullan, D. Scanning electron microscopy 1928-1965. Scanning 2006, 17, 175–185.

38.   Akhtar, K.; Khan, S.A.; Khan, S.B.; Asiri, A.M. Scanning Electron Microscopy: Principle and Applications in Nanomaterials Characterization. In Handbook of Materials Characterization; Springer International Publishing: Cham, 2018; pp. 113–145.

39.   Ahearne, M.; Yang, Y.; Liu, K. Mechanical Characterisation of Hydrogels for Tissue Engineering Applications. In Topics in Tissue Engineering; Ashammakhi, N., Reis, R., Chiellini, F., Eds.; 2008; Vol. 4.

40.   Sambrook, J.; Fritsch, E.F.; Maniatis, T. Molecular Cloning. A laboratory manual.; Cold Spring Harbor Laboratory, 1989; ISBN 0879695773.

41.   Lepecq, J.B.; Paoletti, C. A fluorescent complex between ethidium bromide and nucleic acids. Physical-Chemical characterization. J. Mol. Biol. 1967, 27, 87–106.

42. Pfaffl, M.W. A new mathematical model for relative quantification in real-time RT-PCR. Nucleic Acids Res. 2001, 29, 45e – 45.

43. Carpentier, G.; Martinelli, M.; Courty, J.; Cascone, I. Angiogenesis Analyzer for ImageJ. 4th ImageJ User Dev. Conf. 2012, 198–201.

44. Drifka, C.R.; Loeffler, A.G.; Mathewson, K.; Mehta, G.; Keikhosravi, A.; Liu, Y.; Lemancik, S.; Ricke, W.A.; Weber, S.M.; Kao, W.J.; et al. Comparison of Picrosirius Red Staining With Second Harmonic Generation Imaging for the Quantification of Clinically Relevant Collagen Fiber Features in Histopathology Samples. J. Histochem. Cytochem. 2016, 64, 519–29.

CHAPTER III

TAILORING GELLAN GUM SPONGY-LIKE HYDROGELS' MICROSTRUCTURE BY CONTROLLING FREEZING PARAMETERS

<div align="right">

CHAPTER III

</div>

<div align="center">

TAILORING GELLAN GUM SPONGY-LIKE HYDROGELS'

MICROSTRUCTURE BY CONTROLLING FREEZING PARAMETERS †

</div>

ABSTRACT

Gellan gum (GG) spongy-like hydrogels have been explored for different tissue engineering applications owed to their highly attractive hydrogel-like features, and improved mechanical resilience and cell performance. Although the whole process for the preparation of these materials is well-defined, we hypothesized that variations occurring during the freezing step leads to batch-to-batch discrepancies. Aiming to address this issue, two freezing devices were tested, to prepare GG spongy-like hydrogels in a more reproducible way. The cooling and freezing rates, the nucleation time and temperature, and the end freezing time were determined at different freezing temperatures (-20 °C, -80 °C, -210 °C). The efficacy of the devices was assessed by analyzing the physicochemical, mechanical, and biological properties of different formulations. The cooling rate and freezing rate varied between 0.1 °C min^{-1} and 128 °C min^{-1}, depending on the temperature used and the device. The properties of spongy-like hydrogels prepared with the tested devices showed lower standard deviation in comparison to the standard process, due to the slower freezing rate of the hydrogels. However, with this method, mean pore size was significantly lower than with the standard method. Cell entrapment, adhesion and viability were not affected as demonstrated with human dermal fibroblasts. This work confirmed that batch-to-batch variations are mostly due to the freezing step and that the tested devices allow to fine tune scaffolds' structure and properties.

III-1.   INTRODUCTION

Porous biomaterials have been extensively used in tissue engineering, holding a great promise for the regeneration and repair of damaged tissues as providers of a three-dimensional structure (3D) for the adhesion, growth, migration, and proliferation of cells [1]. Higher pore size and porosity is generally associated with higher cellular performance [2,3], but attaining the right balance between the pore size and overall porosity still is critical [4]. The architecture and isotropy of scaffolds also influence overall cell behavior, as cells randomly distribute and project filopodia in scaffolds with random pores but elongate along the pores in radially or axially aligned scaffolds [5]. Consequently, host response and neotissue formation have also been found to be influenced by scaffolds' microstructure [6–8], particularly the size [9] and direction [10] of the pores. Although endothelial cells enter and new vessels can be formed through 30–40 μm pores [11,12], higher pore sizes are needed for the full colonization of the structure and efficient diffusion of oxygen, nutrients, and metabolites to the cells to nourish them prior the establishment of a vascular network [13,14]. Higher porosity is also associated with a higher area to support cell adhesion in the first stage, and with faster biodegradability, hence providing additional space for tissue ingrowth [9]. Moreover, scaffolds with multidirectional pores endorse the deposition of non-fibrotic loose and randomly organized collagen fibers in contrast to unidirectional scaffolds [10]. Therefore, small alterations in the scaffolds' microarchitecture impact cell–material interactions and subsequent tissue formation. Hence, a precise control of the pore size, architecture, and interconnectivity of scaffolds is needed.

Gellan gum (GG) spongy-like hydrogels have been previously proposed by us; these structures are characterized by a water content comparable to hydrogels, but improved resilience to deformation and mechanical stability, as well as unprecedented cell-adhesive features [15]. These materials have already demonstrated impressive results regarding the adhesion of cells from different origins, such as skin [16], bone [17], and muscle [18,19]. A proven impact was also shown in terms of *in vivo* skin repair, where a positive effect over the re-epithelization [20,21] and neovascularization [22,23] of full-thickness wounds was observed. Spongy-like hydrogels are prepared from precursor hydrogels through a well-defined processing methodology that includes freezing and freeze-drying the hydrogels to give rise to dried polymeric networks. During freezing, the water already existing in the hydrogels forms ice crystals that are sublimated during freeze-drying, thus creating a porous dried polymeric structure with a particular microarchitecture [24]. These are able to rapidly uptake any solution giving rise to spongy-like hydrogels that comprise features between sponges and hydrogels. While the whole procedure for the spongy-like

hydrogels' formation is well-defined, there are batch-to-batch discrepancies that we hypothesized to result from the temperature variations occurring during the freezing stage. In fact, different parameters such as the cooling rate, the final freezing temperature, and the thermal hold were shown to affect the scaffolds' properties, particularly the pore size [25–29].

Therefore, in this work we tested the effect of two freezing devices, in relation to the standard method, over the pore size of GG dried polymeric networks and spongy-like hydrogels prepared at –20, –80, and –210 °C. The changes of the freezing profiles were analyzed in order to understand the contribution of each freezing parameter. Moreover, different concentrations of GG were used to eliminate potential effects related to the amount of polymer. The maintenance of the characteristic features of spongy-like hydrogels such as cell-adhesive nature was further confirmed.

III-2.   MATERIALS AND METHODS

III-2.1.   Freezing device

The insulated freezing device (IFD) contains a conductive aluminum multiwell plate, with a cover and a base of a thermo-conductive copper alloy and of an insulator. The non-insulated freezing device (NFD) is composed of the same components as the IFD except the insulating outer shell (**Figure III-1**). The conductive multiwell plate (aluminum 6082-T6 alloy, Al) radiates the heat within the plate maintaining an even temperature in all wells. Directly under and above the multiwell plate is placed a layer of a C11000 copper alloy (Cu), a thermo-conductive material to allow a faster and more uniform transfer of thermal energy. The outer shell is constructed from expanded polystyrene (EPS), a thermal insulating material, preventing/reducing vapor formation from an external surface of the device and reducing heat transfer due to the operator's physical contact. A tissue culture polystyrene (TCPS) multiwell plate without any other cover was used in the standard method as previously reported by us [15].

III-2.2.   Spongy-like hydrogel preparation

GG spongy-like hydrogels were prepared as previously described [15]. Briefly, gelzan powder (Sigma-Aldrich, USA) was dissolved in deionized water (0.75 % and 1.25% (w/v)), under stirring at 90 °C. After dissolution, the solution was cast into the desired molds (TCPS 24-well plate—standard method, and aluminum 24-well plate—IFD and NFD) and rapidly mixed with the crosslinking solution, cell culture α-

minimal essential medium (α-MEM, Gibco, Portugal) with no further supplementation. After the hydrogel formation, they were stabilized in phosphate buffered saline (PBS, Sigma-Aldrich, Portugal) solution for 48 h. Afterward, hydrogels were frozen at $-210\ °C$ in liquid nitrogen (N_2) for 20 min, or at -20 or -80 $°C$ for 18–20 h before being freeze-dried (LyoAlfa 10/15, Telstar, Spain) for three days to obtain GG dried polymeric structures.
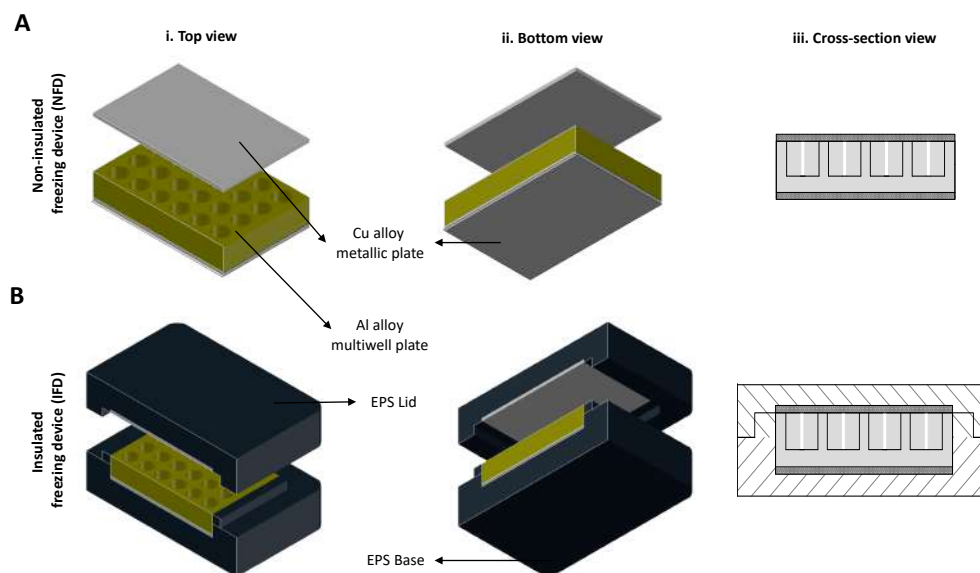
Figure III-1 Scheme of the (i) top, (ii) bottom and (iii) cross-section view of the freezing devices.
A The non-insulated freezing device (NFD) contains a conductive aluminum multiwell plate, with a cover and a base of a thermo-conductive copper alloy. **B** The insulated freezing device (IFD) is composed by the same components of the NFD and an insulating outer shell. EPS—expanded polystyrene.

III-2.3.   Thermal profiles

The thermal profile along the freezing of the hydrogel was determined using temperature sensors (Innovative Sensor Technology AG, Switzerland) that were positioned in the middle part of seven hydrogels randomly distributed throughout the wells. Measurements were recorded every 5 s using a computer program written in Arduino (v1.8.10, MA, USA). The cooling rate, nucleation time and temperature, freezing rate, and end freezing time were determined from the thermal profiles (**Figure III-2A,B**).

III-2.4.   Microscopic analysis

Scanning electron microscopy (SEM) was used to analyze the microstructure of the dried polymeric networks. Prior to analysis, samples were sputter coated with a mixture of gold–palladium. A JSM-6010LV (JEOL, Japan) microscope, operating with an accelerating voltage of 15 kV was used to capture images.

Confocal microscopy was used to analyze the microstructure of spongy-like hydrogels (hydrated dried polymeric structures) after staining with 4′,6-diamidino-2-phenylindole (DAPI, 0.2 mg mL⁻¹, Biotium, Portugal) for 2 h at room temperature (RT), as previously described by da Silva *et al.* [30]. Samples were observed with a Leica TCS SP8 confocal microscope (Leica, Germany). FIJI for ImageJ (version 2.0.0-rc-69, NIH, USA) was used to measure the pore size in five random images for each condition (three independent experiments).

III-2.5.   Micro-computed tomography (μ-CT)

The spongy-like hydrogels' microarchitecture was analyzed using a high-resolution X-ray microtomography system SkyScan 1072 scanner (SkyScan, Belgium). Samples were scanned in high-resolution mode using a pixel size of 11.31 μm (magnification of 23.30×) and an integration time of 1.7 sec. The x-ray source was set at 35 keV of energy and 215 μA of current. Representative datasets of 150 slices were transformed into a binary picture using a dynamic threshold of 45e225 (grey values) to distinguish polymer material from pore voids. Pore size was obtained using the CT Analyzer (v1.5.1.5, SkyScan).

III-2.6.   Compressive tests

The mechanical behaviour of spongy-like hydrogels (hydrated in PBS for 24 h, at RT) was tested, under static compression using an Instron 5543 (Instron, USA). Samples (13.4 mm diameter and 3 mm height) were submitted to a pre-load of 0.1 N and tested up to 60 % of strain, at a loading rate of 2 mm m⁻¹. The compressive modulus was determined from the most linear part of the stress/strain curves using the secant method.

III-2.7.   Water uptake quantification

Dried polymeric networks were immersed in PBS or α–MEM up to 24 h at 37 °C, to determine the water uptake profile. Samples were weighed prior immersion (W$_d$) and after each time point (W$_w$) to calculate the percentage of water uptake along time (**Equation III-1**). The water content was determined for the end time point using the same equation.

$$Water\ uptake\ (\%) = \frac{(W_w - W_d)}{W_d} \times 100$$

Equation III-1 Water uptake.

III-2.8.   Cell isolation and culture

Human skin was obtained from abdominoplasty procedures of healthy donors performed at *Hospital da Prelada* (Porto) after patient's informed consent and under a collaboration protocol approved by the ethical committees of both institutions. Skin specimens were cut into small fragments and incubated with dispase (BD Biosciences, Portugal) overnight at 4 °C. The epidermis was peeled off and the dermis was digested for 3 h at 37 °C using collagenase type II (125 U mL^{-1}, Sigma-Aldrich, Portugal). The resulting cell suspension was filtered through a 70 μm cell strainer and centrifuged at 1500 rpm for 10 min at 4 °C and placed in culture. Human dermal fibroblasts (hDFbs) were cultured in α–MEM, supplemented with 10 % fetal bovine serum (FBS, Gibco, Portugal) and 1 % antibiotic/antimycotic (Gibco, Portugal) at 37 °C in a humidified atmosphere with 5 % CO_2. hDFbs were used at passage 3 and 4.

III-2.9.   Cell seeding/entrapment

The hDFbs cell suspension (5×10^5 cells) was prepared in α-MEM (100 μL). For cell seeding/entrapment, cell suspension was dispensed dropwise on the top of dried polymeric networks. Constructs were incubated for 30 min, at 37 °C, 5 % CO_2 to allow maximum cell entrapment within the structures before fresh medium was added to the well up to a total volume of 1 mL.

III-2.10.   DNA quantification

The cell seeding/entrapment efficiency in the spongy-like hydrogels was determined based on the amount of DNA quantified after 24 h of cell culture (DNA_f) in relation to the quantity corresponding to the cell seeding density (DNA_i). The PicoGreen dsDNA assay kit (Invitrogen, Portugal) was used following the manufacturer's instructions. Briefly, spongy-like hydrogels were incubated with 0.5 mL of ultra-pure water for 1 h at 37 °C and then frozen at −80 °C for 24 h. Afterward, materials were heated to 70 °C for 30 min, dissolved with the help of a vortex and centrifuged for 5 min at 1000 g. The supernatant with the DNA content was collected. Each well of a white 96-well plate received 28.7 μL of each cell lysate followed by the addition of 100 μL of 1× Tris-EDTA buffer and 78.3 μL of PicoGreen reagent. After a 10 min incubation at RT, fluorescence was read at 480/520nm using a Synergy HT plate reader (BioTek, USA).

The concentration of DNA present in each sample was determined against a standard curve. The following equation (**Equation III-2**) was used to quantify the entrapment efficiency:

$$Entrapment\ efficiency\ (\%) = \frac{DNA_f}{DNA_i} \times 100$$

Equation III-2 Entrapment efficiency of cells within GG spongy-like hydrogels.

III-2.11. Cell survival and cytoskeleton organization analysis

After three and seven days, cell-laden spongy-like hydrogels were incubated with calcein-AM (Ca-AM, 1 µg mL^{-1}, Invitrogen, Portugal) and propidium iodide (PI, 2µg mL^{-1}, Invitrogen, Portugal) for 1 h at 37 °C in a humidified tissue culture incubator with 5 % CO_2 atmosphere. Then, constructs were fixed and counter-stained with DAPI (0.02 mg mL^{-1}) and the percentage of live/dead cells was assessed with a Leica TCS SP8 confocal microscope. The number of live and dead cells for each condition was quantified in five random images (three independent experiments) using the Cell Counter plugin of FIJI for ImageJ. The percentage of live cells was calculated as followed (**Equation III-3**):

$$\%\ live\ cells = \frac{number\ of\ live\ cells}{total\ number\ of\ cells} \times 100$$

Equation III-3 Percentage of live cells within GG spongy-like hydrogels.

For visualization of the cytoskeleton F-actin fibers and nuclei, cells were fixed and stained with phalloidin-TRITC (0.1 mg mL^{-1}, Sigma-Aldrich, Portugal) and DAPI (0.02 mg mL^{-1}), respectively. Samples were observed with a Leica TCS SP8 confocal microscope.

III-2.12. Statistical analysis

GraphPad Prism 8 software (La Jolla, CA, USA) was used to perform statistical analysis. Data were analyzed by Shapiro–Wilk normality test. A one-way analysis of variance (ANOVA) with a Tukey post-test was used to analyze the results with a normal distribution. Otherwise, data were analyzed with the Kruskal–Wallis test with Dunn's multiple comparison post-test. The significance of data variability was determined with the Brown–Forsythe test. Results are presented as mean ± standard deviation (SD) and as coefficient of variation (reproducibility analysis) and the significance level between groups was set for * $p < 0.05$.

III-3. RESULTS

III-3.1. Thermal profile features

The thermal profile is divided in two main phases, the cooling phase occurring until the nucleation temperature is reached, and the freezing phase that follows it, starting when the nucleation temperature is reached (**Figure III-2B**). Thus, the cooling rate was calculated from the linear region of the cooling phase, while the freezing rate was obtained from the linear region of the profile corresponding to the beginning of the freezing slope up to the end freezing temperature (set temperature of the freezer) was reached (**Figure III-2B**).

Thermal curves and consequently the freezing parameters (cooling rate, nucleation time and temperature, freezing rate, and end freezing time) were significantly affected by the freezing temperature (−20, −80, and −210 °C) and freezing device (**Figure III-2C–E**) but not by the concentration of polymer used to produce the materials (Supplementary Figure III-1). The final freezing temperature reached was only coincident with the freezing temperature for the −20 °C condition (**Figure III-2Ci**). The lowest temperature reached for the −80 °C condition was −60 °C (**Figure III-2Cii**). Regarding the −210 °C group (**Figure III-2Ciii**), the immersion time in the liquid nitrogen was not enough to reach the freezing temperature, except when the standard method was used. No measures were obtained for NFD due to the inability to properly seal the device to prevent the entrance of liquid nitrogen.

The nucleation time and the end freezing time (**Figures III-2D and 6**) successively increased in relation to the standard method for the NFD and IFD and decreased with the freezing temperature. On the other hand, the cooling rate (**Figures III-2Ei and 6**) significantly decreased ($p < 0.001$) in relation to the standard method for the NFD and IFD. The cooling rates ranged from 0.2 to 1.5 °C min⁻¹ for the −20 °C, from 0.4 to 4.4 °C min⁻¹ for −80 °C, and from 4.8 to 32.2 °C min⁻¹ for −210 °C. The nucleation temperature (**Figures III-2Eii and 6**) was affected by the freezing device but not by the freezing temperature. The nucleation temperature decreased with insulation ($p < 0.001$ for 20 °C; $p < 0.01$ for −80 °C) in relation to the standard method. The freezing rate (**Figures III-2Eiii and 6**) followed the same trend as the cooling rate; it ranged from 0.1 to 0.8 °C min⁻¹ for −20 °C, 0.2–3.6 °C min⁻¹ for −80 °C, and 3.9–128 °C min⁻¹ for −210 °C.
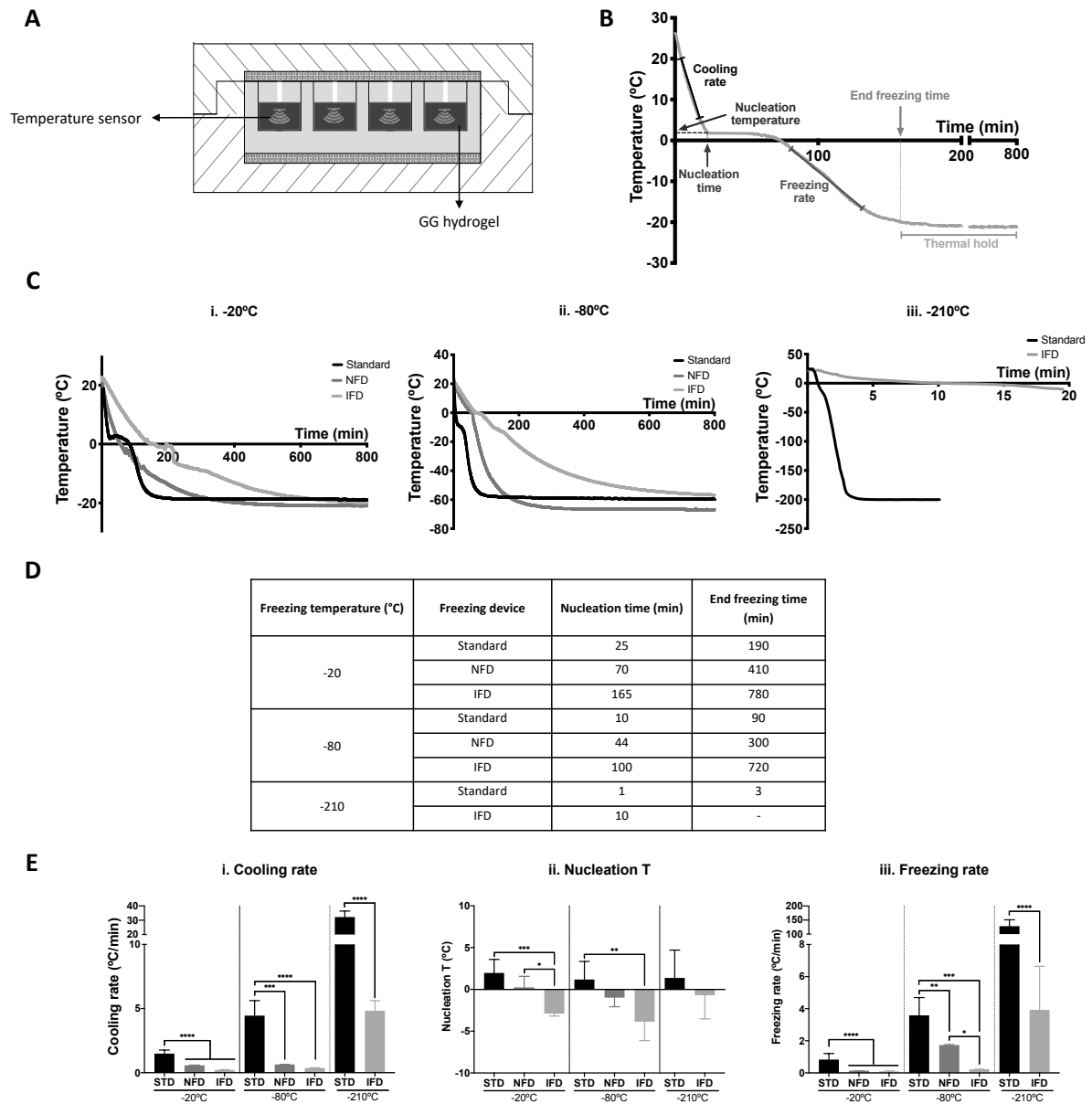
Figure III-2 Freezing profiles of 1.25% gellan gum (GG) hydrogels.
A Cross-section of the insulated freezing device with GG hydrogels. The temperature curves were measured using a temperature sensor that was placed inside the hydrogel. **B** Schematic of a thermal profile of a GG hydrogel with the cooling, nucleation temperature (T) and time, freezing rate, and end freezing time marked. **C** Mean temperature profiles of GG hydrogels during freezing at (i) −20, (ii) −80, and (iii) −210°C with the three different freezing molds. **D** Characteristic values of the freezing of GG hydrogels. **E** Effect of both temperature and freezing mold on the (i) cooling rate, (ii) nucleation T, and (iii) freezing rate of GG hydrogels. STD refers to materials prepared with the standard method. $*$ $p < 0.05$, $**$ $p < 0.01$, $***$ $p < 0.001$, $****$ $p < 0.0001$, one-way ANOVA with Bonferroni multiple comparison post-test.

III-3.2.   Effect of freezing conditions over the properties of dried polymeric structures and spongy-like hydrogels

The microarchitecture of GG dried polymeric networks was affected by both the freezing device and the freezing temperature (**Figures III-3Ai,ii and 6**). Regarding the freezing device, a narrower pore size

spectrum was successively observed for the materials prepared with the NFD and the IFD in relation to those prepared with the standard method. A similar tendency was observed considering the freezing temperature and independently of the GG concentrations (**Figures III-3Ai** and Supplementary Figure III-2Ai). This impacted the mean pore size of these materials that decreased accordingly.

For the 1.25 % GG dried polymeric networks (**Figure III-3Ai**), the pore size ranged from 11 to 577 µm with the standard method, from 11 to 306 µm with NFD, and from 11 to 441 µm with IFD for materials prepared at −20 °C. For materials prepared at −80 °C, the pore size varied from 11 to 577 µm with the standard method and from 11 to 215 µm for both NFD and IFD. The materials prepared at −210 °C, depicted pores from 11 to 238 µm with the standard method and 11 to 192 µm for IFD. Overall, similar pore sizes were attained for 0.75 % GG dried polymeric structures (Supplementary Figure III-2Ai) although different densities were observed for specific values. The mean pore size decreased from scaffolds prepared with the standard method to those prepared with the IFD. A similar effect was observed when the freezing temperature was diminished (**Figure III-3Ai,ii**) and for lower concentrations of GG (Supplementary Figure III-2A).

Spongy-like hydrogels were obtained from dried polymeric networks after hydration. When immersed in aqueous solutions, the dried structures took up water rapidly reaching stable values after 2 h in both α-MEM (Supplementary Figure III-3) and PBS (data not shown). The microstructure of the spongy-like hydrogels (**Figure III-3Bi**) was slightly affected after hydration but the differences in relation to the dried polymeric networks were not significant. A reduced water uptake capacity was detected for materials prepared with lower freezing temperatures (**Figures III-3Biii, 6** and Supplementary Figure III-3), around 2800 %, 2500 %, and 2200 % of their dry weight for materials prepared at −20, −80, and −210 °C, respectively (**Figures III-3Biii and 6**). For 0.75 % GG materials, those values changed respectively to 2500 %, 2400 %, and 2100 %. No significant differences were detected in the mean pore size between dried polymeric networks and spongy-like hydrogels (**Figures III-3Bii and 6**). Again, a decrease in the mean pore size was successively observed for the materials prepared with the NFD and the IFD in relation to those prepared with the standard method. For 1.25 % GG spongy-like hydrogels the mean pore size was 252, 151, and 127 µm for materials prepared at −20 °C with the standard method, the NFD and the IFD, respectively (**Figures 3Bii and 6**), 191, 108, and 107 µm for those prepared at −80 °C, and 110 µm (standard) and 79 µm (IFD) when prepared at −210 °C. A similar effect was observed when the freezing temperature was diminished (**Figure 3Bii**) and for lower concentrations of GG (Supplementary Figure III-2Bii and **Figure 6**).
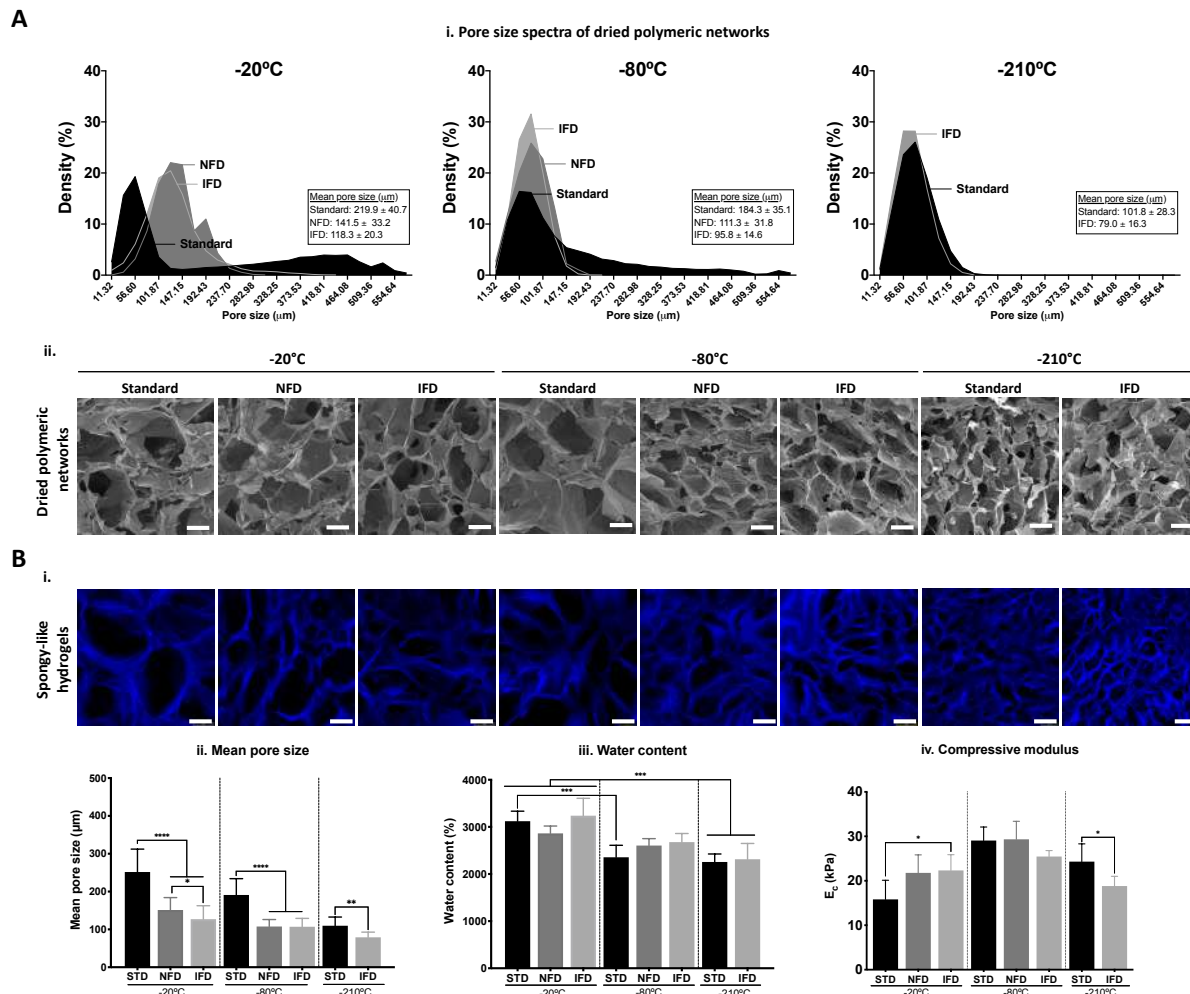
Figure III-3 Effect of freezing conditions (standard method (STD), NFD, and IFD at −20, −80, and −210 °C) over the properties of 1.25% GG dried polymeric structures and spongy-like hydrogels.
A (i) Pore size spectra and mean pore size obtained from micro-computed tomography (μ-CT) and (ii) representative scanning electron microscopy micrographs of dried polymeric structures. **B** (i) Representative confocal images of the microarchitecture of spongy-like hydrogels after staining with DAPI (blue). Representation of the variations of the (ii) mean pore size obtained from the analysis of images acquired by confocal microscopy, (iii) water content, and (iv) compressive modulus of spongy-like hydrogels prepared under different freezing conditions. * $p < 0.05$, ** $p < 0.01$, *** $p < 0.001$, **** $p < 0.0001$, one-way ANOVA with Bonferroni multiple comparison post-test. Scale bar = 75 μm.

The mechanical properties of GG spongy-like hydrogels were measured after the water uptake equilibrium was reached. Both the freezing device and the freezing temperature affected the compressive modulus in a non-linear way (**Figures 3Biv, 6** and Supplementary Figure III-2Biv). For materials prepared with 1.25 % GG, a significant ($p < 0.05$) increase and decrease in the compressive modulus was observed for materials respectively frozen at −20 and at −210 °C with the IFD in relation to the standard condition (**Figures 3Biv and 6**). No significant differences in the compressive modulus were observed when materials were prepared at −80 °C. Moreover, the highest compressive modulus, ~27.7 kPa, was

obtained at this temperature. The same trend was not observed for materials prepared with 0.75 % GG (Supplementary Figure III-2Biv and **Figure 6**). While a significant decrease (p < 0.05) was obtained for materials frozen at −20 °C with the IFD in relation to the standard condition, no differences in the compressive modulus were observed between freezing devices, either at −80 or −210 °C (Supplementary Figure III-2Biv and **Figure 6**).

III-3.3. Reproducibility analysis

The variation of the data related to the microstructure, physicochemical, and mechanical properties of GG-based dried polymeric structures and spongy-like hydrogels was evaluated in order to assess the level of homogeneity/standardization attained using the freezing devices. There seemed to be a lower coefficient of variation for 1.25 % GG materials when the freezing temperatures are lower. More importantly, a reduction in the coefficient of variation was achieved when using the freezing devices. The
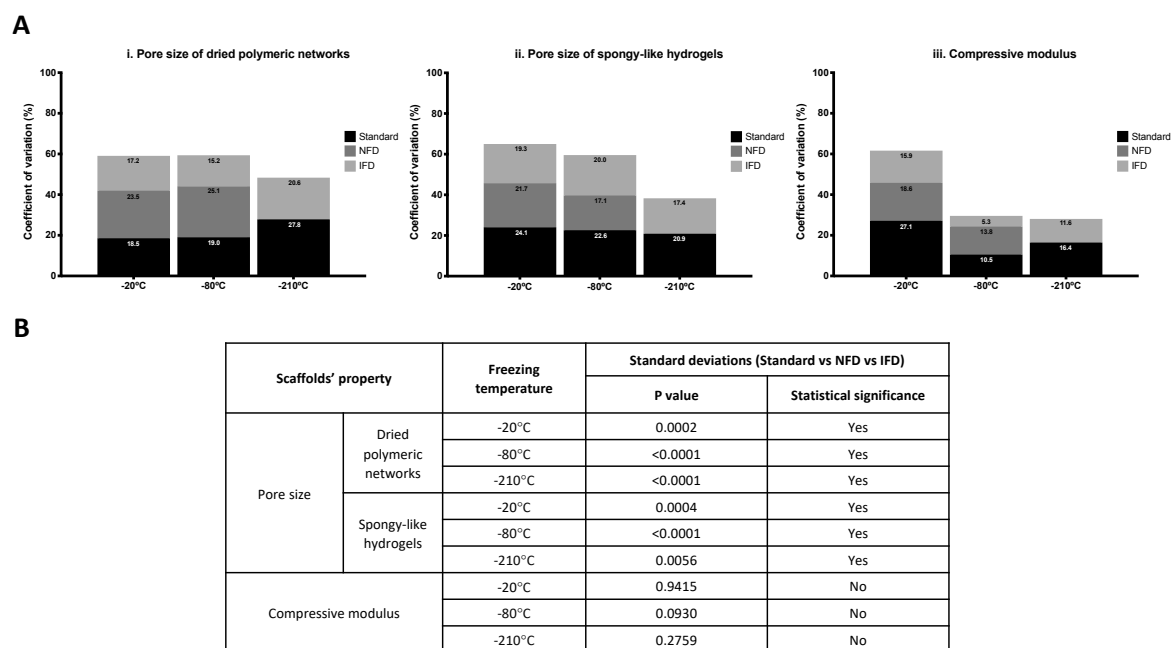
Scaffolds' property		Freezing temperature	Standard deviations (Standard vs NFD vs IFD)	
			P value	Statistical significance
Pore size	Dried polymeric networks	-20°C	0.0002	Yes
		-80°C	<0.0001	Yes
		-210°C	<0.0001	Yes
	Spongy-like hydrogels	-20°C	0.0004	Yes
		-80°C	<0.0001	Yes
		-210°C	0.0056	Yes
Compressive modulus		-20°C	0.9415	No
		-80°C	0.0930	No
		-210°C	0.2759	No

Figure III-4 Scaffolds reproducibility.
A Representation of the coefficient of variation of the pore size of 1.25% GG (i) dried polymeric networks and (ii) spongy-like hydrogels, and of the (iii) compressive modulus of spongy-like hydrogels according to the tested freezing conditions, standard method, NFD and IFD at −20, −80, and −210 °C. **B** p values obtained from the Brown–Forsythe test showing the statistical

significance of the standard deviations for the pore size and compressive modulus among the different freezing devices (standard method, NFD, and IFD).

coefficient of variation for the pore size of the dried polymeric networks that ranged from 18.5 to 27.8 for the materials prepared with the standard method, decreased to 15.2–20.6 when IFD was used (**Figure III-4Ai**). Similarly, it decreased from 20.9–24.1 to 17.4–20.0 for the spongy-like hydrogels (**Figure III-4Aii**). Notwithstanding, the ranges of the coefficient of variation of the compressive modulus were 15.5–27.1 and 15.9–5.3, respectively for the standard method and IFD condition (**Figure III-4Aiii**). The analysis of the standard deviations (**Figure III-4B**) confirmed significant differences in the pore size variation of both dried polymeric networks and spongy-like hydrogels produced with the different freezing systems and independently of the freezing temperature. The same tendency was observed for all the properties of 0.75 % GG materials (Supplementary Figure III-4).

III-3.4.   hDFbs survival and viability within spongy-like hydrogels

Regarding the capacity of spongy-like hydrogels to support hDFbs entrapment, adhesion, and viability, after 24 h of cell seeding, 70 % of the total number of seeded cells remained in the structure (**Figure III-5A**). No differences were observed when cells were entrapped on materials prepared with different freezing devices and different freezing temperatures (**Figure III-5A**). After three days of culture, the percentage of live cells was higher in the materials prepared in the IFD at the lowest temperature, but a significant difference ($p < 0.05$) was only observed between the materials frozen at -20 °C using the standard method and those frozen at -210 °C in the IFD (**Figure III-5Bi**). Overall, the percentage of live cells was higher than 60 % in all conditions after three and seven days (**Figure III-5B**). Regarding cell morphology (**Figure III-5C**), cells showed a round-like shape after three days but a well-organized actin cytoskeleton and a spread and spindle-like morphology after seven days in all conditions. Moreover, hDFbs seemed clustered after three days but after seven days, cells were able to colonize the spongy-like hydrogels, organizing in higher-density adherent colonies in the materials prepared at -210 °C (**Figure III-5C**). The same tendency was observed for 0.75 % GG spongy-like hydrogels (Supplementary Figure III-5).
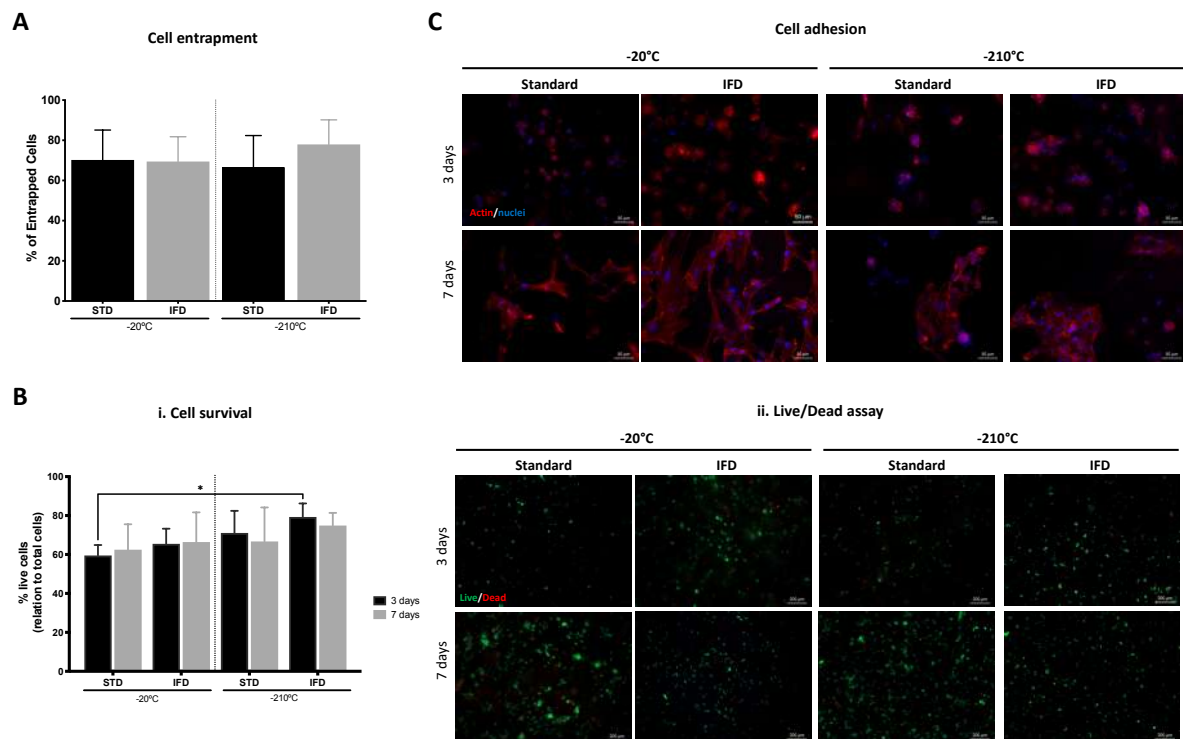
Figure III-5 Effect of freezing conditions (standard method (STD), NFD, and IFD at −20 and −210°C) over human dermal fibroblasts' (hDFbs) behavior in 1.25% GG spongy-like hydrogels.
A Representation of the entrapment efficiency 24 h after cell seeding. **B** (i) Representation of the percentage of the live cells three and seven days of culture. (ii) Representative fluorescence microscopy images showing the dead (red) and the live (green) cells, respectively stained with propidium iodide (PI) and calcein-AM (Ca-AM) after three and seven days of culture. Scale bar = 200 μm. **C** Representative fluorescence microscopy images of hDFbs after three and seven days of culture showing the F-actin cytoskeleton (phalloidin-TRITC, red) and nuclei (DAPI, blue). Scale bar = 50 μm. Data were obtained from three independent experiments with three replicates for each condition, * $p < 0.05$, two-way ANOVA and Bonferroni's post-hoc test.

III-3.5. Mapping of thermal parameters used for scaffold preparation and scaffolds' properties

A gradient color mapping of thermal parameters used for scaffold preparation and scaffolds' properties is illustrated in **Figure III-6**. Considering the different freezing devices (standard/NFD/IFD), the cooling rate, nucleation temperature, and freezing rate decrease from the standard to the IFD. In opposition, the nucleation time and end freezing time increased (standard < NFD < IFD). These variations impacted scaffolds' properties by decreasing the mean pore size in dry and wet state (standard < NFD < IFD) but did not significantly affect the water uptake. These profiles are valid for any of the temperatures tested as well as for both 1.25 % and 0.75 % GG concentrations. Interestingly, there seemed to be a tendency for the modulus to be less affected by the freezing device when lower temperatures were used.

Within each freezing device, an increase of the cooling rate, nucleation temperature, and freezing rate was observed as the freezing temperature decreases (−20 °C < −80 °C < −210 °C) while the

opposite was observed for the nucleation time and end freezing time (−20 °C > −80 °C > −210 °C). These impacted the mean pore size of scaffolds in the dry and wet state, and the water uptake, all of them reduced for lower freezing temperatures (−20 °C > −80 °C > −210 °C). In what concerns the modulus, there seemed to be a tendency to be less affected when lower temperatures were used, however, higher amounts of GG led to an increase in this mechanical property.
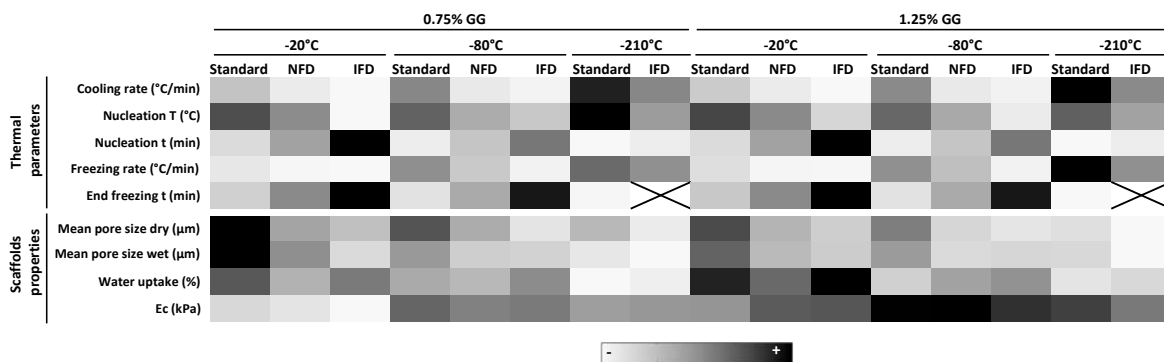
Figure III-6 Heat map showing the relative effect of the freezing devices and temperatures, and polymer concentration on the different thermal parameters and scaffolds' properties.

T = temperature, t = time.

III-4. Discussion

In the last years, we have been assessing the potential of GG spongy-like hydrogels for a range of tissue engineering and regenerative medicine applications [15–23]. Although the whole procedure for preparing spongy-like hydrogels is well defined, it is important to recognize that batch-to-batch variability affects the final scaffolds' architecture and overall properties. Thus, we hypothesized that these variations are dependent on the freezing conditions. The freezing stage is the most critical step during spongy-like hydrogels' formation since it determines ice nucleation and crystal growth, thus influencing their particular micro-architecture. As the GG dried polymeric structures are formed from precursor hydrogels, the water content and the way ice crystals are formed during freezing and then sublimed with the freeze-drying determine pore size and overall porosity [15]. Ice crystals start to form from a nucleation point, and then grow and merge until a solid–liquid system equilibrium is reached [31]. Ice crystal nucleation and growth is highly influenced by the freezing thermodynamics [31]. Therefore, freezing parameters, such as nucleation and freezing time, cooling and freezing rate, and nucleation temperature play a key role.

Aiming to understand those freezing parameters and consequentially to be able to tailor dried polymeric network/spongy-like hydrogels' properties, different freezing devices/strategies were

considered. In addition to the standard approach that has been followed to prepare those structures [32], a non-insulated and highly thermo-conductive freezing device (NFD) and an insulated freezing device (IFD) were used at −20, −80, and −210 °C. The NFD and the IFD were designed considering thermo-conductive metals (aluminum and copper) to allow the control of heat transference in a more homogeneous way. Thus, hydrogels were placed in a 24-well (comparable to the polystyrene one used in the standard method) aluminum plate, which was then held between two (top/bottom) copper plates. In the case of IFD, an extra insulating layer (lid/base) was added to the system. This means that, despite the use of the thermo-conductive materials, a higher thermal resistance was also added. As the temperature difference is the driving force for heat transfer, the larger the difference, the higher is the transfer rate and the faster is the freezing [33]. Thus, higher energy was required for heat transfer with the addition of thermal plates and insulation materials (standard < NFD < IFD). As a consequence, both cooling and freezing rate decreased (standard > NFD > IFD), thus also impacting the nucleation and end freezing time. The time for latent heat removal increased and, thus, the nucleation time increased (standard < NFD < IFD) and the nucleation temperature decreased. Consequently, the time for crystal growth (after end freezing time) decreased, which culminates in a reduced pore size after freeze-drying. Moreover, the thermal hold for materials prepared with the standard method was higher, since hydrogels reached the end freezing temperature faster. Higher thermal holds impact ice growth, as they create larger ice crystals at the expense of smaller ones [34,35]. Therefore, a broader pore size range and higher mean pore size were obtained when the time for ice growth was higher (standard method), and the narrowest pore size spectrum and the lower mean pore size (IFD) occurred when the time for ice growth was lower. With the decrease of the cooling and freezing rates due to the use of the freezing devices, a more controlled freezing was achieved, as reflected by the smaller coefficients of variation as well as statistical significances of the standard deviations. As expected, polymer concentration did not affect the assessed freezing parameters, but affected the properties of the scaffolds, particularly the pore size range and the compressive modulus. This is also in agreement with previous works that did not show significant differences in the cooling rate with the increase of polymer concentration but showed a reduced pore size due to a lower nucleation temperature [36]. These same variations observed in the mean pore size for the dried polymeric networks were also noticed on the wet structures, as the mean pore size decreased for the IFD in relation to the standard method. Moreover, when comparing the mean pore size of the dried polymeric networks and the spongy-like hydrogels, a slight increase was observed. This effect that resulted from the water uptake of the pore walls of the dried scaffolds was not statistically significant. Moreover, these differences in the pore size obtained from the different freezing methods did not affect the capacity

of hDFbs to survive, adhere, and colonize within these structures, as already shown by others [15]. The hDFbs adhered to the pore walls and organized their cytoskeleton, exhibiting their typical morphology along the time of culture.

When comparing different freezing temperatures within each device/method, lower temperatures were associated with larger intervals between the settled and the hydrogel temperatures. These differences were responsible for higher cooling and freezing rates, leading to a faster nucleation and to less time to stabilize and reach the final temperature. Cooling rates have been directly linked to the isotropy/anisotropy of scaffolds. Dried polymeric structures obtained with −20 and −80 °C freezing procedures depicted an open honeycomb-like structure, whereas a parallel laminar porous structure was obtained at −210 °C. Nonetheless, this was only observed for samples prepared by the standard method associated with the highest cooling rate. This is in concordance with other works that showed that rapid cooling rates at very low temperatures, such as liquid nitrogen, cause reduction of the pore size and orientation of the ice crystals [25,37]. With regard to the nucleation temperature, no differences were observed when directly comparing the same device/method at different freezing temperatures. These results are in line with others that also did not show differences in the nucleation temperature when collagen freezing was varied from −20 to −40 °C [26]. Interestingly, although nucleation temperature is often cited as a predictive measure of pore size [38], the results herein presented, as also shown by others [26], confirm that, in opposition to nucleation temperature, the pore size of the obtained scaffolds decreased for lower freezing temperature. This can be explained by the efficiency of latent heat removal (dependent on the freezing temperature) that determines the final pore size due to the decreased time of ice nucleation and growth [39].

Herein, we demonstrated the link between the thermal parameters and the properties of the dried polymeric networks/spongy-like hydrogels by showing that altering the freezing system and the freezing temperature changed the microstructure of the GG structures. This is particularly evident for the pore size, which is justified by the expected differences in the efficiency of latent heat removal from the hydrogel [26]. From the performed analysis we could confirm that by changing either the method (standard vs. IFD) or the freezing temperature (from −20 to −210 °C within the same method) spongy-like hydrogels with lower pore size can be obtained. While changing the method (standard vs. IFD) did not affect water uptake capability, when the freezing temperature is varied from −20 to −210 °C (within the same method), lower pore size is accompanied with lower water content. Interestingly those variations did not significantly affect the compressive modulus of the spongy-like hydrogels.

The mapping of the effect of the freezing device and temperatures will allow guiding the preparation of spongy-like hydrogels with a specific pore size knowing whether and how the water content is affected without compromising the compressive modulus. Overall, the freezing devices did not disturb the characteristic features of the spongy-like hydrogels but allowed obtaining highly reproducible materials and a powerful procedure to fine tune their microarchitecture according to specific needs.

III-5. REFERENCES

1   Hollister SJ. Porous scaffold design for tissue engineering. Nat. Mater. 4(7), 518–24 (2005).

2   Lien SM, Ko LY, Huang TJ. Effect of pore size on ECM secretion and cell growth in gelatin scaffold for articular cartilage tissue engineering. Acta Biomater. 5(2), 670–9 (2009).

3   da Silva LP, Santos TC, Rodrigues DB *et al*. Stem Cell-Containing Hyaluronic Acid-Based Spongy Hydrogels for Integrated Diabetic Wound Healing. J. Invest. Dermatol. 137(7), 1541–1551 (2017).

4   Mygind T, Stiehler M, Baatrup A *et al*. Mesenchymal stem cell ingrowth and differentiation on coralline hydroxyapatite scaffolds. Biomaterials 28(6), 1037–47 (2007).

5   Mandal BB, Kundu SC. Cell proliferation and migration in silk fibroin 3D scaffolds. Biomaterials 30(15), 2956–65 (2009).

6   Feng X, Xu P, Shen T, Zhang Y, Ye J, Gao C. Influence of pore architectures of silk fibroin/collagen composite scaffolds on the regeneration of osteochondral defects *in vivo*. J. Mater. Chem. B 8, 391–405 (2020).

7   Kuboki Y, Jin Q, Takita H. Geometry of carriers controlling phenotypic expression in BMP-induced osteogenesis and chondrogenesis. J. Bone Joint Surg. Am. 83-A Suppl(Pt 2), S105-15 (2001).

8   Tsuruga E, Takita H, Itoh H, Wakisaka Y, Kuboki Y. Pore size of porous hydroxyapatite as the cell-substratum controls BMP-induced osteogenesis. J. Biochem. 121(2), 317–24 (1997).

9   Mantila Roosa SM, Kemppainen JM, Moffitt EN, Krebsbach PH, Hollister SJ. The pore size of polycaprolactone scaffolds has limited influence on bone regeneration in an *in vivo* model. J. Biomed. Mater. Res. - Part A 92(1), 359–68 (2010).

10   Wang Y, Xu R, Luo G *et al*. Biomimetic fibroblast-loaded artificial dermis with 'sandwich' structure

and designed gradient pore sizes promotes wound healing by favoring granulation tissue formation and wound re-epithelialization. Acta Biomater. 30, 246–257 (2016).

11   Fontanilla MR, Casadiegos S, Bustos RH, Patarroyo MA. Comparison of healing of full-thickness skin wounds grafted with multidirectional or unidirectional autologous artificial dermis: differential delivery of healing biomarkers. Drug Deliv. Transl. Res. 8(5), 1014–1024 (2018).

12   Madden LR, Mortisen DJ, Sussman EM *et al*. Proangiogenic scaffolds as functional templates for cardiac tissue engineering. Proc. Natl. Acad. Sci. U. S. A. 107(34), 1511–6 (2010).

13   Oliviero O, Ventre M, Netti PA. Functional porous hydrogels to study angiogenesis under the effect of controlled release of vascular endothelial growth factor. Acta Biomater. 8(9), 3294–301 (2012).

14   Khademhosseini A, Langer R. Microengineered hydrogels for tissue engineering. Biomaterials 28(34), 5087–92 (2007).

15   Yannas I V. Tissue regeneration by use of collagen-glycosaminoglycan copolymers. Clin. Mater. 9(3–4), 179–87 (1992).

16   da Silva LP, Cerqueira MT, Sousa R a., Reis RL, Correlo VM, Marques AP. Engineering cell-adhesive gellan gum spongy-like hydrogels for regenerative medicine purposes. Acta Biomater. 10, 4787–4797 (2014).

17   Cerqueira MT, da Silva LP, Correlo VM, Reis RL, Marques AP. Epidermis recreation in spongy-like hydrogels. Mater. Today 18, 468–9 (2015).

18   Gantar A, Da Silva LP, Oliveira JM *et al*. Nanoparticulate bioactive-glass-reinforced gellan-gum hydrogels for bone-tissue engineering. Mater. Sci. Eng. C 43, 27–36 (2014).

19   Berti F V., Srisuk P, Da Silva LP, Marques AP, Reis RL, Correlo VM. Synthesis and characterization of electroactive Gellan gum spongy-like hydrogels for skeletal muscle tissue engineering applications. Tissue Eng. - Part A 23(17–18), 968–979 (2017).

20   Srisuk P, Berti F V., Da Silva LP, Marques AP, Reis RL, Correlo VM. Electroactive Gellan Gum/Polyaniline Spongy-Like Hydrogels. ACS Biomater. Sci. Eng. 4(5), 1779–1787 (2018).

21   Cerqueira MT, Da Silva LP, Santos TC *et al*. Human skin cell fractions fail to self-organize within a gellan gum/hyaluronic acid matrix but positively influence early wound healing. Tissue Eng. - Part A 20(9–10), 1369–78 (2014).

22   Da Silva LP, Oliveira S, Pirraco RP *et al*. Eumelanin-releasing spongy-like hydrogels for skin re-

epithelialization purposes. Biomed. Mater. 12(2), 025010 (2017).

23   da Silva LP, Pirraco RP, Santos TC *et al*. Neovascularization Induced by the Hyaluronic Acid-Based Spongy-Like Hydrogels Degradation Products. ACS Appl. Mater. Interfaces 8(49), 33464–33474 (2016).

24   Cerqueira MT, Da Silva LP, Santos TC *et al*. Gellan gum-hyaluronic acid spongy-like hydrogels and cells from adipose tissue synergize promoting neoskin vascularization. ACS Appl. Mater. Interfaces 6(22), 19668–79 (2014).

25   Madihally S V., Matthew HWT. Porous chitosan scaffolds for tissue engineering. Biomaterials 20(November 1998), 1133–1142 (1999).

26   Pawelec KM, Husmann A, Best SM, Cameron RE. A design protocol for tailoring ice-templated scaffold structure. J. R. Soc. Interface 11(92), 20120958 (2014).

27   O'Brien FJ, Harley B a., Yannas I V., Gibson L. Influence of freezing rate on pore structure in freeze-dried collagen-GAG scaffolds. Biomaterials 25(6), 1077–1086 (2004).

28   Grenier J, Duval H, Barou F, Lv P, David B, Letourneur D. Mechanisms of pore formation in hydrogel scaffolds textured by freeze-drying. Acta Biomater. 94, 195–203 (2019).

29   Haugh MG, Murphy CM, O'Brien FJ. Novel Freeze-Drying Methods to Produce a Range of Collagen–Glycosaminoglycan Scaffolds with Tailored Mean Pore Sizes. Tissue Eng. Part C Methods 16(5), 887–94 (2010).

30   Murphy CM, Haugh MG, O'Brien FJ. The effect of mean pore size on cell attachment, proliferation and migration in collagen-glycosaminoglycan scaffolds for bone tissue engineering. Biomaterials 31(3), 461–6 (2010).

31   Zachariassen KE, Kristiansen E. Ice nucleation and antinucleation in nature. Cryobiology 41(4), 257–279 (2000).

32   da Silva LP, Cerqueira MT, de Sousa RPRA, Marques AMP, da Silva VMC, dos Reis RLG. WO2014167513 (A1) (2014).

33   Cengel YA, Boles MA. Energy, energy transfer, and general energy analysis. In: Thermodynamics: an Engineering Approach (Chap. 2, 8th Editio Edition). McGraw-Hill Education, 51–109 (2015).

34   Deville S, Adrien J, Maire E, Scheel M, Di Michiel M. Time-lapse, three-dimensional *in situ* imaging of ice crystal growth in a colloidal silica suspension. Acta Mater. 61(6), 2077–2086 (2013).

35   Myerson AS, Ginde R. Crystals, crystal growth, and nucleation. In: Handbook of Industrial Crystallization. 33–65 (2002).

36   Pawelec KM, Husmann A, Best SM, Cameron RE. Understanding anisotropy and architecture in ice-templated biopolymer scaffolds. Mater. Sci. Eng. C 37, 141–7 (2014).

37   Deville S, Saiz E, Tomsia AP. Freeze casting of hydroxyapatite scaffolds for bone tissue engineering. Biomaterials 27(32), 5480–5489 (2006).

38   Arsiccio A, Sparavigna AC, Pisano R, Barresi AA. Measuring and predicting pore size distribution of freeze-dried solutions. Dry. Technol. 37, 435–447 (2019).

39   Searles JA, Carpenter JF, Randolph TW. The ice nucleation temperature determines the primary drying rate of lyophilization for samples frozen on a temperature-controlled shelf. J. Pharm. Sci. 90(7), 860–71 (2001).

III-6.   SUPPLEMENTARY INFORMATION
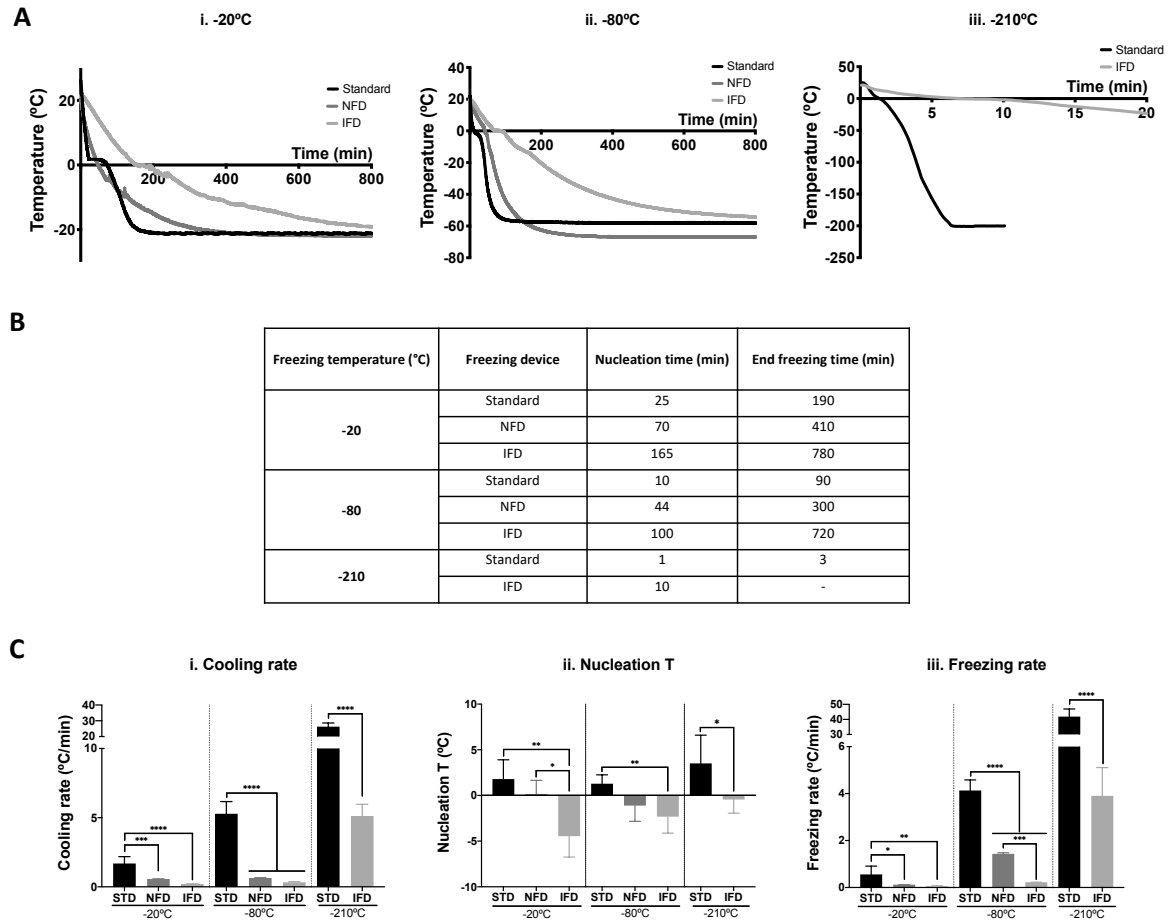
Supplementary Figure III-1 Freezing profiles of 0.75% GG hydrogels.
A Mean temperature profiles of GG hydrogels during freezing at (i) -20°C, (ii) -80°C and (iii) -210°C with the 3 different freezing molds. **B** Characteristic values of the freezing of GG hydrogels. **C** Effect of both temperature and freezing mold on the (i) Cooling rate, (ii) Nucleation T and (iii) Freezing rate of GG hydrogels. Data was obtained from 7 different measurements, * p < 0.05, ** p < 0.01, *** p < 0.001, **** p < 0.0001, One-way ANOVA with Bonferroni multiple comparison post-test.

117
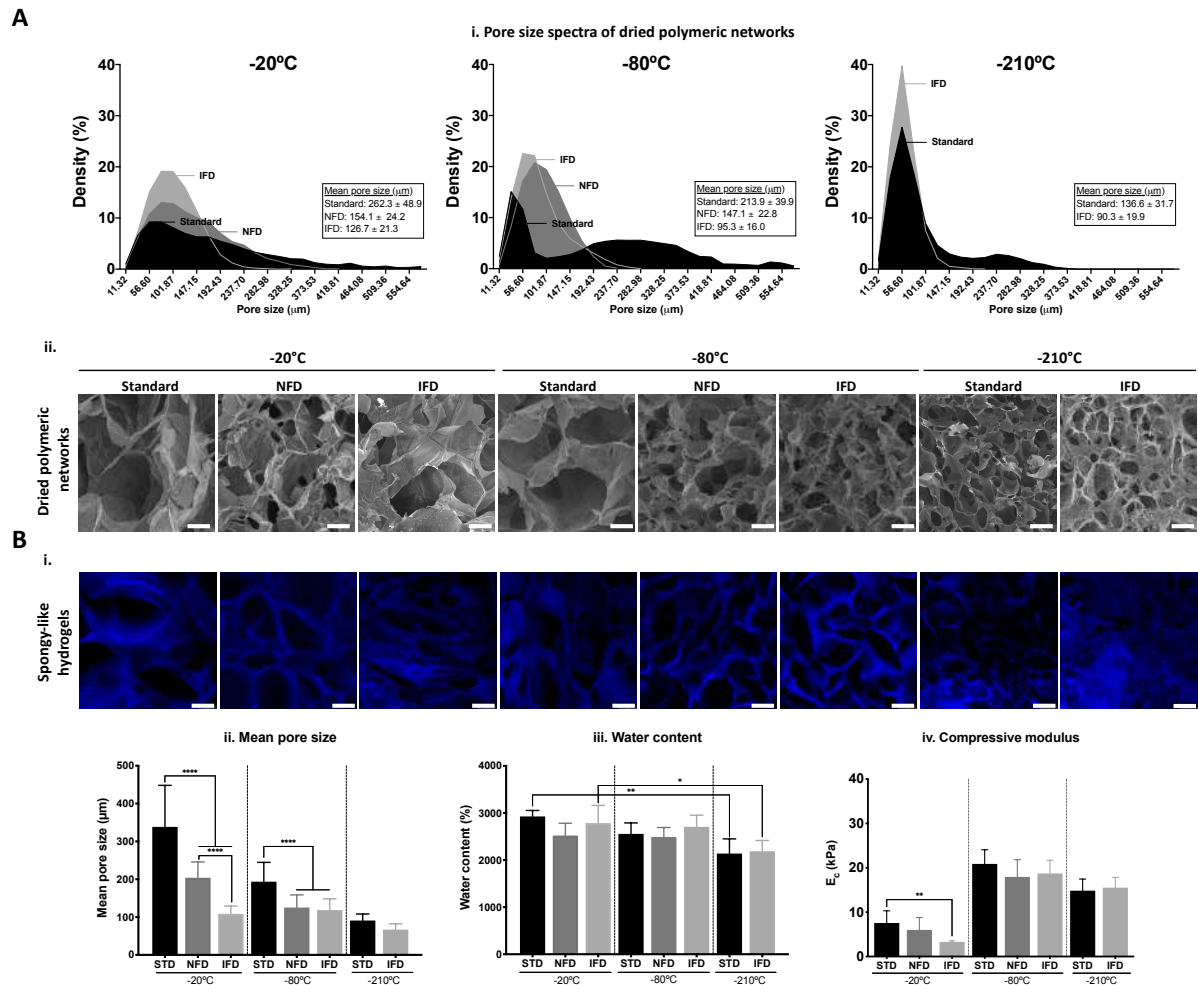
Supplementary Figure III-2 Effect of freezing conditions (standard method, NFD and IFD at -20°C, -80°C and -210°C) over the properties of 0.75% GG dried polymeric structures and spongy-like hydrogels.
A (i) pore size spectra and mean pore size obtained from μ-CT and (ii) representative scanning electron microscopy micrographs of dried polymeric structures. **B** (i) Representative confocal images of the microarchitecture of spongy-like hydrogels after staining with DAPI (blue). Representation of the variations of the (i) mean pore size analyzed from images obtained by confocal microscopy, (ii) water content and (iii) compressive modulus of spongy-like hydrogels prepared under different freezing conditions. * $p < 0.05$, ** $p < 0.01$, *** $p < 0.001$, **** $p < 0.0001$, One-way ANOVA with Bonferroni multiple comparison post-test. Scale bar = 75 μm.

Supplementary Figure III-3 Water uptake of 1.25% GG dried polymeric structures prepared at -20°C, -80°C and -210°C and using different freezing systems.

Supplementary Figure III-4 Scaffolds reproducibility.
A Representation of the coefficient of variation of the pore size of 0.75% GG (i) dried polymeric networks and (ii) spongy-like hydrogels, and of the (iii) compressive modulus of spongy-like hydrogels according to the tested freezing conditions, standard method, NFD and IFD at -20°C, -80°C and -210°C. **B** p values obtained from the Brown-Forsythe test showing the statistical significance of the standard deviations for the pore size and compressive modulus among the different freezing devices (standard method, NFD and IFD).
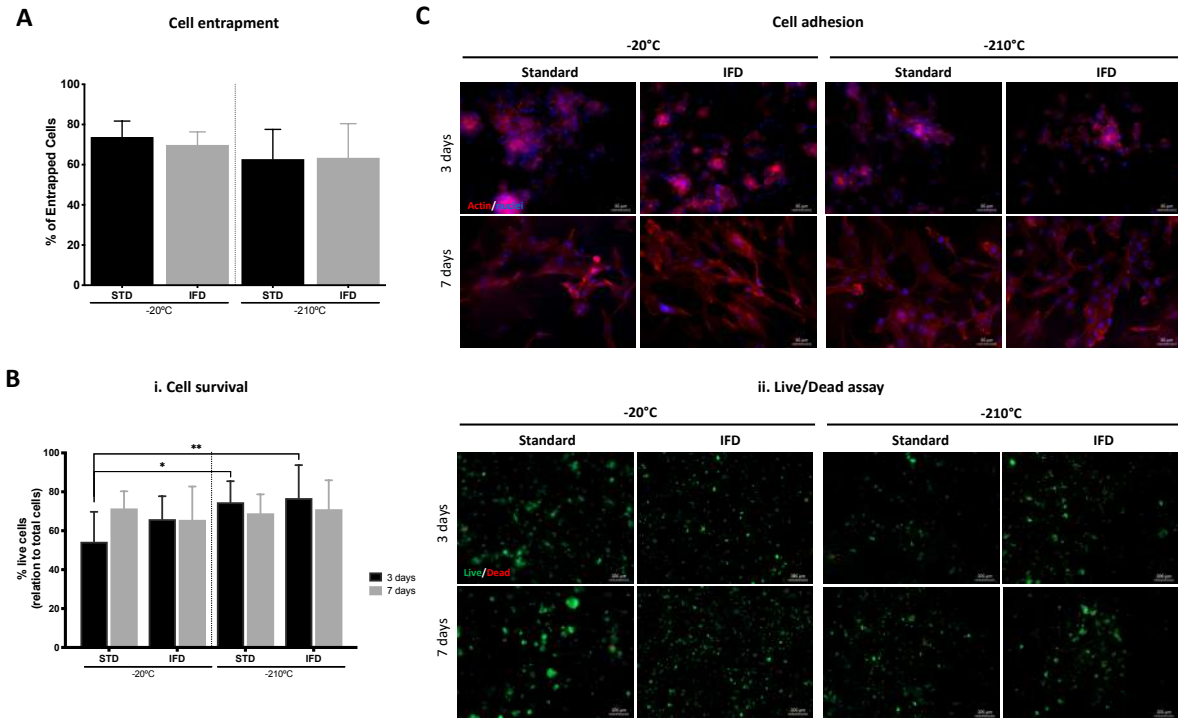
Supplementary Figure III-5 Effect of freezing conditions (standard method, NFD and IFD at -20°C and -210°C) over hDFbs behaviour in 0.75% GG spongy-like hydrogels.
A Representation of the entrapment efficiency 24 hours after cell seeding. **B** (i) Representation of the percentage of the live cells 3 and 7 days of culture. (ii) Representative fluorescence microscopy images showing the dead (red) and the live (green) cells, respectively stained with PI and Ca-AM after 3 and 7 days of culture. Scale bar = 200 μm. **C** Representative fluorescence microscopy images of hDFBs after 3 and 7 days of culture showing the F-actin cytoskeleton (phalloidin-TRITC, red) and nuclei (DAPI, blue). Scale bar = 50 μm. Data was obtained from three independent experiments with three replicates for each condition, * p < 0.05, two-way ANOVA and Bonferroni's post-hoc test.

CHAPTER IV

PRE-SELECTION OF FIBROBLASTS SUBSETS PROMPT PREVASCULARIZATION OF TISSUE ENGINEERED SKIN ANALOGUES

CHAPTER IV

PRE-SELECTION OF FIBROBLASTS SUBSETS PROMPT PREVASCULARIZATION OF TISSUE ENGINEERED SKIN ANALOGUES ‡

ABSTRACT

The papillary and reticular dermis harbor phenotypically distinct fibroblasts, which functions such as maintenance of skin's microvasculature are also distinct. Thus, we hypothesized that pre-selection of the subpopulations of fibroblasts would benefit the generation of skin tissue engineered (TE) constructs, promoting its prevascularization *in vitro*. We first isolated papillary and reticular fibroblasts using fluorescence-activated cell sorting and studied the effect of their secretome and extracellular matrix (ECM) on human dermal microvascular endothelial cell (hDMECs) organization. Subsequently, we developed a bilayered 3D polymeric structure with distinct layer-associated features to house the subpopulations of fibroblasts, to generate a skin analogue. Both papillary and reticular fibroblasts were able to stimulate capillary-like network formation in a Matrigel assay. However, the secretome of the two subpopulations was substantially different being enriched in VEGF, IGF-1 and Angio-1 in the case of papillary fibroblasts, and in HGF and FGF-2 for the reticular subset. In addition, the fibroblast subpopulations deposited varied levels of ECM proteins, more collagen I by the papillary and more laminin by the reticular, differently impacting hDMECs organization. Vessel-like structures with lumen were observed earlier in the 3D skin analogue prepared with the sorted fibroblasts, although ECM deposition was not affected by the cell's pre-selection. Moreover, a more differentiated epidermal layer was attained in the skin analogue formed by the sorted fibroblasts, confirming that its whole structure was not affected. Overall, we provide evidence that pre-selection of papillary and reticular fibroblasts is relevant for promoting the *in vitro* prevascularization of skin TE constructs.

---

‡ This chapter is based on the following publication:

IV-1. INTRODUCTION

Skin dermis plays a detrimental role in establishing microenvironments that regulate tissue's physiology. This connective tissue is divided into the upper papillary and the lower reticular layers, which differ both structurally and functionally [1]. The papillary dermis is a loose matrix containing fibroblasts at a high density, and microvascular and sensory components [2]. While the microvascular component provides nutrients to the epidermis [3], and contributes to the skin immune surveillance [4] and to regulate the temperature of the skin and thus the body as a whole [5], the sensory components allow nociception and perceiving temperature and touch [6]. In turn, the reticular dermis comprises a lower number of cells in a denser matrix involving the skin appendages (sebaceous and sweat glands and hair follicles), in addition to other sensory components [2]. This matrix besides providing strength and elasticity to the skin, allows detecting hair movement, skin deflection, pressure, and vibration through the neural receptors [6]. While much is still to be understood, those differences have been also linked to the distinct functional identities of fibroblasts found in the papillary and reticular dermis [7].

The distinct identities of dermal papillary and reticular fibroblasts have long been alleged [8], however it was only some years ago that they were confirmed in mouse skin [7]. Along development, fibroblasts in the mouse dermis switch from a homogenous population - Dlk1$^+$Pdgfr-α^+Lrig1$^+$ at embryonic day (E) 12.5 - to two subpopulations at E16.5 - Dlk1$^+$Pdgfr-α^+ cells in the reticular and Lrig1$^+$CD26$^+$Pdgfr-α^+Dlk1$^-$ cells in the papillary dermis. From E16.5, the developing dermis undergoes fate restrictions such that cells in the upper dermis cells that express Lrig1 give rise to papillary fibroblasts, whereas Dlk1$^+$ cells in the lower dermis give rise to the reticular ones [7]. Because many of the cell surface markers identified in the developing mouse dermis were not conserved in humans [9], distinguishing human fibroblasts subpopulations is still uncertain. Data generated from isolated superficial and lower dermal layers is also ambiguous since fibroblast identity is not spatially restricted within the dermis, but instead defines an opposing gradient of papillary and reticular fibroblasts from the skin surface to the deep dermis [9,10]. It was only recently that two major human dermal fibroblast subpopulations were identified using a combination of spatial and single-cell transcriptional profiling [9]. This work identified the lin$^-$CD90$^+$CD36$^+$ population, which expresses high levels of ACTA2, MGP, PPARγ, and transglutaminase-2 (TGM2) in the lower dermis, and the lin$^-$CD90$^+$CD39$^+$CD26$^-$ subset, which is characterized by the expression of specific collagen chains such as COL6A5, in the upper dermis. Notwithstanding, there is still no agreement regarding the specific signature of papillary fibroblasts, as they have also been identified as lin$^-$CD90$^-$FAP$^+$ cells expressing high levels of CD26 [10], podoplanin (PDPN) and netrin-1 [10,11].

Despite the uncertainty regarding the markers that characterize fibroblast's subpopulations, *in vitro* studies have confirmed that papillary and reticular fibroblasts, isolated from dermatomed skin tissue at different depths, have distinct features. Papillary fibroblasts showed higher *in vitro* proliferation rates and longer replicative lifespans than their reticular counterparts [8,12]. Additionally, these are more sensitive to the culture density, slowing their exponential growth if at lower densities [8,12–14]. Several other studies have also suggested that fibroblast's matrissome and secretome appears to be dictated by their location within the skin dermis and to specific communications with neighboring cells. Distinctively, the expression of collagen type VII (COLVII) is upregulated in papillary fibroblasts when compared to the reticular subset [15,16], which is consistent with the role of papillary fibroblasts in promoting dermo-epidermal junction [17]. Moreover, type IV collagen was evenly expressed in the presence of papillary fibroblasts forming an uninterrupted layer resembling the basement membrane in which laminin 5 and fibronectin were also found [18]. Interestingly, papillary fibroblasts released less amounts of keratinocyte growth factor (KGF) than the reticular ones [14,18] but the exact implications of this in the communication with keratinocytes was not established. Skin dermis architecture also seems to determine the interactions between fibroblasts and other cell types such as vascular ones. Indeed, papillary fibroblast supported the formation of vessel-like structures by macrovascular endothelial cells which has been not only related to secreted factors such as vascular endothelial growth factor (VEGF) or hepatocyte growth factor (HGF) [19,20] but, importantly, to the deposited extracellular matrix (ECM) [21]. Components such as collagen type I and III have been suggested to be deposited in higher amounts by papillary fibroblasts [22] while others have alluded to the presence of proteins other than collagen I and elastin in the surrounds of the capillary loops in the papillary dermis [23]. Additionally, MMP-1 is highly secreted by papillary fibroblasts [21] which, although still to be proven, can be related to the endothelial cells sprouting through the degraded ECM during angiogenesis.

Taken together, all these works suggest that fibroblasts subpopulations generate and modulate their own and neighboring microenvironments, which might be critical in the construction of skin tissue-engineered (TE) constructs that better reflect the native tissue. To the best of our knowledge, so far only one approach has considered the use of both subpopulations combining layered cell-laden collagen gels [24]. Yet, the generation of a dermal-epidermal skin equivalent did not follow, and the communication between fibroblasts subpopulations and neighboring cells in this context has not been addressed. Thus, herein, we hypothesized that pre-selection of the two subpopulations of fibroblasts would promote *in vitro* prevascularization of skin TE constructs. We took advantage of papillary and reticular fibroblasts isolated using fluorescent-activated cell sorting (FACS) based on recently revealed markers [9], and studied their

124

effect on endothelial cell organization, considering both secretome and ECM production. We then developed a bilayered 3D polymeric structure with distinct layer-associated features capable of housing the sub-populations of fibroblasts, generating an *in vitro* vascularized skin bilayered 3D structure.

IV-2. MATERIALS AND METHODS

IV-2.1. Human keratinocytes and endothelial cells isolation and culture

Cells were isolated from human skin specimens of healthy donors (IMC 20.8 – 26.8) undergoing abdominoplasties after informed consent and under the protocol established and approved by the Ethical Committee of Hospital S. João (Porto, Portugal) (Nr 477/2020) and the *Comissão de Ética para a Investigação em Ciências da Vida e da Saúde* (Braga, Portugal) (Nr 135/2020). Skin pieces were cut into small fragments and incubated with 2.4 U mL^{-1} of dispase (BD Biosciences, USA) overnight at 4 °C. The epidermis was peeled off and digested at 37 °C for 8 min using 0.05 % (w/v) trypsin/ethylenediaminetetraacetic acid (EDTA, Invitrogen, UK). Digestion was stopped with fetal bovine serum (FBS, Invitrogen, USA) and epidermal cells were scraped from the remaining matrix. The cell suspension was filtered through a sterile 100 μm cell strainer, centrifuged (300 g, 5 min), and re-suspended and cultured in Keratinocyte serum-free media (Life Technology, Scotland) supplemented with human recombinant epidermal growth factor (5 ng mL^{-1}, Gibco, USA), bovine pituitary extract (50 μg mL^{-1}, Gibco, USA), 1 % (v/v) penicillin-streptomycin solution (PenStrep, Lonza, Switzerland) and the ROCK pathway inhibitor Y-27632 (10 μM, STEMCELL Technologies, Canada). Cultures were maintained at 37 °C in a humidified tissue culture incubator with 5 % CO_2 atmosphere. hKCs were routinely passaged with TryplE™ Express (Life Technologies, UK) and re-suspended at a density of $1x10^5$ cells/cm^2.

Human dermal microvascular endothelial cells (hDMECs) were obtained from the dispase solution and cultured in gelatin (0.7 % (w/v), Sigma, USA) coated flasks with EGM-2 MV (Lonza, USA). Cells were passaged at 70-90 % confluence and used at passage (P) 3–4.

IV-2.2. Papillary and reticular fibroblast sorting and flow cytometry analysis

After removal of the epidermis, the dermis was digested overnight at 37 °C using the whole skin dissociation kit (Miltenyi Biotec, USA) as *per* the manufacturer's instructions. A suspension of freshly isolated human dermal fibroblasts with $7x10^6$ cells/mL was incubated with the surface markers antibodies

125

(Supplementary Table 1) for 30 min at room temperature (RT). After washing in PBS, cells were resuspended and then cultured in Minimal Essential Medium (α-MEM, Invitrogen, USA) supplemented with 10 % (v/v) FBS and 1 % (v/v) PenStrep. The selection of the lin$^-$ (i.e. CD324$^-$CD45$^-$CD31$^-$)CD39$^+$CD26$^-$ population corresponding to the papillary subpopulation, and the lin$^-$CD36$^+$ population corresponding to the reticular subpopulation, was performed using a FACSAriaIII Cell Sorter and FACSDiva software (BD Biosciences, USA).

Fibroblasts subpopulations at P1 and P2, were also analyzed with the same apparatus after being labelled at RT for 20 min with fluorochrome-labeled antibodies (Supplemental Table 2) at manufacturer recommended concentrations.

IV-2.3.   Cell proliferation analysis

Fibroblasts subpopulations cells in P1 and P2 were seeded at 2×10^3 cells/cm^2 and cultured up to 7 days. Cell proliferation was determined using PicoGreen dsDNA assay kit (Invitrogen, USA) following the manufacturer's instructions.

IV-2.4.   Matrigel assay

Matrigel (Corning, USA) was added to 96 well plates that were then kept in a humidified incubator for 30 min. hDMECs were seeded on the top of the formed gel at a density of 1.3×10^4 cells/well and incubated for 24 h in a humidified incubator at 37 °C, 5 % of CO$_2$ in the presence of filtered fibroblasts conditioned media obtained from 3 days cultures of cells seeded at 2×10^4 cells/cm^2 plus a starvation period of 24 h in α-MEM without FBS. hDMECs cultured in α-MEM medium and in EGM-2 MV-containing VEGF were included respectively as negative and positive controls of the assay. The organization of cells into capillary-like structures was assessed after 8 h and 24 h. Micrographs were taken using an Axio Observer inverted Microscope with the ZEN Blue 2012 software (Zeiss, Germany). Formation and organization of the capillary-like structures was quantitatively analyzed using an angiogenesis plug-in for ImageJ2 (v2.3.0/1.53m).

IV-2.5.   Growth factors quantification

The levels of VEGF, basic fibroblast growth factor (FGF-2, R&D Systems, UK), HGF (Millipore, USA), insulin growth factor-1 (IGF-1, Elabscience, USA) and angiopoietin-1 (Angio-1, Booster Biological

Technology, USA) in the fibroblasts conditioned media were quantified by ELISA. Assays were carried out according to the manufacturer's instructions and the absorbance of each sample was read at 450 nm using a Varioskan Flash multimode plate reader. DNA values were used to normalize results.

IV-2.6.   Collagen and non-collagenous proteins quantification

Sorted fibroblasts were seeded at a density of $5x10^4$ cells/cm^2 to maximize ECM deposition. After 3 days, cells were fixed with 10 % (v/v) formalin for 24 h at RT. The production of collagen (COL) and non-collagenous (NCOL) proteins was determined using the Sirius Red/Fast Green Collagen Staining Kit (Chondrex Inc., USA) following the manufacturer's instructions. Absorbances were measured at 540 nm (sirius red) and 605 nm (fast green) using the Varioskan Flash multimode plate reader. The color equivalences were used to calculate the quantity of COL and NCOL proteins.

IV-2.7.   Fibroblast and hDMECs co-cultures

Sorted fibroblasts were seeded at sub-confluency ($5x10^4$ cells/cm^2) and inactivated with mitomycin C (100 μg mL^{-1}, Sigma, USA) for 4 h at RT after 3 days of culture. hDMECs were seeded on the top at a density of $2.5x10^4$ cells/cm^2 and co-cultures were kept for 7 days in EGM-MV VEGF medium.

IV-2.8.   Immunocytochemistry

Cells were fixed with 10 % (v/v) formalin for 24 h at RT, permeabilized with 0.2 % (v/v) Triton X-100 (Sigma-Aldrich, USA) for 30 min at RT and unspecific staining was blocked with 3 % (w/v) bovine serum albumin (BSA, Sigma-Aldrich, USA) for 1 h. Afterwards, cells were incubated overnight at 4 °C with anti-human primary antibodies (Supplementary Table 2) diluted in 1 % (w/v) BSA solution in PBS. After washing with PBS, samples were incubated for 1 h at RT with the secondary antibodies (Supplementary Table 2) prepared in 1 % (w/v) BSA solution in PBS. Nuclei were counter-stained with 4',6-diamidino-2-phenylindole (DAPI, Biotium, USA). Cells were observed using an Axio Observer inverted Microscope with the ZEN Blue 2012 software.

127

IV-2.9. Cytoskeleton Staining

For visualization of the cytoskeleton F-actin fibers and nuclei, cells were fixed with 10 % (v/v) formalin for 1 h at RT, and stained with phalloidin-TRITC (Sigma, USA) and DAPI for 1 h at RT. Cells were observed using an Axio Observer inverted Microscope with the ZEN Blue 2012 software.

IV-2.10. Bilayered gellan gum-based spongy-like hydrogels fabrication

Gellan gum (0.25% (w/v), GG, Sigma, USA) was chemically modified with vinyl moieties (DVS) as previously described [25]. GG/GGDVS-RGD spongy-like hydrogels were prepared similarly to GG spongy-like hydrogels [26,27] but with modifications using a two-step approach. Briefly, a solution of 0.5 % (w/v) GGDVS was reacted with thiol-cyclo-RGD (RGD, Cyclo(-RGDfC), >95 % purity, GeneCust Europe) for 1 h at RT. Meanwhile, a 1 % (w/v) GG solution was prepared by dissolving the gelzan powder at 90 °C for 30 min. The GG solution was allowed let to reach 40 °C before mixing with the GGDVS-RGD and casting into the desired mold. The hydrogel was progressively formed until room temperature was reached. Afterwards, hydrogels were frozen at -80 °C overnight and then freeze-dried (Telstar, Spain) for 24 h to obtain the reticular-like layer. The second layer was then added by pipetting the GG/GGDVS-RGD solution (75 % of the volume used for the first layer) on the top of the reticular-like layer. After stabilization, constructs were frozen at -80 °C overnight and then freeze-dried (Telstar, Spain) for 24 h to obtain the bilayer structures. Cylindrical scaffold samples of 5 mm diameter were cut using a metal punch for further analysis. Bilayered spongy-like hydrogels were formed after rehydration of the dried polymeric networks.

IV-2.11. Scanning electron microscopy

Scanning electron microscopy (SEM) was used to analyze the microstructure of the dried polymeric networks. Prior to analysis, samples were sputter coated with a mixture of gold–palladium. A JSM-6010LV (JEOL, Japan) microscope, operating with an accelerating voltage of 15 kV was used to capture images.

IV-2.12. Micro-Computed Tomography (μ-CT)

The spongy-like hydrogels' microarchitecture was analyzed using a high-resolution X-ray microtomography system SkyScan 1072 scanner (SkyScan, Belgium). Samples were scanned in high-resolution mode using a pixel size of 11.31 μm (magnification of 23.30×) and an integration time of 1.7

s. The x-ray source was set at 35 keV of energy and 215 μA of current. Representative datasets of 150 slices were transformed into a binary picture using a dynamic threshold of 45e225 (gray values) to distinguish polymer material from pore voids. Pore size was obtained using the CT Analyzer (v1.5.1.5, SkyScan).

IV-2.13. Compressive tests

The spongy-like hydrogels (hydrated in PBS for 24 h, at RT) were tested under static compression using an Instron 5543 (Instron, Norwood, MA, USA). Samples (13.4 mm diameter and 3 mm height) were submitted to a pre-load of 0.1 N and tested up to 60 % of strain, at a loading rate of 2 mm m^{-1}. The compressive modulus was determined from the most linear part of the stress/strain curves using the secant method.

IV-2.14. Water uptake quantification

Dried polymeric networks were immersed in α-MEM up to 72 h at 37 °C, to determine the water uptake profile. Samples were weighed prior immersion (Wd) and after each time point (Ww) to calculate the percentage of water uptake along time (**Equation VI-1**).

$$Water\ uptake\ (\%) = \frac{(W_w - W_d)}{W_d} \times 100$$

Equation IV-1 Water uptake

IV-2.15. Cell-laden bilayer spongy-like hydrogels

A suspension containing 0.5x10^{6} reticular fibroblasts was added onto the reticular-like layer of the bilayered GG spongy-like hydrogel. Structures were transferred into polycarbonate transwells with the reticular part facing down and kept in culture for 7 days in α-MEM, supplemented with 10 % (v/v) FBS and 1 % (v/v) antibiotic/antimycotic. Afterwards, a 2.5 x10^{6} cell suspension containing 1:4 papillary fibroblasts:hDMECs was added on the top papillary-like layer. Constructs were cultured for further 7 days in EGM-2 MV-VEGF. hKCs (5 x10^{5}) were then seeded on the surface of the papillary-like layer and cultured for 3 days in KSFM. This medium was then replaced by FAD complete medium (110 mL DMEM (Sigma-Aldrich, USA), 110 mL DMEM:Ham's F12 medium (Sigma-Aldrich, USA) and supplemented with 1.8x10^{-4} M adenine (Sigma-Aldrich, USA), 10 % (v/v) non-inactivated FBS, 0.5 μg μL^{-1} hydrocortisone (Sigma-

Aldrich, USA), 5 μg mL⁻¹ insulin (Sigma-Aldrich, USA), 10^{-10} M cholera toxin (Sigma-Aldrich, USA), 10 ng mL⁻¹ epidermal growth factor (EGF, Peprotech, UK), 1.8 mM calcium chloride (Merck, Germany) and 1 % (v/v) PenStrep), and constructs were cultured for additional 14 days.

To evaluate the retention of the fibroblasts' subpopulations in the bilayered construct, reticular fibroblasts were labelled with Cell Tracker™ Orange CMRA (Invitrogen, USA) and papillary fibroblasts with Cell Tracker™ Green CMFDA before seeding, following the manufacturer's instruction.

IV-2.16. Histological analysis

Constructs were fixed in 10 % (v/v) formalin, dehydrated, embedded in paraffin (Thermo Scientific, USA) and cut into 4.5 μm sections. Sections were stained with hematoxylin and eosin (Sigma, USA) and masson's trichrome kit (Bio-Optica, Italy) following routine protocols. For immunohistochemistry, sections were deparaffinized in xylene, re-hydrated and boiled for 5 min in Tris-EDTA buffer (10 mM Tris Base, 1 mM EDTA solution and, 0.05 % (v/v) Tween 20, pH 9) for antigen retrieval. Cells were then permeabilized with 0.2 % (v/v) Triton X-100 and non-specific staining was blocked with 2.5 % (v/v) Horse Serum (Vector Labs, USA). Primary antibodies (Supplementary Table 3) were incubated overnight at 4 °C. After washing with PBS, samples were incubated 1 h at RT with the secondary antibody (Supplementary Table 3) in 1 % (w/v) BSA solution in PBS. Nuclei were counter-stained with DAPI. Samples were observed using an Axio Observer inverted Microscope with the ZEN Blue 2012 software.

IV-2.17. Image analysis

Five images of random fields were acquired for each condition and independent experiment and used to calculate the cell area with the Cell Profiler software (v 4.2.1) and to count the vessel-like structures using ImageJ software. The vessel-like structures were considered hollow continuous CD31⁺ cell arrangements. Number of vessel-like structures is presented as an average of the counted fields and expressed as number of vessels mm⁻².

IV-2.18. Statistical analysis

GraphPad Prism software (v 8.2.1, La Jolla, USA) was used to perform the statistical analysis. Data was analyzed using the Shapiro-Wilk normality test. A one-way or two-way analysis of variance (ANOVA) with a Tukey multiple comparison post-test was used to analyze the results with a normal distribution.

Otherwise, data were analyzed with the two-tailed unpaired Mann-Whitney test or Kruskal–Wallis test with Dunn's multiple comparison post-test. Significance was set to * $p < 0.05$.

IV-3.   RESULTS

IV-3.1.   Fibroblasts subpopulations phenotype

The uncovering of human dermal fibroblasts subpopulations has confirmed the existence of two subsets particularly localized in the upper or lower dermis [9]. Based on these findings, we assumed these cells respectively as papillary and reticular fibroblasts and flow sorted them from the digested dermis after enzymatic removal of the epidermis (**Figure VI-1a i**). We first started to select the cells negative for epidermal- (CD324), hematopoietic- (CD45) and endothelial-associated (CD31) markers – the lineage negative (lin$^-$)(i.e. CD324$^-$CD45$^-$CD31$^-$) dermal cells, and then the positive cells for CD90 within that group (**Figure VI-1a ii**). This selected sub-set of cells corresponded to 12.0 ± 6.4 % (n = 6) of the initial population (**Figure VI-1a iii**). From this, the two distinct human fibroblasts subpopulations were sorted, the lin$^-$CD90$^+$CD39$^+$CD26$^-$ subpopulation corresponding to the papillary subset, and the lin$^-$CD90$^+$CD36$^+$, the reticular subset (**Figure VI-1a ii**). Analysis of both subpopulations showed that while papillary fibroblasts corresponded to 4.0 ± 2.1 % of the initial population (about 35 % of the lin$^-$CD90$^+$ population), 1.0 ± 0.6 % (about 13 % of the lin$^-$CD90$^+$ population) were reticular fibroblasts (**Figure VI-1a iii**, Supplementary Figure VI-1). When put in culture (passage 0), papillary fibroblasts displayed a more spindle-shape morphology while a more epithelioid shape with a significantly lower surface area ($p < 0.05$) was observed for the reticular fraction (**Figure VI-1b i**). This apparently different phenotype was further confirmed by the high expression of podoplanin (PDPN) and fibroblast activation protein (FAP) in the papillary subpopulation, and of transglutaminase-2 (TGM2) in the reticular one (**Figure VI-1bii**, Supplementary Figure VI-2a). Unsorted fibroblasts expressed all the analysed markers as expected (Supplementary Figure VI-2b). Considering that *in vitro* culture conditions can lead to loss of phenotype, we then assessed the expression of CD39, CD36 and CD26 as these are the differentiating markers in
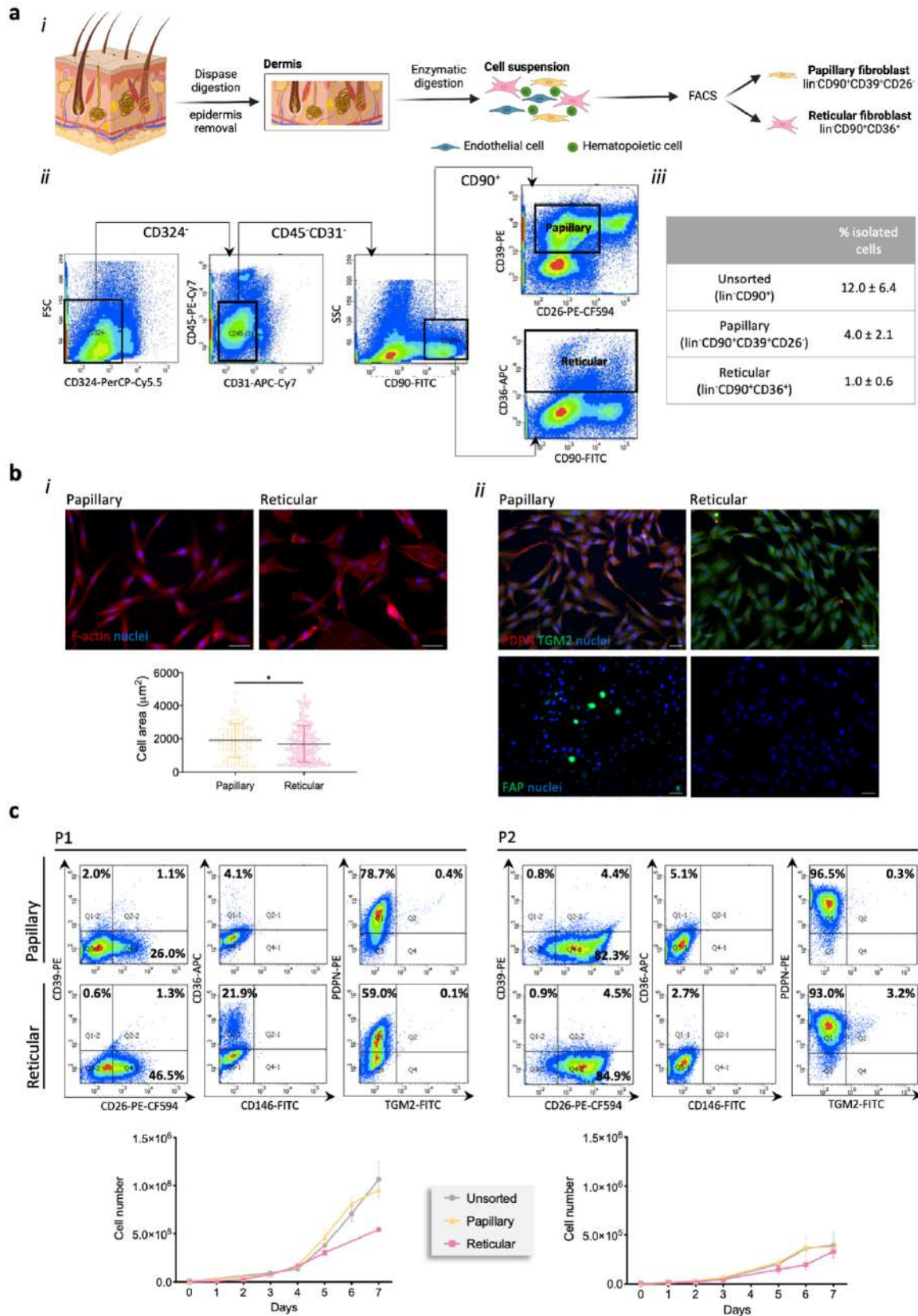
Figure IV-1 Phenotype of the fibroblast subpopulations.

a i) Schematics of the procedure followed for the isolation of papillary and reticular fibroblasts and (ii) the representative gating strategy of the sorting. After negative selection for CD324-, CD45- and CD31- and positive selection for CD90-, two populations were FACS sorted – CD39-CD26- cells corresponded to the papillary fibroblasts, while CD36- cells to the reticular fraction. (iii)

Percentage of isolated fibroblasts after sorting. b (i) Representative images of the F-actin stained cytoskeleton and respective quantification of the area of the cells. Scale bar = 50 µm. (ii) Representative immunocytochemistry images of the expression of podoplanin (PDNP), transglutaminase-2 (TGM2) and fibroblast activated protein (FAP) after isolation. Scale bar = 100 µm. Cell nuclei were counter-stained with DAPI. Individual channels images are presented in Supplementary Figure 2. c i) Phenotype of the papillary and reticular fibroblasts after passage 1 (P1) and 2 (P2) determined by flow cytometry and respective ii) representation of their proliferation as *per* DNA quantification along the culture time. Quantitative results are expressed as the mean ± standard deviation where n = 3, * $p < 0.05$, two-tailed unpaired Mann-Whitney test.

the lin⁻CD90⁺ population, and of CD146 a perivascular marker that has also been attributed to the reticular fraction [10], after passage 1 and 2. The expression of CD39 and TGM2 was almost lost in papillary fibroblasts after P1, while the percentage of cells expressing PDPN increased with the passage. Additionally, the initially papillary fibroblasts started to express CD26 being around 82.3 % of the whole cell population at P2 (**Figure VI-1c**). Interestingly, the expression of CD36 was very low (4-5 %) and did not change with the passage. Regarding the reticular fibroblasts, the expression of CD36 was only present in 21.9 % of the population at P1, being almost absent at P2. Like for the papillary sub-population, the expression of TGM2 was lost with the culture and the percentage of cells expressing PDPN increased with the passage. The percentage of initially reticular fibroblasts expressing CD26 also increased with the passages. The expression of CD146 was absent in both subpopulations and independently of the passage. Moreover, these phenotypic changes were linked with alterations in the proliferative rate of the subpopulations which was identical at P2 and lower than at P1. These results demonstrate that there are phenotypic changes in both cell populations after culture, therefore, in the following experiments only cells at P1 were used, being impossible to use cells P0 due to limited numbers.

IV-3.2. Fibroblasts influence on endothelial cells organization

Fibroblasts have been known to influence endothelial cell behaviour in a paracrine manner due to their angiogenic secretome [19,20]. To understand if the subpopulations we isolated could differently influence microvascular endothelial cells through secreted factors, a Matrigel assay with the conditioned media from their cultures was performed. A strong stimulation of capillary-like network formation was attained when media collected from papillary and reticular fibroblasts was used (**Figure VI-2a i**). The analysis of several angiogenic parameters of the formed capillary-like network showed that the medium from the reticular fibroblasts seemed to led to the formation of more complex and interconnect capillary-like network (**Figure VI-2a ii**, Supplementary Figure VI-3). Significant differences ($p < 0.05$) were observed
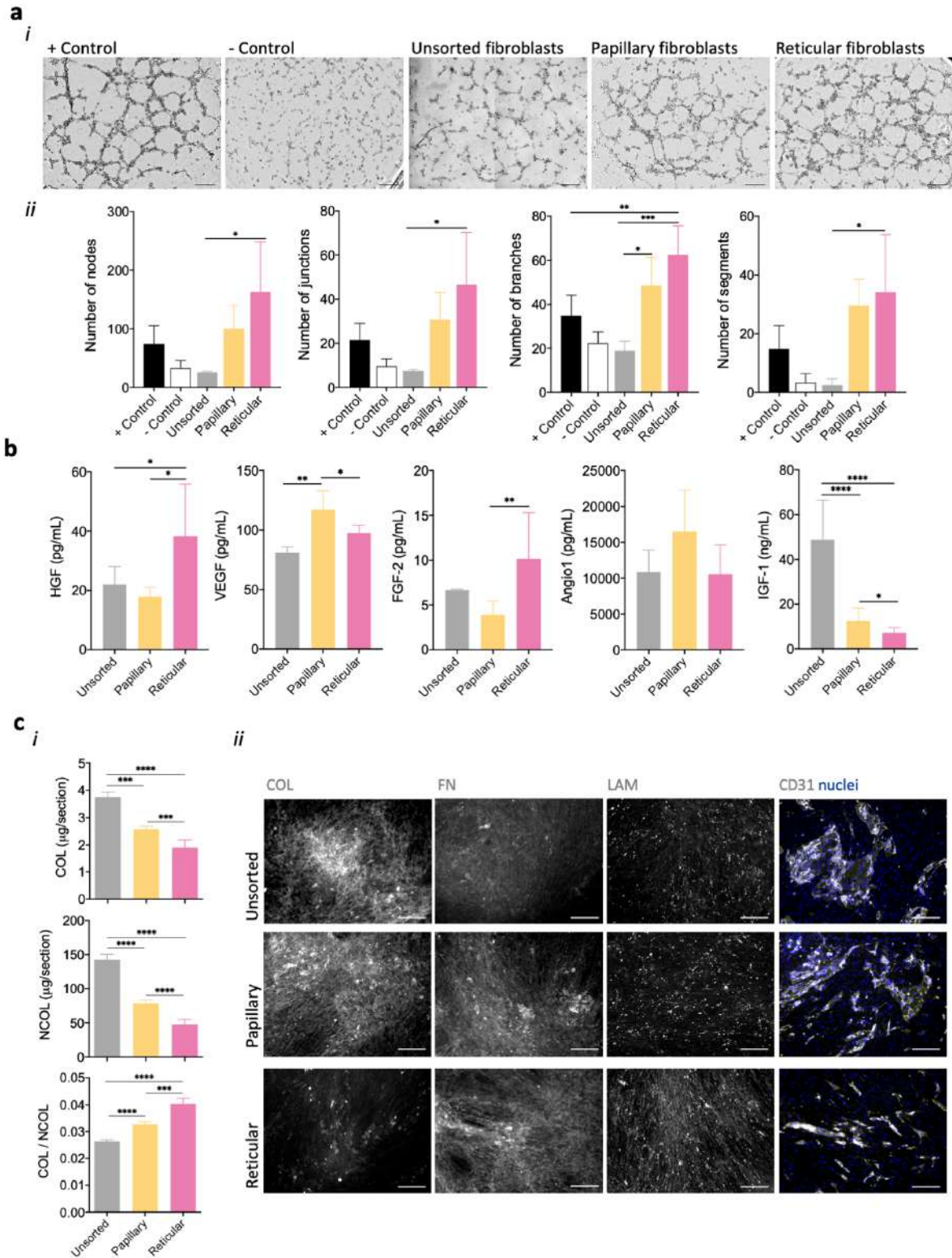
Figure IV-2 Fibroblast subpopulations ability to signal microvascular endothelial cells.
a (i) Tubular-like structures formation after 24 h by hDMECs cultured on matrigel with conditioned media obtained from unsorted, papillary and reticular fibroblasts, and respective (ii) number of nodes, junctions, branches and segments. Controls were set with VEGF-containing medium (+ Control) and with α-MEM (- Control). Scale bar = 100 μm. **b** Amount of growth factors secreted by unsorted, papillary and reticular fibroblasts as quantified in the conditioned media. **c** (i) Amount of collagen (COL) and non-collageneous (NCOL) proteins secreted by the different subpopulations of fibroblasts. (ii) Representative images

of the expression of collagen type I (COL1), fibronectin (FN) and laminin (LAM) by the subpopulations of fibroblasts and of the organization of CD31 hDMECs on that matrix. Nuclei were counter-stained with DAPI. Scale bar = 100 μm. Images of merged channels are represented in Supplementary Figure 6. Quantitative results are expressed as the mean ± standard deviation where n = 3, * $p < 0.05$, ** $p < 0.01$, *** $p < 0.001$, **** $p < 0.0001$, one-way ANOVA with Tukey multiple comparison post-test or Kruskal–Wallis test with Dunn's multiple comparison post-test.

in comparison with the unsorted cells (except for the number of meshes), but not with the papillary sub-population. Moreover, the time taken for the capillary-like structures to form in the presence of the fibroblast's conditioned media – 24 hours – was higher than in the positive control – 8 hours (Supplementary Figure VI-4). In order to better comprehend which angiogenic factors were being secreted by both papillary and reticular fibroblasts, HGF, VEGF, FGF-2, Angio-1 and IGF-1 [28–31] were quantified (**Figure VI-2b**). The conditioned medium from papillary fibroblasts was significantly enriched ($p < 0.05$) in VEGF and IGF-1 in comparison with the one from reticular fibroblasts. In turn, the reticular fibroblasts conditioned medium showed significantly higher ($p < 0.05$) HGF and FGF-2 amounts than the medium from papillary cells. Yet, the differences observed in the FGF-2 total secretion were due to the number of cells in each condition and do not reflect a higher level of secretion by reticular fibroblasts (Supplementary Figure VI-5). The level of all the factors in the subpopulation's media was significantly higher ($p < 0.05$) than in the medium from the unsorted cells, except for IGF-1. Although there were no significant differences in the amount of Angio1 among conditions, there is a tendency for a higher secretion by the papillary fibroblasts (**Figure VI-2b**), as sustained by the normalized data (Supplementary Figure VI-5).

In addition to a paracrine effect, it is known that fibroblasts also indirectly regulate endothelial cells activity through their ECM [19]. Thus, we analyzed the ECM secreted by the subpopulations of fibroblasts and its effect over hDMECs organization. Papillary fibroblasts deposited significantly higher amounts of COL and NCOL proteins ($p < 0.05$) than reticular fibroblasts although resulting in a significantly lower COL/NCOL ratio ($p < 0.05$). These results were corroborated by what seems to be a higher deposition of collagen type 1 (COL1) by the papillary fibroblasts, and laminin (LAM) by the reticular subset (**Figure VI-2c ii**). No substantial differences were observed regarding the fibronectin (FN) deposition. It seems that the differences in the content of the ECM secreted by the subpopulations of fibroblast also affect the organization of microvascular endothelial cells. While hDMECs organized in large cell colonies on the papillary fibroblast's cultures, they tend to be arranged in elongated structures on the reticular fibroblasts (**Figure VI-2c ii**, Supplementary Figure VI-6). Unsorted fibroblast secreted significantly higher ($p < 0.05$) amounts of both COL and NCOL proteins than the subpopulations with a deposition pattern similar to the

one observed for the papillary subset (**Figure VI-2c i, ii**) that also resulted in a similar hDMECs organization (**Figure VI-2c ii**, Supplementary Figure VI-6).

IV-3.3.   Bilayered spongy-like hydrogels properties

As mentioned before, papillary and reticular fibroblasts are respectively localized in the upper and lower dermis thus, we fabricated a bilayer structure integrating both the papillary- and a reticular-like dermal parts to accommodate each one of those cells (**Figure VI-3a**). The structural continuity of the bilayer structure was evident, with the individual layers being seamlessly integrated (**Figure VI-3b**). Each layer showed a homogeneous pore structure with a high degree of pore interconnectivity. A thin 220 μm in thickness layer with a mean pore size of 104.99 $\pm$ 19.52 μm and 83.38 $\pm$ 20.50 % pore interconnectivity outlined the papillary-like layer. The reticular-like part comprised a 1500 μm in thickness layer with lower mean pore size (67.43 $\pm$ 3.88 μm) and a pore interconnectivity of 40.00 $\pm$ 13.10 %.

The bilayer structures were prepared in a dry state and formed spongy-like hydrogels after hydration, as previously demonstrated for other structures processed with the same methodology [26,27]. With the fabricated bilayer structures, an equilibrium was reached as early as 1 h after immersion in α-MEM, after up taking 2134 $\pm$ 224 % of their weight in water (**Figure VI-3c**). When comparing each layer processed independently, we found that the papillary-like layer was able to uptake 3534 $\pm$ 533 % of their weight in water, while 2317 $\pm$ 289 % was retained by the reticular-like part. We further assessed the compressive modulus of the hydrated structure–- spongy-like hydrogel–- after the water uptake equilibrium was reached (**Figure VI-3d**). The compressive modulus of the bilayer scaffold was 103.5 $\pm$ 7.6 kPa. It seems that both layers contributed to it since the papillary-like and the reticular-like parts analyzed separately showed compressive modulus of 22.9 $\pm$ 2.5 kPa and 67.1 $\pm$ 15.5 kPa, respectively.

Then we wanted to understand if the overall and layer-specific properties of the bilayer structure were suitable to retain the respective fibroblasts subpopulations in the intended location. More than 90 % of both papillary and reticular fibroblasts remained in its destined layer, despite a minor escape of papillary fibroblasts to the reticular-like layer (**Figure VI-3e**). Independently of the fibroblast subpopulation, cells adhered to the material homogenously colonizing the structure layer into which they were seeded.
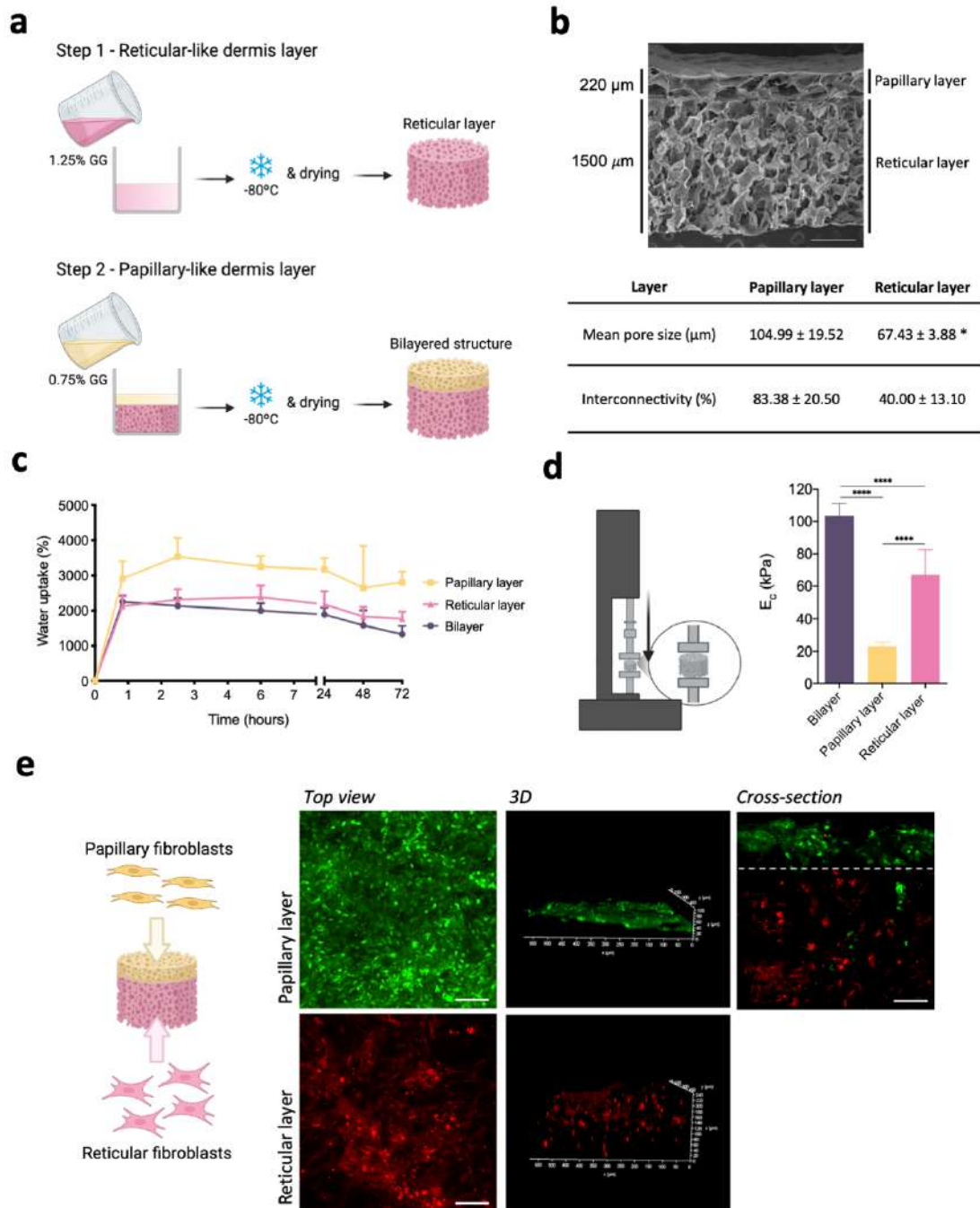
Figure IV-3 Bilayer structures preparation and characterization.
a Schematic representation of the fabrication of bilayer gellan gum (GG) structure. **b** Representative SEM micrograph of the bilayer dried polymeric structure and respective mean pore size and interconnectivity obtained by μ-CT analysis. Scale bar = 500 μm. **c** Water uptake ability of the bilayer structure and of the respective layers when processed independently. **d** Schematic representation of the compressive test and respective compressive modulus (Ec) values of the bilayer structure and of the respective layers when processed independently. **e** Schematic representation of the seeding of the subpopulations of fibroblasts in the different layers of the bilayered structure and representative images of papillary (green, Cell Tracker™ Green CMFDA) and reticular fibroblasts (red, Cell Tracker™ Orange CMRA) after 3 days of culture. Scale bar = 100 μm. Quantitative results are expressed as the mean $\pm$ standard deviation where n = 3, * $p < 0.05$, **** $p < 0.0001$, one-way ANOVA with Tukey multiple comparison post-test.

IV-3.4. *In vitro* vascularized skin-like construct

In order to validate our hypothesis, we prepared a skin-like construct in which dermis was either formed by sorted or unsorted fibroblasts (**Figure VI-4a**, Supplementary Figure VI-7). The hDMECs remained homogenously distributed in the upper papillary-like layer of the construct 1 day after seeding (day 8, **Figure VI-4b**) but were invading the reticular-like layer at day 14. Organization of hDMECs into what seemed to be vessel-like structures with lumen, was observed at day 21 in the construct prepared with the sorted cell populations. These structures increased in number and remained stable throughout the culture period being also present in the reticular-like layer at day 28 (**Figure VI-4b**). In contrast, hDMECs organization in the construct formed by the unsorted fibroblast seemed to be delayed and only at day 28 could be found in vessel-like structures with lumen. (**Figure VI-4b, c**). The differences in the behavior of hDMECs in the different constructs also affected the keratinocytes (**Figure VI-5**). A more differentiated epidermal layer was observed in the construct formed by the sorted fibroblasts, in opposition to the thin layer observed in the construct containing unsorted fibroblasts. Notwithstanding, it seems that the ECM deposition was not affected by the pre-selection of the sub-populations of fibroblasts as shown by the deposited collagen and laminin. Overall, the organization of the skin constructs was not affected but the earlier triggering of the endothelial cells benefited the formation of a fully differentiated epidermis.

IV-4. DISCUSSION

The papillary and reticular dermis harbour different fibroblast subpopulations responsible for establishing specific microenvironments, including distinctively vascularized dermal layers. Taking into consideration the communications between fibroblasts subpopulations and endothelial cells, we hypothesized that the pre-selection of the subpopulations of fibroblasts would benefit the *in vitro* generation of prevascularized skin TE constructs. We took advantage of specific markers recently identified [9] to isolate human papillary and reticular fibroblasts subpopulations with higher accuracy and reproducibility than the method used so far based on the dermatome. These subpopulations were sorted from the lin-CD90+ population, which corresponded to around 12 % of the initial fibroblast population. This
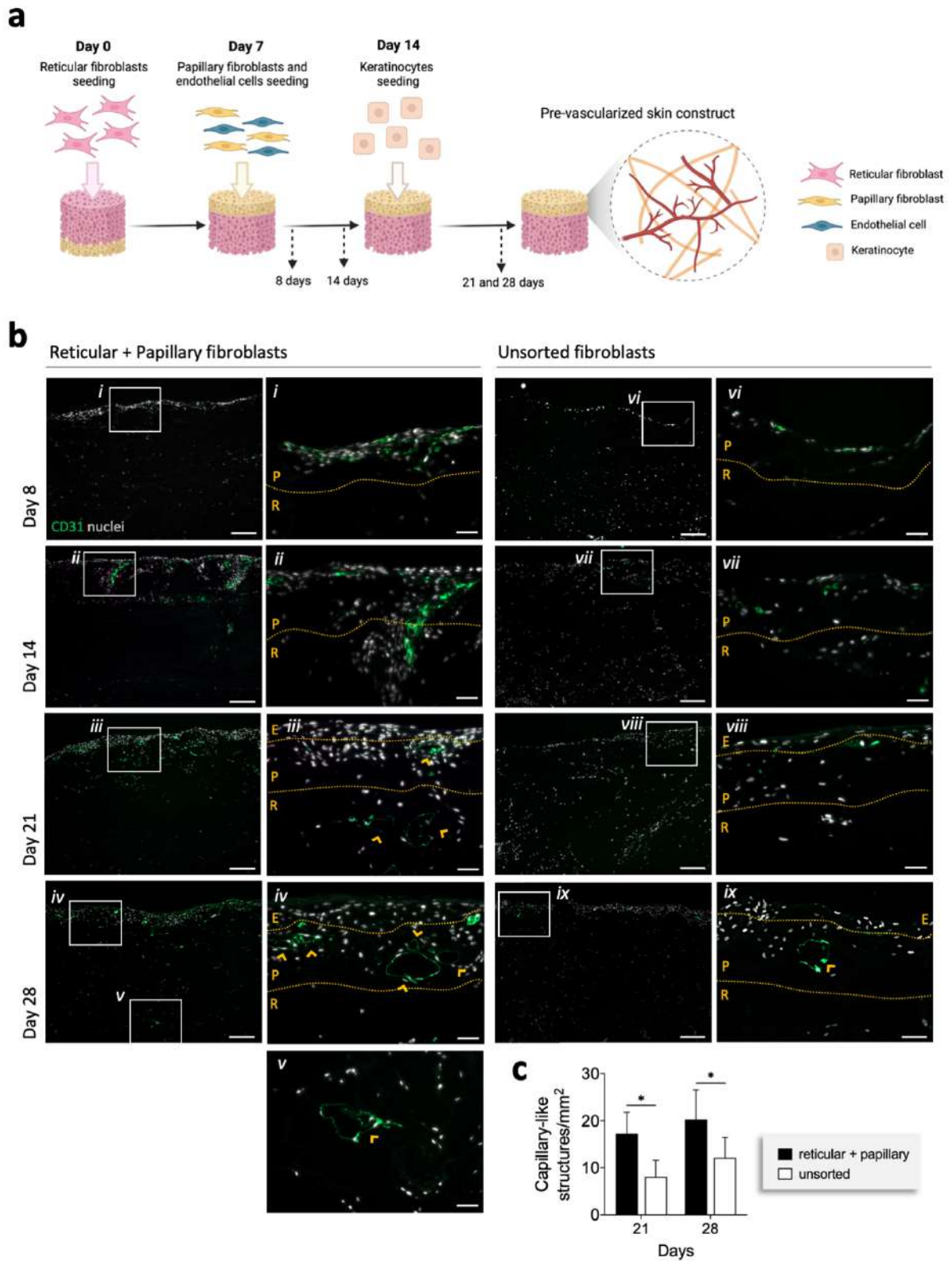
Figure IV-4 Fibroblasts pre-selection fosters prevascularization of the bilayer construct.

a Schematic representation of the reticular and papillary fibroblasts, endothelial cells and keratinocytes seeding strategy on the bilayered structure. **b** Representative immunohistochemistry images of the organization of hDMECs (CD31⁻) in the bilayered skin constructs prepared with reticular and papillary fibroblasts unsorted fibroblasts. Nuclei were counter-stained with DAPI. Scale bar = 200 μm, 50 μm. **c** Quantification of the amount of capillary-like structures at day 21 and 28. Quantitative results

are expressed as the mean ± standard deviation, * p < 0.05, two-way ANOVA with Tukey multiple comparison post-test. E – epidermis, P – papillary-like dermis, R – reticular-like dermis.
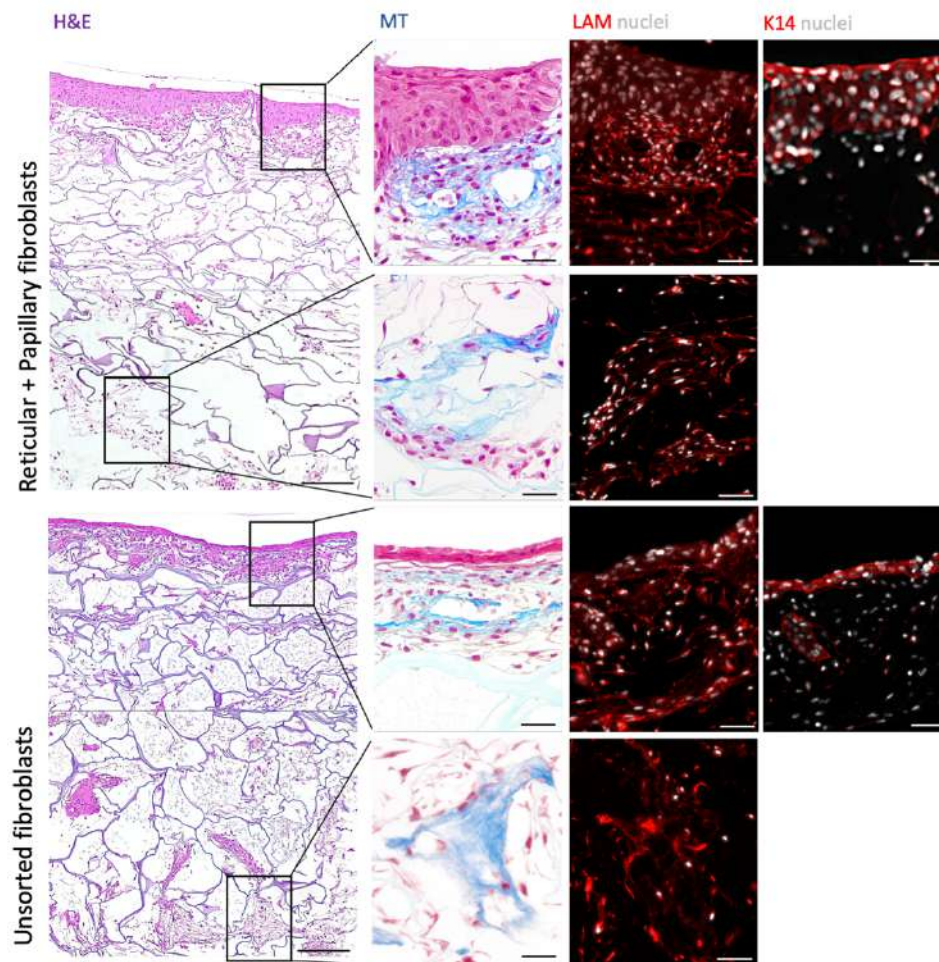
Figure IV-5 Skin-like tissue structure.
Representative Hematoxylin & Eosin (H&E) images of the constructs prepared with a sorted and b unsorted fibroblasts, including a stratified epidermis, and an upper and lower vascularized dermis. Scale bar = 200 μm. Representative Masson's Trichrome (MT) and immunohistochemistry images of specific areas (indicated in the lower magnification H&E images) of the constructs and the expression of laminin (LAM), and cytokeratin 14 (K14), evidencing the stratified epidermis and the deposited extracellular matrix. Nuclei were counter-stained with DAPI. Scale bar = 50 μm.

low percentage of fibroblasts has already been observed by others, as the human dermis comprises endothelial, hematopoietic and neural cells and other cell types [9]. The lin$^-$CD90$^+$CD39$^+$CD26$^-$ and lin$^-$CD90$^+$CD36$^+$, respectively the papillary and reticular fibroblasts, represented only around 4 % and 1 % of the initial population. Thus, the use of these cells to generate skin constructs requires its expansion to attain a higher and relevant cell number. When we passaged the two subsets of fibroblasts, we observed a loss of key markers, as well as a decrease in their proliferative potential after a single passage, which

is in agreement with other works [9,10]. While the mechanisms associated with this phenotype switch are unknown, microenvironment alterations including a pro-ECM secretion signalling has been linked to a shift in the expression of specific markers such as CD26⁺ [32,33]. It has been also speculated that the loss of papillary-specific markers is related to the loss of synergistic Wnt-mediated crosstalk between papillary fibroblasts and keratinocytes that occurs *in vivo* [9]. Interestingly, the ability to support the normal development of an epithelium by papillary fibroblasts after *in vitro* expansion was not affected [14,18,34]. This is in line with our results that confirmed the formation of a more differentiated epidermis in the 3D construct formed by sorted fibroblasts, in which the papillary subpopulation was in closer contact to keratinocytes. Our work further emphasizes the importance of selecting fibroblast subsets for proper development of the epidermis *in vitro*.

The dense microvasculature found in the papillary dermis is sustained by the unique microenvironment provided by papillary fibroblasts. Among other elements, the secretion of pro-angiogenic growth factors has been linked to the modulation of endothelial cell behaviour by papillary fibroblasts [19,20]. The secretome of our papillary subpopulation was enriched in VEGF, Angio-1 and IGF-1, all angiogenic factors, which might be implicated in the observed organization of hDMECS into tubule-like structures. Indeed, both VEGF and Angio-1, known to promote endothelial cell survival, migration and organization and stabilization of capillary-like structures [35,36], were also identified in the secretome of dermatomed papillary fibroblasts [19,20]. Interestingly we also found that our papillary subpopulation secretes high levels of IGF-1, which was previously shown to be responsible for stabilizing capillary-like structure formation but not eliciting endothelial cell organization [37]. Moreover, we found that the level of IGF-1 secreted by the unsorted fibroblasts is significantly higher than by the selected subpopulations, which might explain the reduced formation of capillary-like structures in the presence of their conditioned medium. The angiogenic secretome of dermatomed papillary fibroblasts was shown to be significantly more efficient in promoting capillary-like formation than the one of reticular fibroblasts [19,20]. Surprisingly, we observed strong capillary-like formation elicited by the reticular subset conditioned medium, which has high levels of VEGF and HGF. While this would not be expected, other works with dermatomed reticular fibroblasts have also showed varied levels of these two growth factors [19,20]. Like VEGF, HGF is known to promote endothelial cell migration and organization into tubule-like structures [38,39], therefore, our results might be a consequence of a synergistic effect of the two.

The microenvironment generated by the fibroblast subpopulations as positive regulators of capillary-like structure formation goes beyond their paracrine effect, as their distinct ECM signature can also

141

prompt alterations in endothelial cells [20]. Herein we found that the ECM deposited by the papillary subset was rich in collagen type I, which might explain the early development of vessel-like structures in our bilayer constructs generated from pre-selected fibroblasts. *In vitro*, collagen I interacts with the specific $\alpha 1\beta 1$ and $\alpha 2\beta 1$ integrins from the endothelial cells, which induce precapillary cord organization and, consequently, capillary-like structures formation [40]. Interestingly, the ECM produced by the reticular subset was rich in laminin. This protein is known to trigger the migration of endothelial cells through the activation of $\alpha 3\beta 1$ integrin in these cells [41,42] to expand the vessel-like structures formed [43]. Therefore, the laminin-rich ECM might have prompted the migration of the endothelial cell, initially seeded in the papillary layer, to the reticular part beneath along the culture, while also having a role in the stabilization of the formed structures [44], at latter culture times in both dermal layers.

Therefore, our results seem to further support the existence of an intricate signaling network responsible for the modulation of the vascular network within the different dermal layers that is highly dependent on the environment generated by the respective fibroblasts subpopulation.

Overall, we provide evidence that pre-selection of papillary and reticular fibroblasts is relevant in promoting the *in vitro* prevascularization of skin TE constructs. Notwithstanding, while the optimization of the culture conditions to allow the conservation of fibroblast subpopulation's phenotypes has not been achieved, their use in the construction of skin constructs for tissue engineering applications is hampered. Anyhow, vascularized *in vitro* skin models built from pre-selected fibroblasts subsets offer advantages in terms of representation of tissue functionality being therefore a valuable study platform.

IV-5.   REFERENCES

1   Chu DH. Development and structure of skin. In: Fitzpatrick's Dermatology in General Medicine (Chap. 7, Seventh Edition). Wolff K, Goldsmith LA, Katz SI, Gilchrest BA, Paller AS, Leffell DJ (Ed.), Mc Graw Hill - Medical, 57–73.

2   Brown TM, Krishnamurthy K. Histology, Dermis. StatPearls Publishing (2022).

3   Sorrell JM, Caplan AI. Chapter 4 Fibroblasts-A Diverse Population at the Center of It All. Int. Rev. Cell Mol. Biol. (2009).

4   Kabashima K, Honda T, Ginhoux F, Egawa G. The immunological anatomy of the skin. Nat. Rev. Immunol. 19, 19–30 (2019).

5   Charkoudian N. Skin blood flow in adult human thermoregulation: How it works, when it does not, and why. Mayo Clin. Proc. 78(5), 603–12 (2003).

6   Cobo R, García-Piqueras J, Cobo J, Vega JA. The human cutaneous sensory corpuscles: An update. J. Clin. Med. 10(2), 227 (2021).

7   Driskell RR, Lichtenberger BM, Hoste E *et al*. Distinct fibroblast lineages determine dermal architecture in skin development and repair. Nature 504, 277–281 (2013).

8   Harper RA, Grove G. Human skin fibroblasts derived from papillary and reticular dermis: Differences in growth potential *in vitro*. Science 204(4392), 526–7 (1979).

9   Philippeos C, Telerman SB, Oulès B *et al*. Spatial and Single-Cell Transcriptional Profiling Identifies Functionally Distinct Human Dermal Fibroblast Subpopulations. J. Invest. Dermatol. 138(4), 811–825 (2018).

10   Korosec A, Frech S, Gesslbauer B *et al*. Lineage Identity and Location within the Dermis Determine the Function of Papillary and Reticular Fibroblasts in Human Skin. J. Invest. Dermatol. 139(2), 342–351 (2019).

11   Janson DG, Saintigny G, van Adrichem A, Mahe C, El Ghalbzouri A. Different gene expression patterns in human papillary and reticular fibroblasts. J Invest Dermatol 132(11), 2565–2572 (2012).

12   Azzarone B, Macieira-Coelho A. Heterogeneity of the kinetics of proliferation within the human skin fibroblastic cell populations. J. Cell Sci. 57, 177–87 (1982).

13   Schafer IA, Pandy M, Ferguson R, Davis BR. Comparative observation of fibroblasts derived from the papillary and reticular dermis of infants and adults: Growth kinetics, packing density at confluence and surface morphology. Mech. Ageing Dev. 31(3), 275–93 (1985).

14   Mine S, Fortunel NO, Pageon H, Asselineau D. Aging Alters Functionally Human Dermal Papillary Fibroblasts but Not Reticular Fibroblasts: A New View of Skin Morphogenesis and Aging. PLoS One 3(12), e4066 (2008).

15   Varkey M, Ding J, Tredget EE. Superficial dermal fibroblasts enhance basement membrane and epidermal barrier formation in tissue-engineered skin: Implications for treatment of skin basement membrane disorders. Tissue Eng. - Part A 20(3–4), 540–552 (2014).

16   Nauroy P, Barruche V, Marchand L *et al*. Human Dermal Fibroblast Subpopulations Display

Distinct Gene Signatures Related to Cell Behaviors and Matrisome. J. Invest. Dermatol. 137(8), 1787–1789 (2017).

17   Hashmi S, Marinkovich MP. Molecular organization of the basement membrane zone. Clin. Dermatol. 29(4), 389–411 (2011).

18   Sorrell JM, Baber MA, Caplan AI. Site-matched papillary and reticular human dermal fibroblasts differ in their release of specific growth factors/cytokines and in their interaction with keratinocytes. J Cell Physiol 200(1), 134–145 (2004).

19   Sorrell JM, Baber MA, Caplan AI. Human dermal fibroblast subpopulations; differential interactions with vascular endothelial cells in coculture: Nonsoluble factors in the extracellular matrix influence interactions. Wound Repair Regen. 16(2), 300–309 (2008).

20   Mauroux A, Joncour P, Gillet B *et al*. Papillary and reticular fibroblasts generate distinct microenvironments that differentially impact angiogenesis. bioRxiv (2020).

21   Bahar MA, Bauer B, Tredget EE, Ghahary A. Dermal fibroblasts from different layers of human skin are heterogeneous in expression of collagenase and types I and III procollagen mRNA. Wound Repair Regen. 12(2), 175–82 (2004).

22   Weber L, Kirsch E, Muller P, Krieg T. Collagen type distribution and macromolecular organization of connective tissue in different layers of human skin. J. Invest. Dermatol. 82(2), 156–160 (1984).

23   Shirshin EA, Gurfinkel YI, Priezzhev A V., Fadeev V V., Lademann J, Darvin ME. Two-photon autofluorescence lifetime imaging of human skin papillary dermis *in vivo*: Assessment of blood capillaries and structural proteins localization. Sci. Rep. 7, 1171 (2017).

24   Michael Sorrell J, Baber MA, Caplan AI. Construction of a bilayered dermal equivalent containing human papillary and reticular dermal fibroblasts: Use of fluorescent vital dyes. Tissue Eng. 2(1), 39–49 (1996).

25   da Silva LP, Jha AK, Correlo VM, Marques AP, Reis RL, Healy KE. Gellan Gum Hydrogels with Enzyme-Sensitive Biodegradation and Endothelial Cell Biorecognition Sites. Adv. Healthc. Mater. 7(5), 1700686 (2018).

26   da Silva LP, Cerqueira MT, Sousa R a., Reis RL, Correlo VM, Marques AP. Engineering cell-adhesive gellan gum spongy-like hydrogels for regenerative medicine purposes. Acta Biomater. 10, 4787–4797 (2014).

27   Moreira HR, Silva LP da, Reis RL, Marques AP. Tailoring Gellan Gum Spongy-Like Hydrogels' Microstructure by Controlling Freezing Parameters. Polymers (Basel). 12(2), 329 (2020).

28   Lin S, Zhang Q, Shao X *et al*. IGF-1 promotes angiogenesis in endothelial cells/adipose-derived stem cells co-culture system with activation of PI3K/Akt signal pathway. Cell Prolif. 50(6), e12390 (2017).

29   Nakamura Y, Morishita R, Higaki J *et al*. Hepatocyte growth factor is a novel member of the endothelium-specific growth factors: Additive stimulatory effect of hepatocyte growth factor with basic fibroblast growth factor but not with vascular endothelial growth factor. J. Hypertens. 14(9), 1067–72 (1996).

30   Van Belle E, Witzenbichler B, Chen D *et al*. Potentiated angiogenic effect of scatter factor/hepatocyte growth factor *via* induction of vascular endothelial growth factor: The case for paracrine amplification of angiogenesis. Circulation 97(4), 381–90 (1998).

31   Asahara T, Bauters C, Zheng LP *et al*. Synergistic effect of vascular endothelial growth factor and basic fibroblast growth factor on angiogenesis *in vivo*. Circulation 92, II365-71 (1995).

32   Michalak-Micka K, Klar AS, Dasargyri A, Biedermann T, Reichmann E, Moehrlen U. The influence of CD26+ and CD26− fibroblasts on the regeneration of human dermo-epidermal skin substitutes. Sci. Rep. 12(1), 1944 (2022).

33   Worthen CA, Cui Y, Orringer JS, Johnson TM, Voorhees JJ, Fisher GJ. CD26 Identifies a Subpopulation of Fibroblasts that Produce the Majority of Collagen during Wound Healing in Human Skin. J. Invest. Dermatol. 140(12), 2515-2524.e3 (2020).

34   Haydont V, Neiveyans V, Perez P *et al*. Fibroblasts from the Human Skin Dermo-Hypodermal Junction are Distinct from Dermal Papillary and Reticular Fibroblasts and from Mesenchymal Stem Cells and Exhibit a Specific Molecular Profile Related to Extracellular Matrix Organization and Modeling. Cells 9(2), 368 (2020).

35   Kunz-Schughart LA, Schroeder JA, Wondrak M *et al*. Potential of fibroblasts to regulate the formation of three-dimensional vessel-like structures from endothelial cells *in vitro*. Am. J. Physiol. - Cell Physiol. 290(5), C1385-98 (2006).

36   Kim I, Kim HG, So JN, Kim JH, Kwak HJ, Koh GY. Angiopoietin-1 regulates endothelial cell survival through the phosphatidylinositol 3'-kinase/Akt signal transduction pathway. Circ. Res. 86, 24–29

(2000).

37   Jacobo SMP, Kazlauskas A. Insulin-like growth factor 1 (IGF-1) stabilizes nascent blood vessels. J. Biol. Chem. 290(10), 6349–6360 (2015).

38   Kanda S, Kanetake H, Miyata Y. HGF-induced capillary morphogenesis of endothelial cells is regulated by Src. Biochem. Biophys. Res. Commun. 344(2), 617–22 (2006).

39   Xin X, Yang S, Ingle G *et al*. Hepatocyte growth factor enhances vascular endothelial growth factor-induced angiogenesis *in vitro* and *in vivo*. Am. J. Pathol. 158(3), 1111–20 (2001).

40   Whelan MC, Senger DR. Collagen I initiates endothelial cell morphogenesis by inducing actin polymerization through suppression of cyclic AMP and protein kinase A. J. Biol. Chem. 278(1), 327–34 (2003).

41   Herbst TJ, McCarthy JB, Tsilibary EC, Furcht LT. Differential effects of laminin, intact type IV collagen, and specific domains of type IV collagen on endothelial cell adhesion and migration. J. Cell Biol. 106, 1365–1373 (1988).

42   Gu J, Sumida Y, Sanzen N, Sekiguchi K. Laminin-10/11 and Fibronectin Differentially Regulate Integrin-dependent Rho and Rac Activation *via* p130Cas-CrkII-DOCK180 Pathway. J. Biol. Chem. 276(29), 27090–27097 (2001).

43   Dejana E, Languino LR, Polentarutti N *et al*. Interaction between fibrinogen and cultured endothelial cells. Induction of migration and specific binding. J. Clin. Invest. 75(1), 11–18 (1985).

44   Liu Y, Senger DR. Matrix-specific activation of Src and Rho initiates capillary morphogenesis of endothelial cells. FASEB J. 18(3), 457–68 (2004).

IV-6. SUPPLEMENTARY INFORMATION

Supplementary Table IV-1 Fluorochrome-labeled antibodies used for cell sorting

Antibody	Brand	Ref	Host
CD324 PerCP-Cy5.5	BD Biosciences, USA	563573	Ms
CD45 PE-Cy7	BD Biosciences, USA	557748	Ms
CD31 APC-Cy7	BD Biosciences, USA	563653	Ms
CD90 FITC	eBiosciences, USA	11-0909-42	Dk
CD39 PE	BD Biosciences, USA	555464	Ms
CD26 PE-CF594	BD Biosciences, USA	565158	Ms
CD36 APC	BD Biosciences, USA	550956	Dk

Legend: Dk – donkey, Ms – mouse

Supplementary Table IV-2 Fluorochrome-labeled antibodies used for flow cytometry

Antibody	Brand	Ref	Host
CD39 PE	BD Biosciences, USA	555464	Ms
CD26 PE-CF594	BD Biosciences, USA	565158	Ms
CD36 APC	BD Biosciences, USA	550956	Dk
PDNP PE	Biolegend, USA	337003	Rat
TGM2 FITC	Bioss, USA	bs-8589R-FITC	Rb

Legend: Dk – donkey, Ms – mouse, PDPN – podoplanin, Rb – rabbit, TGM2 – transglutaminase-2

Supplementary Table IV-3 Immunolabelling antibodies

	Antibody	Brand	Ref	Host	Dilution
Primary antibodies	Podoplanin	Abcam, UK	ab10288	Ms	1:250
	Transglutaminase-2	Abcam, UK	ab421	Rb	1:75
	FAP	Abcam, UK	ab53066	Rb	1:100
	CD31	Dako, Denmark	M0823	Ms	1:30
	Collagen type I	Abcam, UK	ab34710	Rb	1:100
	Fibronectin	Abcam, UK	ab2413	Rb	1:100
	Laminin	Abcam, UK	ab11575	Rb	1:30
	Keratin 14	Covance, USA	PRB-160P	Rb	1:800
Secondary antibodies	Alexa fluor 488 anti-rabbit	Invitrogen, USA	A-11008	Gt	1:500
	Alexa fluor 594 anti-mouse	Invitrogen, USA	A-11032	Gt	1:500
	Alexa fluor 594 anti-rabbit	Invitrogen, USA	A-11012	Gt	1:500

Legend: FAP – fibroblast activation protein, Gt – goat, Ms – mouse, Rb – rabbit
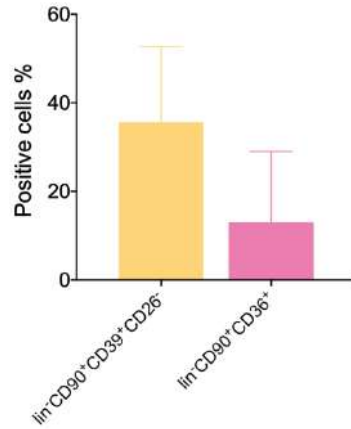
Supplementary Figure IV-1 Percentage of papillary and reticular fibroblasts present in the lin-CD90⁺fraction, N=6.
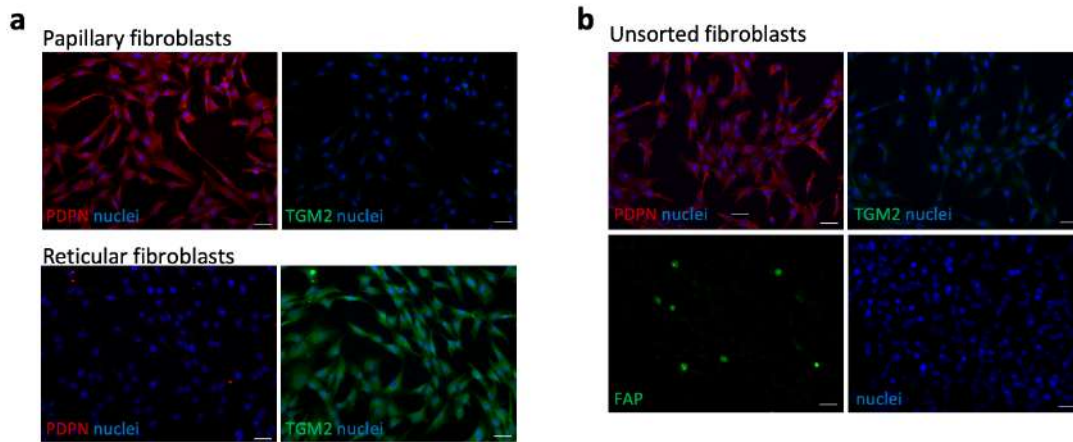
Supplementary Figure IV-2 Individual immunocytochemistry images of the expression of podoplanin (PDNP), transglutaminase-2 (TGM2) and fibroblast activated protein (FAP) by a papillary and reticular and b unsorted fibroblasts populations.

Scale bar = 100 μm. Nuclei were counter-stained with DAPI.
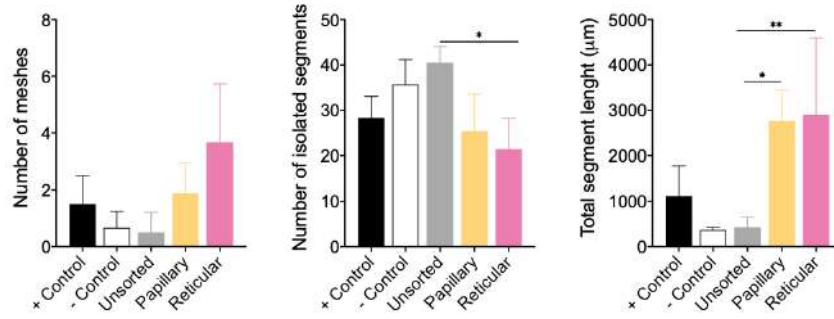
Supplementary Figure IV-3 Quantification of the number of meshes, isolated segments and total segment length of the tubular-like structures formed on Matrigel by hDMECs cultured with conditioned obtained from unsorted, papillary and reticular fibroblasts after 24 h of culture.

Quantitative results are expressed as the mean ± standard deviation where n = 3, * $p < 0.05$, ** $p < 0.01$, one-way ANOVA with Tukey multiple comparison post-test.
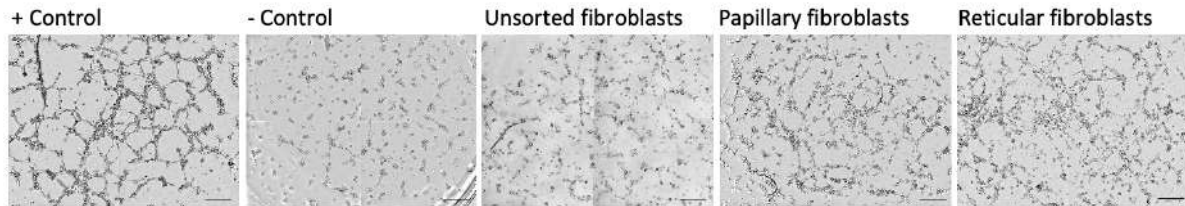
Supplementary Figure IV-4 Tubular-like structures formation after 8 h by hDMECs cultured on matrigel with conditioned media obtained from unsorted, papillary and reticular fibroblasts.

Controls were set with VEGF-containing medium (+ Control) and with α-MEM (- Control). Scale bar = 100 μm.
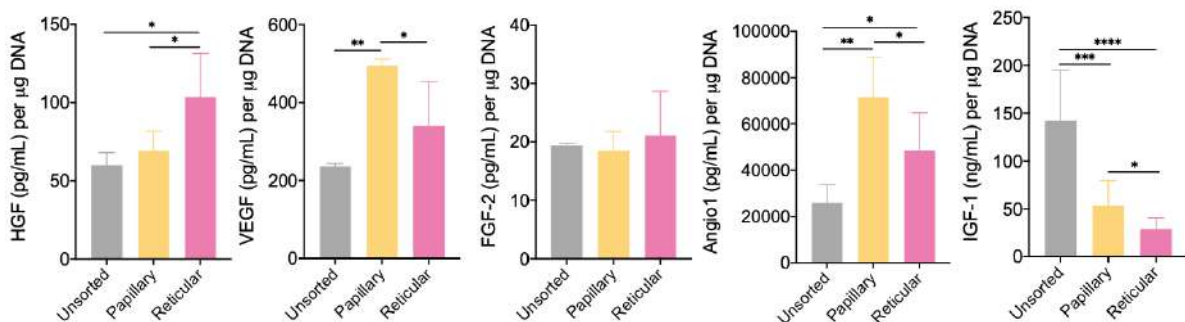
Supplementary Figure IV-5 Amount of growth factors secreted by unsorted, papillary and reticular fibroblasts as quantified in the conditioned media normalized with their respective DNA amount.

Quantitative results are expressed as the mean ± standard deviation where n = 3, * $p < 0.05$, ** $p < 0.01$, *** $p < 0.001$, **** $p < 0.0001$, one-way ANOVA with Tukey multiple comparison post-test.
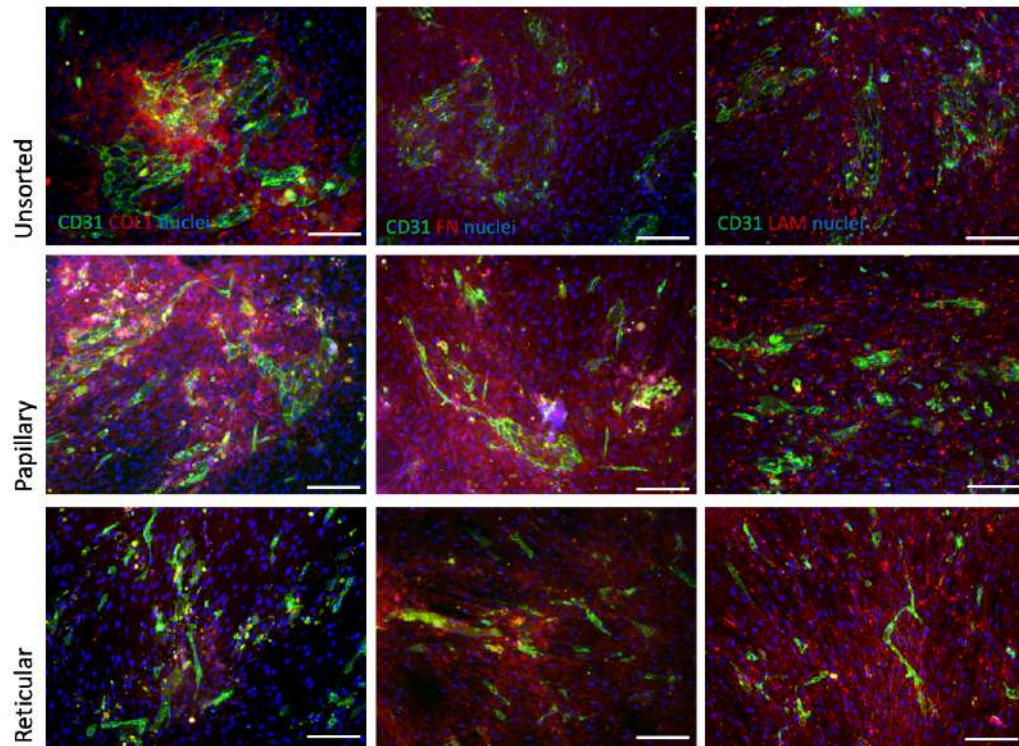
Supplementary Figure IV-6 Representative merged immunocytochemistry images of the expression of collagen type I (COL1), fibronectin (FN) and laminin (LAM) by the subpopulations of fibroblasts with the organization of CD31⁺ hDMECs on that matrix. Nuclei were counter-stained with DAPI. Scale bar = 100 μm.
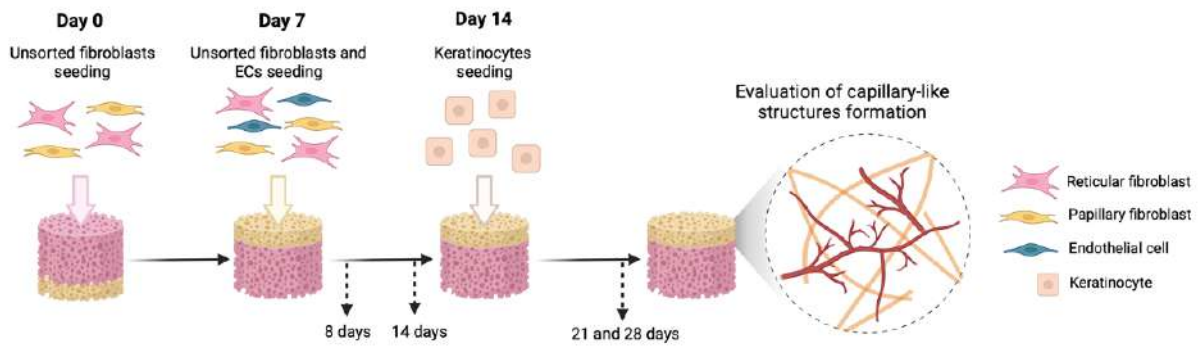
Supplementary Figure IV-7 Schematic representation of the unsorted fibroblasts, endothelial cells (ECs) and keratinocytes seeding strategy on the bilayer structure.

CHAPTER V

IN VITRO VASCULARIZATION OF TISSUE ENGINEERED CONSTRUCTS BY NON-VIRAL DELIVERY OF PRO-ANGIOGENIC GENES

IN VITRO VASCULARIZATION OF TISSUE ENGINEERED CONSTRUCTS BY NON-VIRAL DELIVERY OF PRO-ANGIOGENIC GENES §

ABSTRACT

Vascularization is still one of the major challenges in tissue engineering. In the context of tissue regeneration, the formation of capillary-like structures is often triggered by the addition of growth factors which are associated with high cost, bolus release and short half-life. As an alternative to growth factors, we hypothesized that delivering genes-encoding angiogenic growth factors to cells in a scaffold microenvironment would lead to a controlled release of angiogenic proteins promoting vascularization, simultaneously offering structural support for new matrix deposition. Two non-viral vectors, chitosan (Ch) and polyethyleneimine (PEI), were tested to deliver plasmids encoding for vascular endothelial growth factor (pVEGF) and fibroblast growth factor-2 (pFGF2) to human dermal fibroblasts (hDFbs). hDFbs were successfully transfected with both Ch and PEI, without compromising the metabolic activity. Despite low transfection efficiency, superior VEGF and FGF-2 transgene expression was attained when pVEGF was delivered with PEI and when pFGF2 was delivered with Ch, impacting the formation of capillary-like structures by primary human dermal microvascular endothelial cells (hDMECs). Moreover, in a 3D microenvironment, when PEI-pVEGF and Ch-FGF2 were delivered to hDFbs, cells produced functional pro-angiogenic proteins which induced faster formation of capillary-like structures that were retained *in vitro* for longer time in a Matrigel assay. The dual combination of the plasmids resulted in a downregulation of the production of VEGF and an upregulation of FGF-2. The number of capillary-like segments obtained with this system was inferior to the delivery of plasmids individually but superior to what was observed with the non-transfected cells. This work confirmed that cell-laden scaffolds containing transfected cells offer a novel, selective and alternative approach to impact the vascularization during tissue regeneration.

V-1.   INTRODUCTION

The vascularization of tissue-engineered constructs is still one of the major challenges of the field [1]. Considering vascularization takes place in a highly complex and regulated microenvironment, if a tissue-engineered construct is not able to integrate with surrounding tissues and establish interconnections to host blood vessels after implantation, diffusion of oxygen and nutrients supply becomes limited, resulting in loss of cell viability at the core of the construct, and ultimately, graft failure [2].

Prevascularization by culturing endothelial cells on a scaffold prior to implantation is one of the main strategies used to promote vascularization through the inosculation of pre-formed and host vessel-like structures [3]. To date, the majority of prevascularization strategies rely on the use of endothelial cells in co-culture with perivascular cells [4]. However, one of the major limitations of this approach is the cell source and availability of mature/progenitor endothelial cells [5]. Human pluripotent stem cells and human mesenchymal stem cells have also been used [6], but protocols for the differentiation towards endothelial cells are still not sufficiently robust. Additionally, external growth factors have also been used to develop microvascular networks [6]. The delivery of vascular endothelial growth factor (VEGF), basic fibroblasts growth factor (FGF-2) and/or platelet-derived growth factor, which mediate the recruitment, expansion, and survival of endothelial cells, as well as tubule formation and stabilization [7–11], were also shown to be a powerful strategy to stimulate angiogenesis [12–15]. However, the use of growth factors is associated with several limitations that includes high cost, bolus release of proteins, short half-life, and the requirement of high doses to achieve a therapeutic effect [16], which in the case of angiogenic factors can be linked to tumor development [17]. To tackle this, genes encoding for specific angiogenic proteins, can be delivered as plasmid DNA (pDNA) to induce a sustained production of physiologically appropriate amounts of therapeutic protein, subsequently inducing the formation of stable capillary-like structures.

Viral and non-viral vectors can be used to deliver pDNA. However, non-viral vectors are generally safer, less immunogenic, and are more straightforward to mass-produce with high tunability when compared to viral vectors [18]. However, they are typically limited by lack of efficacy due to low transfection efficiency. Recently, in a number of studies from our lab, chitosan (Ch) [19,20] and polyethyleneimine (PEI) [21,22] have been optimized as vectors demonstrating high transfection efficiency and uncompromised cell viability. The idea of combining cells transfected with non-viral vector and therapeutic genes and scaffolds is an innovative strategy that guarantees a sustainable protein

production, while scaffolds offer structural support and a matrix for new tissue deposition and act as cell delivery devices [16]. Collagen (COL)-based scaffolds [23,24] and gellan gum (GG)-based spongy-like hydrogels [25,26] have been explored for a range of tissue engineering applications, including skin wound healing [5,27]. While COL-chondroitin sulfate (ChS) and GG-hyaluronic acid (HyA) were capable of supporting skin neo-tissue formation, it was also shown that cells and materials in those constructs synergize promoting neovascularization [5,20]. COL-HyA scaffolds were firstly developed for cartilage regeneration [28], but have an enormous interest in the area of skin tissue engineering due to the importance of HyA in skin remodeling and angiogenesis [29].

In this context, we hypothesized that the angiogenic and thus regenerative potential of collagen (COL)-glycosaminoglycans (GAG) scaffolds and gellan gum (GG)-based spongy-like hydrogels would be maximized when combined with cells transfected with genes encoding for angiogenic growth factors. The optimal vector for the delivery of plasmids encoding for VEGF (pVEGF) and for FGF-2 (pFGF2) for the downstream production of angiogenic factors by human dermal fibroblasts (hDFbs) was established. Subsequently the potential of engineering a novel cell-laden scaffold-based strategy for the *in situ* delivery of VEGF and FGF-2 was evaluated by seeding transfected hDFbs and human dermal microvascular endothelial cells (hDMECs) in COL-ChS, COL-HyA and GG-HyA to analyze the behavior of the endothelial cells.

V-2. MATERIALS AND METHODS

V-2.1. Plasmid propagation & purification

Gaussia Luciferase (pGLuc; New England Biolabs, USA), Green Fluorescent Protein (pGFP; Amaxa, Lonza, Germany), Vascular Endothelial Growth Factor (pVEGF; Genecopaeia, USA) and basic Fibroblast Growth Factor (pFGF2; kindly provided by Prof. Henning Madry from Saarland University) were propagated *via* the transformation of Subcloning Efficiency™ DH5α™ chemically competent *Escherichia coli* cells (Life Technologies, Ireland). All plasmid DNA were isolated and purified using an Endotoxin Free Maxi-prep Kit (Qiagen, UK) as *per* the manufacturer's instructions. The obtained plasmid was dissolved in Tris-EDTA buffer at a concentration of 0.5 $\mu g \mu L^{-1}$ and stored at -20 °C until further usage.

154

V-2.2.   Non-viral vector-pDNA polyplex formation

Chitosan (Ch, Mw 7.3 kDa; DD > 97%; Novamatrix, FMC Biopolymer, Norway) nanoparticles were formulated by electrostatic interaction between cationic chitosan and anionic pDNA. Nanoparticles were allowed to equilibrate for 30 min at room temperature before use. The ratio of chitosan to pDNA (N/P ratio, nitrogen:phosphate ratio) was 10 and the pDNA loading dose was 0.33 µg as optimized previously [19]. Branched PEI (Sigma Aldrich, Ireland) was purified *via* dialysis. For this, PEI was dissolved in deionized water and loaded into Cellu-Sep H1 membranes (25 kDa MWCO). This was dialyzed against a 400-fold excess of deionized water a total of four times over night before the remaining PEI was lyophilized for use. 2 µg of pDNA was added to sterile molecular grade water followed by dropwise addition of PEI at a N/P ratio of 7 and 30 min equilibration at room temperature [21].

V-2.3.   Assessment of complexation efficiency

A SYBR® Safe (Life Technologies, Ireland) exclusion assay was used to assess how effectively Ch and PEI binds to the pDNA of interest. SYBR® Safe fluoresces strongly upon intercalation between the base pairs of pDNA. Upon complete and stable binding of Ch or PEI to pDNA, there should be no free pDNA available for intercalation with the probe and the fluorescent signal is quenched [30,31]. Ch-pDNA and PEI-pDNA nanoparticles were prepared as in Section 2.2 and then diluted to 1 mL with molecular grade 20 mM NaCl. 0.5 µL of SYBRSafe DNA stain was then added and the fluorescence signal read (RFU), in triplicate, on a spectrofluorimeter (Bio-Tek Synergy HT 188743, Fisher Scientific, Ireland) at an excitation wavelength of 488 nm and an emission wavelength of 522 nm. Binding efficiency was calculated following **Equation V-1**, as follows.

$$Binding\ efficiency\ (\%) = 100 - \frac{RFU_{vector-pDNA} \times 100}{RFU_{pDNA}}$$

Equation V-1 Binding efficiency.

Gel electrophoresis was also used to confirm complexation efficiency. For that, 5 µL of each non-viral vector-pDNA complex was added to 1 µL 6X loading dye (ThermoFisher) and run on a 1 % (w/v) agarose (Lonza, Switzerland) gel for 45 min, along with controls (pDNA alone, non-viral vector alone and a 10000 bp ladder). The gels were viewed in the 600 channel of an Odyssey Fc Imaging System (LI-COR, US), and imaged and quantified using the Image Studio Software (LI-COR, US).

V-2.4.   Human microvascular endothelial cells isolation and culture

Human microvascular endothelial cells (hDMECs) were harvested from human skin samples obtained from abdominoplasties performed at Hospital da Prelada (Porto, Portugal), after informed consent. Samples were obtained under a collaboration protocol with the 3B's Research Group, approved by the ethical committees of both institutions. Briefly, skin specimens were cut into small fragments and incubated overnight in 2.4 U mL^{-1} dispase (BD Biosciences, USA) at 4 °C. hDMECs were obtained through the filtration and centrifugation of the dispase solution. The remaining skin pieces were discarded. hDMECs were cultured in 0.7 % (w/v) gelatin (Sigma, USA) coated flasks with Endogro-MV VEGF (Millipore, USA). Cells were passaged at 70-90 % confluency and used at passage 3–4.

V-2.5.   Human dermal fibroblast culture

Primary human dermal fibroblasts (hDFbs, ATCC, supplied by LGC Standards, UK) were expanded in Dulbecco's Modified Eagles Medium supplemented with 1 % (v/v) penicillin/streptomycin, 10 % FBS (v/v) (Labtech, UK), 1 % (v/v) glutamax (Biosciences, Ireland). Cells were passaged at 70-90 % confluency and expanded to passage 6 for all experiments.

V-2.6.   hDFbs monolayer transfection

hDFbs were seeded at a density of 2x10^4 cells *per* well in 24-well adherent plates (Corning, Costar, Ireland). After 24 h, cells were washed with PBS and provided with 1 mL of OptiMEM (Gibco, Ireland). After 1 h, complexed nanoparticles were added in OptiMEM. After 5 h, transfection media was removed, cells were washed twice in PBS and growth medium was replenished. Prior to each time point (3, 5, 7, 10 and 14 days), the medium was removed and replaced by DMEM without FBS for a starvation period of 24 h. The supernatant was collected after 24 h for the ELISA assay and Matrigel assay.

V-2.7.   Transfection efficiency assessment

Transfection efficiency was analyzed by quantifying luciferase luminescence intensity or by the quantification of GFP$^+$ cells by flow cytometry and fluorescence microscopy. For the analysis of luciferase production at days 3, 7 and 14, 1 mL of complete medium was removed from each well and replaced with 1 mL of fresh media. Luciferase content was determined using a Pierce^{TM} Gaussia Luciferase Flash

Assay Kit (Thermo Scientific, Ireland) as *per* the manufacturer's instructions. Briefly, 20 μL of the collected media were transferred in triplicate to a black 96 well plate. 50 μL of the working solution was added to each well and luminescence was acquired using a Varioskan Flash multimode plate reader (Fisher Scientific, Ireland). Cells transfected with Chitosan-pGFP or PEI-pGFP were visualized using an Axio Observer inverted Microscope (Zeiss, Germany). All cells (transfected/non-transfected) were labelled with Phalloidin-TRITC (0.5 μg mL^{-1}, Sigma, Ireland) and DAPI (0.02 mg mL^{-1}, Biotium, USA) for visual confirmation. For flow cytometry analysis pGFP transfected hDFbs were analyzed in BD FACSAria III by BD FACSDIVA software (both BD Biosciences, Belgium) where GFP fluorescence was expressed as a percentage of GFP positive over the total number of gated cells.

V-2.8. Non-viral vector-pDNA toxicity assessment

To assess the toxicity of the vector-pDNA complexes, metabolic activity and cell proliferation were quantified at 0, 3, 7 and 14 days post-transfection using CellTiter 96® AQueous One Solution Cell Proliferation Assay (Promega, USA) and Quant-iT PicoGreen dsDNA Assay Kit (Invitrogen, UK), respectively. At each time-point, after washing with PBS, cells were incubated with 20 μL of MTS solution (4:1 medium:MTS) for three hours at 37 °C. Then, 100 μL of the supernatant was transferred in triplicate to a 96 well plate and the absorbance of each sample was read at 490 nm. Metabolic activity was normalized with the dsDNA obtained from the Quant-iT PicoGreen dsDNA Assay and data was expressed as a percentage cell metabolic activity in relation to the non-transfected hDFbs. Briefly, for the quantification of dsDNA, cells were incubated with 0.5 mL of ultra-pure water for 1 h at 37 °C, collected and then frozen at -80 °C. 28.7 μL of each cell lysate was added to each well of a white 96 well plate followed by the addition of 100 μL of 1x Tris-EDTA buffer and 78.3 μL of Picogreen reagent according to manufacturer's instruction. After a 10 min incubation at RT, fluorescence was read at 480/520 nm using a Varioskan Flash multimode plate reader. The concentration of DNA present in each sample was determined against a standard curve.

V-2.9. Collagen-GAG scaffold fabrication

Collagen-GAG scaffolds were fabricated using a lyophilization technique developed by O'Brien *et al* [23,24]. COL-HyA or COL-ChS scaffolds were made by blending 1.8 g of bovine tendon collagen (Southern Lights Biomaterials, New Zealand) in 300 mL of 0.5 M glacial acetic acid (HOAc, Fisher Scientific, Ireland) for 90 min. A total of 0.16 g of glycosaminoglycan (hyaluronic acid sodium salt derived from

Streptococcus equi or chondroitin sulfate sodium salt from shark cartilage (Sigma Aldrich, Ireland), was dissolved in 60 mL of 0.5M HOAc and added to the collagen slurry at a rate of 5 mL/10 min while blending at 15.000 rpm. The slurry was blended for a further 60 min following the addition of all of the GAG. Gas was removed from the slurries using a vacuum pump and freeze-dried (Advantage EL, VisTir Co., Gardiner NY) to a final temperature of −10 °C using a controlled freezing rate of 1 °C *per* minute. Afterwards, the scaffold sheets were crosslinked dehydrothermally (DHT) at 105 °C for 24 h at 0.05 bar in a vacuum oven (Vacucell 22; MMM, Germany). Scaffolds with a diameter of 5 mm were created using a biopsy punch, hydrated with PBS and chemical crosslinked using a mixture of 6 mM *N*-(3-Dimethylaminopropyl)-*N*-ethylcarbodiimide hydrochloride (EDC) and 5.5 mM *N*-Hydroxysuccinimide (NHS).

V-2.10. Gellan gum-based scaffolds fabrication

Gellan gum (GG)-hyaluronic acid (HyA) spongy-like hydrogels were prepared as previously described [25,26]. Briefly, a solution of 0.44 % (w/v) hyaluronate (1.5 MDa, LifeCore Biomedical, USA) [32] and 0.5 % (w/v) gellan gum (Gelzan, Sigma-Aldrich, France) was prepared at 90 °C. Additionally, 0.25 % (v/v) gellan gum chemically modified with divinyl sulfone (GGDVS) [33] was reacted with thiol-cyclo-RGD (800 μM, Cyclo(-RGDfC) 95 %, GeneCust Europe) for 1 h. Hydrogels were prepared by mixing the hyaluronate/GG solution with GGDVSRGD and then caste into the desired molds. The hydrogel was progressively formed until room temperature was reached. Afterwards, hydrogels were frozen at -80 °C overnight and then freeze-dried (Telstar, Spain) for 24 h to obtain GG-HyA dried polymeric networks. Spongy-like hydrogels were formed after rehydration of the dried polymeric networks.

V-2.11. Cell-laden scaffold fabrication

hDFbs were transfected with PEI-pVEGF N/P 7 (2 μg pDNA), Ch-pFGF2 N/P 10 (0.33 μg pDNA) or the dual combination PEI-pVEGF+Ch-pFGF2 (1 μg pVEGF + 0.165 μg pFGF2; P+C) for 5 h at 37 °C. After hDFbs transfection, hDFbs were mixed with hDMECs (1:4) and the cell suspension was seeded on the different scaffolds: COL-HyA, COL-ChS and GG-HyA. The scaffolds were incubated at 37 °C for 30 min and afterwards, 1 mL of a mix of DMEM and EndoGRO MV-VEGF (Millipore, Germany) (1:1) was added to each well. Prior each time point (3 and 7 days), the medium was removed and replaced by DMEM/EndoGRO MV-VEGF (1:1) without FBS and without growth factors for a starvation period of 24 h.

The supernatant, or conditioned media, was collected after 24 h for the ELISA assay and Matrigel assay. Scaffolds were fixed with 10 % formalin (Bio-Optica, Italy) for immunocytochemistry.

V-2.12.   Enzyme-linked immunosorbent assay (ELISA) for VEGF and FGF-2 quantification post transfection

The levels of VEGF and FGF-2 secreted by the transfected cells were quantified by ELISA assays (R&D Systems, UK) in both 2D and 3D systems. Assays were carried out according to the manufacturer's instructions and the absorbance of each sample was read at 450 nm using a Varioskan Flash multimode plate reader. The quantity of VEGF and/or FGF-2 protein was determined against a standard curve.

V-2.13.   Quantification of capillary-like structures formation

Matrigel (Corning, USA) was added to 96-well plates that were then kept in a humidified incubator for 30 min. hDMECs were then seeded on the top of the formed gel at a density of 1.3×10^4 cells/well and incubated for 24 h in a humidified incubator at 37 °C, 5 % of CO_2 in the presence of filtered VEGF or FGF conditioned media. Negative and positive controls were incubated with DMEM medium or with EndoGRO MV-VEGF respectively. For the assay using transfected hDFbs, the conditioned media is the same supernatant as was quantified by ELISA. The organization of cells into capillary-like structures was assessed after 24 h after cell staining with Phalloidin-TRITC and DAPI. Micrographs were taken using an Axio Observer inverted Microscope (Zeiss, Germany) with the ZEN Blue 2012 software (Zeiss, Germany).

For the assay using conditioned media from cell-laden gene-activated scaffolds, organization in capillary-like structures was assessed using time-lapse imaging. Time-lapse brightfield images were obtained every 30 min over 24 h using an Axio Observer inverted microscope with incubation (37 °C, 5 % of CO_2), and ZEN Blue 2012 software (Zeiss, Germany). The capillary-like structures formation peak time and half-life were quantified. Peak time corresponds to the period of time required for relevant tubular-like structure formation to be visible, on the other hand, the retention time corresponds to the period of time required upon peak time establishment to achieve tubule regression. Capillary-like structures were screened and an angiogenesis plug-in for ImageJ 1.48 [34] was used to quantitatively analyze their formation and organization.

V-2.14.   Immunocytochemistry

After fixation, cells were incubated with 1 % (v/v) Triton X-100 (Sigma-Aldrich, Portugal) for 30 min at RT for permeabilization. Samples were then incubated with mouse anti-human primary antibody CD31 (1:30, Dako, USA) diluted in 1 % (w/v) BSA solution in PBS for 18 h at 4 °C. After washing with PBS, samples were incubated for 1 h at RT with the secondary antibody Alexa Fluor 488 donkey anti-mouse (Life Technologies, USA) at a concentration of 1:500 in 1 % (w/v) BSA solution in PBS. Cytoskeleton and nuclei were counter-stained with Phalloidin-TRITC and DAPI, respectively. Scaffolds were observed using a Leica TCS SP8 confocal microscope (Leica, Germany).

V-2.15.   Statistical analysis

GraphPad Prism 8.2.1 software (La Jolla, USA) was used to perform the statistical analysis. The results were compared to a control condition corresponding to non-transfected hDFbs. Data was analyzed using the Shapiro-Wilk normality test. All data followed a normal distribution therefore was analyzed using a two-way ANOVA with Turkey post-test and a one-way ANOVA with Turkey post-test. Significance and confidence were set to 0.05 (95 % of confidence interval), represented by * $p < 0.05$, ** $p < 0.01$, *** $p < 0.001$, **** $p < 0.0001$. All quantitative data refer to 3 independent experiments (n=3) with at least 3 replicates in each condition, in each experiment and are presented as mean ± standard deviation.

V-3.   RESULTS

V-3.1.   Characterization of Ch-pDNA and PEI-pDNA nanoparticles and transfection efficiency on hDFbs

The process of cell transfection starts with complexation between non-viral vectors and plasmids (**Figure V-1A**). The complexation efficiency between Ch or PEI and pVEGF or pFGF2 is shown in **Figure V-1B**. Both pDNA complexes showed high encapsulation efficiency. For Ch, 98.7 % ± 0.7 % and 97.4 % ± 0.5 % were obtained for pVEGF and pFGF-2, respectively. For PEI, 98.5 % ± 1.1 % and 99 % ± 0.7 % efficiency were observed for pVEGF and pFGF2, respectively. Gel electrophoresis (**Figure V-1C**) also confirmed these results, as no bands were observed for both complexed Ch-pDNA and PEI-pDNA, regardless of the pDNA amount. This indicates that the pDNA was strongly complexed with the Ch and PEI.
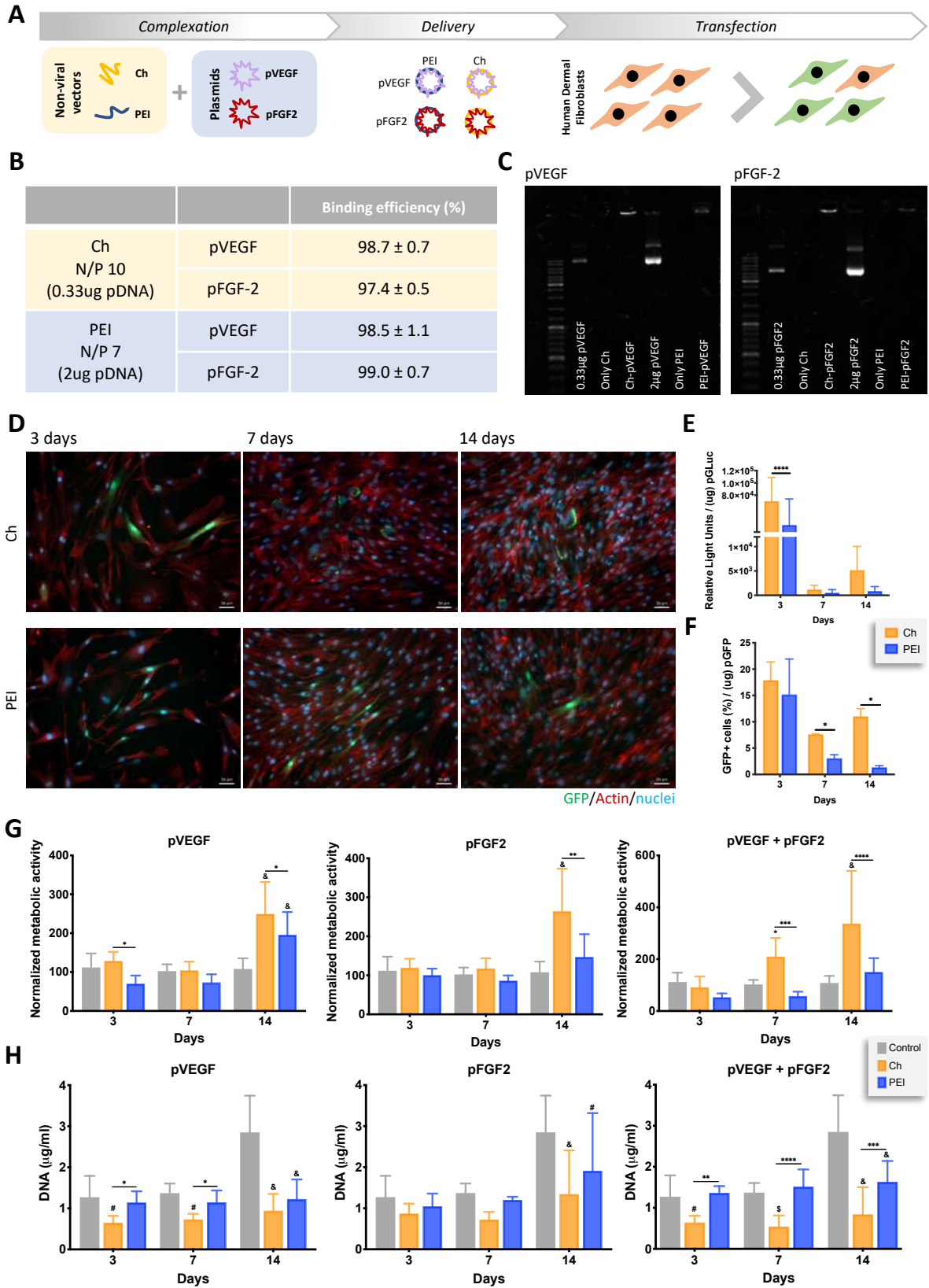
A Scheme of non-viral and plasmid complexation that are delivered to human dermal fibroblasts (hDFbs) and leads to cell transfection. **B** Binding efficiency of Ch or PEI to pVEGF or pFGF2. **C** Complexation of pDNA and the non-viral vectors. From a 1 % Agarose gel is possible to observe a complete complexation between Ch or PEI to pVEGF and pFGF2. **D** GFP positive cells

were visually observable for both formulations at day 3, 7 and 10. Scale bar = 50 μm. **E** Transient gene expression of hDFbs using the report system pGLUC showed that Chitosan-pGLuc N/P 10 formulation resulted in a statistically higher level of pGLuc transgene expression in hDFbs compared to PEI-pGLuc N/P 7 formulations at day 3 (*p*<0.001). **F** Transfection efficiency in hDFbs using the reporter system pGFP. Both the Chitosan-pGFP N/P 10 (0.33 μg pGFP) and PEI-pGFP N/P 7 (2 μg pGFP) resulted in a peak transfection efficiency at day 3 of 17.90 ± 3.5 % and 15.20 ± 6.7 % respectively. **G** Metabolic activity was quantified following treatment with Ch- and PEI-pDNA polyplexes. Formulation with pVEGF showed a significant decrease in cell metabolic activity up to day 7 with PEI when compared to control and Ch. **H** Cell proliferation by DNA quantification showed a significative decrease over all time-points when pVEGF or pVEGF/pFGF2 were delivered together with Ch. No major differences are observed in pFGF2 conditions up to day 14. Results are expressed as the mean ± standard deviation where n=3, * *p* < 0.05, # *p* < 0.01, $ *p* < 0.001, & *p* < 0.0001 in relation to control (non-transfected hDFbs) or * *p* < 0.05, ** *p* < 0.01, *** *p* < 0.001, **** *p* < 0.0001 in relation to each condition, at each time point.

In order to understand the transfection efficiency of Ch-pGLuc and PEI-pGLuc on hDFbs, luciferase activity was quantified for 14 days (**Figure V-1E**). Luciferase expression peaked at day 3 post-transfection for both non-viral vectors at $7.1 \times 10^5 \pm 3.8 \times 10^5$ versus $3.2 \times 10^5 \pm 4.2 \times 10^5$, with Ch-pGLuc significantly (p < 0.001) outperforming PEI-pGLuc. Both non-viral vectors were able to maintain a transient gene expression for 14 days and there were no significant differences on the luciferase expression for the remaining days. Images taken 3-, 7- and 14-days post-transfection show cells expressing GFP, indicating successful transfection of hDFbs (**Figure V-1D**). When quantified (**Figure V-1F**), the transfection efficiency achieved using Ch-pGFP or PEI-pGFP corresponded to 18 % ± 3.5 % and 15 % ± 6.7 % of pGFP-transfected cells, respectively. Significant differences on the number of GFP+ cells were found after 7 days, i.e, Ch-pGFP was higher than PEI-pGFP formulations.

The effect of the Ch-pDNA and PEI-pDNA complexes on hDFbs metabolic activity and proliferation rate was investigated at 3, 7, and 14 days post-transfection with the therapeutic genes pVEGF and/or pFGF2 (**Figure V-1G**). However, right after the transfection the metabolic activity *per* cells was higher in PEI than in control or Ch, in both pVEGF and pFGF2 conditions (Supplementary Figure IV-1). A significant decrease in the metabolic activity of cells transfected with PEI-pVEGF was detected at day 3 when compared to Ch-pVEGF. At day 14, when VEGF was delivered with Ch or PEI, cell metabolic activity showed to be significantly (*p* < 0.0001) higher than the control. No major differences in cell metabolic activity were observed for pFGF2 delivered with Ch or PEI until day 7. At day 14, a significant increase in the metabolic activity (*p* < 0.0001) was achieved for Ch-pFGF2 in relation to control and PEI-pFGF2. The metabolic activity when plasmids were delivered together with Ch was significantly higher (*p* < 0.01) from day 7-onward in comparison with non-transfected cells or PEI. The metabolic activity levels from the dual combination with PEI showed to be similar to the control. The delivery of the non-viral vectors or plasmids alone did not influence negatively cell metabolic activity (Supplementary Figure IV-2A).

When DNA content was measured after transfection, a significant decrease in PEI was observed for both pVEGF and pFGF2 conditions (Supplementary Figure IV-1). As a marker of cell proliferation (**Figure V-1H**), a significant ($p < 0.01$) decrease up to 14 days was observed when pVEGF is delivered with Ch when compared to control and up to 7 days when compared to PEI. For PEI, only at day 14 post-transfection, a significant ($p < 0.001$) decrease is observed in relation to control. Regarding pFGF2, no significant differences in DNA content were observed until day 14 post-transfection when it was significantly ($p < 0.01$) lower with both vectors in relation to control. Concerning pVEGF and pFGF2 delivered together, the trend observed is the same as pVEGF delivered alone. Plasmids delivered with Ch showed a reduction ($p < 0.01$) in DNA content in all time points when comparing with the control, whereas when plasmids were delivered with PEI, only at day 14 there was a significant ($p < 0.0001$) decrease in DNA content in relation to control. In all time time-points there was also a significant difference ($p < 0.01$) in Ch and PEI, since plasmids delivered with PEI showed higher DNA content. The delivery of single vectors or plasmids showed a significantly decrease in the amount of DNA content (Supplementary Figure IV-2B) in relation to control. These results were independent of the vector or plasmid used. In summary, these results showed that Ch did not impact in cells' metabolic activity but decreased the cell proliferation. In contrast, PEI transfected cells showed lower metabolic activity when compared to Ch but the cell proliferation was similar to non-transfected cells up to day 7.

V-3.2. VEGF and FGF-2 post-transfection therapeutic protein production enhances capillary-like structure formation

The production of VEGF and FGF-2 by pVEGF- and pFGF-2-transfected cells was monitored up to 14 post-transfection (**Figure V-2A**). When pVEGF is delivered to hDFBs with Ch, VEGF protein production peaked at day 3 post-transfection (95.5 pg mL^{-1}). On the other hand, when pVEGF was delivered using PEI, VEGF production peaked at 7 days post-transfection (132.1 pg mL^{-1}). From day 10 onward, the amount of VEGF produced by the control was significantly higher ($p < 0.01$) than the remaining conditions. Regarding the production of FGF-2, both vectors yield significantly higher ($p < 0.0001$) production than the control. The FGF-2 production increased until day 5 when pFGF2 was delivered with Ch, peaking at this time-point (1522.6 pg mL^{-1}). From day 5 until day 10, the FGF-2 production was in a plateau state.
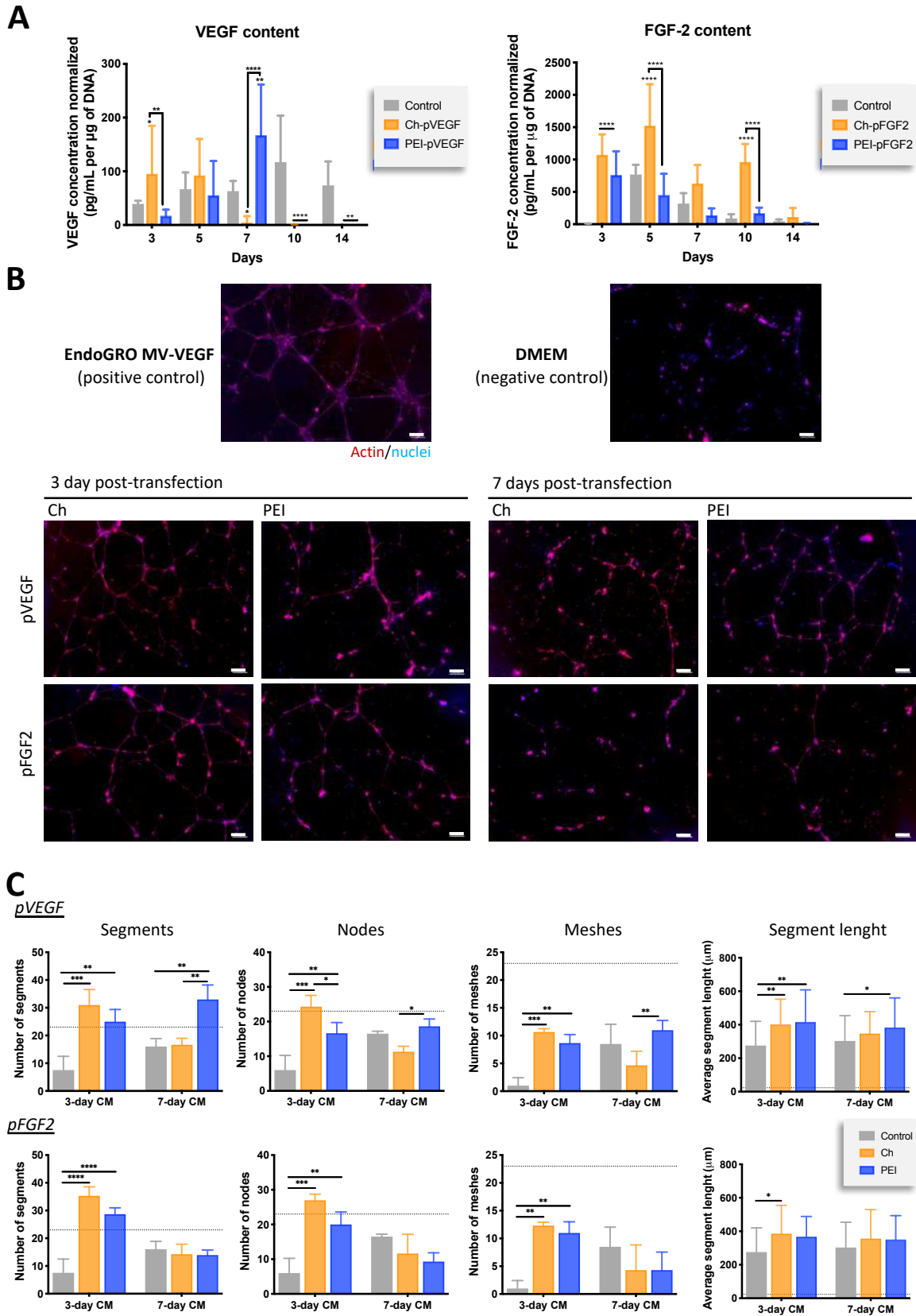
Figure V-2 Assessment of protein production by transfected cells and respective functionality on hDMECs.

hDFbs were transfected with pVEGF or pFGF2 with Chitosan (0.33 µg dose) or PEI (2 µg dose). **A** VEGF and FGF2 proteins were monitored by ELISA at days 3, 5, 7, 10 and 14 post-transfection. Significantly more VEGF protein is produced in Ch-pVEGF at day 3 and PEI-pVEGF at day 7. FGF-2 delivered with Ch showed a significant sustained release up to day 14. Control

164

corresponds to non-transfected hDFbs. **B** Tubular-like structures formed by hDMECs cultured on matrigel with conditioned media obtained from representative transfected hDFbs cultures for (i) 3 and (ii) 7 days. After 24h in Matrigel, tubular-like structures were fixed and labelled with Phalloidin-TRITC and DAPI. Controls were made with VEGF-containing EndoGRO (EndoGRO MV-VEGF) which, as expected, stimulated the *in vitro* formation of capillary-like structures, and with DMEM that did not promote the same. Scale bar = 200 μm. **C** Quantification of the number of segments, nodes, meshes and segments lenght present in hDMECs cultured in the presence of the described conditioned media (CM) at day 3 and 7. Control corresponds to hDFbs non-transfected. Matrigel positive control is the horizontal doted line. Results are expressed as mean ± SD where n = 3, * $p < 0.05$, ** $p < 0.01$, *** $p < 0.001$ and **** $p < 0.0001$.

pFGF2 delivered with PEI lead to significantly higher ($p < 0.0001$) FGF2 production than the control at day 3 but decreased from that time-point onward.

The ability of 3- and 7-day post-transfection conditioned media from the transfected hDFbs to promote the organization of hDMECs into capillary-like structures was evaluated on matrigel (**Figure V-2B-C**). The 3-day conditioned media of cells transfected with all conditions elicited the formation of capillary-like structures (**Figure V-2B**). Moreover, the quantification of the segments and number of nodes (**Figure V-2C**) showed that the results for transfected cells were significantly ($p < 0.01$) superior than the control, independently of the conditions. The same trend was observed regarding the number of meshes and segments length. With the 7-day conditioned media only cells transfected with pVEGF with Ch or PEI exhibited the formation of capillary-like structures (**Figure V-2B**). However, only with PEI-pVEGF the number of segments and nodes was significantly ($p < 0.01$, $p < 0.05$) higher than the control and Ch-pVEGF (**Figure V-2C**). Together with the ELISA results we conclusively demonstrate that the PEI vector was capable of inducing a superior VEGF therapeutic transgene expression in hDFbs, and the Ch a superior FGF-2 transgene expression. For this reason, for subsequent experiments PEI was used to delivery pVEGF and Ch was used to delivery pFGF-2.

V-3.3.   The angiogenic potential of transfected cells in a 3D microenvironment

The angiogenic potential of the transfected hDFbs was evaluated in a 3D microenvironment using hDMECs (**Figure V-3A**) After 3 days in culture, hDMECs adhered to the surface of scaffolds and were in close contact to hDFbs (**Figure V-3B**). Moreover, after 7 days in culture, hDMECs showed the formation of an extensive cell network in both non-transfected and PEI-pVEGF transfected hDFbs. For hDMECs in
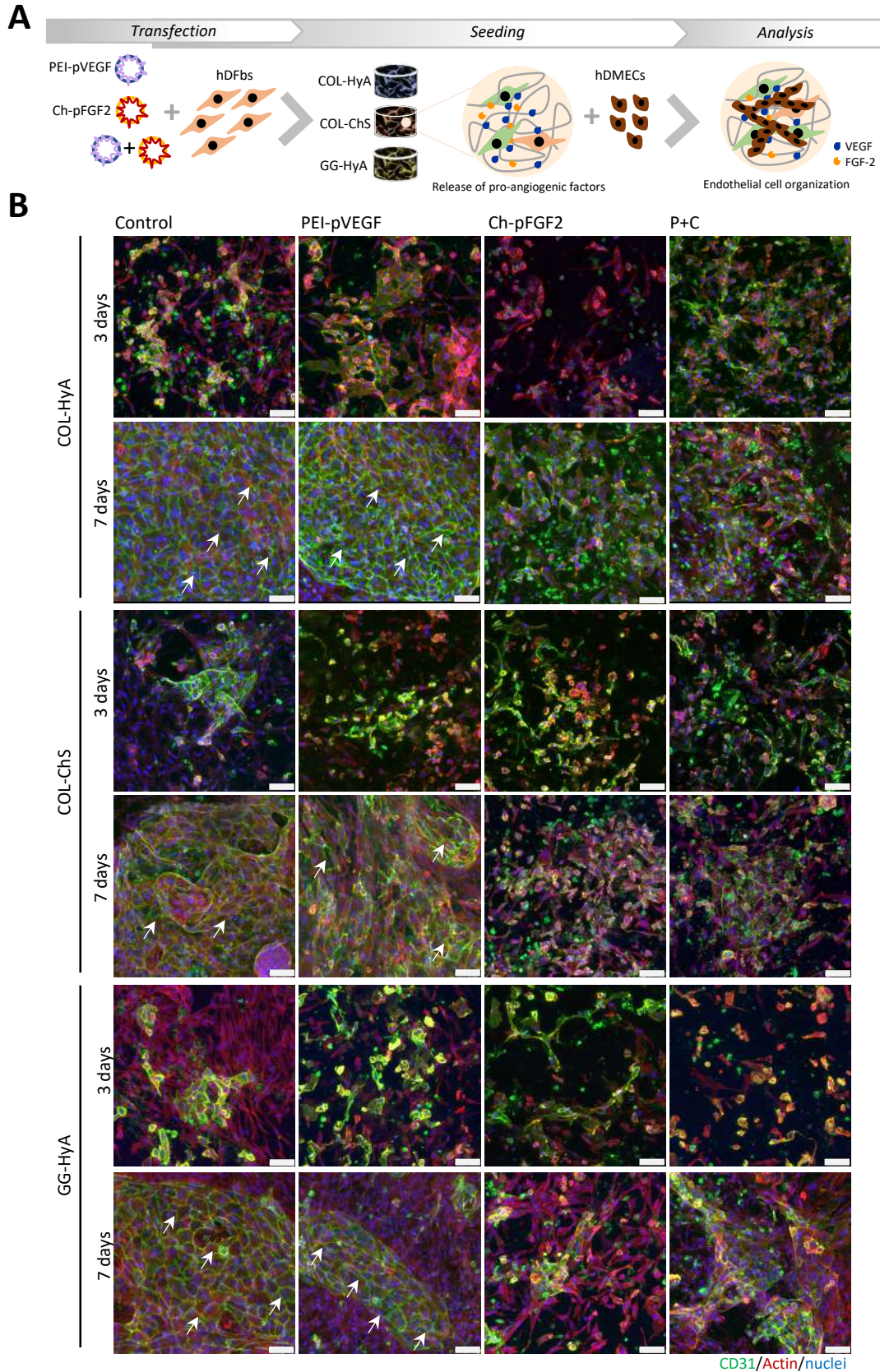
Figure V-3 hDMECs organization on COL-GAG and GG-HyA scaffolds after 3 and 7 days.

A Chosen plasmids were delivered to hDFbs and seeded in different scaffolds. The angiogenic capacity of the system is maximized through the release of angiogenic proteins providing a 3D microenvironment for endothelial cells proliferation and

organization. **B** hDFbs were transfected with PEI-pVEGF, Ch-pFGF2 and the dual combination of both (P+C) and seeded on COL-HyA, COL-ChS and GG-HyA scaffolds with hDMECs. Control corresponds to co-cultures where hDFbs were not transfected. In all scaffolds, co-culture of hDMECs (CD31) with PEI-pVEGF hDFbs showed the formation of an extensive CD31⁺ endothelial network (white arrows) in all conditions after 7 days. Scale bar: 75 µm.

contact with Ch-pFGF2 and P+C transfected hDFbs presented a more elongated form. These results were independent of the type of scaffold used, as in COL-ChS, COL-HyA and GG-HyA, the same tendency was observed.

The analysis of the supernatant of cultures showed increased secretion of VEGF over time (**Figure V-4A**). The amount of VEGF produced by PEI-pVEGF transfected hDFbs was significantly higher ($p < 0.05$) than the control. Moreover, VEGF levels for PEI-pVEGF transfected hDFbs were significantly superior ($p < 0.0001$) than the dual combination transfection. Residual amounts of VEGF close to P+C were obtained for Ch-pVEGF transfected hDFbs. These results were independent of the type of scaffold used. Quantification of the FGF-2 content showed higher production of FGF-2 at day 3 (**Figure V-4A**) in all scaffolds compared to control. In HyA-containing scaffolds (COL-HyA and GG-HyA), all transfection conditions yield significantly ($p < 0.05$) higher FGF-2 values. In COL-ChS scaffolds significant differences ($p < 0.001$) were observed only for the P+C condition. The overexpression of FGF-2 in relation to control was only maintained over time when cells were transfected with the P+C in the COL scaffolds.

The ability of conditioned medium derived from transfected cells in the 3D environment to induce hDMECs formation capillary-like networks in Matrigel was studied for the different scaffolds (**Figure V-4B**). A significant ($p < 0.05$) early peak time (5 h 30 min) was observed with 3-day COL-HyA conditioned media from co-cultures with hDFbs transfected with PEI-pVEGF, Ch-pFGF2 and P+C (**Figure V-4Bii**), when compared to control (7 h 30 min). Moreover, the retention time of these capillary-like structures were higher ($p < 0.05$) than the control, especially in the case of conditioned media from co-cultures of hDMECs and hDFbs transfected with PEI-pVEGF (7 h) and Ch-pFGF2 (7 h 30 min). These findings show that that capillary-like structure formation was faster with 3-day conditioned media from transfected cells and retained the capillaries for a longer time before regression. Additionally, the number of segments produced was significantly ($p < 0.05$) higher in Ch-pFGF2 and P+C conditioned media. With the 7-day COL-HyA conditioned media from the co-cultures, no differences were observed in the capillary-like structures peak time nor retention time. However, a significant ($p < 0.01$) increase in the number of segments was
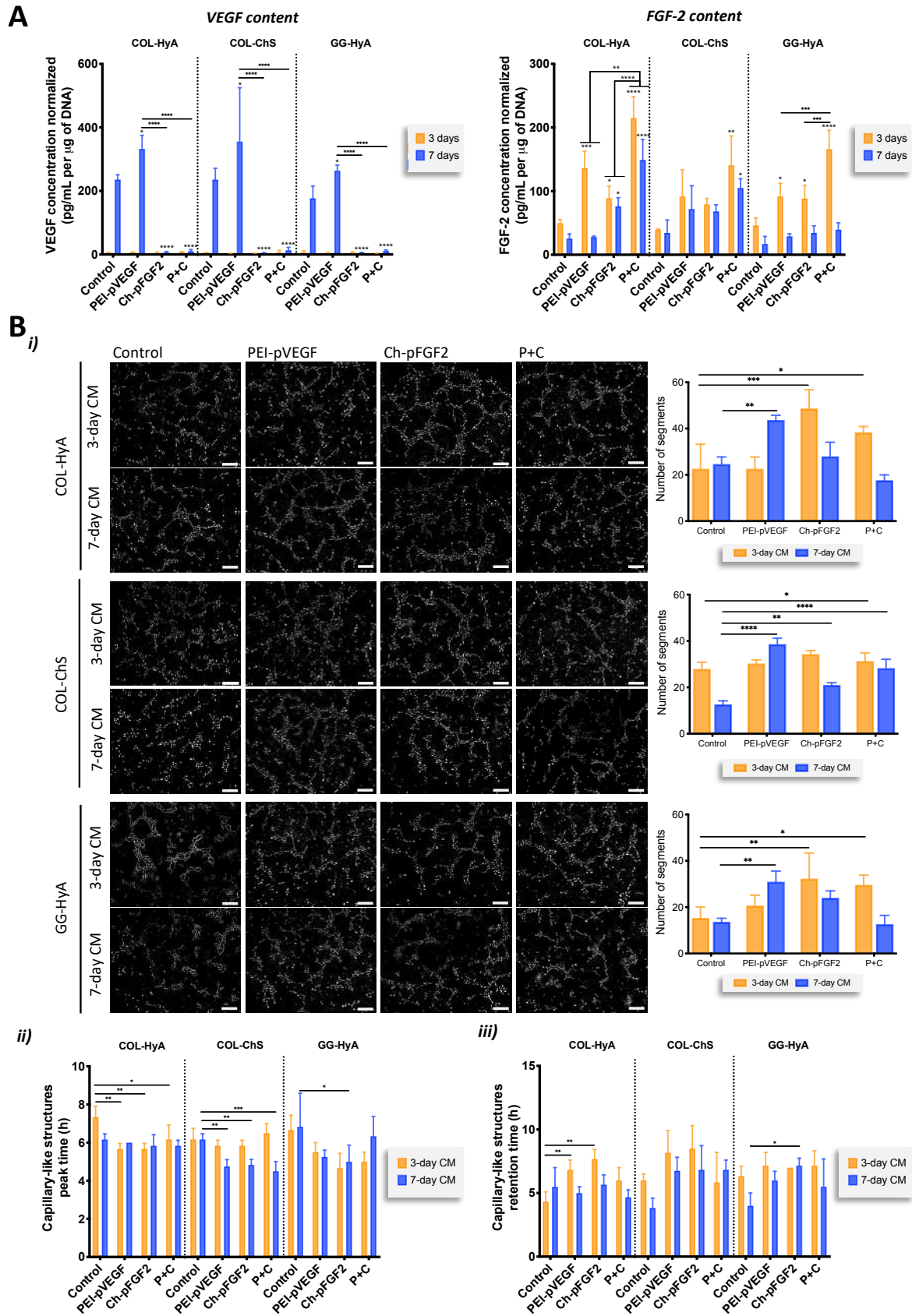
Figure V-4 Assessment of the effects of co-cultures of transfected hDFbs and hDMECs in COL-GAG and GG-HyA scaffolds.
A The production of VEGF is significantly higher in the co-cultures control 7 days post-transfection. Regarding FGF-2 content, 3 days after transfection there is a significand increase in protein content on the HyA containing scaffolds (COL-HyA and GG-

HyA), when hDFbs are transfected by Ch-pFGF2 and P+C. **B** Effect of the conditioned media (CM) of the different scaffolds on hDMECs in a Matrigel assay. (i) Tubular-like structures formed by hDMECs cultured on matrigel with conditioned media obtained from representative transfected hDFbs cultures for 3 and 7 days. Control corresponds to hDFbs non-transfected. Quantification of the number of segments present in hDMECs cultured in the presence of the described conditioned media (CM) at day 3 and 7. (ii) Quantification of the assay showed with 3-day CM, an early peak time of the formation of capillary-like structures as well a (iii) capillary-like structures retention time. Scale bar: 200 μm. Results are expressed as the mean $\pm$ standard deviation where n=3, * *p* <0.05, *** *p* <0.001, **** *p* <0.0001 in relation to control.

obtained for PEI-pVEGF conditioned media. Regarding COL-ChS and GG-HyA, the significant early peaks and increased number of segments in relation to control occur with the 7-day conditioned media.

Taken together, the results showed higher amounts of VEGF were obtained with PEI-pVEGF 7 days post-transfection while significant higher FGF-2 content was detected in transfected cells 3 days post-transfection. Both these conditions led to a faster formation of capillary-like structures with higher number of segments that were retained for longer periods of time. The dual combination (P+C) showed a downregulation of the production of VEGF and an upregulation of FGF-2. However, the formation of capillary-like structures was also faster than the control and a high number of segments were formed.

V-4. DISCUSSION

Growth factors in the form of recombinant proteins have been increasingly used in biomaterial-based strategies to promote vascularization [35–39]. However, the limitations associated with protein delivery, such as high cost, bolus release of proteins, short half-life, and the requirement of high doses to achieve a therapeutic effect [40,41] hinder further developments. Gene therapy might serve as an alternative approach where improved therapeutic responses might be attained due to the sustained protein production over an extended time frame by gene transfected cells. However, the field of gene therapy is typically challenged by the complex regulatory environment with using viral vectors and lack of efficacy with non-viral vectors. We have been working to overcome the challenges with the latter and have shown that when combining transfected cells with scaffolds, besides supporting cell adhesion and proliferation, the scaffold will act to retain the target protein at the site for longer, delaying clearance [19]. Therefore, the hypothesis of this study was that transfected human dermal fibroblasts (hDFbs)-laden scaffolds have their angiogenic capacity maximized through the release of angiogenic factors by the transfected cells. hDFbs were transfected with pro-angiogenic genes, pVEGF and pFGF2, and the effect of these systems on the production of angiogenic factors and formation of vascular-like networks was analysed. VEGF is

required for survival, differentiation, and formation of networks by endothelial cells [42], while FGF-2 promotes the endothelial cells sprouting, required at the first steps of the angiogenesis process, also promoting cell-cell interactions required for vessel maturation [43,44]. Since no ideal vector for hDFbs gene transfer had been reported so far, two different gene delivery systems using Ch or PEI were evaluated [19,22].

Ch- and PEI-pDNA nanoparticles were produced using optimal N/P ratios (N/P 10 for Ch and N/P 7 for PEI) and pDNA doses (0.33 μg and 2 μg, respectively). It was already reported for MSCs that Ch-pDNA formulations do not cause a decrease on cell viability whereas with PEI-pDNA a drop of 40 % in the cytotoxicity is obtained [19]. In this present study, none of the Ch-pDNA formulations lead to a decrease in cell viability. Moreover, the metabolic activity of Ch-pDNA formulations from day 10-onward increased 2-fold in relation to control. Interestingly, impairment in cell proliferation was observed for cells transfected with these Ch nanoparticles. Despite the complexion efficiency being over 97 % for both plasmids with Ch, around 3 % of the vectors and plasmids were not complexed. Therefore, while vectors or plasmids delivered alone showed no cytotoxicity, the decrease in DNA content could be caused by the effect of the non-complexed non-viral vector or naked plasmid [21]. On the other hand, PEI–pDNA polyplexes caused cell death in the pVEGF formulation, but did not significantly affected DNA content when compared to control up to 10 days, in agreement with previously published works [19,21].

When comparing the different non-viral vectors and their transfection efficiency, the results described herein showed that transfected hDFbs were able to maintain a transient gene expression up to 14 days. However, a lower transfection efficiency of hDFbs (15 % for PEI and 18 % for Ch) was obtained in comparison to what was previously demonstrated for MSCs, where transfection efficiency with Ch-pDNA was approximately 45 % [19,45] and 30 % with PEI-pDNA [21]. Moreover, the Ch-pDNA formulation resulted in a more efficient transgene expression at a lower pDNA dose compared to that of the PEI-pDNA formulation. It has been shown that relatively low transfection efficiencies can facilitate sufficient protein to yield the system functional [46]. For example, Curtin *et al* (2012) developed a non-viral vector system for bone tissue engineering using nano-hydroxyapatite that had a transfection efficiency of 11 % in MSCs [46]. However, in the same study, when compared to other non-viral vectors with higher transfection efficiencies, the nano-hydroxyapatite-pDNA system produced more BMP-2 protein and consequentially led to higher levels of MSC-mediated osteogenesis *in vitro* [46] and enhanced bone repair in an *in vivo* study [16]. In our study, the results show that the production of VEGF and FGF-2 by transfected hDFbs, despite the relatively low transfection efficiency, was translated to enhanced functionality with formation

of capillary-like structures, independently of the non-viral vector used. To elucidate the effect and suitability of our system on hDMECs in a 3D microenvironment, these cells were co-cultured with transfected hDFbs in three different scaffolds: COL-HyA, COL-ChS and GG-HyA. After co-culturing the transfected hDFbs with the hDMECs, we noticed that hDMECs were adhering on the top of the hDFbs, keeping close contact with them. Interestingly, hDMECs did not adhere to the scaffold itself despite their composition (containing collagen, chondroitin sulphate or hyaluronic acid) essential for tissue remodeling and angiogenesis. The results indicate that hDMECs only started to form their extensive CD31^{+} networks after hDFbs spread throughout the scaffolds, suggesting that the ECM secreted factors released by hDFbs were required for their sprouting. This explains why in the Ch-pFGF2 and P+C conditions, the hDMECs networking is still forming, as suggested by the fact that hDFbs were still expanding in the 3D microenvironment. Despite the development of *in vitro* capillary-like structures being important for *in vivo* inosculation within a wound, in our current study, only some level of capillary-like structure formation was observed. However, we must give emphases to the importance of non-organized endothelial cells that are present in a construct. In a previous study, we showed an increase in tissue neovascularization, as well as, accelerated wound closure rate and re-epithelization, where endothelial cells, fibroblasts and keratinocytes were seeded in GG-HyA spongy-like hydrogels and implanted in a skin full-thickness wound mice model [27].

Many studies have shown that delivering VEGF or FGF-2 *via* a scaffold enhances angiogenic response *in vivo* [13,14,47]. However, due to their short half-life, the factors are degraded and/or cleared from the wound site, often before an effective dose accumulation at the target site. To address this topic, a system combining a scaffold with transfected cells would allow the sustained protein production over an extended time frame. To determine the therapeutic efficacy of our 3D system and to understanding the impact of factors released by the transfected fibroblasts on neighbor endothelial cells, we analyzed the bioactivity of the conditioned media taken from transfected hDFbs-seeded scaffolds by assessing functionality in hDMECs. In all of these systems, the higher amounts of VEGF were obtained with PEI-pVEGF 7 days post-transfection. Moreover, the conditioned media from the PEI-pVEGF led to a faster formation of capillary-like structures with higher number of segments that were retained for longer periods of time. These results were in concordance with the observations in 2D experiments, since the activity of the system was greater when pVEGF was delivered with PEI. In contrast, a significantly higher FGF-2 content was detected in transfected cells in comparison to non-transfected cells 3 days post-transfection. The amount of FGF-2 that was produced resulted in faster and earlier formation of capillary-like structures with a significant increase in the number of segments with 3-day conditioned media. The results remained consistent with the experiments carried out in 2D, where a significant higher number of segments were formed with

conditioned media from Ch-pFGF2. Interestingly, in the 3D experiments, cells transfected with pVEGF also showed higher production of the growth factor in relation to non-transfected cells. Moreover, the protein amount produced in all our 3D systems equate to mere fractions of the amount of recombinant human VEGF [48] and FGF-2 [49,50] that are routinely delivered in the clinic in order to achieve a therapeutic effect. Furthermore, we demonstrated that our platform can be successfully applied to different scaffolds, leading to maximized angiogenic capacity through the transient release of angiogenic factors by transfected hDFbs. Envisioning the immediate application of our systems as a dermal construct to support skin vascularization and regeneration, an early effect on vascularization promoting its integration is expected, as both angiogenic factors production would be beneficial to support early endothelial cell response. Moreover, the FGF-2 production up to 14 days is expected to induce fibroblast proliferation and impair the phenotypical switch of fibroblasts to myofibroblasts to achieve a less scar [51,52]. Notwithstanding, this system can also be translated into a wide variety of applications for tissue engineering and beyond, such as, pathophysiology studies, models of disease, culture systems and drug screening, or any structure where vasculature is requires for regeneration.

Considering the potential synergistic effect of VEGF and FGF-2 on neovascular formation [53–56], the concomitant delivery of pVEGF and pFGF2 (P+C) was analyzed. To our knowledge, there are no other examples of the dual delivery of pVEGF and pFGF2 within a tissue engineering scaffold. The results for the dual combination showed a downregulation of the production of VEGF and an upregulation of FGF-2. These results were not exclusive for this system, since in fact, only residual amounts of VEGF were detected when hDFbs were transfected with single Ch-pFGF2. Moreover, with single PEI-pVEGF transfections, an upregulation of FGF-2 was confirmed. This could explain why the dual combination led to a downregulation of VEGF but an upregulation of FGF-2 when compared to single transfections. These results highlighted the efficiency of the gene-activated cells but do not uphold upon the synergistic effect of VEGF and FGF-2 in the co-cultures. This could result from different pathways being used by cells to internalize the nanoparticles. PEI-pDNA polyplexes enter in the cell *via* clathrin- or caveolae-mediated endocytosis [57]. However, PEI polyplexes that are internalized *via* clathrin-mediated endocytosis are then targeted to the lysosomal compartment. Polyplexes taken up exclusively *via* caveolae do not reach this compartment and the transfection becomes more efficient [57]. Others hypothesized that only pDNA entering the cell by caveolae-mediated uptake of the polyplexes escapes the lysosomal destination and can become transfection-effective [57], despite the consensus that PEI polyplexes are taken up by the two mechanisms [58]. Interestingly, Ch-pDNA are reported to enter cells only *via* the caveolae route of endocytosis [59]. By negatively attracting charged ions into the endosome, they cause rupture of this

biological compartment enabling the release of the polyplexes into the cytoplasm, a mechanism called "proton-sponge" effect [60–62]. Since both pDNA complexes with non-viral vectors can enter cells *via* caveolae-mediated endocytosis, we assume that cells are prioritizing Ch-pDNA nanoparticles due to their lower size (~109 nm vs ~150 nm) which leads to almost non-production of VEGF and the upper-regulation of FGF-2. These results suggest that future strategies could involve the separate transfection of each vector followed by seeding on the same scaffold thus increasing its yield.

In summary, hDFbs were successfully transfected with Ch- and PEI-pDNA. Despite low transfection efficiency, an increased production of functional VEGF and FGF-2 was obtained with almost no impairment in cell metabolic activity. Moreover, those studies also showed that in order to have a superior VEGF and FGF-2 transgene expression and thus formation of capillary-like structures, pVEGF should be delivered with PEI and pFGF2 with Ch. Furthermore, co-culture of hDMECs and transfected hDFbs comprising PEI-pVEGF (P), Ch-pFGF2 (C) or the combination (P+C) in the scaffolds showed formation of an extensive endothelial cell network in non-transfected and PEI-pVEGF transfected hDFbs conditions. However, when evaluating the overall effect of the system in an external assay with hDMECs that were not directly in contact with transfected hDFbs, greater, faster and higher retention time of thee formed capillary-like structures were observed when VEGF and FGF-2 were delivered and produced separately when compared to non-transfected and P+C conditions. We believe that these cell-laden matrices offer a novel, selective and alternative approach to developed vascularized tissue engineered constructs, providing also a new set of tools for pathophysiology studies, models of disease, culture systems and drug screening. The next step will be to evaluate their performance in an *in vivo* model.

V-5.   REFERENCES

1   Mitchell GM, Morrison WA. *In vitro* and *In vivo* Approaches for Pre-vascularization of 3-Dimensional Engineered Tissues. In: Vascularization for Tissue Engineering and Regenerative Medicine. (2017).

2   Rouwkema J, Rivron NC, van Blitterswijk CA. Vascularization in tissue engineering. Trends Biotechnol. 26(8), 434–441 (2008).

3   Lovett M, Lee K, Edwards A, Kaplan DL. Vascularization strategies for tissue engineering. Tissue Eng. Part B. Rev. 15(3), 353–70 (2009).

4   Sun X, Altalhi W, Nunes SS. Vascularization strategies of engineered tissues and their application in cardiac regeneration. Adv. Drug Deliv. Rev. 96, 183–194 (2016).

5   da Silva LP, Pirraco RP, Santos TC *et al*. Neovascularization Induced by the Hyaluronic Acid-Based Spongy-Like Hydrogels Degradation Products. ACS Appl. Mater. Interfaces 8(49), 33464–33474 (2016).

6   Yang G, Mahadik B, Choi JY, Fisher JP. Vascularization in tissue engineering: fundamentals and state-of-art. Prog. Biomed. Eng. 2(1), 012002 (2020).

7   Montesano R, Pepper MS, Orci L. Paracrine induction of angiogenesis *in vitro* by Swiss 3T3 fibroblasts. J. Cell Sci. 105(4), 1013–24 (1993).

8   Velazquez OC, Snyder R, Liu ZJ, Fairman RM, Herlyn M. Fibroblast-dependent differentiation of human microvascular endothelial cells into capillary-like 3-dimensional networks. FASEB J. 16(10), 1316–8 (2002).

9   Martin TA, Harding KG, Jiang WG. Regulation of angiogenesis and endothelial cell motility by matrix-bound fibroblasts. Angiogenesis 3(1), 69–76 (1999).

10   Cross MJ, Claesson-Welsh L. FGF and VEGF function in angiogenesis: Signalling pathways, biological responses and therapeutic inhibition. Trends Pharmacol. Sci. 22(4), 201–7 (2001).

11   Newman AC, Nakatsu MN, Chou W, Gershon PD, Hughes CCWW. The requirement for fibroblasts in angiogenesis: Fibroblast-derived matrix proteins are essential for endothelial cell lumen formation. Mol. Biol. Cell 22(20), 3791–800 (2011).

12   Cam C, Zhu S, Truong NF, Scumpia PO, Segura T. Systematic evaluation of natural scaffolds in cutaneous wound healing. J. Mater. Chem. B 3, 7986–7992 (2015).

13   Wilcke I, Lohmeyer JAJ, Liu S *et al*. VEGF165 and bFGF protein-based therapy in a slow release system to improve angiogenesis in a bioartificial dermal substitute *in vitro* and *in vivo*. Langenbeck's Arch. Surg. 392(3), 305–14 (2007).

14   Li W, Lan Y, Guo R *et al*. *In vitro* and *in vivo* evaluation of a novel collagen/cellulose nanocrystals scaffold for achieving the sustained release of basic fibroblast growth factor. J. Biomater. Appl. 29(6), 882–893 (2015).

15   Liu Q, Huang Y, Lan Y *et al*. Acceleration of skin regeneration in full-thickness burns by incorporation of bFGF-loaded alginate microspheres into a CMCS–PVA hydrogel. J. Tissue Eng. Regen. Med. 11(5), 1562–1573 (2017).

16   Curtin CM, Tierney EG, Mcsorley K, Cryan SA, Duffy GP, O'Brien FJ. Combinatorial gene therapy

accelerates bone regeneration: Non-viral dual delivery of VEGF and BMP2 in a collagen-nanohydroxyapatite scaffold. Adv. Healthc. Mater. 4(2), 223–7 (2015).

17   Lugano R, Ramachandran M, Dimberg A. Tumor angiogenesis: causes, consequences, challenges and opportunities. Cell. Mol. Life Sci. 77(9), 1745–1770 (2019).

18   Kim J, Mirando AC, Popel AS, Green JJ. Gene delivery nanoparticles to modulate angiogenesis. Adv. Drug Deliv. Rev. 119, 20–43 (2017).

19   Raftery RM, Tierney EG, Curtin CM, Cryan S-AA, O'Brien FJ. Development of a gene-activated scaffold platform for tissue engineering applications using chitosan-pDNA nanoparticles on collagen-based scaffolds. J. Control. Release 210, 84–94 (2015).

20   Raftery RM, Mencía Castaño I, Chen G *et al.* Translating the role of osteogenic-angiogenic coupling in bone formation: Highly efficient chitosan-pDNA activated scaffolds can accelerate bone regeneration in critical-sized bone defects. Biomaterials 149, 116–127 (2017).

21   Tierney EG, Duffy GP, Hibbitts AJ, Cryan SA, O'Brien FJ. The development of non-viral gene-activated matrices for bone regeneration using polyethyleneimine (PEI) and collagen-based scaffolds. J. Control. Release 158(2), 304–311 (2012).

22   Tierney EG, McSorley K, Hastings CL *et al.* High levels of ephrinB2 over-expression increases the osteogenic differentiation of human mesenchymal stem cells and promotes enhanced cell mediated mineralisation in a polyethyleneimine-ephrinB2 gene-activated matrix. J. Control. Release 165(3), 173–82 (2013).

23   O'Brien FJ, Harley B a., Yannas I V., Gibson L. Influence of freezing rate on pore structure in freeze-dried collagen-GAG scaffolds. Biomaterials 25(6), 1077–1086 (2004).

24   O'Brien FJ, Harley BA, Yannas I V., Gibson LJ. The effect of pore size on cell adhesion in collagen-GAG scaffolds. Biomaterials 26(4), 433–441 (2005).

25   da Silva LP, Cerqueira MT, Sousa R a., Reis RL, Correlo VM, Marques AP. Engineering cell-adhesive gellan gum spongy-like hydrogels for regenerative medicine purposes. Acta Biomater. 10, 4787–4797 (2014).

26   da Silva LP, Cerqueira MT, de Sousa RPRA, Marques AMP, da Silva VMC, dos Reis RLG. WO2014167513 (A1) (2014).

27   Cerqueira MT, Da Silva LP, Santos TC *et al.* Human skin cell fractions fail to self-organize within

a gellan gum/hyaluronic acid matrix but positively influence early wound healing. Tissue Eng. - Part A 20(9–10), 1369–78 (2014).

28   Matsiko A, Levingstone TJ, O'Brien FJ, Gleeson JP. Addition of hyaluronic acid improves cellular infiltration and promotes early-stage chondrogenesis in a collagen-based scaffold for cartilage tissue engineering. J. Mech. Behav. Biomed. Mater. 11, 41–52 (2012).

29   Pardue EL, Ibrahim S, Ramamurthi A. Role of hyaluronan in angiogenesis and its utility to angiogenic tissue engineering. Organogenesis 4(4), 203–14 (2008).

30   Sambrook J, Fritsch EF, Maniatis T. Molecular Cloning. A laboratory manual. Cold Spring Harbor Laboratory (1989).

31   Lepecq JB, Paoletti C. A fluorescent complex between ethidium bromide and nucleic acids. Physical-Chemical characterization. J. Mol. Biol. 27(1), 87–106 (1967).

32   Cerqueira MT, Da Silva LP, Santos TC *et al*. Gellan gum-hyaluronic acid spongy-like hydrogels and cells from adipose tissue synergize promoting neoskin vascularization. ACS Appl. Mater. Interfaces 6(22), 19668–79 (2014).

33   da Silva LP, Jha AK, Correlo VM, Marques AP, Reis RL, Healy KE. Gellan Gum Hydrogels with Enzyme-Sensitive Biodegradation and Endothelial Cell Biorecognition Sites. Adv. Healthc. Mater. 7(5), 1700686 (2018).

34   Carpentier G, Martinelli M, Courty J, Cascone I. Angiogenesis Analyzer for ImageJ. 4th ImageJ User Dev. Conf. 198–201 (2012).

35   Park JW, Hwang SR, Yoon I-SS. Advanced Growth Factor Delivery Systems in Wound Management and Skin Regeneration. Molecules 22(8), 1259 (2017).

36   Yu A, Niiyama H, Kondo S, Yamamoto A, Suzuki R, Kuroyanagi Y. Wound dressing composed of hyaluronic acid and collagen containing EGF or bFGF: Comparative culture study. J. Biomater. Sci. Polym. Ed. 24(8), 1015–26 (2013).

37   Mittermayr R, Morton T, Hofmann M, Helgerson S, Van Griensven M, Redl H. Sustained (rh)VEGF165 release from a sprayed fibrin biomatrix induces angiogenesis, up-regulation of endogenous VEGF-R2, and reduces ischemic flap necrosis. Wound Repair Regen. 16(4), 542–50 (2008).

38   Mizuno K, Yamamura K, Yano K *et al*. Effect of chitosan film containing basic fibroblast growth

factor on wound healing in genetically diabetic mice. J. Biomed. Mater. Res. - Part A 64(1), 177–81 (2003).

39   Losi P, Briganti E, Errico C *et al*. Fibrin-based scaffold incorporating VEGF- and bFGF-loaded nanoparticles stimulates wound healing in diabetic mice. Acta Biomater. 9(8), 7814–21 (2013).

40   Storrie H, Mooney DJ. Sustained delivery of plasmid DNA from polymeric scaffolds for tissue engineering. Adv. Drug Deliv. Rev. 58(4), 500–14 (2006).

41   Pack DW, Hoffman AS, Pun S, Stayton PS. Design and development of polymers for gene delivery. Nat. Rev. Drug Discov. 4(7), 581–593 (2005).

42   Kunz-Schughart LA, Schroeder JA, Wondrak M *et al*. Potential of fibroblasts to regulate the formation of three-dimensional vessel-like structures from endothelial cells *in vitro*. Am. J. Physiol. - Cell Physiol. 290(5), C1385-98 (2006).

43   Underwood PA, Bean PA, Gamble JR. Rate of endothelial expansion is controlled by cell:cell adhesion. Int. J. Biochem. Cell Biol. 34(1), 55–69 (2002).

44   Presta M, Dell'Era P, Mitola S, Moroni E, Ronca R, Rusnati M. Fibroblast growth factor/fibroblast growth factor receptor system in angiogenesis. Cytokine Growth Factor Rev. 16(2), 159–78 (2005).

45   Raftery R, O'Brien FJ, Cryan SA. Chitosan for gene delivery and orthopedic tissue engineering applications. Molecules 18(5), 5611–5647 (2013).

46   Curtin CM, Cunniffe GM, Lyons FG *et al*. Innovative collagen nano-hydroxyapatite scaffolds offer a highly efficient non-viral gene delivery platform for stem cell-mediated bone formation. Adv. Mater. 24(6), 749–54 (2012).

47   Li B, Wang H, Zhou G *et al*. VEGF-loaded biomimetic scaffolds: a promising approach to improve angiogenesis and osteogenesis in an ischemic environment. RSC Adv. 7(8), 4253–4259 (2017).

48   Hanft JR, Pollak RA, Barbul A *et al*. Phase I trial on the safety of topical rhVEGF on chronic neuropathic diabetic foot ulcers. J. Wound Care 17(1), 30–2 (2008).

49   Robson MC, Hill DP, Smith PD *et al*. Sequential cytokine therapy for pressure ulcers: Clinical and mechanistic response. Ann. Surg. 231(4), 600–611 (2000).

50   Ohura T, Nakajo T, Moriguchi T *et al*. Clinical efficacy of basic fibroblast growth factor on pressure ulcers: Case-control pairing study using a new evaluation method. Wound Repair Regen. 19(5),

542–51 (2011).

51   Tiede S, Ernst N, Bayat A, Paus R, Tronnier V, Zechel C. Basic fibroblast growth factor: A potential new therapeutic tool for the treatment of hypertrophic and keloid scars. Ann. Anat. 191(1), 33–44 (2009).

52   Akita S, Akino K, Hirano A. Basic Fibroblast Growth Factor in Scarless Wound Healing. Adv. Wound Care 2(2), 44–49 (2013).

53   Pepper MS, Ferrara N, Orci L, Montesano R. Potent synergism between vascular endothelial growth factor and basic fibroblast growth factor in the induction of angiogenesis *in vitro*. Biochem. Biophys. Res. Commun. 189(2), 824–31 (1992).

54   Goto F, Goto K, Weindel K, Folkman J. Synergistic effects of vascular endothelial growth factor and basic fibroblast growth factor on the proliferation and cord formation of bovine capillary endothelial cells within collagen gels. Lab. Investig. 69(5), 508–17 (1993).

55   Asahara T, Bauters C, Zheng LP *et al.* Synergistic effect of vascular endothelial growth factor and basic fibroblast growth factor on angiogenesis *in vivo*. Circulation 92, II365-71 (1995).

56   Kano MR, Morishita Y, Iwata C *et al.* VEGF-A and FGF-2 synergistically promote neoangiogenesis through enhancement of endogenous PDGF-B-PDGFRβ signaling. J. Cell Sci. 118(Pt 16), 3759–68 (2005).

57   Rejman J, Bragonzi A, Conese M. Role of clathrin- and caveolae-mediated endocytosis in gene transfer mediated by lipo- and polyplexes. Mol. Ther. 12(3), 468–74 (2005).

58   Bieber T, Meissner W, Kostin S, Niemann A, Elsasser HP. Intracellular route and transcriptional competence of polyethylenimine-DNA complexes. J. Control. Release 82(2–3), 441–54 (2002).

59   Garaiova Z, Strand SP, Reitan NK *et al.* Cellular uptake of DNA-chitosan nanoparticles: The role of clathrin- and caveolae-mediated pathways. Int. J. Biol. Macromol. 51(5), 1043–51 (2012).

60   Behr J-PP. The Proton Sponge: a Trick to Enter Cells the Viruses Did Not Exploit. Chimia (Aarau). 51(1–2), 34–36 (1997).

61   Liang W, W. Lam JK. Endosomal Escape Pathways for Non-Viral Nucleic Acid Delivery Systems. In: Molecular Regulation of Endocytosis. Ceresa B (Ed.), IntechOpen, (2012).

62   Raftery RM, Walsh DP, Castaño IM *et al.* Delivering Nucleic-Acid Based Nanomedicines on Biomaterial Scaffolds for Orthopedic Tissue Repair: Challenges, Progress and Future Perspectives.

Adv. Mater. 28(27), 5447–69 (2016).

V-6.   SUPPLEMENTARY FIGURES
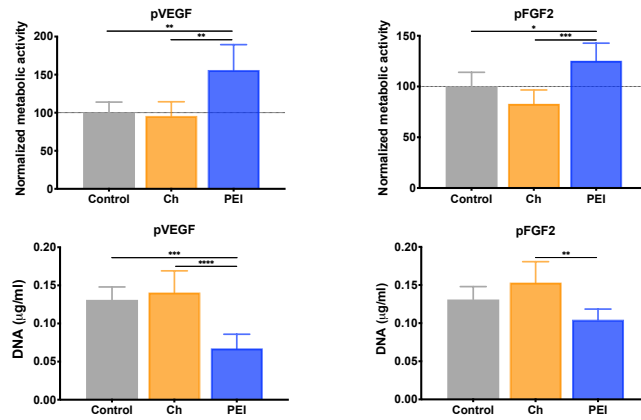
Supplementary Figure V-1 Metabolic activity and DNA quantification in transfected hDFbs immediately after the procedure.

Results are expressed as the mean ± standard deviation where n=3, * $p < 0.05$, ** $p < 0.01$, *** $p < 0.001$, **** $p < 0.0001$.
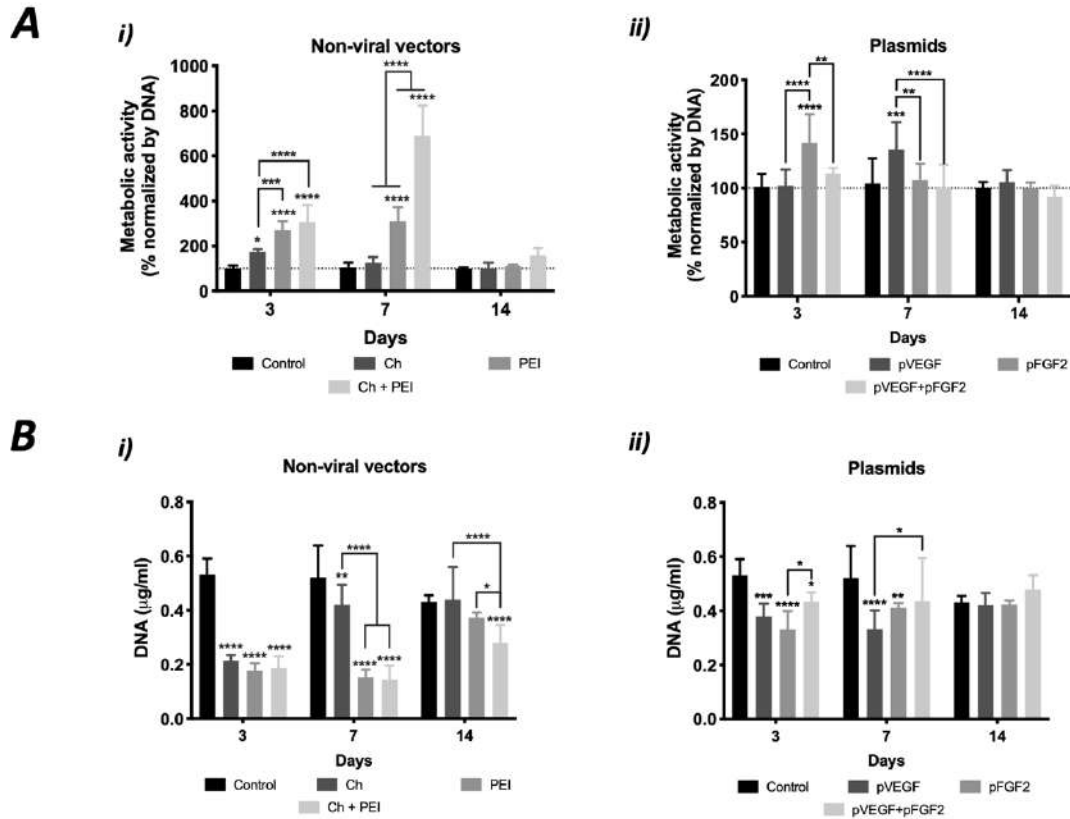
Supplementary Figure V-2 Assessment of the viability of delivering only non-viral vectors on hDFbs (i) and only plasmids (ii) on cell viability.

The amount of non-viral vector or plasmid added was the amount that did not react and was calculated from the SybrSafe exclusion assay. Control corresponds to hDFbs non transfected. Results are expressed as the mean ± standard deviation (n=3), * $p < 0.05$, ** $p < 0.01$, *** $p < 0.001$, **** $p < 0.0001$ in relation to every condition at day 3.

CHAPTER VI

INTEGRIN-SPECIFIC HYDROGELS FOR

GROWTH FACTOR-FREE VASCULOGENESIS

<div align="right">

CHAPTER VI

</div>

<div align="center">

INTEGRIN-SPECIFIC HYDROGELS FOR GROWTH FACTOR-FREE

VASCULOGENESIS [**]

</div>

ABSTRACT

Integrin-binding biomaterials have been extensively evaluated for their capacity to enable de novo formation of capillary-like structures/vessels, ultimately supporting neovascularization *in vivo*. Yet, the role of integrins as vascular initiators in engineered materials is still not well understood. Here, we show that $\alpha v \beta 3$ integrin-specific 3D matrices were able to retain PECAM1^{+} cells from the stromal vascular fraction (SVF) of adipose tissue, triggering vasculogenesis *in vitro* in the absence of extrinsic growth factors. Our results suggest that $\alpha v \beta 3$-RGD-driven signaling in the formation of capillary like-structures prevents the activation of the caspase 8 pathway and activates the FAK/paxillin pathway, both responsible for endothelial cells (ECs) survival and migration. We also show that prevascularized $\alpha v \beta 3$ integrin-specific constructs inosculate with the host vascular system fostering *in vivo* neovascularization. Overall, this work demonstrates the ability of the biomaterial to trigger vasculogenesis in an integrin-specific manner, by activating essential pathways for EC survival and migration within a self-regulatory growth factor microenvironment. This strategy represents an improvement to current vascularization routes for Tissue Engineering constructs, potentially enhancing their clinical applicability.

VI-1.   INTRODUCTION

Vascularization of Tissue Engineering (TE) constructs is a pressing priority in the field since it is a crucial step to ensure construct viability *in vivo*. However, strategies capable of triggering controlled neotissue vascularization by vasculogenesis or angiogenesis are still elusive. Vasculogenesis is defined as the process in which blood vessels are generated in the absence of pre-existing ones [1]. During embryonic development, endothelial cells (ECs) differentiate from precursors termed angioblasts, assemble and form a de novo vascular plexus [2]. This process is orchestrated by a fine-tuned balance between different angio-regulatory growth factors [1]. In TE and regenerative medicine, biomaterials have been extensively evaluated regarding their capacity to support vasculogenesis [3,4]. Due to the recognition of biological cues by cell integrins, peptide-functionalized matrices have been used to independently promote adhesion of different cell types, including ECs. Functionalized peptide hydrogels with binding affinity for $\alpha v\beta 3/\alpha 5\beta 1$ integrins, for instance, support ECs survival and stimulate tube-like structure formation *in vitro* [5]. Others showed that ECs adhesion, migration, proliferation *in vitro* and neovascularization *in vivo* was attained faster when cells specifically recognized $\alpha 4\beta 1$ integrin-binding sites in functionalized scaffolds [6]. While it is assumed that integrins at the cell membrane are involved in these interactions with the biomaterials, a fundamental understanding of their engagement as vasculogenesis initiators is lacking.

Integrins such as $\beta 1$ and $\beta 3$, have been implicated in vasculogenesis. For instance, while loss of $\beta 1$ integrin in nascent endothelium results in a disruption of ECs polarity and lumen formation [7], inhibition of $\beta 3$ integrin resulted in reduced migration, polarization and proliferation of ECs [8]. Moreover, $\beta 1$ and $\beta 3$ integrins are known to be indispensable for proper expression of VE-cadherin and therefore for tight cell–cell junction integrity, critical for generating non-leaky blood vessels [9,10]. Also, integrin $\beta 1$-deficient vascular smooth muscle cells compromise the recruitment of mural cells for vessel stabilization leading to postnatal lethality in mice [11]. A wide variety of cells are known to highly express these integrin heterodimers and have been implicated in influencing and promoting the vasculogenic process. Such cell heterogeneity can be found in the stromal vascular fraction (SVF) of the adipose tissue [12,13]. Besides mesenchymal progenitors, the SVF comprises several other cell types including fibroblasts, pericytes, pre-adipocytes, ECs and hematopoietic cells [14–16]. This complex cellular pool present in the SVF allows for the delivery of angiogenic growth factors in a self-regulating and dynamic manner that enhances the neovascularization of ischemic tissues [13]. Moreover, this angiogenic environment allows for complex and interconnected *in vitro* capillary-like networks in the absence of extrinsic growth factors [17].

Taking into consideration the angiogenic properties of SVF cells and what is known about ECs response to peptide-modified materials, we hypothesized that integrin-specific 3D matrices are able to retain cells from the SVF capable of triggering and supporting vasculogenesis *in vitro* in the absence of extrinsic growth factors. Specific integrin engagement was confirmed as a vascular morphogenic signal within engineered matrices by activating essential pathways for EC survival and migration, in a self-regulatory growth factor microenvironment. Additionally, we provide evidence that triggering vasculogenesis *in vitro* benefits neovascularization *in vivo*, which guarantees engraftment and indicates that the proposed strategy can enhance the efficacy of TE constructs.

VI-2.   MATERIALS AND METHODS

VI-2.1.   Gellan gum (GG) chemical modifications and characterization

Gelzan powder (0.25 % w/v, Sigma, USA) was dissolved in deionized water (DI), under stirring at 90 °C. After dissolution, the temperature was lowered to room temperature (RT) and the pH adjusted to 12. Vinyl sulfone moieties (DVS, SIGMA, USA) was added in excess (molar ratio of 30:1) to the GG solution and left to react for 1 h under stirring. Gellan gum-divinyl sulfone (GGDVS) was purified by three series of precipitation in cold diethyl ether (1:5) and dialysis against DI water for 3 days at 37 °C. The purified GGDVS was freeze-dried for further use.

GGDVS was dissolved in ultra-pure (UP) water (pH 8) at RT. Thiol-cyclo-RGD peptide (RGD, Cyclo(-RGDfC), >95 % purity, GeneCust Europe) and T1 peptide (CTTSWSQCSKS, >95 % purity, GeneCust Europe) were dissolved in UP water. A peptide solution (800 µM) was added to GGDVS solution (0.25-0.5 % (w/v)) and left to react for 1 h at RT under agitation. After dissolution, GGDVS-peptide solution was dialyzed against UP water for 3 days and freeze-dried. The amount of peptide conjugated to the GGDVS polymer was quantified using micro-bicinchoninic acid assay (BCA) assay according to the manufacturers' instructions (Fisher Scientific, USA). Calibration curves were prepared with the respective peptide (ranging from 0 to 200 µg mL^{-1}), and GGDVS-RGD and GGDVS-T1 (ranging from 1 and 0.5 mg mL^{-1}) solutions.

VI-2.2. Gellan gum-based spongy-like hydrogels fabrication

GG/GGDVS-peptide spongy-like hydrogels were prepared similarly to GG spongy-like hydrogels [18–20] with modifications. A solution of GGDVS-peptide (0.25-0.5 % (w/v) with 800 μM of peptide) was prepared for 1 h at RT. Meanwhile, a GG solution (0.5-1 % (w/v)) was prepared at 90 °C for 30 min and allowed to reach 40 °C afterwards. Hydrogels were prepared by mixing the GGDVS-peptide solution with the GG solution (final concentration 400 μM). The dual peptide hydrogels were prepared by mixing, GGDVS-RGD:GGDVS-T1 solutions (1:1) with the GG solution. Hydrogels were cast into desired molds, frozen at -80 °C overnight and then freeze-dried (Telstar, Spain) for 24 h to obtain GG/GGDVS-peptide(s) dried polymeric networks. Spongy-like hydrogels were formed after rehydration of the dried polymeric networks (Supplementary Table VI-1).

VI-2.3. Micro-Computed Tomography (μ-CT)

The dried polymeric structures' microarchitecture was analyzed using a high-resolution X-ray microtomography system SkyScan 1072 scanner (SkyScan, Kontich, Belgium). Samples were scanned in high-resolution mode using a pixel size of 11.31 μm (magnification of 23.30×) and an integration time of 1.7 s. The x-ray source was set at 35 keV of energy and 215 μA of current. Representative datasets of 150 slices were transformed into a binary picture using a dynamic threshold of 45e225 (gray values) to distinguish polymer material from pore voids. Pore size and interconnectivity was obtained using CT Analyzer software (v1.5.1.5, SkyScan).

VI-2.4. Stromal vascular fraction isolation and characterization

Adipose tissue was harvested from lipoaspirates or fat tissue from skin specimens of healthy donors (IMC 20.8 – 26.8) undergoing abdominoplasties after written informed consent and under the protocol established and approved between the Ethical Committees of Hospital S. João (Porto, Portugal) (Nr 477/2020) and University of Minho (CEICVS Nr 135/2020). Adipose tissue was digested with 0.05 % (w/v) collagenase type II (Sigma, USA) under agitation for 45 min at 37 °C. Stromal vascular fraction (SVF) was obtained after filtration and centrifugation (800 g, 10 min, 4 °C). SVF pellet was re-suspended in red blood cell lysis buffer (155 mM of ammonium chloride, 12 mM of potassium bicarbonate and 0.1 mM of ethylenediaminetetraacetic acid (EDTA), all from Sigma-Aldrich, Germany) and incubated for 10

min at RT. After centrifugation (300 g, 5 min, RT), the supernatant was discarded, and the cell pellet was re-suspended for immediate use.

SVF characterization was preformed using flow cytometry regarding the expression of surface cell markers CD105, CD73, CD90, CD45, CD34, PECAM1 and CD146. Furthermore, cells were labelled with DRAQ5 (eBioscoence, USA) for nuclear staining to discern the cells of interest from any remaining erythrocytes and tissue debris (Supplementary Figure VI-1). Flow cytometry was conducted right after isolation for each biological sample. The referred antibodies (Supplementary Table VI-2) were added to $2.5x10^5$ cells, incubated according to manufacturer's concentrations for 20 min at RT, washed with PBS and resuspended in PBS with 1 % (v/v) formalin (Bio-Optica, Italy). $2x10^4$ events were acquired in a BD FACSCalibur and analyzed using the Cyflogic version1.2.1 software.

VI-2.5.   Endothelial cell isolation and culture

Human dermal microvascular endothelial cells (hDMECs) were harvested from human skin samples obtained from abdominoplasties after written informed consent and under the protocol mentioned before. Briefly, skin specimens were cut into small fragments and incubated overnight in 2.4 U mL^{-1} dispase (BD Biosciences, USA) at 4 °C. hDMECs were obtained through the filtration and centrifugation of the dispase solution. hDMECs were cultured in 0.7 % (w/v) gelatin (Sigma, USA) coated flasks with EGM-2 MV (Lonza, USA). Cells were passaged at 70-90 % confluence and used at passage 3–4.

Human Umbilical Vein Endothelial Cells (HUVECs) were purchased from Lonza (USA) and routinely cultured under the conditions defined by the company on 0.7 % (w/v) gelatin type A coated plates and EndoGRO-VEGF Complete Media Kit (Millipore, USA). Cells were passaged at 70-90 % confluence and expanded up to passage 6 for all experiments.

VI-2.6.   Peptide-integrin binding assay

SVF cells were pre-incubated with RGD peptide (100 μg, 200 μg or 600 μg) in suspension in α-MEM without FBS for 30 min at 37 °C. The amount of peptide in the supernatant was quantified using micro-BCA assay according to manufacturers' instructions and the percentage of peptide-integrin binding was determined in relation to the initial quantity.

VI-2.7. Function blocking peptide studies

SVF cells were pre-incubated with i) RGD peptide (100 μg or 200 μg) in suspension in α-MEM without FBS for 30 min at 37 °C, ii) anti-integrin αvβ3 (10 μg mL^{-1}, clone LM609, MAB1976, Millipore, Portugal) in α-MEM without FBS for 1 h at 4 °C or iii) anti-integrin αvβ3 for 1 h at 4 °C plus 7 day period in 37 °C. Afterwards, cells were seeded at a density of 1.5x10^6 cells in 6-well plates and further cultured for 7 days in complete α-MEM media before analysis of the organization of the cells.

For the hDMECs (micro ECs) and HUVECs (macro ECs), cells were pre-incubated with the same amounts of RGD peptide in their respective media without growth factors or FBS prior plating on Matrigel. Matrigel (Corning, USA) was added to 96-well plates and kept in a humidified incubator for 30 min prior seeding the hDMECs or HUVECs at a density of 1.5x10^4 cells/well. The organization of the cells into capillary-like structures was assessed after 24 h of culture in a humidified incubator at 37 °C, 5 % of CO_2.

Micrographs were taken using an Axio Observer inverted Microscope (Zeiss, Germany) with the ZEN Blue 3.2 software (Zeiss, Germany).

VI-2.8. Apoptosis assay

SVF cells were pre-incubated with RGD (100 μg) in suspension or with 100 μg mL^{-1} mitomycin C (Sigma, Portugal) as a positive control of apoptosis, prior seeding at a density of 1.5x10^6 cells/well in a 6-well plate. After 24 h, cells were collected for western blot analysis or stained with Picogreen (1:1000, Invitrogen, USA) for 20 min at RT. Nuclei images were taken using an Axio Observer inverted Microscope (Zeiss, Germany) with the ZEN Blue 3.2 software (Zeiss, Germany).

VI-2.9. Cell-laden GG/GGDVS-peptide(s) spongy-like hydrogels

A SVF cell suspension containing 1.5 x 10^6 cells was prepared in 30 μL of Minimal Essential Medium (α-MEM, Invitrogen, USA) supplemented with 10 % (v/v) fetal bovine serum (FBS, Invitrogen, USA) and 1 % (v/v) antibiotic/antimycotic solution (Invitrogen, USA) and dispensed dropwise on the top of the dried polymeric networks. Constructs were incubated for 30 min, at 37 °C, 5% CO_2 to allow maximum cell entrapment within the structures and then fresh medium was added up to a total volume of 1 mL. For the function blocking peptide study, SVF cells were pre-incubated with RGD (100 μg) or T1 (200 μg) in suspension prior seeding.

VI-2.10. Total RNA extraction and cDNA synthesis

Constructs were collected in Tri-reagent (400 μL, Sigma-Aldrich, Portugal) and preserved at −80 °C. For RNA extraction, samples were thawed, and chloroform (80 μL, Sigma-Aldrich, Portugal) was added. Following an incubation period of 15 min at RT, samples were centrifuged at 4 °C for 20 min at 12000 rpm. The aqueous phase was then collected and isopropanol (200 μL, VWR, Portugal) were added. Samples were further incubated for 10 min at RT and then centrifuged at 4 °C for 10 min at 12000 rpm. The supernatants were discarded, and the pellets were washed once with 100 % ethanol and twice with 70 % ethanol, by centrifugation at 4 °C for 5 min each at 12000 rpm. Extracted RNA was kept in RNAse/DNAse free water (10 μL, Lonza, Belgium).

RNA quantity and purity were assessed using a NanoDrop N-1000 Spectrophotometer (Thermo Fischer Scientific, USA). Samples with a 260/280 nm ratio between 1.6 and 2.2 were used for cDNA synthesis. Synthesis was performed using a QSCript cDNA SuperMix (Quanta Biosciences, USA) and a Reverse Transcription Polymerase Chain Reaction (RT-PCR) Mastercycler (Eppendorf, Germany). An initial amount of 1 μg of RNA in RNAse/DNAse free water was used for a total volume of 20 μL.

VI-2.11. Quantitative Real-Time PCR (qPCR)

qPCR was used to detect the expression of vasculogenesis-associated genes (Supplementary Table VI-3). Candidate primers and the reference beta-2 microglobulin (β2M) genes were designed using the Primer-Blast database (NCBI, USA). For qPCR reactions, synthesized cDNA (1 μL) was used in a 20 μL reaction containing PerfeCTa® SYBR Green FastMix (10 μL, Quanta Biosciences, USA) and sense and antisense primers (300 nM) using a MasterCycler Realplex4 (Eppendorf, Germany). Reaction conditions comprised an initial 2 min denaturation step at 95 °C, followed by 45 cycles of 95 °C denaturation for 10 s, a 30 s annealing step at the required temperature (Supplementary Table VI-3) and a 10 s elongation step at 72 °C. Transcripts abundances were normalized to the expression of β2M. Samples were run in triplicate in each assay. Normalized expression values were calculated following the mathematical model proposed by Pfaffl using the formula: $2^{-\Delta\Delta_{ct}}$ [21].

VI-2.12. Western blot

Cell-laden spongy-like hydrogels were collected in loading buffer (0.05 % (w/v) bromophenol blue, glycerol (30 % (v/v)), 5 M ethylenediamine tetraacetic acid solution (EDTA), NaOH solution, 6 % (w/v)

SDS and 1.875 M Tris pH 8.8 solution) and 1 % (v/v) Dithiothreitol, all from Sigma-Aldrich (Portugal). Samples were macerated and denatured for 1 h at 65 °C. For SDS-PAGE, 30 μL equivalents of each sample were loaded in a 4-8 % and 4-14 % SDS polyacrylamide gel (Sigma-Aldrich, Portugal) and subsequently transferred onto a nitrocellulose membrane (GE Healthcare, UK). For the identification of the proteins of interest, unspecific staining was blocked with 4 % (w/v) bovine serum albumin (BSA) solution in tris-buffered saline with 0.1 % (v/v) tween 20 (TBST) for 90 min. The blot was incubated overnight at 4 °C with different antibodies (Supplementary Table VI-4) and with a rabbit polyclonal GAPDH antibody (1:10000, loading control, Abcam, UK). The bound antibodies were detected with an anti-rabbit/mouse IR680/800Cw secondary antibody (1:15000, Sigma-Aldrich, Portugal) after 1 h incubation. Proteins were visualized in the 700 or 800 channel of an Odyssey Fc Imaging System (LI-COR, US). Bands were imaged and quantified using the Image Studio Software (LI-COR, US). All blots and gels derived from the same experiment and were processed in parallel.

VI-2.13. Enzyme-linked immunosorbent assay (ELISA)

The levels of vascular endothelial growth factor (VEGF) and basic fibroblast growth factor (FGF-2) secreted by the SVF cells in the spongy-like hydrogels were quantified by ELISA assays (R&D Systems, UK) after 7 days of culture. Assays were carried out according to the manufacturer's instructions and the absorbance of each sample was read at 450 nm using a Synergy HT plate reader (BioTek, USA). The quantity of VEGF and FGF-2 protein was determined against a standard curve.

VI-2.14. Immunocytochemistry

Cell-laden spongy-like hydrogels were fixed with 10 % (v/v) formalin for 24 h at RT and then incubated with 0.2 % (v/v) Triton X-100 (Sigma-Aldrich, Portugal) for 30 min at RT for cell permeabilization. Afterwards, samples were blocked with 3 % (w/v) BSA for 1 h and then incubated with anti-human primary antibodies (Supplementary Table VI-5) diluted in 1 % (w/v) BSA solution in PBS overnight at 4 °C. After washing with PBS, samples were incubated for 1 h at RT with the secondary antibody Alexa Fluor 488 donkey anti-mouse (Life Technologies, CA, USA) at a dilution of 1:500 in 1 % (w/v) BSA solution in PBS. Nuclei were counter-stained with DAPI. Constructs were observed using a Leica TCS SP8 confocal microscope (Leica, Germany).

VI-2.15. *In vivo* assay

The implantation procedure was approved by the *Direcção Geral de Alimentação Veterinária* (DGAV), the Portuguese National Authority for Animal Health, and all the surgical procedures respected the national regulations and the international animal welfare rules, according to the Directive 2010/63/EU. Athymic nude mice NU(NCr)-Foxn1nu (Charles River, France), 6 weeks old, were used. One full thickness wound with a 5 mm diameter was created in the back of each mice. Animals were randomly assigned to 3 groups: A) GG/GGDVS-RGD spongy-like hydrogels – CTRL; B) GG/GGDVS-RGD spongy-like hydrogels with freshly isolated SVF cells – SVFfr; C) GG/GGDVS-RGD spongy-like hydrogels cultured for 7 days with SVF cells – SVFpv. A total of 36 animals, 6 animals *per* condition and *per* time point (5 and 28 days) were used. Mice were anaesthetized with an i.p injection of a mixture of ketamine (75mg kg^{-1}, Imalgene, Merial, France) and metedomidine (1 mg kg^{-1}, Domitor, Orion Pharma, Finland). The back of the animals was disinfected with betaisodone and 70 % ethanol and a full-thickness skin excision at approximately 0.5 cm caudal to the left scapula was performed using a 5 mm biopsy punch. A donut-shaped 5 mm silicone splint (ATOS Medical, Sweden) was glued and sutured around the wound to minimize wound contraction. After transplantation of the constructs, wounds were successively covered with Tegaderm transparent dressing (3M, USA), Omnifix (Hartmann, USA) and Leukoplast (Essity, Spain) to avoid any dislocation and to protect the whole treatment set. After surgery, atipamezole (1 mg kg^{-1}, Antisedan, Pfizer, Finland) was administered to the animals. The animals were kept separately and received daily analgesia with metamizole (200 μg g^{-1} BW, Nolotil, Boehringer Ingelheim, Germany) in the drinking water for the first 72 h. At each time-point the assigned animals were sacrificed by CO_2 inhalation and the constructs/tissue were explanted for histological analysis.

VI-2.16. Histological analysis

Explanted tissue was fixed in 10 % (v/v) formalin, dehydrated, embedded in paraffin (Thermo Scientific, USA) and cut into 4.5 μm sections. Tissue sections were deparaffinized in xylene, re-hydrated and boiled for 5 min in Tris-EDTA buffer (10 mM Tris Base, 1 mM EDTA solution and 0.05 % (v/v) Tween 20, pH 9) for antigen retrieval. Afterwards, sections were permeabilized with 0.2 % (v/v) Triton X-100 and unspecific staining was blocked with 2.5 % (v/v) Horse Serum (Vector Labs). Primary antibodies (Supplementary Table VI-5) were incubated overnight at 4 °C. For detection, VECTASTAIN Elite ABC Kit (Vector Labs) was used according to the manufacturer's instruction. Nuclei were stained with Gill's

hematoxylin. All samples were examined under a Leica DM750 microscope, using LEICA Acquire software.

VI-2.17. Image analysis

Images of five different random fields were acquired for each condition and experiment and used for image analyses. ImageJ software was used to count the number of PECAM1+ cells, in relation to the total number of cells (DAPI), as well as to quantify the number of nodes, junctions, meshes, segments, branches and segment length of the capillary-like structures using the angiogenesis plug-in [22].

Images of six different random fields of four non-consecutive tissue sections *per* time-point and *per* animal were acquired and used to quantify the number of vessels and respective diameter. Vessels in the implantation site were quantified from the PECAM1 immunostained tissue sections. ImageJ software was used to count the vessels and measure all the vessels diameter for each image. Number of vessels is presented as an average of the counted fields and expressed as number of vessels mm^2. Vessel diameter is presented as an average of all measured vessels *per* condition and expressed in μm.

VI-2.18. Statistical analysis

Statistical analysis was performed using PRISM software, version 8.2.1 for Mac OS X (GraphPad Software Inc., San Diego, USA). Shapiro–Wilk test was performed to validate normality of data prior to statistical testing. A one-way or two-way analysis of variance (ANOVA) with a Tukey multiple comparison post-test was used to analyze the results with a normal distribution. Otherwise, data were analyzed with the Kruskal–Wallis test with Dunn's multiple comparison post-test. Significance was set to 0.05 (95 % of confidence interval). All quantitative data refer to 3 independent experiments (n=3) with at least 3 replicates in each condition in each experiment and are presented as mean ± standard deviation.

VI-3. RESULTS

VI-3.1. Integrin-specific spongy-like hydrogels modulate vasculogenesis triggering

GG spongy-like hydrogels were designed to present integrin-specific peptides to SVF cells capable of triggering vasculogenesis (**Figure VI-1a**). Using Michael type addition chemistry, GG was functionalized
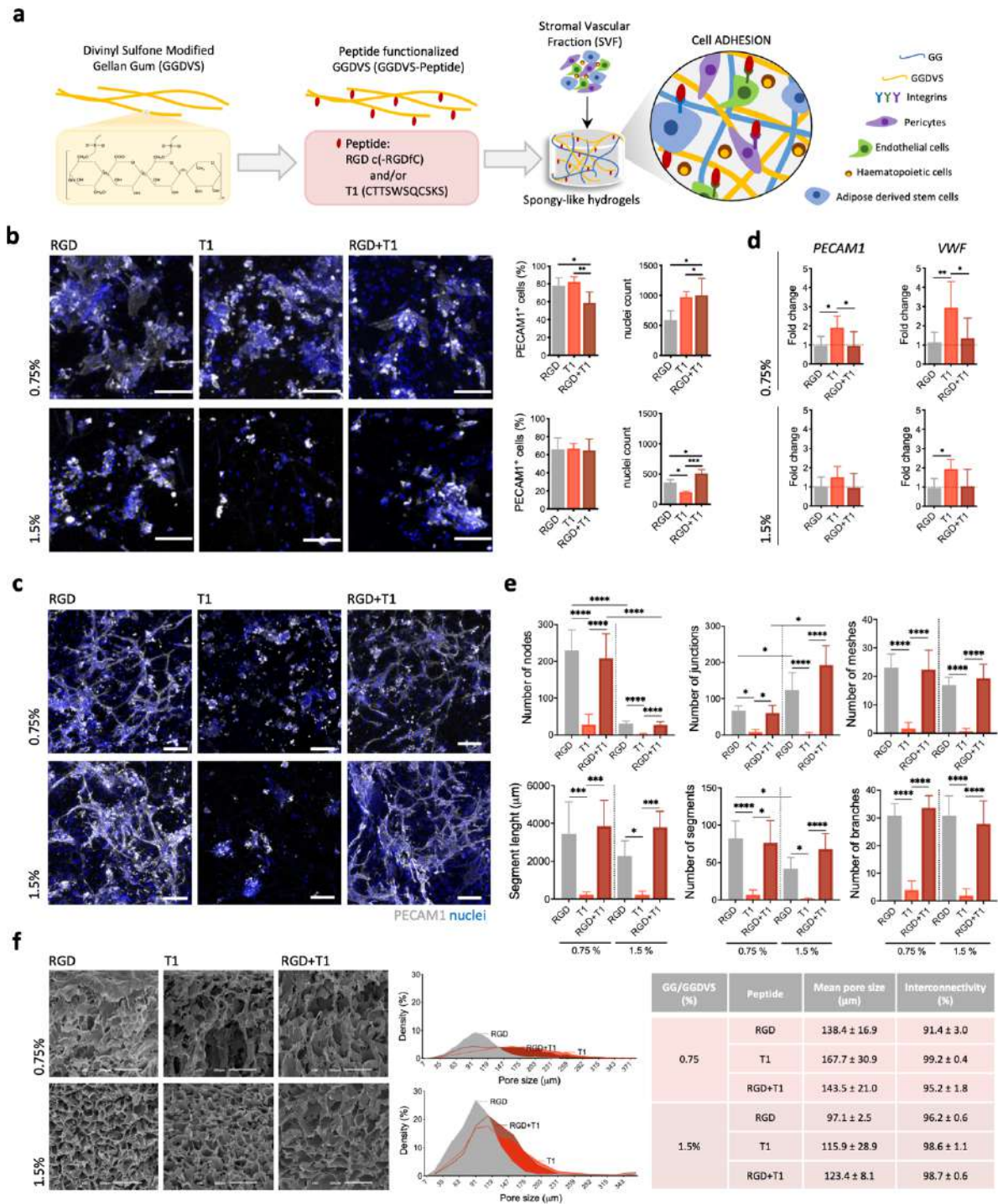
Figure VI-1 Integrin-specific spongy-like hydrogels modulate vasculogenesis triggering.
a Schematic representation of the rationale of using GGDVS functionalized with T1 and RGD peptides to capture cells involved in vasculogenesis from the stromal vascular fraction (SVF) of adipose tissue. **b** Representative immunocytochemistry images of the expression of PECAM1 in SVF cells kept in the functionalized materials after 3 days of culture and respective quantification of the percentage of PECAM1$^+$ cells and total number of cells. Scale bar = 100 μm. **c** Representative immunocytochemistry images of the organization of PECAM1$^+$ cells in the functionalized materials after 7 days of culture. Scale bar = 100 μm. **d** *PECAM1* and *VWF* mRNA expression in cells kept in the functionalized materials at day 7. mRNA expression was determined by qPCR using *β2M* as reference gene and normalized to the respective expression at day 5 to understand the variation along time for each condition. **e** Quantification of the number of nodes, junctions, meshes, segments, branches

and segments length in the capillary-like structures formed after 7 days of culture. **f** Microstructural features (pore size and interconnectivity) of GG/GGDVS-peptides dried polymeric networks visualized by SEM and quantified by μ-CT. Scale bar = 100 μm. Quantitative results are expressed as the mean ± standard deviation where n = 5, * $p < 0.05$, ** $p < 0.01$, *** $p < 0.001$, **** $p < 0.0001$, one-way or two-way ANOVA with Tukey multiple comparison post-test.

with DVS to allow the conjugation of cysteine-terminated peptides *via* reaction with the thiol group. Two peptides with different integrin binding specificities, cyclic RGD (RGD, cyclo-RGDfC) derived from fibronectin-III domain with high binding affinity for $\alpha v \beta 3$ integrin [23], and T1 (GQKCIVQTTSWSQCSKS) present in CCN1 (CYR61) III domain as an $\alpha 6 \beta 1$ integrin-binding peptide [24], were conjugated to GGDVS with >89 % conjugation efficiency (Supplementary Figure VI-2A). A formulation containing both RGD and T1 with affinity for both $\alpha v \beta 3$ and $\alpha 6 \beta 1$ integrins was also prepared. The integrin-specific spongy-like hydrogels were prepared as previously described [18], combining the GGDVS-peptide with unmodified GG at the time of hydrogel formation to form a semi-interpenetrating network (Supplementary Figure VI-2B). Two formulations with 0.75 % and 1.5 % total polymer concentration (Supplementary Table VI-1), were prepared to take into consideration the properties of the scaffolds, known to impact overall cellular behavior [20].

Vasculogenic cells, such as endothelial progenitor and endothelial cells, highly express $\alpha 6 \beta 1$ integrin and $\alpha v \beta 3$ integrin [25,26]. The populations retained in our spongy-like hydrogels are enriched in those cells, present in the SVF (Supplementary Figure VI-3), as demonstrated by the number of PECAM1+ cells (**Figure VI-1b**). After 3 days of culture, 80 % (0.75 % spongy) and 60 % (1.5 % spongy) of the captured cells were PECAM1+, for both RGD- and T1-presenting spongy-like hydrogels. Moreover, the simultaneous presentation of RGD and T1 led to a significantly lower percentage of PECAM1+ captured cells (60 %) in comparison with single peptide-presenting materials, although only for those with lower concentration of polymer. Interestingly, these results are independent of the total number of cells within each material since the total number of nuclei counts was significantly higher in the RGD+T1-presenting spongy-like hydrogels than in the RGD and T1 counterparts. Moreover, while the number of PECAM1+ cells is similar in RGD- and T1-presenting spongy-like hydrogels, the total number of cells decreases with increased polymer concentration.

Knowing that $\alpha v \beta 3$ has a key role in EC survival, migration, and differentiation [27], and that the activation of $\alpha 6 \beta 1$ regulates endothelial tube formation [28], we next assessed the ability of our integrin-specific spongy-like hydrogels to support SVF-derived ECs organization and formation of capillary-like structures in the absence of extrinsic angiogenic growth factors. The presence of PECAM1+ capillary-like structures was only observed in the RGD- or RGD+T1-containing materials (**Figure VI-1c**). The SVF cells in

the T1-containing materials tended to cluster in roundish aggregates, similarly to what is observed in the control materials without peptide (**Figure VI-1c**, Supplementary Figure VI-4A). Interestingly, the expression of *PECAM1* and *VWF* was upregulated in the cells adhered to the T1-containing materials at day 7 (**Figure VI-1d**, Supplementary Figure VI-4B). The analysis of the capillary-like structures showed that the number of nodes, junctions, meshes, segments, branches and segment length was significantly higher in the RGD-containing spongy-like hydrogels than in the T1 materials (**Figure VI-1e**, Supplementary Figure VI-5). No differences were observed between RGD- and RGD+T1-modified materials, regardless of the polymer concentration. Nonetheless, the number of nodes and junctions respectively diminished and increased in the RGD and RGD+T1 with higher polymer concentration. This might be related with a higher small pore density within the materials with higher polymer amount (**Figure VI-1f**), potentially enclosing higher cell densities at specific areas fostering the formation of junctions (four or more segments) rather than new nodes (three or more segments connected) formation.

Since VEGF and FGF-2 pathways are key in promoting ECs migration and proliferation during vasculogenesis, we looked at the gene expression of *VEGF*, *FGF2* and respective receptors, *KDR* and FGF receptor (*FGFR*) 1 and 2 to assess their involvement in the response to the functionalized materials. In RGD-containing materials where capillary-like structures were able to form, the angiogenic genes *VEGF* and *FGF2* were expressed in higher amounts than in T1-containing materials. In opposition, the respective receptors, *KDR* and *FGFR2*, but not *FGFR1*, were upregulated for the T1-containing materials (**Figure VI-2a**). Both *FGF2* and *FGFR2* were downregulated in relation to the control material without peptide.

When the RGD-containing materials were kept in culture over 14 days, the capillary-like structures formed an intricate network within the whole structure in which lumens were clearly identified (**Figure VI-2b**, Supplementary Figure VI-6). Considering that the SVF also contains stromal cells capable of acting as mural cells, we then analyzed changes in the expression of angiopoietin 1 (*ANGPT1*) and its receptor (Tyrosine-protein kinase receptor, *TEK*) (**Figure VI-2b**), known to be involved in pericyte recruitment and vessel maturation [29,30]. The expression of both *ANGPT1* and *TEK* was higher in the T1-containing materials, and the presence of RGD did not involve alterations in the expression of the *TEK* in comparison with the controls without peptides. These results were independent of polymer concentration.

Overall, our results indicate that RGD-mediated adhesion of PECAM1+ cells from the SVF triggers vasculogenesis and supports the formation and maturation of capillary-like structures *in vitro*, without the addition of extrinsic growth factors. Since the number of PECAM1+ cells was superior in RGD- than in RGD+T1-containing materials, and the survival rate of SVF cells was significantly higher in the materials
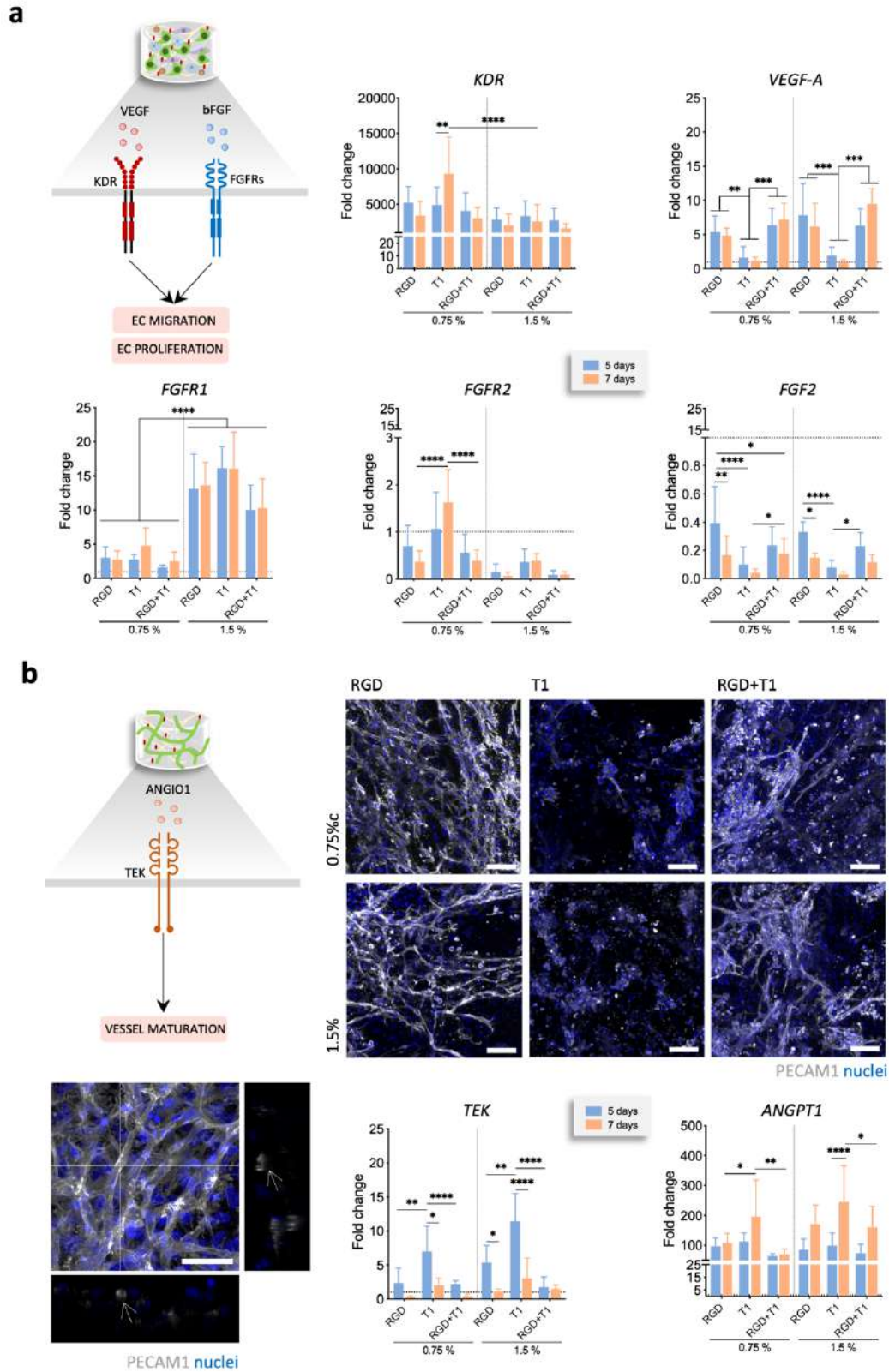
Figure VI-2 VEGF and FGF2 are involved in EC migration and proliferation that result in the formation of vascular structures.
a Schematic representation of the hypothesized involvement of VEGF and FGF2 pathways. Representative immunocytochemistry images of the organization of PECAM1⁺ cells in the functionalized materials after 14 days of culture. Scale bar = 100 μm. *KDR*, *VEGF*, *FGFR1*, *FGFR2* and *FGF2* mRNA expression in cells cultured in the functionalized materials at day 5 and 7. mRNA expression was determined by qPCR using *β2M* as reference gene and normalized to the results for

non-modified material at day 5. **b** Schematic representation of the hypothesized involvement of ANGPT1 pathway in vessel maturation. Representative immunocytochemistry images of SVF cells expressing PECAM1 in the functionalized materials after 14 days of culture. Scale bar = 100 μm. Detail of the vascular-like network formed by PECAM1·cells in the 0.75 % GG/GGDVS-RGD spongy-like hydrogel after 14 days in culture showing several lumen (white arrows). Nuclei were counter-stained with DAPI. Scale bar = 50 μm. *TEK* and *ANGPT1* mRNA expression in cells cultured in the functionalized materials at days 5 and 7. mRNA expression was determined by qPCR using *β2M* as reference gene and normalized to the results for non-modified material at day 5 to allow comparison among the conditions. Quantitative results are expressed as the mean ± standard deviation where n = 5, * *p* < 0.05, ** *p* < 0.01, *** *p* < 0.001, **** *p* < 0.0001, two-way ANOVA with Tukey multiple comparison post-test.

with lower amount of polymer, 0.75 % GG/GGDVS-RGD spongy-like hydrogels were used in the subsequent assays.

VI-3.2. Vasculogenesis in integrin-specific spongy-like hydrogels is prompted by FAK/paxillin signaling while apoptosis is prevented

Given our results confirming the triggering of vasculogenesis *in vitro* by αvβ3-specific spongy-like hydrogels, we wanted to understand the underlying mechanisms. To infer about the involvement of VEGF and FGF2 pathways during the interaction of the SVF cells' αvβ3 integrin with the RGD present in the spongy-like hydrogels, function-blocking peptide studies were carried out. When in suspension, cyclic RGD is known to act as an antagonist of its high affinity binding integrins (αvβ3, αvβ5 or αIIIβ3), leading to cell apoptosis and suppressed angiogenesis [31,32] (**Figure VI-3a**). Thus, SVF cells were incubated with RGD in suspension prior to their seeding in the RGD-containing spongy-like hydrogels. The formation of capillary-like structures in the RGD-containing spongy-like hydrogels was impaired when SVF cells were pre-incubated with RGD (**Figure VI-3b**). Moreover, the involvement of αvβ3 integrin was further confirmed by function blocking antibody studies. Vasculogenesis was completely inhibited in the presence of a function blocking antibody against αvβ3 over the course of a 7 day culture period in RGD-containing spongy-like hydrogels (**Figure VI-3b**). An inhibition of capillary-like structure formation similar to what was observed when SVF cells were pre-incubated with RGD was seen when the blocking antibody was also incubated with cells prior to seeding, suggesting partial recovery of αvβ3 expression when the blockage was removed. These results demonstrate the specificity of the SVF vasculogenic cells interaction with the materials *via* αvβ3 integrin. Moreover, we further confirmed the activation of the apoptosis cascade by caspase 8 and caspase 3 cleavage when cells were pre-incubated with RGD (**Figure VI-3c**, Supplementary Figure VI-7). The amount of RGD peptide (100 μg) was defined based on the binding efficiency (**Figure VI-3d**), as well as on the impaired capacity of the cells to form vascular-like structures in standard culture

196
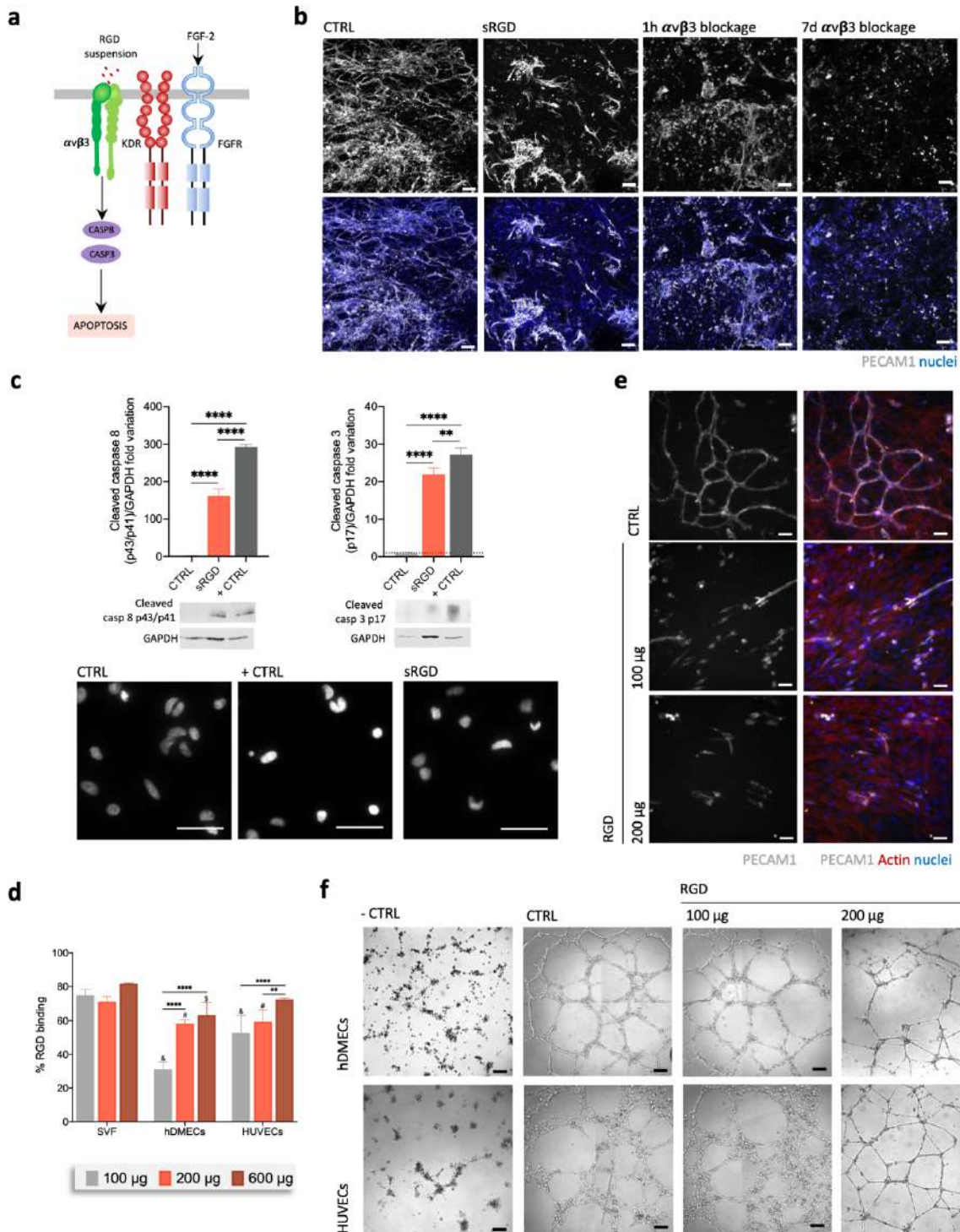
Figure VI-3 Integrin-specific spongy-like hydrogels prevent apoptosis of cells involved in the vasculogenic process.
a Schematic representation of the studied apoptosis signaling pathway. **b** Representative images of the organization of SVF
PECAM1⁻ cells after 7 days of culture in the 0.75 % GG/GGDVS-RGD when pre-incubated with RGD peptide (sRGD) or with
integrin αvβ3 blocking antibody for 1 h (1h αvβ3 blockage), or in the presence of αvβ3 blocking antibody (7d αvβ3 blockage).
Control (CTRL) refers to SVF cells directly seeded in the material. Scale bar = 100 μm. **c** Protein level of cleaved caspase 8
and cleaved caspase 3 in SVF cells 24 h after peptide exposure or mitomycin C (+ CTRL) with correspondent representative
western blot bands. Plotted western blot data was determined in relation to GAPDH expression. Representative nuclei images
from SVF cells labelled with Picogreen 24 h after exposure to RGD peptide or mitomycin C (+ CTRL). Scale bar = 50 μm. **d**

197

Percentage of RGD peptide binding to SVF cells, hDMECs and HUVECs after 30 min incubation. **e** Representative images of the organization of PECAM1· SVF cells pre-incubated with different amounts of the RGD peptide and cultured on standard 2D surfaces for 7 days. Scale bar = 50 μm. **f** Representative images of hDMECs and HUVECs in a Matrigel assay, pre-incubated with different amounts of the RGD peptide or in their respective basal media without any angiogenic growth factors (negative control (- CTRL)). In the positive control condition (+ CTRL), cells were cultured in their optimized media without pre-incubation with RGD peptide. Scale bar = 200 μm. Quantitative results are expressed as the mean ± standard deviation where n = 3, * $p < 0.05$, ** $p < 0.01$, *** $p < 0.001$, **** $p < 0.0001$, one-way ANOVA with Tukey multiple comparison post-test or Kruskal–Wallis test with Dunn's multiple comparison post-test.

surfaces (SVF) (**Figure VI-3e**) and in Matrigel (control micro and macrovascular endothelial cells) (**Figure VI-3f**). These results suggest the involvement of αvβ3 and of RGD-driven signaling in the formation of the capillary like-structures in our materials, preventing the activation of the caspase 8 pathway.

We next assessed which pathways were activated due to this integrin-ligand interaction. The focal adhesion kinase (FAK) is the main transducer of the integrin-mediated signaling pathway required for EC adhesion and motility, using paxillin as a major substrate for focal adhesion turnover during cell migration [33] (**Figure VI-4a**). When αvβ3 in SVF cells was blocked by the RGD peptide, phosphorylated FAK as well as paxillin were significantly downregulated, indicating an interference in the FAK/paxillin signaling response (**Figure VI-4b**). Moreover, no differences were found in both talin 1/2 and vinculin, which seems to confirm the lack of integrin engagement and of the subsequent formation of focal adhesion complexes that require those proteins [34,35]. Migration and survival of endothelial cells, and tube-like formation, are also regulated through signaling triggered by the crosstalk between αvβ3 integrin and KDR after VEGF binding [36–38]. In particular, the VEGF-A/KDR signaling cascade leads to the partial activation of the phosphatidylinositol 3-kinase (PI3K)/AKT and mitogen-activated protein kinase (MAPK)/extracellular-signal-regulated kinase-1/2 (ERK 1/2) signal transduction pathways [39]. The pre-incubation with RGD peptide resulted in a decreased amount of secreted VEGF, although without alteration in the expression and quantity of its receptor KDR (**Figure VI-4c**, Supplementary Figure VI-8A). Moreover, although AKT1 phosphorylation was upregulated, phospho-ERK 1/2 was not altered, which seems to indicate that VEGF signaling might be contributing at some extent to the observed response.

On the other hand, it is known that FGF-2 depends on αvβ3 integrin to initiate angiogenesis [40]. Upon binding of the FGF-2 to αvβ3 integrin, ERK1/2 phosphorylation occurs inducing EC adhesion and proliferation [41]. Moreover, when this integrin is blocked, the produced FGF-2 binds to the FGFRs which is not sufficient to induce endothelial cell proliferation [41]. The pre-incubation of SVF cells with RGD
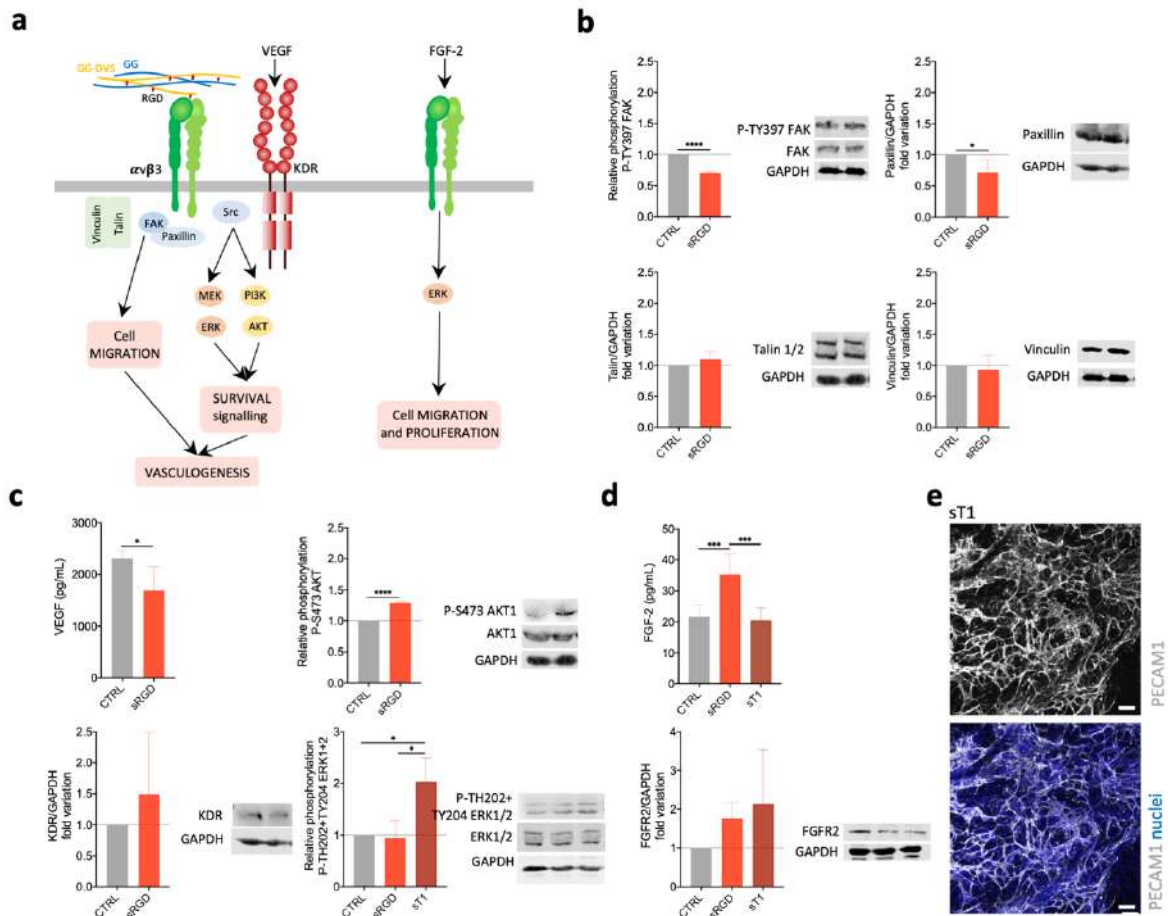
Figure VI-4 Involvement of VEGF and FGF2 pathways in the vasculogenesis in integrin-specific spongy-like hydrogels.
a Schematic representation of the studied signaling pathways. **b** Expression of P-TY397 FAK, FAK, Paxillin, Talin 1+2. **c** VEGF secretion, and KDR, P-TH202-TY204 ERK1/2, ERK1/2, P-S473 AKT1 and AKT1 expression. Expression of the proteins (B, C) was determined by western blot in SVF cells, with and without pre-incubation with RGD peptide, cultured in the 0.75 % GG/GGDVS-RGD materials for 7 days. Expression of P-TH202-TY204 ERK1/2, ERK1/2 was also determined when SVF cells were pre-incubation with T1 peptides. **d** FGF-2 secretion, and FGFR2 expression determined by western blot in SVF cells, with and without pre-incubation with RGD and T1 peptides, cultured in the 0.75 % GG/GGDVS-RGD materials for 7 days. All plotted western blot data was determined in relation to GAPDH expression. **e** Representative images of the organization of SVF PECAM1+ cells after 7 days of culture in the 0.75 % GG/GGDVS-RGD when pre-incubated with T1 peptide. Results are expressed as the mean ± standard deviation where n = 3, * $p < 0.05$, ** $p < 0.01$, *** $p < 0.001$, **** $p < 0.0001$, one-way ANOVA with Tukey multiple comparison post-test or two-tailed unpaired t test.

peptide did not influence ERK1/2 phosphorylation but resulted in an increased amount of secreted FGF-2 and FGFR2, while no differences were observed for the FGFR1 receptor (**Figure VI-4d,** Supplementary Figure VI-8A,B). In opposition, a significantly higher ERK1/2 phosphorylation (**Figure VI-4d**), accompanied by the formation of capillary-like structures (**Figure VI-4e**), was observed when SVF cells were pre-incubated with the T1 peptide which blocks the α6β1 integrins. This seems to confirm that the interaction

199

of FGF-2 with αvβ3 integrin occurs at a significantly higher level when α6β1 integrin is blocked and thus might not be predominant in triggering vasculogenesis in our materials.

VI-3.3.   Pre-formed human capillaries foster neovascularization *in vivo*

Prevascular networks have been shown to accelerate the vascularization of 3D tissue-engineered constructs and enhance their ability to anastomose with the host's vascular networks [42]. We wanted to understand if the integrin specificity of the spongy-like hydrogels would be enough to overcome the need of an *in vitro* prevascularization step to ensure *in vivo* neovascularization. For that, freshly isolated SVF cells were seeded in the material and immediately implanted (SVFfr) or cultured for 7 days *in vitro* prior to implantation (SVFpv) (**Figure VI-5a**). In the latter condition, PECAM1+ cells of the SVF were able, *in vitro*, to promote homotypic interactions through VE-cadherin and form stable capillary-like structures characterized by the presence of basement membrane proteins such as laminin and collagen type IV (**Figure VI-5b**).

Given the relevance of determining if prevascularization of the constructs contributed to a faster vascularization, we assessed the total number of vessels and vessel diameter at the implantation site as early as 5 days post-transplantation (**Figure VI-5c**, Supplementary Figure VI-9A). The number of vessels in the prevascularized group was significantly higher than in the control and non-prevascularized groups. The vessel diameter was also significantly higher than in the non-prevascularized group, but not different from the control. After 28 days of transplantation, both the number and diameter of vessels were significantly higher in the prevascularized group.

We further inquired about the fate of the human PECAM1+ cells from the SVF and their involvement in neotissue vascularization. Vessels with human PECAM1+ cells were identified in both experimental groups (**Figure VI-5d**, Supplementary Figure VI-9B) but at a significantly higher percentage in the prevascularized condition. Moreover, both chimeric and human PECAM1+ vessels contained mouse erythrocytes in their lumen (**Figure VI-5d**), evidencing the functionality of the *in vitro*-formed capillary-like structures. These results indicate that the prevascularization of the constructs was essential to foster vascularization and the connection with the host circulatory system.
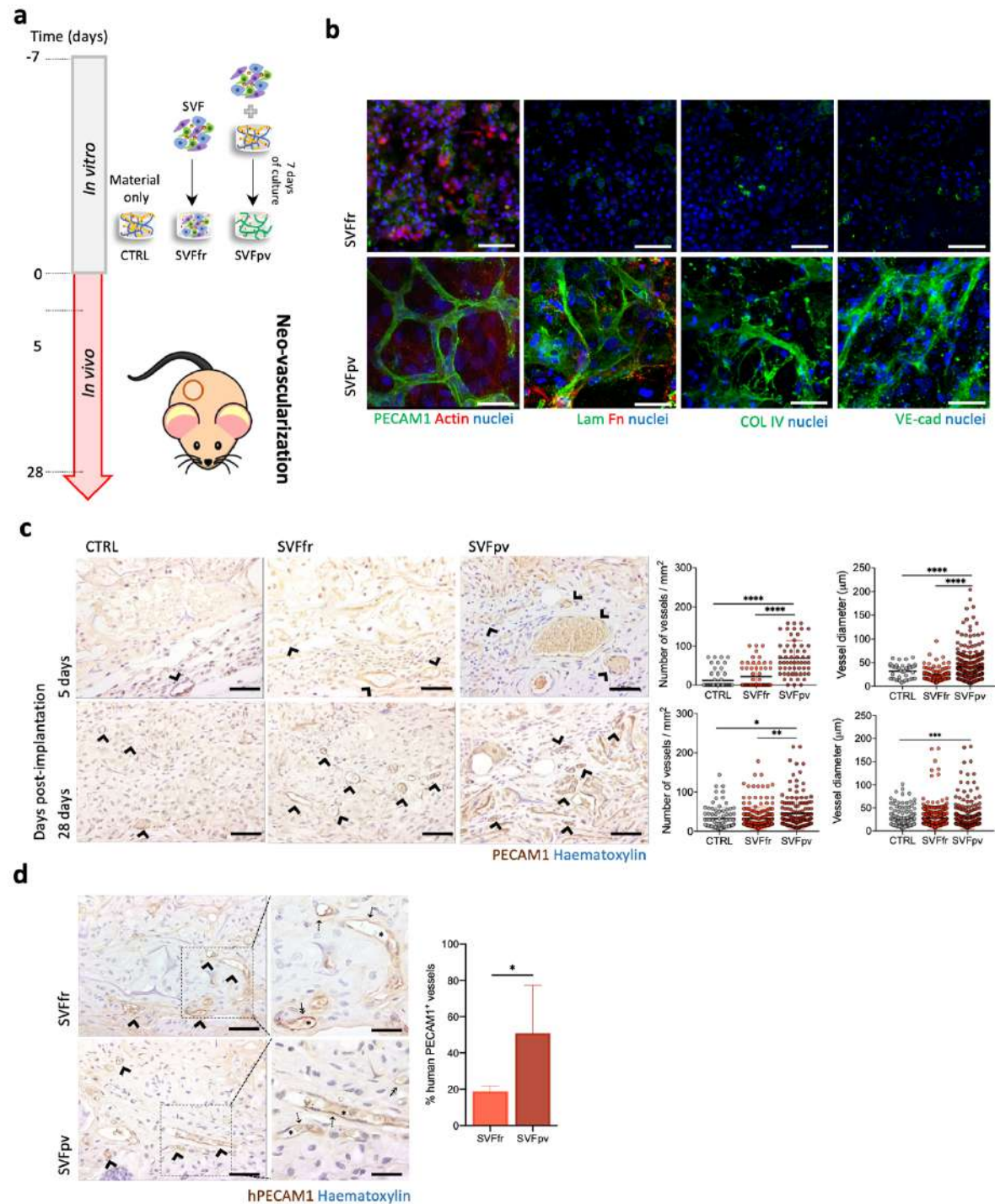
Figure VI-5 Pre-formed human capillaries foster neovascularization *in vivo*.
a Schematic representation of the test conditions: CTRL (GG/GGDVS-RGD spongy-like hydrogels without cells), SVFfr (freshly isolated SVF seeded in the material), SVFpv (SVF seeded in the material and cultured for 7 days *in vitro* prior to implantation). **b** Representative immunocytochemistry images of the expression of PECAM1 (anti-human), Collagen type IV (COL4), Laminin (Lam), Fibronectin (Fn), VE-cadherin (VE-cad) and F-actin in SVF cells seeded in the 0.75 % GG/GGDVS-RGD spongy-like hydrogels, without (SVFfr) and after 7 days of vitro pre-culture (SVFpv). Nuclei were counter-stained with DAPI (nuclei). Scale bar = 50 μm. **c** Representative immunocytochemistry images showing PECAM1·vessels (arrow head, anti-mouse and anti-human) at the transplantation site at days 5 and 28, and respective quantification of the number of vessels and diameter. Scale bar = 100 μm. **d** Representative immunocytochemistry images of vessels incorporating human PECAM1· cells (arrow

head, anti-human) at the transplantation site at day 28 and respective quantification. Higher magnification images show chimeric (↑) and human (⬆) vessels containing mouse erythrocytes (*). Scale bar = 100 μm, 50 μm. Quantitative results are expressed as the mean ± standard deviation, * $p < 0.05$, ** $p < 0.01$, *** $p < 0.001$, **** $p < 0.0001$, Kruskal–Wallis test with Dunn's multiple comparison post-test or two-tailed unpaired t test.

VI-4. DISCUSSION

Strategies towards *in vitro* vasculogenesis are a challenging and a pressing priority in TE. Biomaterials with integrin-binding specificities have been extensively evaluated for their capacity to enable de novo formation of capillary-like structures/vessels and ultimately support neovascularization, but the role of integrins as vascular initiators in engineered materials is poorly understood. Considering this, we used integrin-specific biomaterials to understand whether the response of SVF cells would be capable of triggering vasculogenesis.

Taking into consideration the knowledge on ECs responses to peptide-modified materials, different peptides targeting $\alpha v \beta 3$ and $\alpha 6 \beta 1$ integrins were used to engineer spongy-like hydrogels. In the 3D microenvironment, we showed that RGD spongy-like hydrogels ($\alpha v \beta 3$ integrin ligand), but not T1 ($\alpha 6 \beta 1$ integrin ligand), support the spontaneous formation of a microvascular network *in vitro* by SVF cells. Moreover, SVF cells response was similar in both RGD+T1 spongy-like hydrogels and RGD-only spongy-like hydrogels. This suggests that the presence of T1 peptide does not negatively interfere with the formation of the capillary-like structures. Interestingly, this formation is independent of spongy-like hydrogel's capacity to retain PECAM1+ cells from the SVF since the number of PECAM1+ cells in the RGD+T1-containing materials is significantly lower than in the other structures. Thus, it seems that the content of angiogenic cells in the SVF in conjunction with the proposed materials support a reduction of the initial cell number without compromising the triggering of the vasculogenesis, which might be beneficial in the clinical context. Moreover, considering these distinct findings, the data reported herein strongly supports the view that ECs in the SVF require binding and activation of $\alpha v \beta 3$ integrin, but not $\alpha 6 \beta 1$, to start vasculogenesis. In the presence of a function blocking antibody against $\alpha v \beta 3$ integrin the capillary-like structure formation was completely inhibited in the RGD-containing materials. When the blockage was limited to a partial time frame, some capillary-like structures were observed, suggesting some recovery of the $\alpha v \beta 3$ integrin expression along the culture. These results were further confirmed by using $\alpha v \beta 3$ integrin-specific soluble RGD peptides. Thus, while scrambled RGD experiments would further strengthen our conclusions, we believe the two types of $\alpha v \beta 3$-specific blocking studies are sufficiently demonstrative of the integrin specificity of the observed results. In addition to this, it was clear

that no capillary-like structures were observed in the T1-only materials that interact with an integrin other than αvβ3. The T1 peptide ligand, α6β1 integrin, is highly express by pericytes and PECAM1^{+} cells, the latter also expressing αvβ3 integrin [26]. This dual linkage possibility provided by T1 could be linked to the positive modulation of some of the markers (*PECAM1*, *VWF*, *FGFR2*, *TEK* and *ANGPT1*) in the T1-containing materials. However, we showed that it is the interaction of the αvβ3 integrin with the RGD present in the spongy-like hydrogels that is responsible for the capillary-like structure formation, potentially due to an effect over ECs survival and migration. Upon blocking of the αvβ3 integrin, SVF cells entered in the apoptosis cascade as demonstrated by the increase in cleaved caspase 8 and cleaved caspase 3. Considering the above we can strongly suggest that SVF PECAM1^{+} cells respond to the vasculogenic signal provided by the RGD peptide in our biomaterials. This is in agreement with what has been already observed regarding both progenitor and mature endothelial cells expressing elevated levels of αvβ3 integrin [25,26], that this integrin has a high affinity to the RGD moiety used in this study [23] and ultimately that the RGD-αvβ3 integrin interaction is key to vasculogenesis [43]. Moreover, phosphorylated FAK, the main transducer of the integrin-binding with the ECM [33], and paxillin, a signal transduction adapter protein associated with focal adhesions and one of the major substrates of FAK [44], were downregulated. Other works have shown that the downregulation of those molecules is associated with impaired ECs motility, migration and spreading [45].

The cell complexity present in the SVF allows for a self-regulating dynamic of angiogenic and vasculogenic growth factors secretion [13], including VEGF and FGF-2. Both are known to modulate vasculogenesis by promoting activation of downstream pathways associated to the αvβ3 integrin [46]. Therefore, those factors could be involved in the vasculogenesis observed in our system. When VEGF binds to KDR and the αvβ3 integrin is engaged with the ECM, αvβ3 integrin and KDR form a physical complex and synergize to regulate several cellular processes. These include maximal transduction of angiogenic growth factors, and tube formation [36–38], *via* activation of the ERK1/2 and PI3K/Akt signal transduction pathways [39,47]. Our study demonstrated that after αvβ3 integrin blockage, the production of VEGF was downregulated although without alteration in the expression of its receptor KDR. Moreover, Akt was upregulated while no differences were observed for the phosphorylation of the ERK1/2 when αvβ3 integrin was blocked. Thus, the reduced secretion of VEGF might be linked to the overall need of cells to avoid apoptosis, as previously shown with the blockage of the αvβ3 integrin in ECs [48], which in turn is in agreement with the activation of the Akt pathway, a critical regulator of PI3K-mediated cell survival [49]. While we do not demonstrate the direct involvement of VEGF, when the formation of VEGF-

dependent vessels in a co-culture of pericytes and ECs is suppressed, pericytes activate the FGF pathway and start to express high levels of FGF-2 in a juxtacrine manner [50]. Our results are in agreement with this since FGF-2, potentially produced by other SVF cells, and the receptor FGFR2 were significantly upregulated when the αvβ3 integrin was blocked. However, it is also known that FGF-2/FGFRs-mediated signaling is not sufficient to induce endothelial cell migration and binding of FGF-2 to αvβ3 integrin is necessary, promoting ERK1/2 phosphorylation [41]. The levels of phosphorylated ERK1/2 did not vary with the blocking of αvβ3 integrins in the SVF cells, despite the suppression of the formation of capillary-like structures. In opposition, when α6β1 integrins were blocked (T1 soluble peptide) this effect was reverted, and the levels of phosphorylated ERK1/2 were significantly upregulated. Therefore, our results seem to indicate that FGF-2-αvβ3 integrin interaction occurs at a significantly higher level when α6β1 integrin is blocked and thus might not be predominant in triggering the vasculogenesis in our αvβ3 integrin-specific 3D matrices. Thus, vasculogenesis in our αvβ3 integrin-specific biomaterials does not seem to be primarily linked to the self-regulating dynamic of the growth factors produced by SVF cells.

As a second goal, we wanted to validate our integrated tissue engineering approach as promoter of neovascularization by triggering vasculogenesis in the absence of extrinsic growth factors. For this, we compared prevascularized with non-prevascularized constructs in terms of engraftment and reparative activities in a skin wound healing model. The prevascular network formed in the αvβ3 integrin-specific materials is stable and mature, as shown by the presence of the basement membrane proteins and the involvement of VE-cadherin in cell-cell interaction. According to previous works [51–55], prevascular networks can lead to improved anastomosis with the host blood vessels after transplantation, promoting neotissue formation. Our results after implantation of the prevascularized materials in a full-thickness skin wound are in agreement with those reports. Moreover, the presence of human-origin vessels perfused with mouse erythrocytes confirmed that the vascular network formed *in vitro* was able to inosculate with the host vasculature.

Overall, we demonstrate the αvβ3 integrin-specific biomaterials ability to trigger vasculogenesis by activating essential pathways for EC survival and migration, in a growth factor self-regulatory microenvironment. Moreover, triggering vasculogenesis *in vitro* benefits the engraftment of the prevascularized integrin-specific constructs indicating that this strategy can enhance the efficacy of tissue engineered constructs.

VI-5. REFERENCES

1   Risau W, Flamme I. Vasculogenesis. Annu. Rev. Cell Dev. Biol. 11, 73–91 (1995).

2   Vailhé B, Vittet D, Feige JJ. *In vitro* models of vasculogenesis and angiogenesis. Lab. Investig. 81(4), 439–52 (2001).

3   Novosel EC, Kleinhans C, Kluger PJ. Vascularization is the key challenge in tissue engineering. Adv. Drug Deliv. Rev. 63(4–5), 300–311 (2011).

4   Sharma D, Ross D, Wang G, Jia W, Kirkpatrick SJ, Zhao F. Upgrading prevascularization in tissue engineering: A review of strategies for promoting highly organized microvascular network formation. Acta Biomater. 95, 112–130 (2019).

5   Miklas JW, Dallabrida SM, Reis LA, Ismail N, Rupnick M, Radisic M. QHREDGS Enhances Tube Formation, Metabolism and Survival of Endothelial Cells in Collagen-Chitosan Hydrogels. PLoS One 8(8), 72956 (2013).

6   Wang W, Guo L, Yu Y, Chen Z, Zhou R, Yuan Z. Peptide REDV-modified polysaccharide hydrogel with endothelial cell selectivity for the promotion of angiogenesis. J. Biomed. Mater. Res. - Part A 103(5), 1703–12 (2015).

7   Zovein AC, Luque A, Turlo KA *et al.* β1 Integrin Establishes Endothelial Cell Polarity and Arteriolar Lumen Formation *via* a Par3-Dependent Mechanism. Dev. Cell 18(1), 39–51 (2010).

8   Soldi R, Mitola S, Strasly M, Defilippi P, Tarone G, Bussolino F. Role of α(v)β3 integrin in the activation of vascular endothelial growth factor receptor-2. EMBO J. 18(4), 882–892 (1999).

9   Yamamoto H, Ehling M, Kato K *et al.* Integrin β1 controls VE-cadherin localization and blood vessel stability. Nat. Commun. 10(6), 6429 (2015).

10   Alghisi GC, Ponsonnet L, Rüegg C. The integrin antagonist cilengitide activates αVβ3, disrupts VE-cadherin localization at cell junctions and enhances permeability in endothelial cells. PLoS One 4(2), e4449 (2009).

11   Abraham S, Kogata N, Fässler R, Adams RH. Integrin β1 subunit controls mural cell adhesion, spreading, and blood vessel wall stability. Circ. Res. 102, 562–570 (2008).

12   Sumi M, Sata M, Toya N, Yanaga K, Ohki T, Nagai R. Transplantation of adipose stromal cells, but not mature adipocytes, augments ischemia-induced angiogenesis. Life Sci. 80(6), 559–65 (2007).

13   Rehman J, Traktuev D, Li J *et al*. Secretion of Angiogenic and Antiapoptotic Factors by Human Adipose Stromal Cells. Circulation 109(10), 1292–1298 (2004).

14   Planat-Benard V, Silvestre J-S, Cousin B *et al*. Plasticity of Human Adipose Lineage Cells Toward Endothelial Cells. Circulation 109(5), 656–663 (2004).

15   Yoshimura K, Shigeura T, Matsumoto D *et al*. Characterization of freshly isolated and cultured cells derived from the fatty and fluid portions of liposuction aspirates. J. Cell. Physiol. 208(1), 64–76 (2006).

16   Eto H, Ishimine H, Kinoshita K *et al*. Characterization of human adipose tissue-resident hematopoietic cell populations reveals a novel macrophage subpopulation with CD34 expression and mesenchymal multipotency. Stem Cells Dev. 22(6), 985–97 (2013).

17   Costa M, Cerqueira MT, Santos TC *et al*. Cell sheet engineering using the stromal vascular fraction of adipose tissue as a vascularization strategy. Acta Biomater. 55, 131–143 (2017).

18   da Silva LP, Cerqueira MT, Sousa R a., Reis RL, Correlo VM, Marques AP. Engineering cell-adhesive gellan gum spongy-like hydrogels for regenerative medicine purposes. Acta Biomater. 10, 4787–4797 (2014).

19   da Silva LP, Jha AK, Correlo VM, Marques AP, Reis RL, Healy KE. Gellan Gum Hydrogels with Enzyme-Sensitive Biodegradation and Endothelial Cell Biorecognition Sites. Adv. Healthc. Mater. 7(5), 1700686 (2018).

20   Moreira HR, Silva LP da, Reis RL, Marques AP. Tailoring Gellan Gum Spongy-Like Hydrogels' Microstructure by Controlling Freezing Parameters. Polymers (Basel). 12(2), 329 (2020).

21   Pfaffl MW. A new mathematical model for relative quantification in real-time RT-PCR. Nucleic Acids Res. 29(9), 45e – 45 (2001).

22   Carpentier G, Martinelli M, Courty J, Cascone I. Angiogenesis Analyzer for ImageJ. 4th ImageJ User Dev. Conf. 198–201 (2012).

23   Kapp TG, Rechenmacher F, Neubauer S *et al*. A comprehensive evaluation of the activity and selectivity profile of ligands for RGD-binding integrins. Sci. Rep. 7, 39805 (2017).

24   Leu SJ, Liu Y, Chen N, Chen CC, Lam SCT, Lau LF. Identification of a Novel Integrin α6β1 Binding Site in the Angiogenic Inducer CCN1 (CYR61). J. Biol. Chem. 278(36), P33801-33808 (2003).

25   Weis SM, Cheresh DA. αv Integrins in Angiogenesis and Cancer. Cold Spring Harb Perspect Med

1(1), a006478 (2011).

26   Silva R, D'Amico G, Hodivala-Dilke KM, Reynolds LE. Integrins: The keys to unlocking angiogenesis. Arterioscler. Thromb. Vasc. Biol. 28(10), 1703–1713 (2008).

27   Eliceiri BP, Klemke R, Strömblad S, Cheresh DA. Integrin αvβ3 requirement for sustained mitogen-activated protein kinase activity during angiogenesis. J. Cell Biol. 140(5), 1255–63 (1998).

28   Chabut D, Fischer AM, Colliec-Jouault S *et al.* Low molecular weight fucoidan and heparin enhance the basic fibroblast growth factor-induced tube formation of endothelial cells through heparan sulfate-dependent α6 overexpression. Mol. Pharmacol. 64(3), 696–702 (2003).

29   Fukuhara S, Sako K, Noda K, Nagao K, Miura K, Mochizuki N. Tie2 is tied at the cell-cell contacts and to extracellular matrix by Angiopoietin-1. Exp. Mol. Med. 41(3), 133–139 (2009).

30   Teichert M, Milde L, Holm A *et al.* Pericyte-expressed Tie2 controls angiogenesis and vessel maturation. Nat. Commun. 8(1), 1–12 (2017).

31   Mas-Moruno C, Rechenmacher F, Kessler H. Cilengitide: The First Anti-Angiogenic Small Molecule Drug Candidate. Design, Synthesis and Clinical Evaluation. Anticancer. Agents Med. Chem. 10(10), 753–768 (2011).

32   Danilucci TM, Santos PK, Pachane BC *et al.* Recombinant RGD-disintegrin DisBa-01 blocks integrin α v β 3 and impairs VEGF signaling in endothelial cells. Cell Commun. Signal. 17(1), 27 (2019).

33   Hu YL, Lu S, Szeto KW *et al.* FAK and paxillin dynamics at focal adhesions in the protrusions of migrating cells. Sci. Rep. 4, 6024 (2014).

34   Baker EL, Zaman MH. The biomechanical integrin. J. Biomech. 43(1), 38–44 (2010).

35   Pasapera AM, Schneider IC, Rericha E, Schlaepfer DD, Waterman CM. Myosin II activity regulates vinculin recruitment to focal adhesions through FAK-mediated paxillin phosphorylation. J. Cell Biol. 188(6), 877–890 (2010).

36   Ross RS. Molecular and mechanical synergy: Cross-talk between integrins and growth factor receptors. Cardiovasc. Res. 63(3), 381–90 (2004).

37   Mahabeleshwar GH, Feng W, Reddy K, Plow EF, Byzova T V. Mechanisms of integrin-vascular endothelial growth factor receptor cross-activation in angiogenesis. Circ. Res. 101(6), 570–80 (2007).

38   Somanath PR, Malinin NL, Byzova T V. Cooperation between integrin αvβ3 and VEGFR2 in angiogenesis. Angiogenesis 12(2), 177–85 (2009).

39   Dellinger MT, Brekken RA. Phosphorylation of Akt and ERK1/2 is required for VEGF-A/VEGFR2-induced proliferation and migration of lymphatic endothelium. PLoS One 6(12), e28947 (2011).

40   Brooks PC, Clark RAF, Cheresh DA. Requirement of vascular integrin αvβ3 for angiogenesis. Science (80-.). 264(5158), 569–571 (1994).

41   Rusnati M, Tanghetti E, Dell'Era P, Gualandris A, Presta M. α(V)β3 integrin mediates the cell-adhesive capacity and biological activity of basic fibroblast growth factor (FGF-2) in cultured endothelial cells. Mol. Biol. Cell 8(12), 2449–2461 (1997).

42   Unger RE, Ghanaati S, Orth C *et al.* The rapid anastomosis between prevascularized networks on silk fibroin scaffolds generated *in vitro* with cocultures of human microvascular endothelial and osteoblast cells and the host vasculature. Biomaterials 31(27), 6959–6967 (2010).

43   Li S, Nih LR, Bachman H *et al.* Hydrogels with precisely controlled integrin activation dictate vascular patterning and permeability. Nat. Mater. 16(9), 953–961 (2017).

44   Schaller MD, Borgman CA, Cobb BS, Vines RR, Reynolds AB, Parsons JT. pp125FAK, a structurally distinctive protein-tyrosine kinase associated with focal adhesions. Proc. Natl. Acad. Sci. U. S. A. 89(11), 5192–5196 (1992).

45   Avraham HK, Lee TH, Koh Y *et al.* Vascular endothelial growth factor regulates focal adhesion assembly in human brain microvascular endothelial cells through activation of the focal adhesion kinase and related adhesion focal tyrosine kinase. J. Biol. Chem. 278(38), 36661–36668 (2003).

46   Somanath PR, Ciocea A, Byzova T V. Integrin and growth factor receptor alliance in angiogenesis. Cell Biochem. Biophys. 53(2), 53–64 (2009).

47   Mahabeleshwar GH, Feng W, Phillips DR, Byzova T V. Integrin signaling is critical for pathological angiogenesis. J. Exp. Med. 203(11), 2495–2507 (2006).

48   Montenegro CF, Salla-Pontes CL, Ribeiro JU *et al.* Blocking αvβ3 integrin by a recombinant RGD disintegrin impairs VEGF signaling in endothelial cells. Biochimie 94(8), 1812–1820 (2012).

49   Sun G, Ding XA, Argaw Y, Guo X, Montell DJ. Akt1 and dCIZ1 promote cell survival from apoptotic caspase activation during regeneration and oncogenic overgrowth. Nat. Commun. 11(1), 5726 (2020).

50   Ichikawa K, Watanabe Miyano S, Minoshima Y, Matsui J, Funahashi Y. Activated FGF2 signaling pathway in tumor vasculature is essential for acquired resistance to anti-VEGF therapy. Sci. Rep. 10(1), 2939 (2020).

51   Chouhan D, Dey N, Bhardwaj N, Mandal BB. Emerging and innovative approaches for wound healing and skin regeneration: Current status and advances. Biomaterials 216, 119267 (2019).

52   Gibot L, Galbraith T, Huot J, Auger FA. A preexisting microvascular network benefits *in vivo* revascularization of a microvascularized tissue-engineered skin substitute. Tissue Eng. - Part A 16(10), 3199–206 (2010).

53   Miyazaki H, Tsunoi Y, Akagi T, Sato S, Akashi M, Saitoh D. A novel strategy to engineer pre-vascularized 3-dimensional skin substitutes to achieve efficient, functional engraftment. Sci. Rep. 9, 7797 (2019).

54   Riemenschneider SB, Mattia DJ, Wendel JS *et al.* Inosculation and perfusion of pre-vascularized tissue patches containing aligned human microvessels after myocardial infarction. Biomaterials 97, 51–61 (2016).

55   Laschke MW, Vollmar B, Menger MD. Inosculation: Connecting the life-sustaining Pipelines. Tissue Eng. - Part B Rev. 15(4), 455–465 (2009).

VI-6.   SUPPLEMENTARY INFORMATION

Supplementary Table VI-1 GG/GGDVS-peptide(s) formulations

% GG (w/v)	% GGDVS (w/v)	Peptide(s)	Name
0.5	0.25	RGD	0.75%RGD
		T1	0.75%T1
		RGD+T1	0.75%RGD+T1
1	0.5	RGD	1.5%RGD
		T1	1.5%T1
		RGD+T1	1.5%RGD+T1
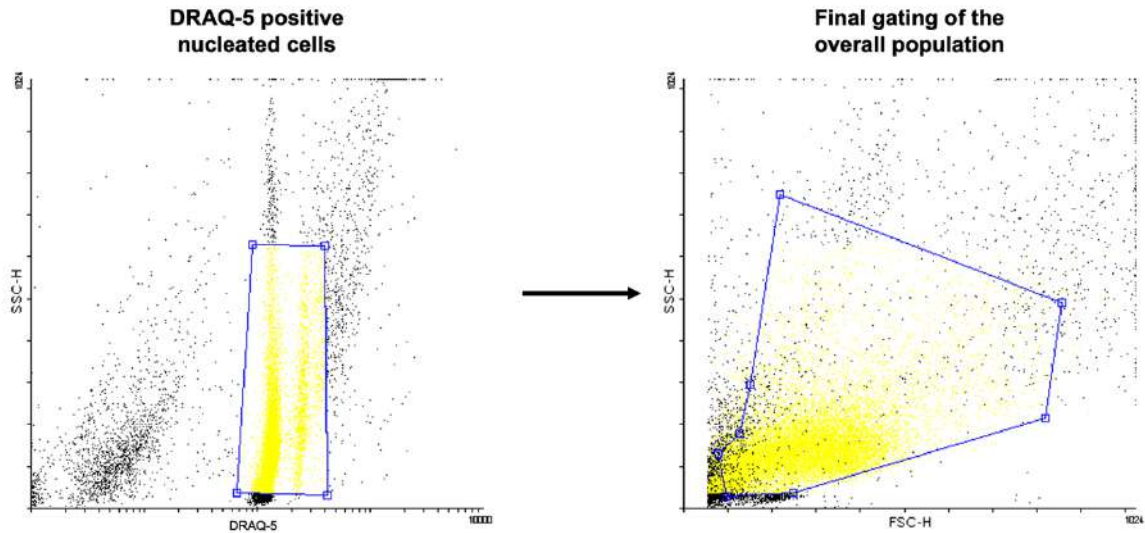
Supplementary Figure VI-1 Flow cytometry sequential gating strategy for SVF cells.

Debris and eunucleated cells are eliminated by selecting for low SSC, DRAQ-5 positive cells. Final gating of the overall population is then made on the FSC vs SSC plot.

Supplementary Table VI-2 Flow cytometry antibodies

Antibody	Brand	Ref	Dilution	Host
CD105-FITC	Bio-Rad	MCA1557F	1 μl *per* 10^5 cells	Ms
CD73-PE	BD Biosciences, USA	550257	10 μl *per* 10^5 cells	Ms
CD90-APC	BD Biosciences, USA	559869	1 μl *per* 10^5 cells	Ms
CD45-FITC	BD Biosciences, USA	555482	10 μl *per* 10^5 cells	Ms
CD31/PECAM1-APC	R&D Systems, USA	FAB3567A	1 μl *per* 10^5 cells	Ms
CD34-PE	BD Biosciences, USA	555822	10 μl *per* 10^5 cells	Ms
CD146-PE	BD Biosciences, USA	561013	10 μl *per* 10^5 cells	Ms

Legend: Ms – mouse

210

Supplementary Table VI-3 Primers sequences

Gene and accession number	Sequence (5'-3')	Annealing temperature (°C)
Human β2M NM_004048.4	TGGAGGCTATCCAGCGTACT CGGATGGATGAAACCCAGACA	59.5
Human VEGFA NM_ 003376.6	GATCCGCAGACGTGTAAATG CCCTCCCAACTCAAGTCCAC	59
Human KDR NM_002253.4	CTAGGTGCCTGTACCAAGCC GCCCCTTTGGTCTTGTAGGG	59
Human FLT-1 NM_002019.4	CGGACTGTGGCTGTGAAAATG TGGCCAATGTGGGTCAAGAT	59.8
Human FGF2 NM_001361665.2	CACCTATAATTGGTCAAAGTGG CAGAAATTCAGTAGATGTTTCCC	59
Human FGFR1 NM_023110.3	ACCAAACCGTATGCCCGTAG CCCACTGGAAGGGCATTTGA	57.5
Human FGFR2 NM_000141.5	CCTCTCGTTCCCCAAATC GAGTGGTCCTTGGGTCTT	59
Human ANGPT1 NM_001146.5	TGCAGAGAGATGCTCCACAC TCTCAAGTTTTTGCAGCCACT	56.6
Human TEK NM_000459.5	TGCGAGATGGATAGGGCTTG AGGATGGGAAAGGCTGTATCTT	59.2
Human PECAM1 NM_000442.5	GAGGGGCCACATGCATCTAT AGACCTGCTCGGTTCTCTCT	59.7
Human VWF NM_000552.5	CCCTGGGTTACAAGGAAGAAAAT AGTGTCATGATCTGGCCTCCTCTTAG	59

Supplementary Table VI-4 Western blot antibodies

Antibody	Brand	Ref	Dilution	Host
FAK	Abcam, UK	ab40794	1:500	Rb
Phospho-FAK	Cell Signaling, USA	1673283S	1:1000	Rb
AKT1	Cell Signaling, USA	9272S	1:1000	Rb
Phospho-AKT	Abcam, UK	ab81283	1:1000	Rb
ERK 1+2	Abcam, UK	ab17942	1:1000	Rb
Phospho-ERK 1+2	Abcam, UK	ab50011	1:1000	Ms
Paxillin	Abcam, UK	ab32084	1:5000	Rb
Talin 1+2	Abcam, UK	ab11188	1:1000	Ms
Vinculin	Sigma, Portugal	V9131	1:200	Ms
KDR	Abcam, UK	ab39256	1:500	Rb
FGFR2	Abcam, UK	ab10648	1:1000	Rb
Caspase 8	Santa Cruz Biotechnology, USA	sc-81656	1:200	Ms
Caspase 3	Abcam, UK	ab32351	1:1000	Rb
GAPDH	Abcam, UK	ab181602	1:10000	Rb

Legend: Rb – rabbit, Ms – mouse

211

Supplementary Table VI-5 Immunolabelling antibodies

	Antibody	Brand	Ref	Dilution	Host
ICC	PECAM1 (CD31)	Dako, Denmark	M0823	1:30	Ms
	von Willbrand factor (vWF)	Abcam, USA	ab201336	1 µg mL^{-1}	Ms
	Fibronectin	Abcam, UK	ab2413	1:100	Rb
	Laminin	Abcam, USA	ab11575	1:30	Rb
	Collagen type IV	Abcam, USA	ab6586	1:100	Rb
	VE-cadherin	Abcam, USA	ab33168	1 µg mL^{-1}	Rb
IHC	human PECAM1	Dako, Denmark	M0823	1:30	Ms
	total PECAM1	Abcam	ab28364	1:25	Rb

Legend: ICC – immunocytochemistry, IHC – immunohistochemistry, Rb – rabbit, Ms – mouse

A

Peptide	% GGDVS (w/v)	Conjugation efficiency
RGD	0.25%	95.3 ± 0.9
	0.5%	91.5 ± 1.6
T1	0.25%	89.0 ± 2.3
	0.5%	89.7 ± 1.0

B
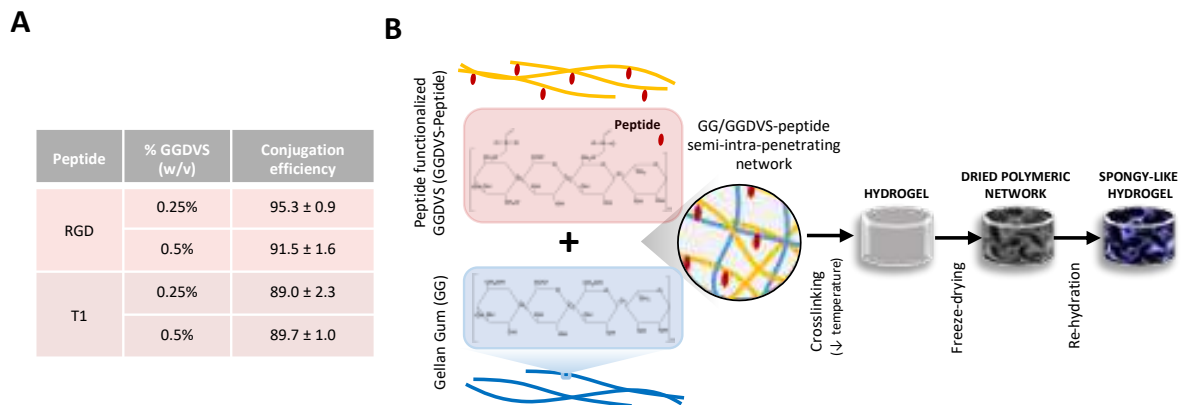
Supplementary Figure VI-2 A Peptide conjugation efficiency. B Schematic representation of GGDVS functionalization and processing methodology to attain the spongy-like hydrogels.
GGDVS is functionalized with the peptide sequences RGD and T1 and combined with unmodified GG at the time of the hydrogel formation obtaining a semi-interpenetrating network. After stabilization of the networks, hydrogels are freeze-dried resulting in dried polymeric structures. Integrin-specific spongy-like hydrogels are obtained after re-hydration of the dried structures.
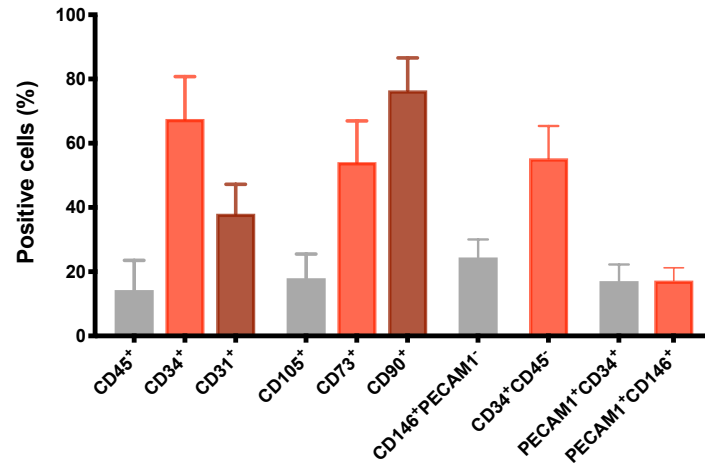
Supplementary Figure VI-3 Expression profile of membrane markers of SVF cells after isolation determined by flow cytometry.
Markers typically linked to mesenchymal (CD105, CD73 and CD90), pericytic (CD146-PECAM1-), endothelial (PECAM1-CD146- and PECAM1-CD34-) and endothelial progenitor (CD34-CD45-) cells [1] were analysed.
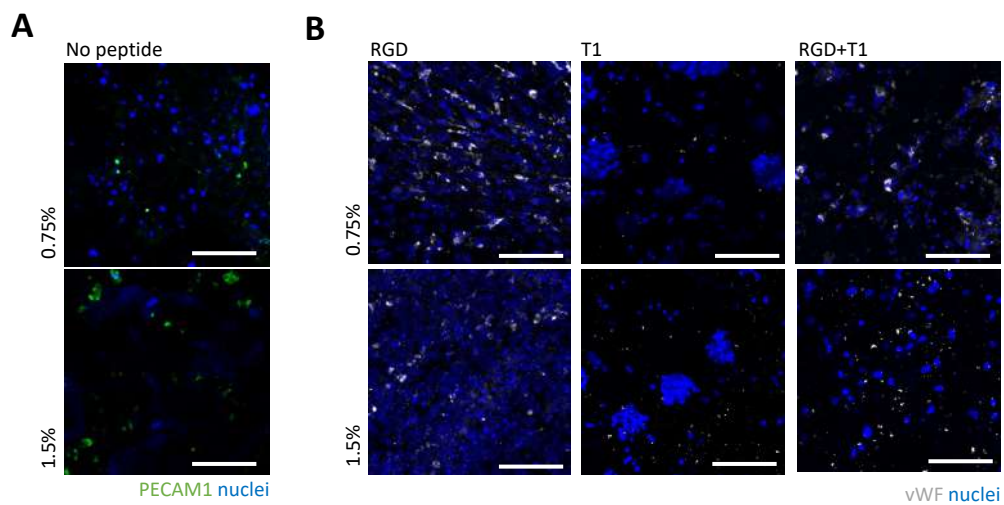
Supplementary Figure VI-4 A Representative immunocytochemistry images of SVF cells expressing PECAM1 in the non-functionalized materials after 7 days of culture. **B** Representative images of the expression of vWF by SVF cells in the functionalized materials after 7 days.
Nuclei were counter-stained with DAPI. Scale bar = 100 μm.
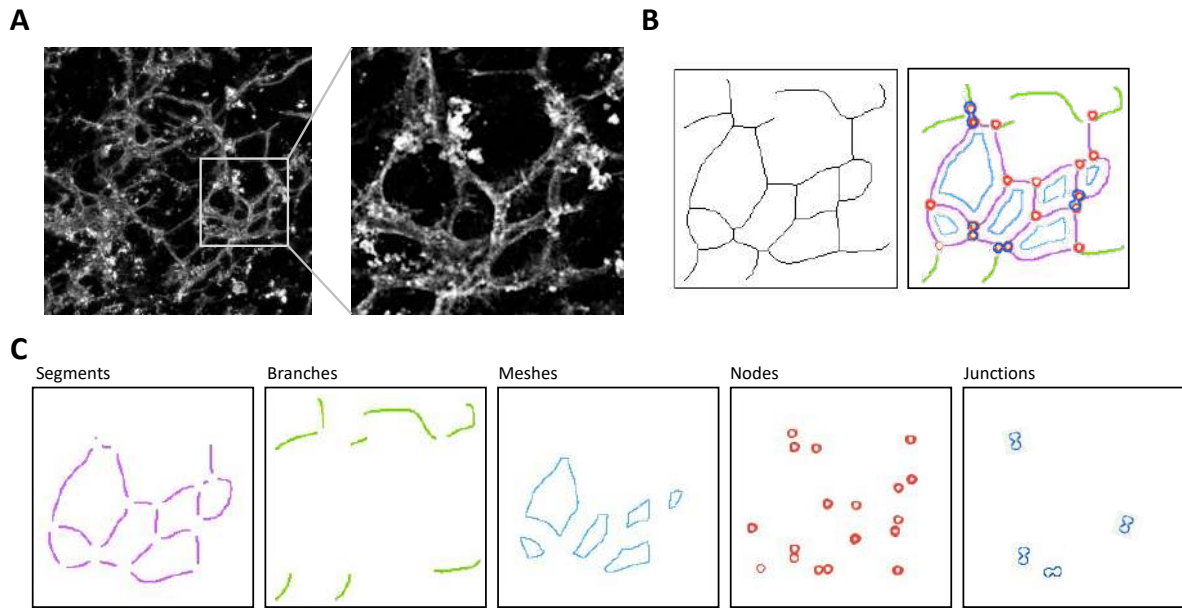
Supplementary Figure VI-5 Schematic representation of the measurements obtained from the Angiogenesis Analyzer in ImageJ.
A Initial image used for the measurements. **B** Skeleton of the image. **C** Detection of segments (purple) – lines connected by two nodes, branches (green) – lines connected by a node, meshes (ligh blue) – closed areas surrounded by segments, nodes (red) – minimum structure allowing a bifurcation, and junctions (dark blue) – four of more connected segments.
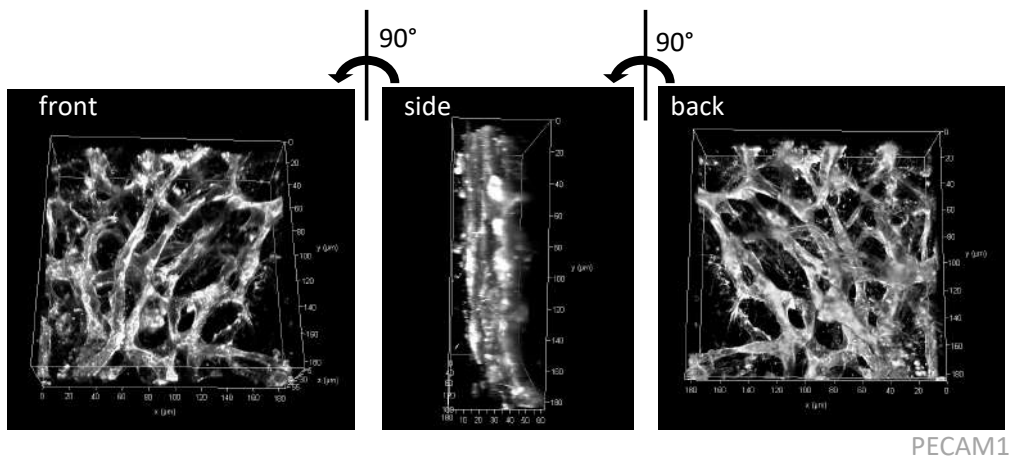
PECAM1

Supplementary Figure VI-6 3D view of a representative PECAM1⁺ vascular-like structure formed in the 0.75 % GG/GGDVS-RGD spongy-like hydrogel after 14 days in culture.

214
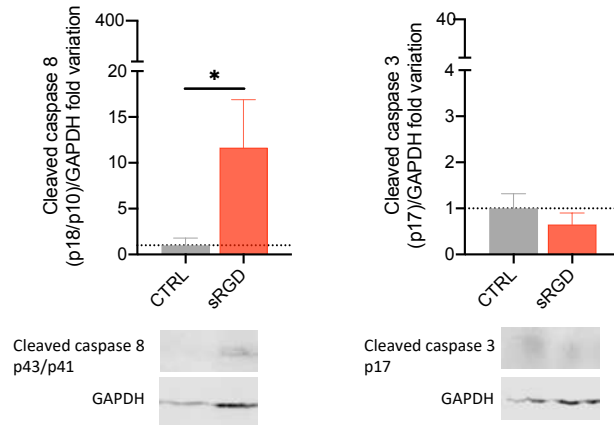
Supplementary Figure VI-7 Expression of Caspase 8 and Caspase 3 right after peptide exposure to SVF cells determined by western blot.

Plotted data was determined in relation to GAPDH expression. Quantitative results are expressed as the mean ± standard deviation where n = 3, * $p < 0.05$, ** $p < 0.01$, *** $p < 0.001$, **** $p < 0.0001$, two-tailed unpaired t test.
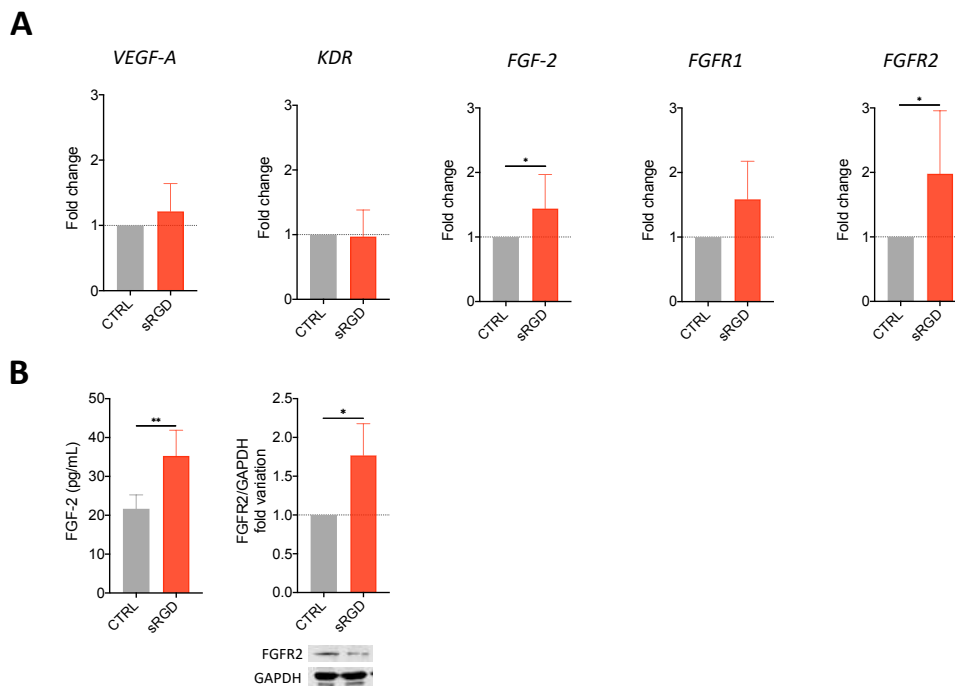
Supplementary Figure VI-8 VEGF, KDR, FGF2, FGFR2 and FGFR1 mRNA expression, FGF-2 secretion and FGFR2 and ERK1/2 protein expression.

A *VEGF*, *KDR*, *FGF2*, *FGFR2* and *FGFR1* mRNA expression in SVF cells pre-incubated with RGD peptide and cultured for 7 days in the 0.75 % GG/GGDVS-RGD spongy-like hydrogels. mRNA expression was determined by qPCR using *β2M* as reference gene and compared to mRNA expression of the Control (0.75 % GG/GGDVS-RGD spongy-like hydrogels with SVF cells after 7 days of culture). **B** FGF-2 secretion and FGFR2 and ERK1/2 protein expression, determined by western blot, in SVF cells pre-incubated with RGD peptide and cultured for 7 days in the 0.75 % GG/GGDVS-RGD spongy-like hydrogels. Plotted western blot data was determined in relation to GAPDH expression. Results are expressed as the mean ± standard deviation where n = 3, * $p < 0.05$, ** $p < 0.01$, *** $p < 0.001$, **** $p < 0.0001$, two-tailed unpaired t test.

215

A

Human skin   Mouse skin

PECAM1 Haematoxylin

B

Human skin   Mouse skin

hPECAM1 Haematoxylin
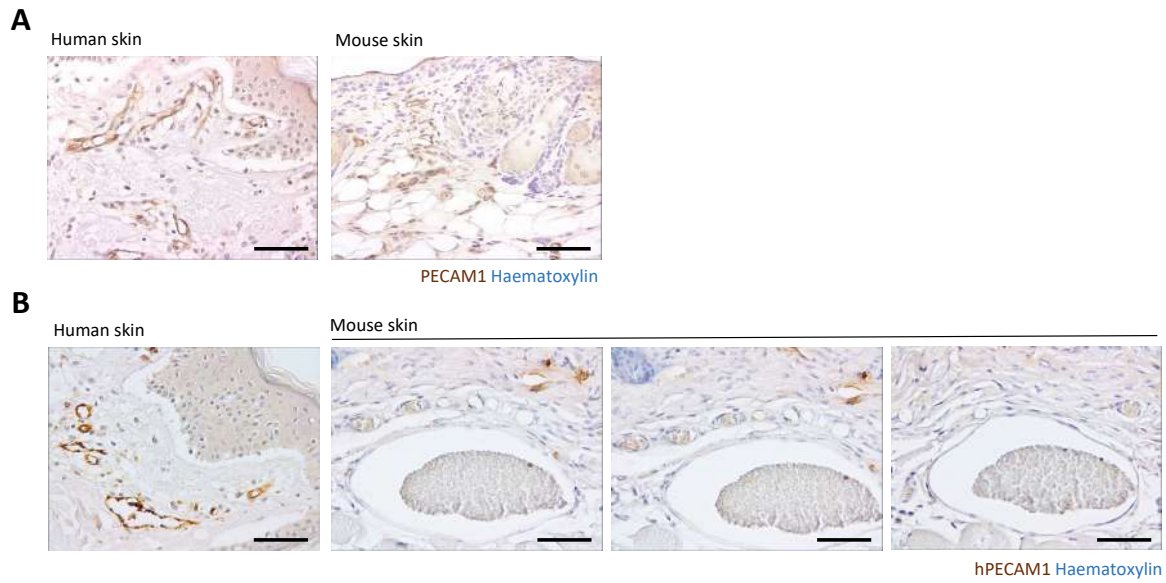
Supplementary Figure VI-9 Specificity of anti-PECAM1 antibodies.
A Representative immunocytochemistry images for the antibody with cross reactivity to human and mouse used to quantify the total number of vessels and determine their diameter. **B** Representative immunocytochemistry images for the anti-human PECAM1 antibody with reactivity to human skin but not to mouse skin (3 consecutive sections) used to determine the number of vessels incorporating human cells. Scale bar = 50 μm.

Supplementary references

1   Yoshimura K, Shigeura T, Matsumoto D *et al.* Characterization of freshly isolated and cultured cells derived from the fatty and fluid portions of liposuction aspirates. J. Cell. Physiol. 208(1), 64–76 (2006).

CHAPTER VII

SPONGY-LIKE HYDROGELS PREVASCULARIZATION WITH THE ADIPOSE TISSUE VASCULAR FRACTION DELAYS CUTANEOUS WOUND HEALING BY SUSTAINING INFLAMMATORY CELL INFLUX

CHAPTER VII

SPONGY-LIKE HYDROGELS PREVASCULARIZATION WITH THE ADIPOSE TISSUE VASCULAR FRACTION DELAYS CUTANEOUS WOUND HEALING BY SUSTAINING INFLAMMATORY CELL INFLUX [††]

ABSTRACT

In vitro prevascularization is one of the most explored approaches to foster engineered tissue vascularization. We previously demonstrated a benefit in tissue neovascularization by using integrin-specific biomaterials prevascularized by stromal vascular fraction (SVF) cells, which triggered vasculogenesis in the absence of extrinsic growth factors. SVF cells are also associated to biological processes important in cutaneous wound healing. Thus, we aimed to investigate whether *in vitro* construct prevascularization with SVF accelerates the healing cascade by fostering early vascularization vis-à-vis SVF seeding prior to implantation. Prevascularized constructs delayed re-epithelization of full-thickness mice wounds compared to both non-prevascularized and control (no SVF) groups. Our results suggest this delay is due to a persistent inflammation as indicated by a significantly lower M2(CD163+)/M1(CD86+) macrophage subtype ratio. Moreover, a slower transition from the inflammatory to the proliferative phase of the healing was confirmed by reduced extracellular matrix deposition and increased presence of thick collagen fibers from early time-points, suggesting the prevalence of fiber crosslinking in relation to neodeposition. Overall, while prevascularization potentiates inflammatory cell influx, which negatively impacts the cutaneous wound healing cascade, an effective wound healing was guaranteed in non-prevascularized SVF cell-containing spongy-like hydrogels confirming that the SVF can have enhanced efficacy.


VII-1. INTRODUCTION

In cutaneous wounds, neovascularization is critical for tissue repair. From the early onset of the healing cascade, capillaries sprout from the host vasculature invading the fibrin clot and vascularizing the granulation tissue [1]. This pro-angiogenic phase is critical to provide nutrients and oxygen to a metabolically active wound bed and is directly associated to an immature capillary network that also potentiates extravasation of inflammatory cells into the wound bed. In turn, a healthy vascularized granulation tissue provides the support for the growth and migration of keratinocytes that start the re-epithelialization of the wound. As the healing progresses and the inflammation is resolved, the dense neovascular network matures experiencing a significant regression regulated by antiangiogenic stimuli. It is then understandable that given all this interplay among the different stages/processes, any alteration in the angiogenic signaling - e.g., reduced production of pro-angiogenic cytokines, overproduction of anti-angiogenic cytokines, overgranulation - may compromise the whole process impairing healing and skin repair [2].

The strategies used to promote neovascularization in cutaneous wounds have been mainly focusing on the *in situ* controlled delivery of angiogenic growth factors [3–6] or respective encoding genetic material [7,8], transplantation of adult stem cells [9–13] or, on the implantation of prevascularized constructs using both mature [14,15] and progenitor [16,17] endothelial cells. Despite the significant achievements, all these strategies have issues that are still far from being resolved and have been hampering its clinical translation. While growth factors sustained temporal delivery is possible, it is also often associated to bolus release and unmatched profile with the wound requirements. Short half-life due to lack of protection from proteolytic degradation, and high doses to achieve a therapeutic effect [18] are also shortcomings that might be tackled by the *in situ* secretion of growth factors by genetically modified cells. Yet, reduced transfection efficiency, and immunogenicity issues and potential long-term side effects are still associated to these strategies. *In vitro* prevascularization is one of the most successful approaches in fostering vascularization at wound site. However, the clinical use of those angiogenic cells is highly hampered by an insufficient number required for therapy due to highly difficult isolation procedures and limited expansion *in vitro* [19]. Other cellular approaches with less manipulation have been showing a positive impact in the vascularization of cutaneous wounds mostly provided by an angiogenic secretome, such as the case of adipose derived stem cells (hASCs) [20–22]. Yet, their potential might still be maximized by enhancing their residence time at the wound site.

Interestingly, several works have also suggested an impact of ASCs in cutaneous wounds that goes beyond neovascularization including a paracrine interaction with the resident cells that affects epidermal morphogenesis [9,23], and regulates inflammation [24,25]. Moreover, clinical trials with the stromal vascular fraction (SVF) of the adipose tissue, which comprises cells subpopulations other than the ASCs [26,27] showed that 93% of the patients with chronic non-healing diabetic foot ulcers achieved full closure - the remaining had a wound closure > 85 % - after autologous SVF transplantation [28]. Comparable outcomes were attained with SVF incorporated in a fibrin-collagen hydrogel confirming a faster re-epithelialization in the presence of SVF [29]. While the mechanism of action is yet to be determined, pre-clinical studies revealed a faster progression in the healing of full-thickness wounds treated with SVF characterized by earlier resolution of the inflammatory phase accompanied by fibroblasts proliferation [30].

In our previous work we demonstrated a benefit in tissue neovascularization with integrin-specific biomaterials prevascularized by SVF cells capable of triggering vasculogenesis in the absence of extrinsic growth factors [31]. Herein, we hypothesized that an *in vitro* prevascularization stage would accelerate the healing cascade by fostering the early vascularization of the wound by inosculating with the host vasculature, further potentiating the effect of SVF. To validate this, we assessed the capacity of prevascularized and non-prevascularized - containing freshly isolated SVF cells - constructs to modulate wound inflammation and re-epithelization, and neotissue deposition and remodeling (**Figure VII-1**).
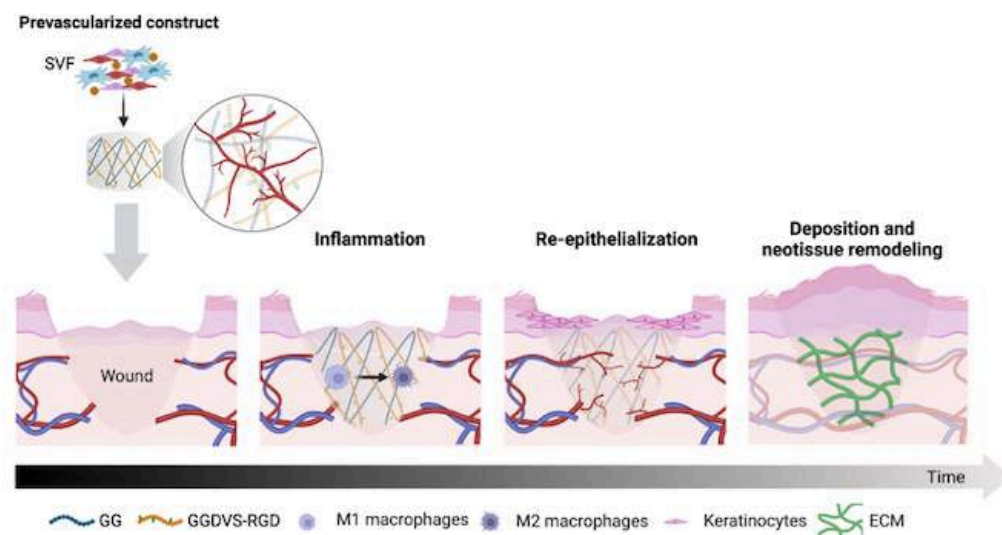
Figure VII-1 Schematic representation of the rationale.
Vasculogenic cells present in the stromal vascular fraction (SVF) of adipose tissue are retained in the integrin-specific gellan gum (GG) spongy-like hydrogels prevascularizing the construct in the absence of extrinsic growth factors. The prevascular

network will inosculate with the host vasculature accelerating the healing cascade fostering the resolution of the inflammation and the re-epithelialization of the wound which then impacts extracellular matrix (ECM) deposition and neotissue remodeling.

VII-2. MATERIALS AND METHODS

VII-2.1. Gellan gum (GG) spongy-like hydrogels fabrication

Gellan gum was modified with vinyl sulfone moieties (DVS) as previously described [32]. Briefly, 0.25 % (w/v) gelzan powder (Sigma, USA) was dissolved in deionized water (DI) at 90 °C. After dissolution, the pH was adjusted to 12 and DVS (Sigma, USA) was added in excess (molar ratio of 30:1) and left to react for 1 h. Gellan gum-divinyl sulfone (GGDVS) was purified by precipitation in cold diethyl ether (1:5) and dialysis against DI water for 3 days at 37 °C. The purified GGDVS was freeze-dried for further use. GG/GGDVS-RGD spongy-like hydrogels were prepared similarly to GG spongy-like hydrogels [32,33] with modifications. GGDVS was dissolved in ultra-pure (UP) water (pH 8) at RT. A solution of GGDVS-peptide (0.25 % (w/v) with 800 μM of peptide) was prepared by letting the thiol-cyclo-RGD peptide (RGD, Cyclo(-RGDfC), >95 % purity, GeneCust Europe) and GGDVS react for 1 h at RT under agitation. Meanwhile, a GG (0.5 % w/v) solution was prepared as described above and allowed to reach 40 °C before mixing with the GGDVS-RGD solution. The solution (400 μM peptide) was cast into desired molds to form the hydrogels which were then frozen at -80 °C overnight and freeze-dried (Telstar, Spain) for 24 h to obtain the GG/GGDVS-peptide(s) dried polymeric networks. Spongy-like hydrogels were formed after rehydration of the dried polymeric networks with the cell suspension.

VII-2.2. SVF isolation

Adipose tissue was harvested from fat tissue from skin specimens of healthy donors (IMC 20.8 – 26.8) undergoing abdominoplasties after written informed consent and under the protocol established and approved between the Ethical Committee of Hospital S. João (Porto, Portugal) (Nr 477/2020) and the *Comissão de Ética para a Investigação em Ciências da Vida e da Saúde* (CEICVS) (Nr 135/2020). Adipose tissue was digested with 0.05 % (w/v) collagenase type II (Sigma, USA) under agitation for 45 min at 37 °C. SVF was obtained after filtration and centrifugation (800 g, 10 min, 4 °C). SVF pellet was re-suspended in red blood cell lysis buffer (155 mM of ammonium chloride, 12 mM of potassium bicarbonate and 0.1 mM of ethylenediaminetetraacetic acid (EDTA), all from Sigma-Aldrich, Germany)

and incubated for 10 min at RT. After centrifugation (300 g, 5 min, RT), the supernatant was discarded, and the cell pellet was re-suspended for immediate use.

VII-2.3. Flow cytometry

Flow cytometry was conducted right after cell isolation and after 3 and 7 days of culture in the spongy-like hydrogels. After culture, cells were tripsinized from the spongy-like hydrogels using TrypLE™ Express Enzyme (Gibco, USA) for 15 min at 37 °C, 5 % CO_2. The obtained cell suspension was filtered and centrifuged (5 min, 300 g, RT). Cells were incubated with CD105, CD73, CD90, CD45, CD34, CD31 and CD146 (Supplementary Table VII-1) antibodies for 20 min at RT at the concentrations advised by the manufacturer's, washed with PBS and resuspended in PBS with 1 % (v/v) formalin (Bio-Optica, Italy). Cells were also labelled with DRAQ5 (eBioscience, USA) for nuclear staining to discern the cells of interest from the any remaining erythrocytes or tissue debris. $2x10^4$ events were acquired in a BD FACSCalibur and analyzed using the Cyflogic version1.2.1 software.

VII-2.4. Viability and cytoskeleton staining

Cell-laden spongy-like hydrogels were incubated with calcein-AM (Ca-AM, 1 µg mL^{-1}, Invitrogen, USA) and propidium iodide (PI, 2 µg mL^{-1}, Invitrogen, USA) for 1 h at 37 °C in a humidified incubator with 5 % CO_2 atmosphere. For visualization of the cytoskeleton F-actin fibers and nuclei, cells were fixed with 10 % (v/v) formalin for 1 h at RT, and stained with phalloidin-TRITC (0.1 mg mL^{-1}, Sigma, USA) and DAPI (0.02 mg mL^{-1}) for 2 h at RT. Both cell viability and cytoskeleton organization were observed with a Leica TCS SP8 confocal microscope (Leica, Germany).

VII-2.5. Immunocytochemistry

Cell-laden spongy-like hydrogels were fixed with 10 % (v/v) formalin for 24 h at RT and then incubated with 0.2 % (v/v) Triton X-100 (Sigma-Aldrich, Portugal) for 30 min at RT for cell permeabilization. Afterwards, samples were blocked with 3 % (w/v) bovine serum albumin (BSA, Sigma-Aldrich, Portugal) for 1 h and then incubated with anti-human primary antibodies (Supplementary Table VII-2) diluted in 1 % (w/v) BSA solution in PBS overnight at 4 °C. After washing with PBS, samples were incubated 1 h at RT with the secondary antibody Alexa Fluor 488 donkey anti-mouse (1:500, Life Technologies, CA, USA)

in 1 % (w/v) BSA solution in PBS. Nuclei were counter-stained with DAPI. Constructs were observed using a Leica TCS SP8 confocal microscope (Leica, Germany).

VII-2.6.   *In vivo* assay

The experiment was approved by the *Direcção Geral de Alimentação Veterinária* (DGAV), the Portuguese National Authority for Animal Health, and all the surgical procedures respected the national regulations and the international animal welfare rules, according to the Directive 2010/63/EU. Athymic nude mice NU(NCr)-Foxn1nu (Charles River, France) with 6 weeks old were randomly assigned to 3 groups: (i) GG/GGDVS-RGD spongy-like hydrogels – control; (ii) GG/GGDVS-RGD spongy-like hydrogels with freshly isolated SVF cells – SVFnpv; (iii) GG/GGDVS-RGD spongy-like hydrogels cultured for 7 days with SVF cells – SVFpv. A total of 54 animals, 6 animals *per* condition and *per* time point (5 and 28 days) were used. Mice were anaesthetized with an i.p injection of a mixture of ketamine (75 mg kg^{-1}, Imalgene, Merial, France) and metedomidine (1 mg kg^{-1}, Domitor, Orion Pharma, Finland). The back of the animals was disinfected with betaisodone and 70 % ethanol. A 5 mm $\varnothing$ skin full-thickness excision was created and a donut-shaped 5 mm silicone splint (ATOS Medical, Sweden) was glued and sutured around the wound to minimize wound contraction. After transplantation of the constructs, wounds were successively covered with Tegaderm transparent dressing (3M, USA), Omnifix (Hartmann, USA) and Leukoplast (Essity, Spain). After surgery, atipamezole (1 mg kg^{-1}, Antisedan, Pfizer, Finland) was administered to the animals. The animals were kept separately and received daily analgesia with metamizole (200 µg g^{-1} BW, Nolotil, Boehringer Ingelheim, Germany) in the drinking water for the first 72 h. At each time-point the assigned animals were sacrificed by CO_2 inhalation and the constructs/tissue were explanted for histological analysis.

VII-2.7.   Wound closure quantification

Wound closure was calculated according to **Equation VII-1**, by analyzing the wound area in the digital images taken at the time of material implantation (A) and 5, 11 and 28 days post-implantation (B) in five animals *per* condition and time-point.

$$Wound\ closure\ (\%) = \frac{(A - B)}{A} \times 100$$

Equation VII-1 Wound closure.

VII-2.8. Histological analysis

Explanted tissue was fixed in 10 % (v/v) formalin, dehydrated, embedded in paraffin (Thermo Scientific, USA) and cut into 4.5 μm sections. Tissue sections were stained with hematoxylin and eosin (Sigma, USA), masson's trichrome kit (Bio-Optica, Italy) and picrosirius red kit (Bio-Optica, Italy) following routine protocols. For immunohistochemistry, paraffin tissue sections were deparaffinized in xylene, re-hydrated and boiled for 5 min in Tris-EDTA buffer (10 mM Tris Base, 1 mM EDTA solution and, 0.05 % v/v Tween 20, pH 9) for antigen retrieval. Afterwards, permeabilization was carried out with 0.2 % (v/v) Triton X-100 and unspecific staining was blocked with 2.5 % (v/v) Horse Serum (Vector Labs, USA). Primary antibodies (Supplementary Table VII-2) were incubated overnight at 4 °C. For detection, VECTASTAIN Elite ABC Kit (Vector Labs) was used according to the manufacturer's instructions. Nuclei were stained with Gill's hematoxylin. All samples were examined under a Leica DM750 microscope, using LEICA Acquire software.

VII-2.9. Image analysis

Five images of random fields were acquired for each condition and experiment and used to calculate the number of cells (DAPI stained) with the Cell Profiler software.

To infer about the number of CD163 and CD86 positive cells, six images of random fields of four non-consecutive tissue sections *per* time-point and *per* animal were used with the Cell Profiler software using an algorithm for the identification of nuclei (hematoxylin)-associated DAB staining. Results are presented as positive cells *per* total cell amount. Ratio of the CD163 positive cells *per* CD86 positive cells (CD163+/CD86+) was calculated from the average values of positive cells for each animal. From the Masson's Trichrome stained sections, a custom-written algorithm was used to identify the blue pixels (collagen) keeping the same color segmentation settings for each image. The amount of collagen was calculated as percentage of total pixels. The same algorithm was used to identify the different color pixels from the Picrosirius Red stained sections - green pixels were considered thin, yellow pixels were considered mixed, and red pixels were considered thick fibers [34]. The respective type of collagen fibers was calculated as percentage of total pixels.

Neoepidermis thickness at the end-point was measured at the wounded area, considering the basal epidermis layer up to the outermost layer of nucleated cells.

VII-2.10. Statistical analysis

Statistical analysis was performed using the PRISM software, version 8.2.1 for Mac OS X or Windows (GraphPad Software Inc., USA). Shapiro–Wilk test was performed to validate normality of data prior to statistical testing and all data followed a normal distribution. Therefore, the one-way or two-way analysis of variance (ANOVA) with a Tukey multiple comparison post-test was used to analyze the results. Significance was set to 0.05 (95 % of confidence interval). All quantitative data refer to 3 independent experiments (n=3) with at least 3 replicates in each condition in each experiment and are presented as mean ± standard deviation.

VII-3.   RESULTS

VII-3.1.   Popularization of the constructs by SVF cells

Besides endothelial progenitor and mature cells which highly express the $\alpha v \beta 3$ integrin [35,36] and are the ones responsible for the prevascularization of the constructs, SVF contains a multitude of other cells (**Figure VII-2a**). Overall, SVF cells were entrapped in the spongy-like hydrogels after seeding. However, a significant ($p < 0.05$) reduction (about 50 %) in the number of cells was observed from day 0 to day 3 of culture (**Figure VII-2b**). At this timepoint, most of the remnant cells were alive (**Figure VII-2c**) although they did not seem to proliferate with increasing culture time (Figure VII-2b). When we looked at the phenotype of the cells entrapped in the spongy-like hydrogels, we confirmed that at day 0 SVF cells displayed the typically characteristics [27] linked to the mesenchymal (CD105, CD73, CD90), pericytic (CD146), mature/progenitor endothelial (CD31, CD34, CD105) and hematopoietic (CD45) phenotype (**Figure VII-2d, i**). Along the culture, a significant ($p < 0.05$) decrease was noticed regarding the percentage of positive cells expressing CD73 and CD90 markers while the opposite trend was observed for CD31 and CD105 demonstrating a preferred retention of angiogenic/vasculogenic cells in the spongy-like hydrogels. Interestingly, these cells seem to be supported along time by other adherent cells (CD31-) to organize in capillary-like structures (**Figure VII-2d, ii**). After 7 days of culture a prevascularized construct
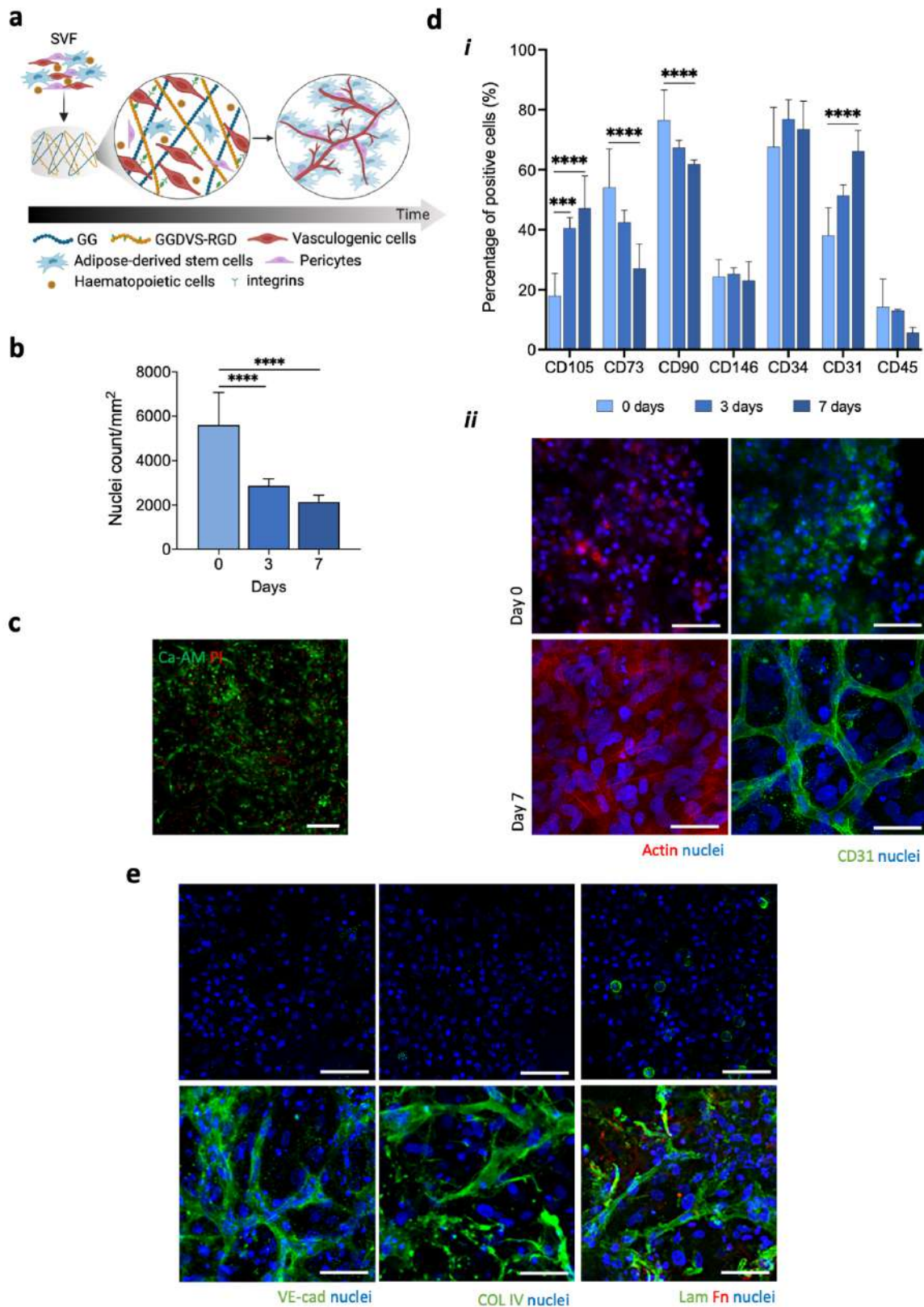
Figure VII-2 Performance of SVF cells in the integrin-specific gellan gum (GG) spongy-like hydrogels.
a Schematic representation of the different cell subpopulations present in the stromal vascular fraction (SVF) of adipose tissue and how they organize within the spongy-like hydrogel along the culture. **b** Total number of SVF cells entrapped in the materials after seeding (day 0) and 3 and 7 days of culture. **c** Survival of SVF cells after 3 days in culture determined after calcein AM

(Ca-AM, live, green) and propidium iodide (PI, dead, red) staining. Scale bar = 500 µm. **d** (i) Expression profile of membrane markers by SVF cells after seeding (day 0) and 3 and 7 days of culture determined by flow cytometry. (ii) Representative images of the F-actin cytoskeleton and expression of CD31 after seeding (day 0) and 7 days of culture. Scale bar = 50 µm. **e** Representative immunocytochemistry images of the expression of VE-cadherin (VE-cad), Collagen type IV (COL IV), Laminin (Lam), Fibronectin (Fn) after seeding (0 days) and 7 days of culture. Nuclei were counter-stained with DAPI (nuclei). Scale bar = 50 µm. Quantitative results are expressed as the mean ± standard deviation where n = 3, * $p < 0.05$, *** $p < 0.001$, **** $p < 0.0001$, one-way ANOVA with Tukey multiple comparison post-test.

with these structures lined by basement membrane proteins such as laminin, fibronectin and collagen type IV was attained (**Figure VII-2e**).

VII-3.2.   Wound healing progression

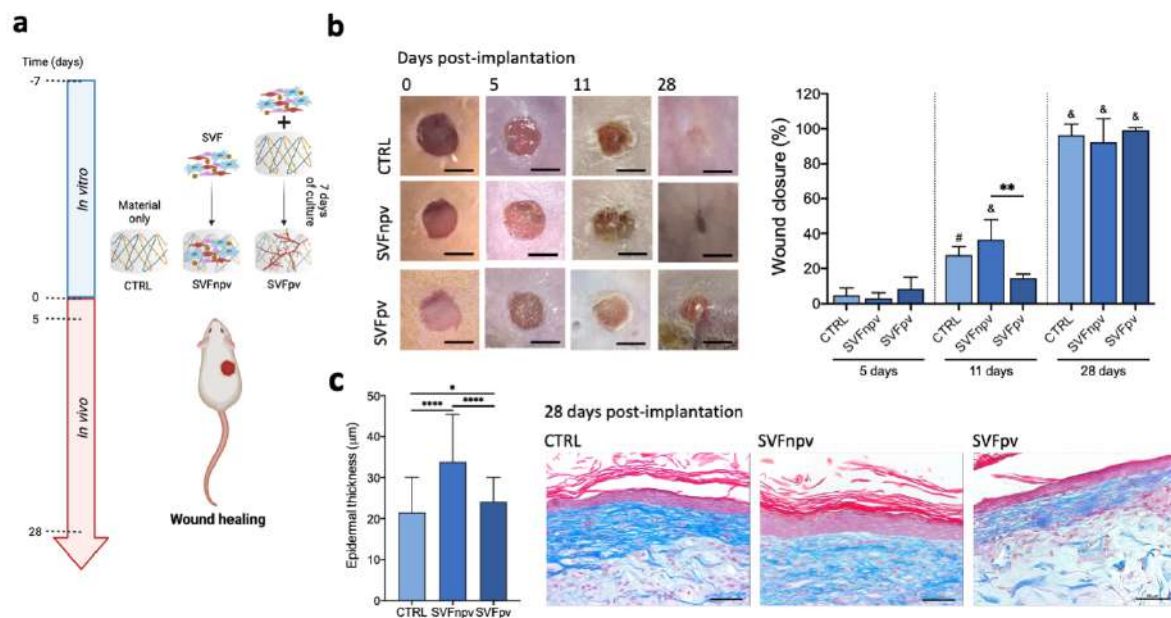In order to confirm that the prevascularization of the construct had a positive impact in the overall wound healing cascade, we analyzed the different stages in comparison with the non-prevascularized conditions - freshly isolated SVF was seeded in the material and immediately implanted (SVFnpv) (**Figure VII-3a**).

Figure VII-3 Impact in the re-epithelialization.
a Schematic representation of the test groups: CTRL (GG/GGDVS-RGD spongy-like hydrogels without cells), SVFnpv (freshly isolated SVF seeded in the material), SVFpv (SVF seeded in the material and cultured for 7 days *in vitro* prior to implantation). **b** Representative macroscopic images of the wounds and representation of the percentage of wound closure up to 28 days of implantation. Scale bar = 5 mm. **c** Quantification of the epidermal thickness and representative images of Masson's Trichrome (MT) staining at day - 28 detailing the neoepidermis features. Scale bar = 50 µm. Quantitative results are expressed as the

mean ± standard deviation where n = 3, * $p < 0.05$, **, # $p < 0.01$, *** $p < 0.001$, ****, & $p < 0.0001$, one-way or two-way ANOVA with Tukey multiple comparison post-test. #, & refers to the significance difference of the same group related to day 5.

VII-3.2.1.   Wound closure and neoepidermis structure

Upon implantation, although complete wound closure was reached at day 28 in all group (**Figure VII-3b**), there seems to be a tendency of slower wound closure rate for the prevascularized group. Indeed, the wound closure percentage at day 11 in this condition was significantly lower ($p < 0.05$) than in the other groups (Figure VII-3b). This delayed re-epithelialization led to a significantly ($p < 0.05$) thinner neoepidermis consisting of 2-3 layers of keratinocytes in the prevascularized group, similar to the control at day 28 post-implantation (**Figure VII-3c**). Interestingly, the neoepidermis in the prevascularized groups was also characterized by the absence or the presence of a very thin stratum corneum, in opposition to the prominent layer observed in the non-prevascularized condition, which was akin to the control.

VII-3.2.2.   Inflammatory response

Neovascularisation cannot be dissociated from the inflammatory response since vascular hyperpermeability allows inflammatory mediators and immune cells to infiltrate the injured site [37]. In cutaneous wounds, persistent inflammation and compromised transition to the proliferative phase is linked to delayed and even pathological healing [38,39]. Therefore, we wanted to understand how prevascularization correlates with the progression of the healing of the wound. Integrin-specific biomaterials were well integrated in the wound site and infiltrated with an inflammatory exudate 5 days after implantation independently of the group (**Figure VII-4a**). At day 28 post-implantation, this inflammatory exudate was only observed in the prevascularized group (Figure VII-4a, i-iii), which can be associated to the presence of the transplanted material, which was barely detected in the non-prevascularized and control groups.

The analysis of the inflammatory infiltrate at day 5 showed a significantly ($p < 0.05$) higher percentage of M1-polarized (CD86+) macrophages in the prevascularized group (**Figure VII-4b**). In turn, the percentage of M2-polarized (CD163+) macrophages in both experimental conditions (SVFnpv and SVFpv) was significantly ($p < 0.05$) higher than in the control. With time, the percentage of CD86+ macrophages decreased for all the conditions but the differences among the groups remained. On the other hand, the percentage of CD163+ macrophages at day 28 post-transplantation was lower in the
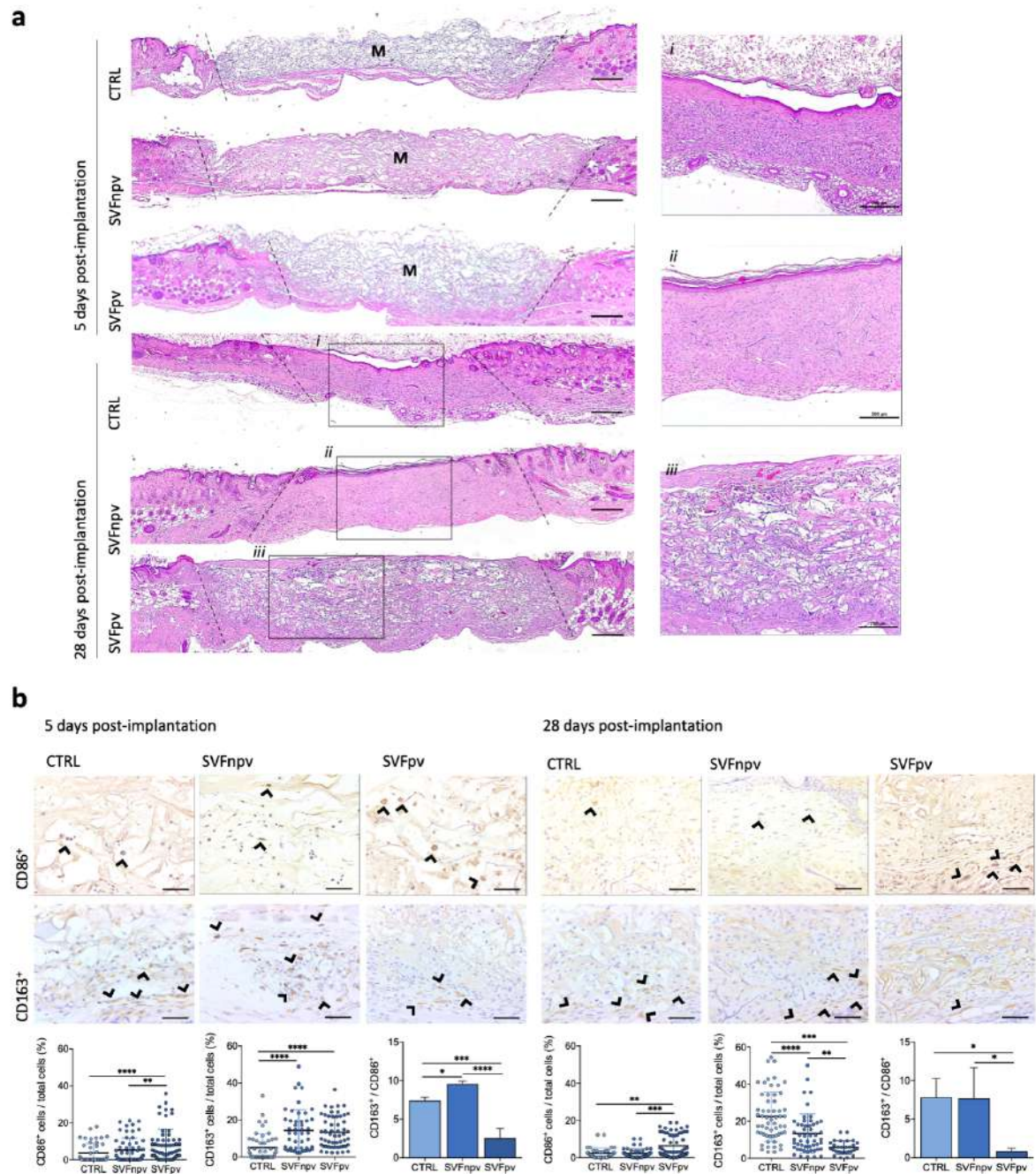
Figure VII-4 Progression of the inflammatory process.

a Representative images of hematoxylin and eosin (H&E) staining 5- and 28-days post-implantation. Scale bar = 1 mm. (i-iii) Higher magnification images of the area limited by the boxes in the lower magnification ones. Scale bar = 200 μm. **b** Macrophage's recruitment and polarization 5- and 28-days post-transplantation. Representative immunostaining images of CD86 and CD163 (arrow heads) and quantification of the of CD86+, CD163+ cells and respective ratio. Scale bar = 50 μm.

Quantitative results are expressed as the mean ± standard deviation where n = 3, * $p < 0.05$, ** $p < 0.01$, *** $p < 0.001$, **** $p < 0.0001$, one-way ANOVA with Tukey multiple comparison post-test. —— wound margins; M – material
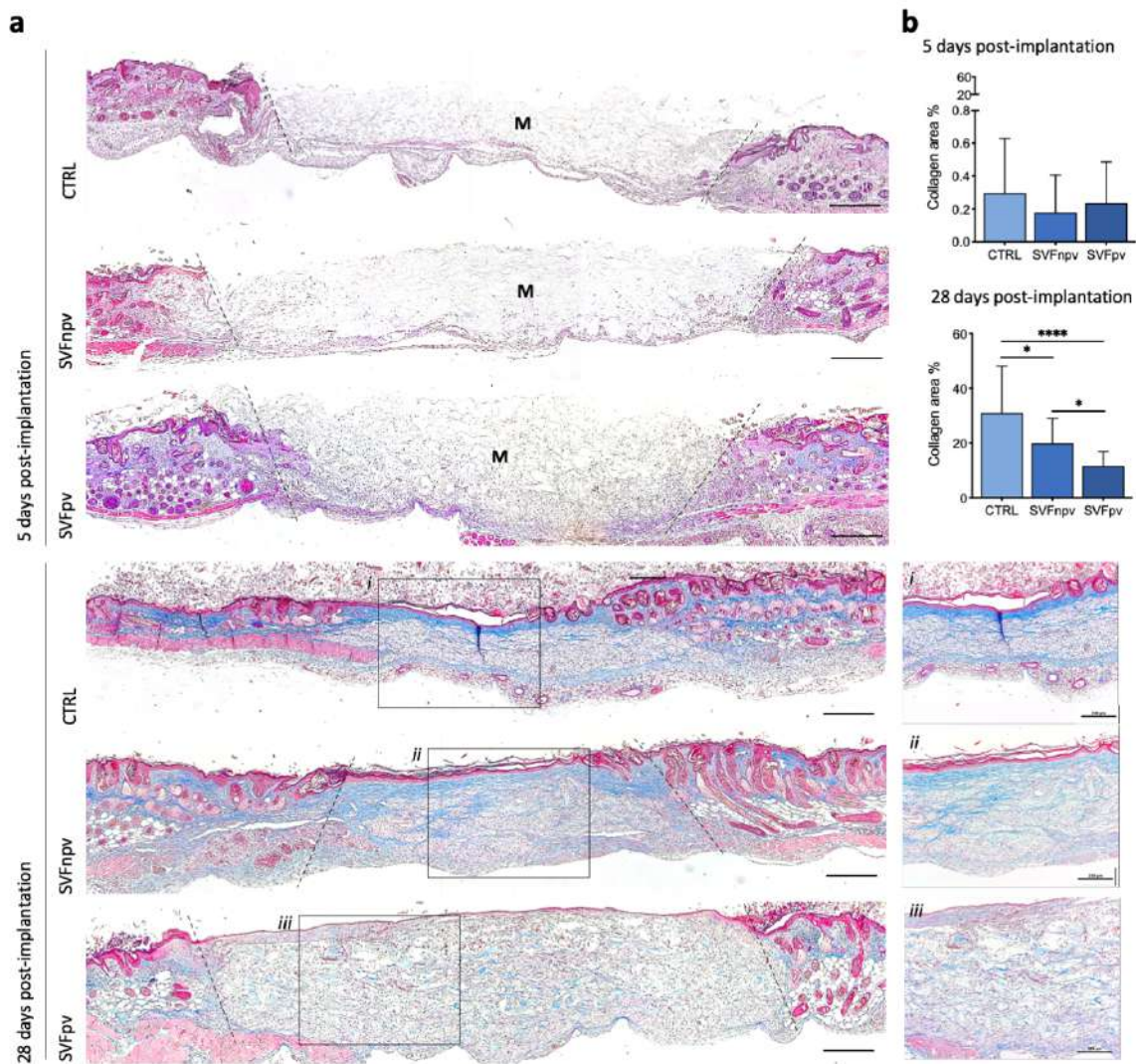
Figure VII-5 Extracellular matrix deposition.
a Representative images of Masson's Trichrome (MT) staining 5- and 28-days post-implantation. Scale bar = 1 mm. (i-iii) Higher magnification images of the area limited by the boxes in the lower magnification ones. Scale bar = 200 μm. **b** Quantification of collagen relative to total area. Quantitative results are expressed as the mean ± standard deviation where n = 3, * p < 0.05, **** p < 0.0001, one-way ANOVA with Tukey multiple comparison post-test. —— wound margins, M – material.

prevascularized condition while decreasing in the SVFpv group and increasing in the control. These variations resulted in a CD163+/CD86+ ratio similar for SVFnpv and control conditions but significantly ($p < 0.05$) lower for the SVFpv group, suggesting a persistence in the inflammatory stage of the wound healing for this group.

VII-3.2.3. ECM deposition

Based on the persistent inflammation results from the prevascularised constructs, we further analyzed the deposition of new extracellular matrix to confirm the status of the healing process. As expected at the early time-point, no differences were observed among the different conditions regarding the deposited collagen (**Figure VII-5a,b**). At day 28 post-implantation, the abundance of collagen was significantly ($p < 0.05$) lower in the SVFpv condition than in the SVFnpv and control ones (Figure VII-5a,b). In the SVFpv condition, the collagen fibers were randomly distributed mostly within the construct structure, whereas in the SVFnpv and control groups those fibers were more organized and located both within and in the surroundings of the structure (Fig. VII-5a i-iii). Interestingly, in the SVFpv group collagen was mostly organized as thick fibers as from early time-points (**Figure VII-6a,b**, Supplementary Figure VII-1) suggesting the prevalence of fibers crosslinking in relation to neodeposition. In opposition, the abundance of thin collagen fibers at the latter timepoint was significantly higher in the SVFnpv and control groups than in the SVFpv, while the amount of thick fibers was residual (Supplementary Figure VII-1). This suggests a reduced fibroblast's activity in the prevascularized condition, characteristic of the proliferative wound healing stage.

VII-4. DISCUSSION

Neovascularization is a critical step in the wound healing cascade being therefore determinant for a successful outcome. While different strategies have been used to tackle neovascularization at the wound site, prevascularization is one of the most effective. However, its clinical translation has been highly hampered by an insufficient number required for therapy. We previously shown that SVF cells respond to integrin-specific 3D matrices triggering vasculogenesis *in vitro* in the absence of extrinsic growth factors [31]. Moreover, we provided evidence that this prevascularization *in vitro* benefits the engraftment of the constructs indicating that this strategy can be an alternative to other similar strategies that rely on cells with limited availability.

Importantly, SVF is composed by a myriad of cells, including ASCs, that have been associated to biological processes with high relevance in cutaneous wound healing [20–22]. In this work, when SVF cells were cultured in the integrin-specific spongy-like hydrogels, despite the predominance of a

231
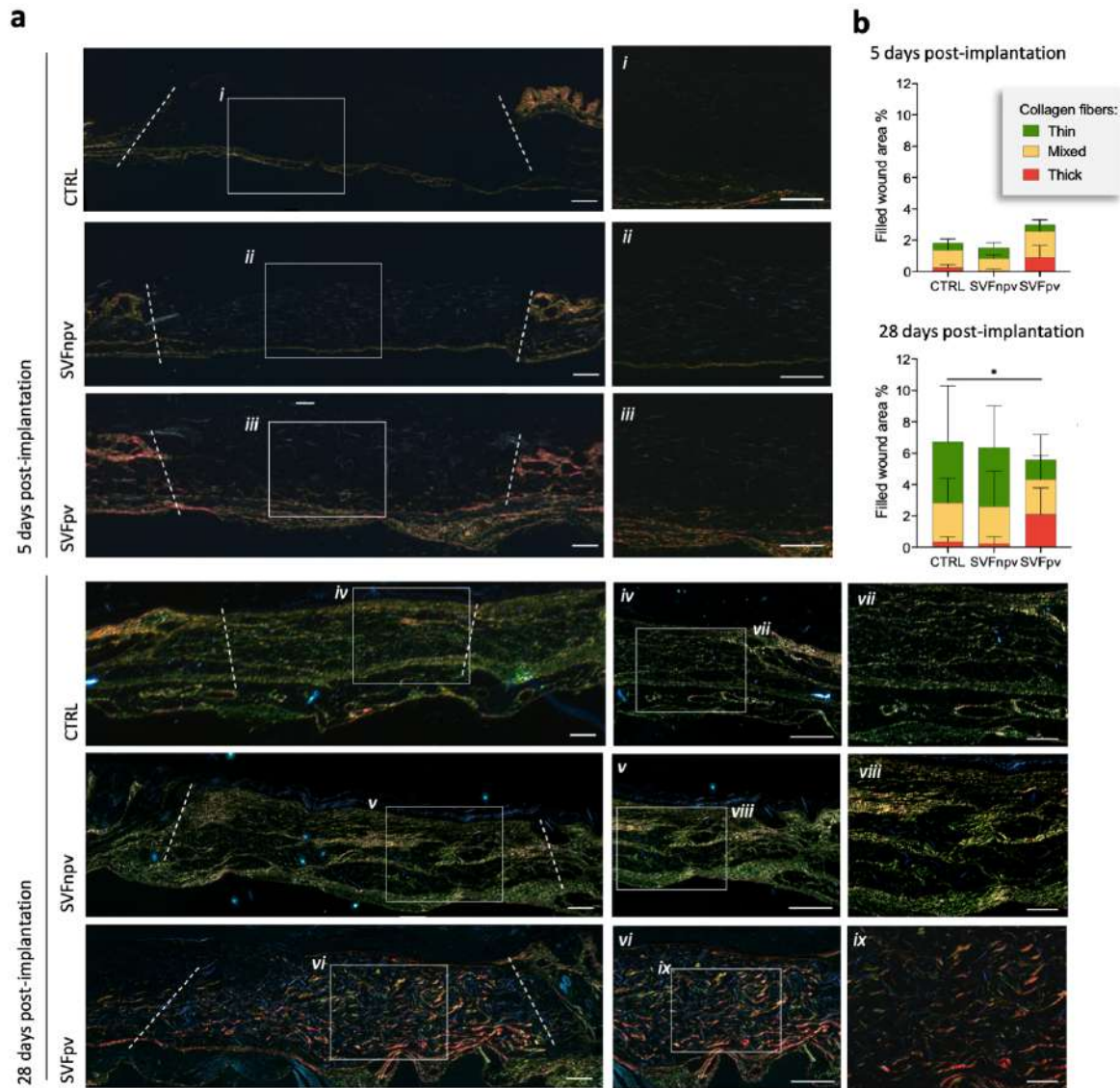
Figure VII-6 Nature of deposited collagen.
a Representative images of Picrosirius red staining of the wound site at day 5 and 28 post-implantation showing thick (red), mixed (yellow) and thin (green) collagen fibers. Scale bar = 500 μm. (i-ix) Higher magnification images of the area limited by the boxes in the lower magnification ones. Scale bar = 200 μm. **b** Percentage of the wounded area filled with different types of collagen fibers (see Supplementary Figure 1 for all individual comparisons). Quantitative results are expressed as the mean ± standard deviation where n = 3, * p < 0.05, one-way ANOVA with Tukey multiple comparison post-test. —— wound margins

vasculogenic phenotype [40] - progenitor CD34+ and mature CD31+ endothelial, and CD146+ pericytic cells, we also found a sub-population expressing mesenchymal-associated markers - CD105+, CD73+ and CD90+ [41,42]. While it is difficult to quantify the subset of cells corresponding to the ASCs due to their shared markers (CD34, CD105 and CD146) with the remaining cells and the respective changes associated to the culture conditions [43–46], it seems that the level of expression of all those markers

increased or is maintained with time. This suggests that the vasculogenic process previously studied is accompanied by an enrichment of the mesenchymal population. Moreover, it appears that the mesenchymal population is supporting the vasculogenic cells to organize in capillary-like structures. This is in agreement with other works that showed the role of ASCs goes beyond modulation of mature endothelial cell migration through paracrine interactions [47] and capillary-like structure stabilization assuming a pericytic-like phenotype [45]. In fact, the potential of ASCs to stimulate vasculature morphogenesis has been also attributed to the fibronectin, laminin, perlecan-1 rich ECM produced by ASCs [48], some of the proteins that we found lining the prevascular network formed in our constructs.

Several works have suggested that the impact of SVF in cutaneous wounds goes beyond neovascularization, with both pre-clinical and clinical studies showing faster healing progression affecting re-epithelialization, inflammation and ECM deposition [28–30,49]. In agreement, we demonstrated that freshly isolated SVF incorporated in the spongy-like hydrogels foster re-epithelization leading to an epidermis with a higher degree of differentiation than the control condition. Moreover, we also confirmed the ability of the SVF to accelerate the resolution of the inflammatory phase as shown by the faster decay of proinflammatory M1 (CD86+) macrophages and maintenance of the anti-inflammatory M2 (CD163+) subtype. While the associated mechanism of action of the SVF is not well understood, it might be linked to the ASCs subpopulation that acts as homeostatic regulator of inflammation [24,25,49]. Moreover, as ASCs are entrapped within the integrin-specific biomaterials, their potential modulator secretome, including inflammatory mediators, such as interleukin (IL)-6, IL-10, granulocyte macrophage colony-stimulating factor, prostaglandin E2 and arginase-1 that are known to play a role in the M1 to M2 switch [24,25,50], might be maximized. However, a deeper understanding of this potential communication with macrophages and the exact mechanism behind M1 toM2 switch is still required.

According to previous works [51–55], prevascular networks that lead to improved anastomosis with the host blood vessels after transplantation, promote neotissue formation in cutaneous wound healing. Successful inosculation involves vascular remodeling of the readily perfusable networks with the host vessels [55]. While this process results in infiltration of inflammatory cells to the wound bed, it ensures the supply of nutrients and oxygen and the filling of the wound with a granulation tissue through which keratinocytes can migrate and re-epithelialize the wound. Our results showed that wound closure was slower in the prevascularized group than in the non-prevascularized, resulting in a lower degree of epidermal morphogenesis. We believe that this delayed re-epithelization in the prevascularized constructs might be related with the inflammatory phase of the wound healing process, as we detected significantly

stronger response characterized by a higher percentage of M1 pro-inflammatory macrophages in this condition. The inosculation of the pre-formed vessels in our constructs with the host vessels seems to have facilitated the infiltration of inflammatory cells into the integrin-specific spongy-like hydrogels. Moreover, the low M2/M1 macrophages ratio observed in the prevascularized materials group, due to the persistence of CD86+ macrophages along the time, is indicative of persistent inflammation. During the healing process, the transition from the inflammatory to the proliferative phase represents a key step towards wound closure [38]. The less-differentiated neodermis composed of a lower collagen density with thick collagen fibers in the prevascularized materials group further suggests that the healing process is not progressing. This also resulted in a delayed degradation of the material, in opposition to what was observed for the non-prevascularized construct that follows a sustained progression in the degradation of the material as well as the healing, in agreement with what was previously reported by us [49,56,57].

Based on our results, it can be assumed that the prevascularized system is not desired for cutaneous wound healing in which fast re-epithelialization is mandatory such as in the case of life-threatening extensive burns. Burn injuries lead to pathological scarring which is accompanied by aesthetic and functional sequelae thus, the quality of the healed tissue after a burn is also of outmost importance. We have previously shown that temporal modulation of the inflammatory stage in the healing of full-thickness wounds in diabetic mice impacts the quality of the neoskin formed suggesting that a slower, yet controlled, inflammation might be beneficial to that end [49]. Therefore, in less extensive burns in which the restoration of the external skin barrier is not the most immediate requirement, the prevascularized system might contribute to reduce the level of pathological scarring by modulating the healing temporal profile. In what concerns chronic wounds, since these are characterized by delayed re-epithelialization, it would be also reasonable to consider that while the prevascularized system would not be beneficial for these types of wounds, the system containing SVF cells (non-prevascularized) would help to achieve fast wound closure with formation of the neodermis with adequate properties (collagen synthesis). Yet, delayed healing of chronic wounds is determined by a deficient angiogenic response therefore, from a vascularization point of view, the fast engraftment of the prevascularized system after anastomosis with the host vessels might allow overcoming the need for that priming of host angiogenesis. It is although evident that using a completely growth factor-free strategy that capable of improving wound neovascularization represents a very promising prospect for acute wounds.

Overall, we provide evidence that triggering vasculogenesis *in vitro* benefits neovascularization that also potentiates inflammatory cell influx, which negatively impact the progression of the cutaneous wound

healing cascade. Despite this, the ability of SVF in non-prevascularized integrin-specific biomaterials in promoting an effective wound healing was guaranteed indicating that the proposed strategy can have enhanced efficacy.

VII-5. REFERENCES

1   Tonnesen MG, Feng X, Clark RAF. Angiogenesis in wound healing. J. Investig. Dermatology Symp. Proc. 5(1), 40–46 (2000).

2   Bodnar RJ. Chemokine Regulation of Angiogenesis During Wound Healing. Adv. Wound Care 4(11), 641–650 (2015).

3   Vijayan A, A. S, Kumar GSV. PEG grafted chitosan scaffold for dual growth factor delivery for enhanced wound healing. Sci. Rep. 9, 19165 (2019).

4   Long G, Liu D, He X *et al*. A dual functional collagen scaffold coordinates angiogenesis and inflammation for diabetic wound healing. Biomater. Sci. 8(22), 6337–6349 (2020).

5   Qu Y, Cao C, Wu Q *et al*. The dual delivery of KGF and bFGF by collagen membrane to promote skin wound healing. J. Tissue Eng. Regen. Med. 12(6), 1508–1518 (2018).

6   Ishihara J, Ishihara A, Fukunaga K *et al*. Laminin heparin-binding peptides bind to several growth factors and enhance diabetic wound healing. Nat. Commun. 9, 2163 (2018).

7   Lou D, Luo Y, Pang Q, Tan WQ, Ma L. Gene-activated dermal equivalents to accelerate healing of diabetic chronic wounds by regulating inflammation and promoting angiogenesis. Bioact. Mater. 5(3), 667–679 (2020).

8   Wang P, Huang S, Hu Z *et al*. *In situ* formed anti-inflammatory hydrogel loading plasmid DNA encoding VEGF for burn wound healing. Acta Biomater. 100, 191–201 (2019).

9   Cerqueira MT, Pirraco RP, Santos TC *et al*. Human adipose stem cells cell sheet constructs impact epidermal morphogenesis in full-thickness excisional wounds. Biomacromolecules 14(11), 3997–4008 (2013).

10   Fujiwara O, Prasai A, Perez-Bello D *et al*. Adipose-derived stem cells improve grafted burn wound healing by promoting wound bed blood flow. Burn. trauma 8, tkaa009 (2020).

11   Nagano H, Suematsu Y, Takuma M *et al*. Enhanced cellular engraftment of adipose-derived

mesenchymal stem cell spheroids by using nanosheets as scaffolds. Sci. Rep. 11, 14500 (2021).

12   Burmeister DM, Stone R, II *et al*. Delivery of Allogeneic Adipose Stem Cells in Polyethylene Glycol-Fibrin Hydrogels as an Adjunct to Meshed Autografts After Sharp Debridement of Deep Partial Thickness Burns. Stem Cells Transl. Med. 7(4), 360 (2018).

13   Ebrahim N, Dessouky AA, Mostafa O *et al*. Adipose mesenchymal stem cells combined with platelet-rich plasma accelerate diabetic wound healing by modulating the Notch pathway. Stem Cell Res. Ther. 12(1), 392 (2021).

14   Montaño I, Schiestl C, Schneider J *et al*. Formation of human capillaries *in vitro*: The engineering of prevascularized matrices. Tissue Eng. - Part A 16(1), 269–82 (2010).

15   Cerqueira MT, Pirraco RP, Martins a. R, Santos TC, Reis RL, Marques a. P. Cell sheet technology-driven re-epithelialization and neovascularization of skin wounds. Acta Biomater 10(7), 3145–3155 (2014).

16   Sasagawa T, Shimizu T, Yamato M, Okano T. Endothelial colony-forming cells for preparing prevascular three-dimensional cell-dense tissues using cell-sheet engineering. J. Tissue Eng. Regen. Med. 10(9), 739–47 (2016).

17   Baltazar T, Merola J, Catarino C *et al*. Three Dimensional Bioprinting of a Vascularized and Perfusable Skin Graft Using Human Keratinocytes, Fibroblasts, Pericytes, and Endothelial Cells. Tissue Eng. - Part A 26(5–6), 227–238 (2020).

18   Raftery RM, Tierney EG, Curtin CM, Cryan S-AA, O'Brien FJ. Development of a gene-activated scaffold platform for tissue engineering applications using chitosan-pDNA nanoparticles on collagen-based scaffolds. J. Control. Release 210, 84–94 (2015).

19   Medina RJ, O'Neill CL, O'Doherty TM *et al*. *Ex vivo* Expansion of Human outgrowth Endothelial Cells Leads to IL-8-Mediated Replicative Senescence and Impaired Vasoreparative Function. Stem Cells 31(8), 1657–1668 (2013).

20   Melchiorri AJ, Nguyen BNB, Fisher JP. Mesenchymal stem cells: Roles and relationships in vascularization. Tissue Eng. - Part B Rev. 20(3), 218–228 (2014).

21   Laschke MW, Kleer S, Scheuer C *et al*. Vascularisation of porous scaffolds is improved by incorporation of adipose tissue-derived microvascular fragments. Eur. Cells Mater. 24, 266–77 (2012).

22   Rehman J, Traktuev D, Li J *et al.* Secretion of Angiogenic and Antiapoptotic Factors by Human Adipose Stromal Cells. Circulation 109(10), 1292–1298 (2004).

23   Moriyama M, Sahara S, Zaiki K *et al.* Adipose-derived stromal/stem cells improve epidermal homeostasis. Sci. Rep. 9(1), 18371 (2019).

24   Zomer HD, Jeremias T da S, Ratner B, Trentin AG. Mesenchymal stromal cells from dermal and adipose tissues induce macrophage polarization to a pro-repair phenotype and improve skin wound healing. Cytotherapy 22(5), 247–260 (2020).

25   Wang J, Hao H, Huang H, Chen D, Han Y, Han W. The effect of adipose-derived stem cells on full-thickness skin grafts. Biomed Res. Int. 2016, 1464725 (2016).

26   Planat-Benard V, Silvestre J-S, Cousin B *et al.* Plasticity of Human Adipose Lineage Cells Toward Endothelial Cells. Circulation 109(5), 656–663 (2004).

27   Yoshimura K, Shigeura T, Matsumoto D *et al.* Characterization of freshly isolated and cultured cells derived from the fatty and fluid portions of liposuction aspirates. J. Cell. Physiol. 208(1), 64–76 (2006).

28   Carstens MH, Quintana FJ, Calderwood ST *et al.* Treatment of chronic diabetic foot ulcers with adipose-derived stromal vascular fraction cell injections: Safety and evidence of efficacy at 1 year. Stem Cells Transl. Med. 10(8), 1138–1147 (2021).

29   Nilforoushzadeh MA, Sisakht MM, Amirkhani MA *et al.* Engineered skin graft with stromal vascular fraction cells encapsulated in fibrin–collagen hydrogel: A clinical study for diabetic wound healing. J. Tissue Eng. Regen. Med. 14(3), 424–440 (2020).

30   Atalay S, Coruh A, Deniz K. Stromal vascular fraction improves deep partial thickness burn wound healing. Burns 40(7), 1375–83 (2014).

31   Moreira HR, Rodrigues DB, Freitas-Ribeiro S *et al.* Integrin-specific hydrogels for growth factor-free vasculogenesis. npj Regen. Med. 7, 57 (2022).

32   da Silva LP, Jha AK, Correlo VM, Marques AP, Reis RL, Healy KE. Gellan Gum Hydrogels with Enzyme-Sensitive Biodegradation and Endothelial Cell Biorecognition Sites. Adv. Healthc. Mater. 7(5), 1700686 (2018).

33   Moreira HR, Silva LP da, Reis RL, Marques AP. Tailoring Gellan Gum Spongy-Like Hydrogels' Microstructure by Controlling Freezing Parameters. Polymers (Basel). 12(2), 329 (2020).

34   Drifka CR, Loeffler AG, Mathewson K *et al.* Comparison of Picrosirius Red Staining With Second Harmonic Generation Imaging for the Quantification of Clinically Relevant Collagen Fiber Features in Histopathology Samples. J. Histochem. Cytochem. 64(9), 519–29 (2016).

35   Weis SM, Cheresh DA. αv Integrins in Angiogenesis and Cancer. Cold Spring Harb Perspect Med 1(1), a006478 (2011).

36   Silva R, D'Amico G, Hodivala-Dilke KM, Reynolds LE. Integrins: The keys to unlocking angiogenesis. Arterioscler. Thromb. Vasc. Biol. 28(10), 1703–1713 (2008).

37   DiPietro LA. Angiogenesis and wound repair: when enough is enough. J. Leukoc. Biol. 100(5), 979–984 (2016).

38   Landén NX, Li D, Ståhle M. Transition from inflammation to proliferation: a critical step during wound healing. Cell. Mol. Life Sci. 73(20), 3861–3885 (2016).

39   Eming SA, Martin P, Tomic-Canic M. Wound repair and regeneration: Mechanisms, signaling, and translation. Sci. Transl. Med. 6(265), 265sr6 (2014).

40   Miranville A, Heeschen C, Sengenès C, Curat CA, Busse R, Bouloumié A. Improvement of postnatal neovascularization by human adipose tissue-derived stem cells. Circulation 110(3), 349–55 (2004).

41   Mitchell JB, McIntosh K, Zvonic S *et al.* Immunophenotype of Human Adipose-Derived Cells: Temporal Changes in Stromal-Associated and Stem Cell–Associated Markers. Stem Cells 24(2), 376–85 (2006).

42   Costa M, Cerqueira MT, Santos TC *et al.* Cell sheet engineering using the stromal vascular fraction of adipose tissue as a vascularization strategy. Acta Biomater. 55, 131–143 (2017).

43   Peng Q, Alipour H, Porsborg S, Fink T, Zachar V. Evolution of asc immunophenotypical subsets during expansion *in vitro*. Int. J. Mol. Sci. 21(4), 1408 (2020).

44   Dominici M, Le Blanc K, Mueller I *et al.* Minimal criteria for defining multipotent mesenchymal stromal cells. The International Society for Cellular Therapy position statement. Cytotherapy 8(4), 315–7 (2006).

45   Klar AS, Güven S, Zimoch J *et al.* Characterization of vasculogenic potential of human adipose-derived endothelial cells in a three-dimensional vascularized skin substitute. Pediatr. Surg. Int. 32(1), 17–27 (2016).

46   Suga H, Matsumoto D, Eto H *et al*. Functional implications of CD34 expression in human adipose-derived stem/progenitor cells. Stem Cells Dev. 18(8), 1201–10 (2009).

47   Nielsen FM, Riis SE, Andersen JI *et al*. Discrete adipose-derived stem cell subpopulations may display differential functionality after *in vitro* expansion despite convergence to a common phenotype distribution. Stem Cell Res. Ther. 7, 177 (2016).

48   Merfeld-Clauss S, Gollahalli N, March KL, Traktuev DO. Adipose tissue progenitor cells directly interact with endothelial cells to induce vascular network formation. Tissue Eng. - Part A 16(9), 2953–66 (2010).

49   da Silva LP, Santos TC, Rodrigues DB *et al*. Stem Cell-Containing Hyaluronic Acid-Based Spongy Hydrogels for Integrated Diabetic Wound Healing. J. Invest. Dermatol. 137(7), 1541–1551 (2017).

50   Glenn JD. Mesenchymal stem cells: Emerging mechanisms of immunomodulation and therapy. World J. Stem Cells 6(5), 526–539 (2014).

51   Chouhan D, Dey N, Bhardwaj N, Mandal BB. Emerging and innovative approaches for wound healing and skin regeneration: Current status and advances. Biomaterials 216, 119267 (2019).

52   Gibot L, Galbraith T, Huot J, Auger FA. A preexisting microvascular network benefits *in vivo* revascularization of a microvascularized tissue-engineered skin substitute. Tissue Eng. - Part A 16(10), 3199–206 (2010).

53   Miyazaki H, Tsunoi Y, Akagi T, Sato S, Akashi M, Saitoh D. A novel strategy to engineer pre-vascularized 3-dimensional skin substitutes to achieve efficient, functional engraftment. Sci. Rep. 9, 7797 (2019).

54   Riemenschneider SB, Mattia DJ, Wendel JS *et al*. Inosculation and perfusion of pre-vascularized tissue patches containing aligned human microvessels after myocardial infarction. Biomaterials 97, 51–61 (2016).

55   Laschke MW, Vollmar B, Menger MD. Inosculation: Connecting the life-sustaining Pipelines. Tissue Eng. - Part B Rev. 15(4), 455–465 (2009).

56   Cerqueira MT, Da Silva LP, Santos TC *et al*. Human skin cell fractions fail to self-organize within a gellan gum/hyaluronic acid matrix but positively influence early wound healing. Tissue Eng. - Part A 20(9–10), 1369–78 (2014).

57   Cerqueira MT, Da Silva LP, Santos TC *et al*. Gellan gum-hyaluronic acid spongy-like hydrogels and cells from adipose tissue synergize promoting neoskin vascularization. ACS Appl. Mater. Interfaces 6(22), 19668–79 (2014).

VII-6.   SUPPLEMENTARY INFORMATION
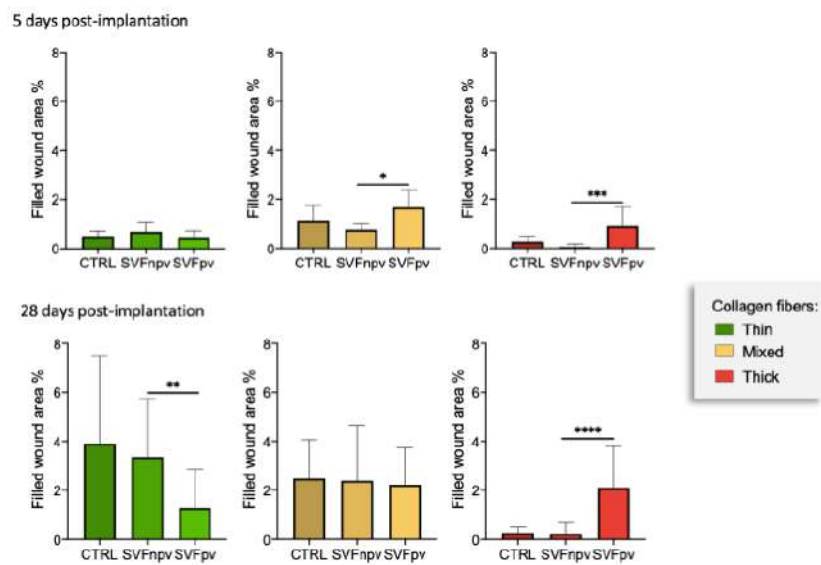
Supplementary Figure VII-1 Representation of the independent quantification of the percentage of wounded area filled with the thick (red), mixed (yellow) and thin (green) collagen fibers from Picrosirius red images at days 5 and 28 post-implantation. Quantitative results are expressed as the mean ± standard deviation where n = 3, * $p < 0.05$, ** $p < 0.01$, *** $p < 0.001$, **** $p < 0.0001$, one-way ANOVA with Tukey multiple comparison post-test.

Supplementary Table VII-1 Flow cytometry antibodies

Antibody	Brand	Ref	Dilution	Host
CD105-FITC	Bio-Rad	MCA1557F	1 μl *per* 105 cells	Ms
CD73-PE	BD Biosciences, USA	550257	10 μl *per* 105 cells	Ms
CD90-APC	BD Biosciences, USA	559869	1 μl *per* 105 cells	Ms
CD45-FITC	BD Biosciences, USA	555482	10 μl *per* 105 cells	Ms
CD31/PECAM1-APC	R&D Systems, USA	FAB3567A	1 μl *per* 105 cells	Ms
CD34-PE	BD Biosciences, USA	555822	10 μl *per* 105 cells	Ms
CD146-PE	BD Biosciences, USA	561013	10 μl *per* 105 cells	Ms

Legend: Ms - mouse

Supplementary Table VII-2 Immunolabelling antibodies

	Antibody	Brand	Ref	Dilution	Host
Immunocytochemistry	PECAM1 (CD31)	Dako, Denmark	M0823	1:30	Ms
	Fibronectin	Abcam, UK	ab2413	1:100	Rb
	Laminin	Abcam, USA	ab11575	1:30	Rb
	Collagen type IV	Abcam, USA	ab6586	1:100	Rb
	VE-cadherin	Abcam, USA	ab33168	1 μg mL^{-1}	Rb
Immunocytochemistry	CD86	Cell Signaling, USA	19589S	1:100	Rb
	CD163	Abcam, USA	ab182422	1:500	Rb

Legend: Ms – mouse, Rb - rabbit

241

CHAPTER VIII

GENERAL CONCLUSIONS

AND FUTURE PERSPECTIVES

GENERAL CONCLUSIONS AND

FUTURE PERSPECTIVES

Neovascularization is critical for the repair of cutaneous wounds. As such, changes in signaling that delay or impair the angiogenic process ultimately compromise healing progression, thus impacting the quality of the neotissue formed. To date, prevascularization of tissue-engineered (TE) constructs using both mature and progenitor endothelial cells (ECs) is one of the most successful approaches for fostering vascularization at the wound site. However, the clinical use of these angiogenic cells is still hampered by an insufficient number of cells due to difficulties associated to isolation procedures and limited expansion *in vitro*. Alternative strategies, such as *in situ*-controlled delivery of angiogenic growth factors or transplantation of adult stem cells, are also associated to issues that have precluded their clinical translation and are still far from being solved. This creates an opportunity to develop alternative approaches to modulate ECs behavior *in vitro* and hence, direct wound angiogenesis and the overall healing cascade. Therefore, the work reported in this thesis attempts to contribute with relevant knowledge to support the development of new or improved strategies for the *in vitro* prevascularization of TE constructs.

The batch-to-batch discrepancies associated to the processing of gellan gum (GG) spongy-like hydrogels, the 3D polymeric platform used to address our hypotheses, were minimized by understanding the link between the thermal parameters and the properties of the dried polymeric networks/spongy-like hydrogels. The mapping of these correlations allowed guiding the preparation of spongy-like hydrogels with specific pore size/microstructure knowing whether and how the bulk properties, such as the water content and compressive modulus, are affected. As such, we defined a powerful procedure to fabricate highly reproducible materials with fine-tuned microarchitecture according to specific needs. Indeed, the off-the-shelf availability as the dried polymeric networks that become spongy-like hydrogels after hydration, also allows extending the application of these materials beyond skin TE. The dried polymeric networks can be prepared with different forms and promptly combined with cells or bioactive molecules/drugs immediately before implantation in the surgical room according to the intended application.

As the different fibroblast's subpopulations have distinct functions in skin physiology, we provide evidence that pre-selection of papillary and reticular fibroblasts based on specific markers that allowed a higher accuracy in distinguishing cell phenotype than the dermatome-based isolation, is relevant for promoting the *in vitro* prevascularization of skin TE constructs. We further showed that both fibroblast-derived mediators and ECM differ among papillary and reticular cells, being therefore involved in a particular mode in the formation of the vascular network. Despite these promising results, to take advantage of the features of papillary and reticular fibroblasts in skin TE applications, the challenge to attain relevant cell numbers is still to be overcome. Adaptation of the culture conditions mostly to avoid loss of phenotype must be proposed. Yet, the developed vascularized bilayer construct built from pre-selected fibroblasts subsets holds potential as an *in vitro* platform to study the mechanisms controlling cutaneous microvasculature, such as microvascular maintenance and remodeling.

Aiming at maximizing the communication between fibroblasts and ECs, we sucessfully achieved the released of angiogenic proteins by transfected fibroblasts within a 3D microenvironment, in which new matrix capable of retaining the produced proteins was also secreted. With this, we propose a novel, selective and alternative approach to impact the vascularization of TE constructs, taking advantage of cells that are more accessible than ECs. Potentially, this *in situ* secretion of growth factors by genetically modified cells might tackle the limitations of other approaches such as the bolus release and short half-life of the delivered molecules as well as the high doses needed to achieve the desired effect. Vascularization is a process that undergoes short-term up- and down-regulation of several angiogenic growth factors, which can be precisely attained with the transient gene expression of non-viral vectors. Therefore, other vectors and factors might be further explored to target the respective expression window along the vascularization process.

For the first time we proposed an *in vitro* vasculogenesis platform that relies in the interaction between vasculogenic cells present in the stromal vascular fraction (SVF) of adipose tissue and integrin-specific spongy-like hydrogels within a self-regulated growth factor microenvironment. The matured platform forms a construct that benefits neovascularization upon implantation by fostering inosculation with the host vasculature confirming that prevascularization using other sources, such as SVF, are relevant to explore. While this confirms that prevascularization fosters the formation of new vessels in the neotissue, we also provide evidence that it might not be beneficial for cutaneous wound healing progression. This might be related to a faster influx of inflammatory cells to the injury site potentially due to its milieu. As different types of wounds and healing stages differ in that environment, in the future it is

imperative to address this hypothesis and tailor the therapeutic approaches to those specificities. Moreover, the phenotype of the SVF cells, considering an autologous context, is expected to vary with the etiology of the wound and the patient's status. For example, diabetes is associated with vascular disease and systemic alterations in endothelial progenitor cells not only at wound site but also in the adipose tissue affecting directly the cell source. In contrast, burns are characterized by a localized (although extensive in large wounds) and time limited inflammatory environment that can impact the outcome of the approach and potentially be determinant on deciding the need for the prevascularization step.

Overall, the works explored in the context of this thesis provides valuable contributions in the field of vascularization of TE constructs, proposing complementary and alternative approaches to the use of ECs, thus taking a step towards the development of improved therapies for cutaneous wounds.